Interactions of the Air Electrode with Electrolyte and Interconnect in Solid Oxide Cells

Tongan Jin

Dissertation submitted to the faculty of the Virginia Polytechnic Institute and State University in partial fulfillment of the requirements for the degree of

Doctor of Philosophy
In
Materials Science and Engineering

Kathy Lu, Chair
Guo-Quan Lu
William T. Reynolds, Jr.
Michael R. von Spakovsky

August 8, 2011
Blacksburg, Virginia

KeyWords: Solid Oxide Cells, Air Electrode, Interconnect, Chromium Poisoning, Sr-doped Lanthanum Manganite

Interactions of the Air Electrode with Electrolyte and Interconnect in Solid Oxide Cells

Tongan Jin

Abstract

The interactions between different components of solid oxide cells (SOCs) are critical issues for achieving the tens of thousands of hour's goal for long-term performance stability and lifetime. The interactions between the ceramic electrolyte, porous ceramic air electrode, and metallic interconnect materials — including solid state interfacial reactions and vaporization/deposition of some volatile elements — have been investigated in the simulated SOC operating environment. The interactions demonstrate the material degradation mechanisms of the cell components and the effects of different factors such as chemical composition and microstructure of the materials, as well as atmosphere and current load on the air electrode side. In the aspect of materials, this work contributes to the degradation mechanism on the air electrode side and provides practical material design criteria for long-term SOC operation.

In this research, an yttria-stabilized zirconia electrolyte (YSZ)/strontium-doped lanthanum manganite electrode (LSM)/AISI 441 stainless steel interconnect tri-layer structure has been fabricated in order to simulate the air electrode working environment of a real cell. The tri-layer samples have been treated in dry/moist air atmospheres at 800°C for up to 500 h. The LSM air electrode shows slight grain growth, but the growth is less in moist atmospheres. The amount of Cr deposition on the LSM surface is slightly more for the samples thermally treated in the moist atmospheres. At the YSZ/LSM interface, La enrichment is significant while Mn depletion occurs. The Cr deposition at the YSZ/LSM interface is observed.

The stoichiometry of the air electrode is an important factor for the interactions. The air electrode composition has been varied by changing the x value in $(La_{0.8}Sr_{0.2})_xMnO_3$ from 0.95 to 1.05 (LSM95, LSM100, and LSM105). The enrichment of La at the YSZ/LSM interface inhibits the Cr deposition. The mechanisms of Cr poisoning and LSM elemental surface segregation are discussed.

A 200 $mA \cdot cm^{-2}$ current load have been applied on the simulated cells. Mn is a key element for Cr deposition under polarization. Excessive Mn in the LSM lessens the formation of La-containing phases at the YSZ/LSM interface and accelerates Cr deposition. Deficient Mn in LSM leads to extensive interfacial reaction with YSZ forming more La-containing phase and inhibiting Cr deposition.

Acknowledgements

I would like to express my sincere gratitude to my supervisor Professor Kathy Lu. I am grateful for her invaluable guidance, patience and encouragement. Without her great support, the completion of my PhD would not be possible. I have learned a lot from her for research skill, analytical thinking and her diligence at work.

I would also like to acknowledge my advisory committee, Professor Guo-Quan Lu, Professor William T. Reynolds, Jr., and Professor Michael R. von Spakovsky for their insightful comments and helpful suggestions.

Financial support from Department of Energy under Award Number DE-FC07-06ID14739 and Office of Naval Research under award number N00014-11-1-0266 are sincerely acknowledged. I am indebted to Dr. James Rakowski and Dr Matthew Bender from ATI Allegheny Ludlum for providing interconnect materials for this work.

I would further like to thank Stephen McCartney, John McIntosh, Dr. Jerry Hunter, and Dr. Mitsuhiro Murayama, Nanoscale Characterization and Fabrication Laboratory, Virginia Tech for their kind help during microscopy works. Some X-ray diffraction analysis done in Chemistry Department is based upon work supported by the National Science Foundation under Grant No. DMR-0923107. I am thankful to Gilles Divoux and Mingqiang Zhang from Dr. Robert B. Moore research group, Chemistry department, Virginia Tech for their help for XRD.

The generous help from my colleagues from MSE and other departments is sincerely appreciated. I thank Dr. Manoj Mahapatra, Devid Berry, Dr. Yongke Yan, Dr. Junbo Hou, Dr. Ke Wang, Jianjun Yao, Kewei Xiao, Dr. Raghunath Thridandapani, Dr. Carlos Folgar, Dr. Jingzhong Zhao, Dr. James Shelby, Dr. Wenwei Ge, Zhiguang Wang, Katia Rodriguez, Tianle Cheng, Deepam Maurya, Su Chul Yang, Brain Scott, Tyler Horseman, Andrea Rojas, Chun-Hsien Wu, Dr. Niven Monsegue, Bo Chen, Wenle Li, Yongxuan Liang, Zhipeng Tian, Li Jiang and also all the staffs of the MSE Department for their help in the past three years. Thanks to them so much.

I would also like to thank Tyler Corey, an undergraduate student form MSE, Virginia Tech, for his diligent work helping me in this project.

I would like to take this opportunity to express my sincere gratitude to my former advisor, Professor Qingshan Zhu and my former colleagues, Dr. Huigang Zhang, Dr. Lian Peng, Dr. Bin Yu, Li Zhao, Dr. Zhigang Hao, Dr. Yong Wang, Dr. Tao Zhang, and Ling Tao from Institute of Process Engineering, Chinese Academy of Sciences, for their constant help and encouragements in my research career.

The ultimate admiration and respect are for my parents who have been supporting me in all my endeavors and give me love throughout my life.

Table of Contents

List of Figures

List of Tables

Chapter 1

Introduction

Abstract

This introduction chapter is organized into six sections. In the literature review, the background of the air electrode in the SOCs, the investigation of the interactions, and controversial of the Cr specie mechanism is reviewed. Section 4 and 5 provide the definition and analysis of the existing problems of the interactions and Section 6 discusses the issues of material characterization.

Solid oxide cells (SOCs), including Solid oxide fuel cells (SOFCs) and solid oxide electrolyzer cells (SOECs), are promising electrochemical devices that generate electricity from fuel or produce hydrogen by splitting water. For the SOFC mode, electric power is generated by electrochemical process between the fuel gases (hydrogen or carbon hydride) and air [1-5]. For the SOEC mode, reversibly, hydrogen or carbon monoxide can be produced by the electrolysis process splitting water or carbon dioxide [6-10]. The SOCs have already shown great potentials in new decades of clean energy for its high energy transition efficiency and low pollution exhausting.

SOFCs are being targeted for use in stationary power and heat generation for homes and businesses as well as auxiliary power units for electrical systems in vehicles. SOFCs also can be linked with a gas turbine, in which the hot, high pressure exhaust of the fuel cell can be used to spin the turbine, generating a second source of electricity [5,11]. On the other hand, hydrogen is considered as a clean energy resource and also one of the most acceptable forms of fuel available. SOEC, for hydrogen production, can be used as an efficient hydrogen generation device for instance surplus energy from wind turbines, nuclear power plants and geothermal plants [9,10,12].

The SOC materials, including electrolyte, air electrode, fuel electrode, interconnect, and sealing materials, must work at high temperature (600°C to over 1000°C) and in various atmospheres including fuel gases (hydrogen or hydrocarbon species) and air or oxygen. In order to commercialize SOCs for stationary and mobile applications, the requirement of long time

operation (10,000 – 40,000 h) must be achieved [13,14]. And lower the cost of the SOC materials is another critical issue. It is a great challenge to the materials. Extensive efforts have been devoted to develop new materials to improve the performance, stability, and economical efficiency of the SOC materials. One of the most noticeable achievements in years is that the SOC operational temperature is successfully reduced to 700 - 800°C by the advanced materials and processes. The SOCs working in the medium temperature require much lower cost of heating and give more chooses of materials. The most commonly used electrolyte material is yttria-stabilized zirconia electrolyze (YSZ), the fuel electrode and air electrode materials are Ni/YSZ and strontium-doped lanthanum manganite (LSM), respectively. The sealing and interconnect materials are very important to assembling cell stacks. At this lower temperature range, metallic interconnect materials can be applied replacing the ceramic interconnect, which greatly decreases the cost of material and processing.

However, some technical obstacles from the materials properties still inhibit the long term operation of SOCs. The degradation of electrode materials is an essential issue of the SOC system [14-16]. On the air electrode side, the interaction between the cell components lead to degradation of the SOC stacks. The porous ceramic electrode (usually LSM or other Perovskite ceramics) can fail fast by the effects of the chromia species when the Cr containing metallic interconnect is applied. The phenomenon called Cr poisoning is caused by the diffusion of volatile Cr species evaporating from the Cr-containing metallic interconnect [17-35]. During the operating of the SOCs, the Cr poisoning process is very complicated, which is affected by the diffusion of the volatile Cr species, the atmosphere, the electrical polarization, and the nature of the air electrode material. Until now, the mechanism of the Cr poisoning is not totally clear yet and becomes attractive which is the critical topic to or reduce the degradation and improve the performance of the SOCs. Furthermore, study of other interactions between the cell components such as the air electrode/electrolyte interactions and sealing/interconnect interactions is also current research focus in the SOC stack development.

From application point of view, the interactions are critical for the long-term stability of the SOC stacks. The detailed and quantification analysis of the interactions and degradation mechanism can provide knowledge of material evaluation and selection and microstructure design of the porous electrode layer and the interconnect.

1.1. SOCs: Principles, Materials, and Stacks

1.1.1. Background of SOCs

The concept of fuel cell has been known to science for more than one hundred years. In principle, fuel cells are designed based on the electrolyte providing ion conductivity to maintain the electrochemical reaction between the fuel and the oxidant. The applications of different electrolyte materials make the noticeable improvement of fuel cells. Fuel cells are classified by their electrolyte materials (Table 1-1).

Table 1-1. Types of Fuel Cells

Fuel Cell Type	Electrolyte	Operation Temperature	Electrode Reactions
Polymer Electrolyte	Polymer Membrane	60-140°C	$H_2 = 2H^+ + 2e^-$ $1/2O_2 + 2H^+ + 2e^- = H_2O$
Alkaline	Potassium Hydroxide	150-200°C	$H_2 + 2OH^- = H_2O + 2e^-$ $1/2O_2 + H_2O + 2e^- = 2OH^-$
Phosphoric Acid	Phosphoric Acid	180-200°C	$H_2 = 2H^+ + 2e^-$ $1/2O_2 + 2H^+ + 2e^- = H_2O$
Molten Carbonate	Lithium/Potassium Carbonate	650°C	$H_2 + CO_3^{2-} = H_2O + CO_2 + 2e^-$ $1/2O_2 + CO_2 + 2e^- = CO_3^{2-}$
Solid Oxide	Ionic Conductive Oxide	600-1000°C	$H_2 + O^{2-} = H_2O + 2e^-$ $1/2O_2 + 2e^- = O^{2-}$

The types of fuel cells under active development are summarized in Table 1-1. The alkaline fuel celsl (AFCs), polymeric-electrolyte-membrane fuel cells (PEMFCs) and phosphoric acid fuel cells (PAFCs) essentially require relatively pure hydrogen to be supplied to the anode. The AFC, PEMFC, and PAFC are easily to be poisoned by the impurity of the fuel gas (hydrogen) and oxidizing gas as well. Fox example, the potassium hydroxide electrolyte of the AFC is very sensitive to the carbon dioxide and depredates rapidly. These disadvantages restrict

their application. Accordingly, the use of hydrocarbon or alcohol fuels requires an external fuel processor to be incorporated into the system. This item not only increases the complexity and cost of the system, but also decreases the overall efficiency. In contrast, molten-carbonate fuel cells (MCFCs) and solid-oxide fuel cells (SOFCs) operating at higher temperatures have the advantage that both CO and H_2 can be electrochemically oxidized at the anode. Moreover, the fuel-processing reaction can be accomplished within the stack, and the tolerances of the CO_2, NO_x and sulfur oxides of the MCFCs and SOFCs are relatively higher [36].

SOFC has been widely investigated for over forty years [3-5], some test SOFC generator systems plant in the range of 5-250 kW level have been built since then [11,37]. It has been also known over twenty years ago that SOFC can work in the reversed way electrolyzing water and producing hydrogen (SOEC mode) [7]. The oxide ceramic electrolyte/electrodes are the key materials to obtain the intrinsically high electrical efficiency of the SOCs, which is the reason once the SOFC was called ceramic fuel cell. Recently, the increasing interest in hydrogen production has raised the interest in the SOECs. Both SOFC and SOEC are attracting more attention. The new system can be designed as reversible SOC mode. The material is the critical issue for the development of the SOCs with higher performance, longer life time, and lower cost. For SOFCs, DOE target requirements are 40,000 hours of service for stationary fuel cell applications and greater than 5,000 hours for transportation systems (fuel cell vehicles) at a factory cost of $400/kW for a 10 kW system [38]. For SOECs, the data of long time operation is not sufficient yet. In some research institutes, the long term testing of stacks is ongoing [39].

Doped ZrO_2 is recognized as the solid electrolyte material with the existence of oxygen vacancies at high temperature. The dense ZrO_2 based ceramic materials providing the O^{2-} conductivity made the foundation of further development of the SOCs in 1940-50s, which is still one of the mainstream electrolyte materials now [40]. In the 1960s, electrode materials of early SOFC were also developed. The nickel/yttria-stabilised zirconia (Ni/YSZ) cermet (ceramic-metal composite) is still the state of the art material for the anode. The catalyst property of Ni to hydrogen and the low cost make the composite material of Ni/YSZ based ceramic the choice of anode material for the SOFCs with ZrO_2 based electrolyte [41-45]. Another important improvement settled on the cathode material. Perovskite ceramic materials satisfied the functional requirements by its electron conductivity and catalytic properties to the oxygen reducing [3,4,28,41,42,46,47]. Doped $LaMnO_3$ (LSM) became the choice of the cathode material

for its capability of adjusting CTE by different doses of doping to match with the electrolytes [48-50]. The good chemical stability and compatibility comparing other perovskite oxide materials make LSM the most commonly used cathode material for SOFC [28]. Also, in the SOEC mode, LSM is generally employed for its excellent stability [9,10,51]. Beside the cell components, the SOC stacks design requires interconnect and sealing materials for assembling multiple single cells to obtain desired power output or hydrogen production. The interconnect of SOC stacks electrically and physically connects the fuel electrode of one cell to the air/oxygen electrode of the adjacent fuel cell in the stacks. The interconnect can be ceramic or metallic materials [52-61]. The sealant of SOC stacks working with the interconnect separates the fuel gas and the air/oxygen to avoid the mixing of gases from the two electrodes. And the sealing materials are normally glass or glass-ceramic composite materials [62-68].

The stack design plays a critical role in the commercialization of the SOCs. In order to obtain the desired power output or the hydrogen production, single cells are connected together by the interconnect [5]. In the 1970s, tubular design of SOFC stacks by Westinghouse was state of the art. The tubular SOFCs used the LSM/YSZ/Ni-YSZ material system, and $LaCrO_3$ was employed as the interconnect [37]. The comprehensive performance has been proved very good and stable in thousands of hours, which made it the mostly noticeable SOFC system at that time. Some other types of stacks such as segmented-cell-in-series tubular design and monolithic stacks design. After 2000, planar design of SOFC stacks attracted more attention and became the predominant design of SOCs for its advantages of lower cost by the much simpler cell shape [2,5,11,36,37,39,51,53]. The stack design of SOCs will be discussed in detail in 2.1.3.

Comparing with SOFC, there have been much fewer studies focused on SOEC. Since the investigation of hydrogen production by high temperature steam electrolysis (HTSE) utilizing was reported in early 1980's, SOEC has been designed for synthetic fuel (H_2 or CO) production [8,49]. SOEC has great potential for efficient and economical production of hydrogen fuel. In 1990's, the lower fossil fuel price made the SOEC unfavorable in the cost. After 2000, hydrogen has been identified as a potential alternative fuel as well as an energy carrier for the future energy supply. SOEC is attracting much attention due to its inherently high efficiency of electric energy conversion (over 50%) [5-10,39,51,53,69,70]. Now days, the SOECs are developed based the SOFCs systems, with similar structures and materials, and the working temperature (700-1000°C). In this case, the SOEC can be considered as a reversibly operated SOFC. Some of the

SOECs are reversible systems capable of operating both as a fuel cell and as an electrolyzer [70,71]. The SOEC is a promising energy conversion device to produce hydrogen or other fuel gas by electrolysis. By SOECs, hydrogen can be effectively produced by using wind energy, solar energy, geothermal energy, and nuclear energy, which is a valuable method in developing of alternative clean energy [9].

SOFC system based on the ZrO_2 based electrolyte such as most widely used Sr-doped lanthanum manganite (LSM)/yttria-stabilized zirconia electrolyze (YSZ)/Ni-YSZ SOFC, has been considered as a mature and success system [36]. On the other hand, in the early works, the performance of single tri-layered cells has been extensively studied. The electrochemical properties of the high temperature ceramic electrolyte and ceramic electrodes have been carefully evaluated. More material systems have been developed and investigated based on the different electrolyte materials [72]. For each given electrolyte material, the electrode materials must be evaluated to obtain the chemical and thermal compatibility with the electrolyte. The manufacture process should also be designed to compromise the materials [73,74]. There are more SOFC systems based on other electrolyte materials [75]. Of all the electrolyte materials, beside YSZ, two other types of representative materials have been studied: CeO_2 and $LaGaO_3$. Gadolinia doped ceria (GDC) and $LaGaO_3$-based perovskite type oxides, in particular, Sr- and Mg-doped $LaGaO_3$ (LSGM) both exhibit higher oxygen ion conductivity than YSZ [76-79]. The oxygen ion conductivities of GDC and LSGM at 500°C approximately equal to the oxygen ion conductivity of YSZ at 800°C, which shows a great potential of GDC and LSGM for the application in intermediate temperature SOFCs (ITSOFCs) [41]. However, the phase stability and chemical compatibility of these new electrolyte materials lead to some more problems. The different CTE also requires choosing the CTE matching cathode materials working with GDC and LSGM. Each electrolyte material needs a specific system of electrode materials to avoid the failure caused by the chemical interaction and CTE mismatch [80]. In summary, the ZrO_2 based electrolyte and its SOFC system is the most developed materials systems, the SOFCs based on GDC, LSGM, and other new electrolyte materials are still in development and need more work to improve their stabilities.

For the commercialization of the SOC devices, target of the SOCs long term operation requires the stability of all the components including sealing and interconnect materials to be stable in the various atmospheres and at the operating temperature. Lowering operational

temperature attributes to the long term stability by decreasing the degradation of cell components. The materials selection should also be considered as a factor to balance the performance and durability. Now days, more long term test of SOCs and SOC stacks are ongoing. The target proposed of 40,000 h of operating without significant degradation is still a challenge [38,41,42].

Lowering the operating temperature of SOCs to about 600–800°C is one of the main goals of the researchers in recent years. A reduction in operating temperature can reduce material degradation such as coarsening of the porous electrodes, lessen the coefficient of thermal expansion (CTE) mishmashes and sealing problems, and enable replacement of ceramic interconnects by cheaper metallic materials [42,47]. Furthermore, reducing the operational temperature also reduces the cost of fuel for heating all the cell stacks. So lowering the operational temperature has been recognized as the most important method to build more cost-effective and large scale SOC systems in the power general and clean fuel industry. The efforts have been devoting on the developing of new intermediate temperature SOCs.

1.1.2. Principles and Materials

As introduced above, the working principle of the SOCs is achieving electrochemical reactions of the fuel gases and the oxidant gases to generate electric power without involving the process of combustion (in the SOFC mode), or reversibly electrolyzing water (or other compounds) to general fuel gases and oxidant gases. The electrolyte is the part to obtain the electric/chemical energy conversions. If simply using the H_2/O_2 to represent the fuel/oxidant gases. The overall reaction of the SOCs can be expressed as:

$$\text{SOFC: } 2H_2 + O_2 \rightarrow 2H_2O + \text{heat} + \text{electrical energy} \quad (1\text{-}1)$$

$$\text{SOEC: } 2H_2O + \text{heat} + \text{electrical energy} \rightarrow 2H_2 + O_2 \quad (1\text{-}2)$$

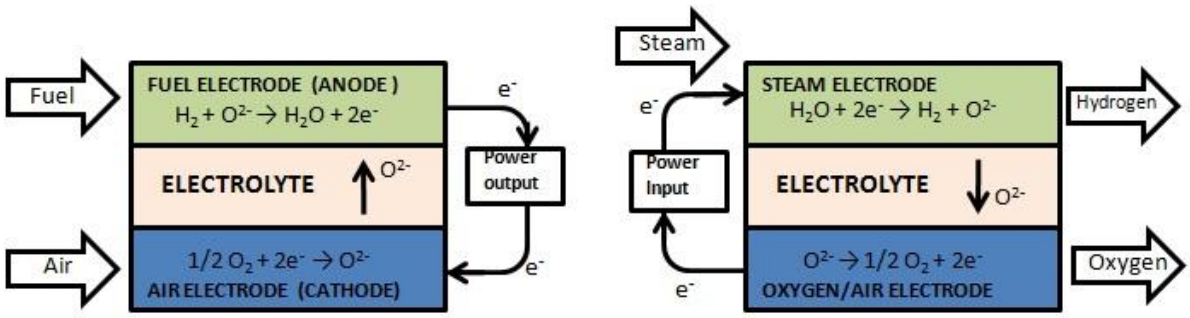

(a) (b)

Fig. 1-1. Principle of SOCs: (a), SOFC mode, (b), SOEC mode.

On each side of the electrolyte, there is an electrode/electrocatalyst obtaining the catalytic functions of oxidizing/reducing the gases to the correspondent ions. Beside the electrolyte, the activation and catalytic properties of the electrode can demandingly affect the performance of the SOCs.

The electrodes of the SOCs work with the fuel/oxidant gases and the solid oxide electrolyte with solid-solid interface. The surface and interface properties become very important as well as the internal properties. In order to provide efficient gas flow route, the electrodes are designed with particular porosity (generally around 40%). On the two sides of the electrolyte, Oxidant is fed to the air electrode, or oxygen electrode (cathode of SOFC), which is almost always oxygen in the form of air, and fuel is supplied to the fuel electrode (anode of SOFC). In SOFC mode, oxygen is reduced at the cathode, producing oxide ions (O^{2-}) which migrate through the electrolyte and react with the fuel at the fuel electrode. In SOEC mode, for the electrolysis of water with a solid oxide, water vapor is fed to the steam electrode to produce oxygen (on the air or oxygen electrode) and hydrogen gas (on the steam electrode, corresponding to the fuel electrode of SOFC).

Like other fuel cells, SOFC can provide more effective, high power density, and low waste way of electric power generation. For the SOFCs, the higher operation temperature produces high-quality waste heat which can be used. One of the most significant and noticeable feature of the SOFC is its high feasibility of fuel gases. Hydrogen is the most favorable fuel for SOFC. On the other hand, the hydrocarbon fuels have been investigated in the SOFC for a long time. The application of natural gas and large molecular hydrocarbon fuels gives SOFC a larger

range of using both fossil and hydrogen fuels [81,82]. Also, for SOFC, the tolerance of sulfur and other catalytic poisoning species is better than other fuel cells, which is potentially lower the cost of purifying the fuel gas [36]. For SOEC, the efficiency is potentially higher that other water electrolysis devices, for its high working temperature [9]. The other advantage is that the revisable mode can work as both SOFC and SOEC, which means that one electrochemical device can work as both electric power generator and hydrogen producer [70].

Materials of the SOC components are essential to the cell performance. Many improvements in the SOC research are brought by the development of new materials. In order to improve the performance and the durability, there are also challenges to the materials development and selection [36,41,42].

The electrolyte is the key material always first selected in one particular SOC system, which decides the working temperature and the CTE requirement of other cell component. The standards of selection of electrolyte materials are more established by practical method. The chemical and thermal compatibility with electrode must be considered comprehensively with the selection of the electrode materials. The main issue on the electrolyte is reducing the ohm resistance and reducing solid/solid interaction with the electrodes. Beside the YSZ and GDC electrolyte, the perovskite LSGM exhibit high oxide ion conductivity. The conductivity of $La_{0.9}Sr_{0.1}Ga_{0.8}Mg_{0.2}O_{3-x}$ is 0.12 S/cm at 800°C and 0.32 S/cm at 1000°C, which is higher by a factor of two compared to 8YSZ (0.16 S/cm) [40,83]. Although the investigation of the ion conductor electrolyte materials has been carried on for decades, there are just a few candidates, such as YSZ, GDC and LSGM, have been investigated extensively. For the processing issue, the dense electrolyte layer is preferred to be made very thin, which can effectively reduce the ohm resistance attributed by the electrolyte [74].

For the fuel/steam electrode, the material selection is mostly porous materials composited by metal (Ni or Cu) and ceramic (generally the corresponding electrolyte material to minimized the interfacial reaction) such as Ni/YSZ and Ni/GDC. The development of the fuel electrode of SOFC is normally aimed to improve the flexibility to different fuel gas. For the hydrocarbon fuel gases, the resistance to the carbon deposition must be considered for the long term stability. Also, the tolerance to the sulfur and other species potentially poisoning gases in the fuel gas should also be considered [84].

The air/oxygen electrode materials has been mostly investigated in the entire SOC electrochemical process and is still the most complicated and controversial part. There are many candidate materials have been applied as the air/oxygen electrode. The requirement of decreasing the polarization resistance is the essential issue. Furthermore, for the SOCs employing Cr-containing metallic interconnects, Cr poisoning becomes a major degradation mechanism of the air electrode. The more detailed discussion of the air/oxygen electrode will be in the following sections.

The electrolyte and electrodes make up a single cell, the sealing and interconnect materials play important roles in the stacks to connect the single cells together. Glass and glass-ceramic materials are considered as the most desirable candidates to seal ceramic electrode-metal interconnect and ceramic electrolyte-metal interconnect at high temperatures because of their ability of forming a hermetic seal [63-65]. The thermal properties and surface/interface stability of the glass based sealing materials are the requirements.

The purpose of the interconnect materials is to connect each cell in series, so that the electricity each cell generates can be combined. Because the interconnect is exposed to both the oxidizing and reducing side of the cell at high temperatures, it must be very stable. Both ceramic and metal materials can be used as the interconnect materials. A detailed introduction of interconnect will be in the following section.

1.1.3. SOC Stacks

In order to obtain desired electric power output or hydrogen production, the single SOCs must be fabricated together to form meet the requirements of application. Since a single cell only produces voltage less than 1 V and power around 1 W/cm^2, many cells are electrically connected together in a cell "stack" to obtain higher voltage and power [2,85,86]. The power and voltage of the fuel cell is increased by connecting individual cells in series to form a stack, with each cell connected to its adjacent cell using an electrically conducting interconnect which also serves to distribute reactant across the surface of the electrodes using flow channels[57,58,86].

In this case, beside the performance of single cells, more issues are brought out such as the more complicated gas flow situation and the temperature distribution in a much larger scale which need to be carefully designed [2,85]. Concerning the material issues, sealing and

interconnect materials play important roles in the SOC stacks, which requires the compatibility of these materials with the electrode and the electrolyte materials.

For the SOFC mode, tubular design is used in high temperature and the planar design is used in intermediate temperature SOFCs (Fig. 1-2). The tubular stacks designed by Westinghouse have been operated for long time [37]. The cells are LSM/YSZ/Ni-YSZ tri-layered and cathode supported. The tubular stack design is for the operational temperature about 1000°C, the interconnect material is $LaCrO_3$, and with a simple sealing solution. The main disadvantage of the tubular stack is the fabrication is relatively complicated so that the manufacture cost is hard to be reduced. The forming of electrolyte layer on the cathode support layer is obtained by vapor deposition or spry method. For the reasons above, the planar designs ("Flat-plate design" in Fig. 1-2) of the SOFC stacks are developed by many researchers [73,74,87]. The fabrication of planar cells can be finished by simpler process such as tape casting and screen printing. The planer cell stacks are mostly used for the intermediate temperature SOFCs. So the material selections and geometry designs are various. Anode support, cathode support and electrolyte support have all been tested. For different material system, the design needs to be adjusted. One of the widely used planar SOFC stacks is still LSM/YSZ/Ni-LSM but with anode support. The sealing becomes important in the planar stacks, and the interconnect materials are normally metal for the lower temperature. For the SOEC mode, just a few reports with stack design have been published, where planar stacks are mostly used.

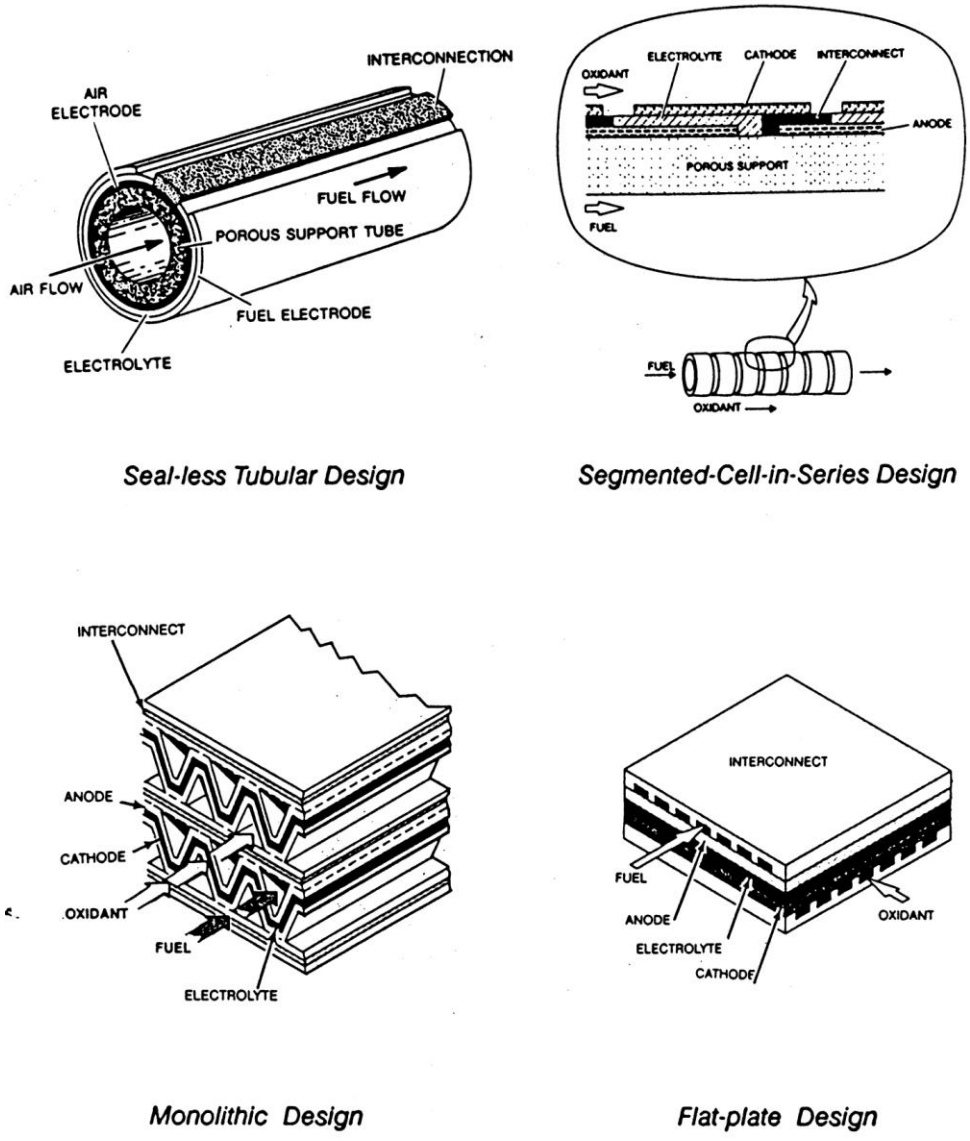

Fig. 1-2. Tubular and planar SOC stacks design [2,86].

1.2. Air Electrode of SOCs

1.2.1. Requirements of Air Electrode Materials

The function of the air electrode to the efficiency and operation stability of SOC devices has been believed critically important. The electrochemical reactions of oxygen occur on the air electrode side require the catalytic activity to oxygen at the first. The overall electrochemical

reactions catalyzed by the air electrode of SOFC/SOEC have been expressed in Equation 1-1 and 1-2, where the detailed process is much more complicated.

Like all the materials in the SOC devices, the air electrode material must maintain the demanding selection criteria. The air electrode materials must maintain the catalytic activity at the high operation temperature and in various atmospheres (the oxygen partial pressure effects). The compatibility with other cell components (such as the electrolyte and the interconnect) including the match of the CTE and the acceptable chemical interaction between the components in touch with each other requires more beside the basic electrochemical property. Furthermore, the air electrode material must keep all the properties stable in order to achieve the long term operation target. Other issues such like processing and cost are also need to be considered [1,2,41,47]. The general requirements of the air electrode materials of the SOCs are listed below:

Intrinsic Properties

- High electrocatalytic activity towards oxygen reduction: to effectively catalyze the oxygen reducing reaction.
- High electronic conductivity: to minimize the ohmic resistance of the air electrode
- Thermal expansion compatible with other SOC materials: to avoid the stress caused by CTE mismatch between cell components, which can lead to cracks of cells.
- Minimal chemical interaction with the electrolyte and interconnect materials during fabrication and operation: prevent the possible solid phase interaction between the electrolyte and the air electrode leading to increasing of interface resistance.

Processing Related

- Porous, stable microstructure to allow gas transport: to optimize the flow paths fuel and oxidant gases to obtain high energy conversion efficiency.
- Adhesion to electrolyte surface: to obtain a stable and conductive electrolyte/air electrode interface.
- Ease of fabrication and low cost: to make the SOCs feasible and promising as alternative energy generation and conversion devices.

Stability

- Stability (chemical, phase, microstructural, dimensional) at high temperature in oxidizing atmosphere: long term stability is the critical requirement for SOC commercialization.

As the SOCs are designed, the air electrode materials should possess high electrical conductivity and high electrocatalytic activity for the oxygen reduction reaction (SOFC) or oxygen ion oxidization reaction (SOEC).

For the SOFC mode, the SOFC cathode must meet the requirements of high catalytic activity for oxygen molecule dissociation and oxygen reduction. Although the SOFC cathode reaction have been investigated for several decades, the process of electrochemical reduction of oxygen reducing remains controversial and lack of explanation Because the oxygen reducing contains a series of elementary reactions and involves the transfer of multiple electrons. The experimental results show that the different steps can be rate-determine for different cathode materials. This difficulty of characterizing and analyzing the oxygen reducing process is not only from the complexity of the multi-step process but also enhanced by the geometric complexity of the porous microstructure where the oxygen reduction reaction occurs. These reasons make it difficult to provide a step-by-step prescription to for the cathode process of the SOFCs [47,48,87,88]. More discussion about the electrochemical process on the air electrode side of the SOCs will be in Section 2.2.3.

Comparing to the activity to the oxygen reducing, the electron conductivity of the cathode of SOFC is simpler. The adoption provides the electron conductivity to the materials. The ohm resistance is relatively low and stable in the working atmosphere and at the operational temperature. The ohm resistance can be decreased by thinner the air electrode thickness. However, the ohm resistance from the electrode material is not the main part of the full cell [89,90].

The cathode must have a stable, porous microstructure so that gaseous oxygen can readily diffuse through the cathode to the cathode/electrolyte interface. The microstructural parameters such as grain size, porosity, and pore size leading to different surface property, geometry of the porous air electrode and the gas flow route. The can significant affect the polarization resistant and the cell performance. However, the porous air electrode layer are mostly formed by screen printing or tape casting and sintered. The effects of grain size, porosity, pore size and even the

pore geometry cannot be easily analyzed separately. Many researches considered the effects of ceramic powder size or sintering conditions getting qualified results [91-94]. Mathematical model is also employed to study the porous structure [95]. Some regular shaped electrode are made by special methods to help studying the three phase boundaries (TPBs) [96,97].

CTE mismatch during the SOC cell fabricating and operation can lead to cracks and failures of the full stacks [98]. The only way to solve the CTE mismatch is choosing compatible materials such like perovskite ceramics for the electrode of the SOCs can obtain different CTEs by adjusting the adopting mount. CTE gives a strict standard of materials selection. The LSM air electrode usually works with YSZ electrode, which has very similar CTE (10.8×10^{-6} K^{-1}) to the LSM (11.8×10^{-6} K^{-1}) [99]. Another important air electric material for SOFC, $La_{1-x}Sr_xCo_{1-y}Fe_yO_3$ (LSCF) has higher CTE which is designed to work with GDC electrolyte (CTE ~12.8×10^{-6} K^{-1}) [100,101] .

At the interface between the air electrode and the electrolyte, for example, LSM cathode and YSZ electrolyte, interaction occurs, where, $La_2Zr_2O_7$ and/or $SrZrO_3$ may be formed, which degrades the long-term performance of SOFCs for the new phases show large electric resistance and CTE mismatch on the interface. The interaction can be inhibited by changing the stoichiometry of the LSM by adding more Mn in the LSM, forming nonstoichiometery compound [102].

As mentioned above, stability is an essential requirement of the target of commercialization of the SOC devices. Extensive efforts have been devoted to lowering the operation temperature which can significantly improve the durability of the SOCs, especially the SOC stacks. Because many harmful degradation processes become much slower in lower temperature, such as chemical interactions between the electrodes/electrolyte or electrode/interconnect interfaces, the change of the porous microstructure, and the inner stress caused by the mismatch of the CTEs. For the SOEC studies, there are few studies about the air electrode process. There is the lack of experimental results and the polarization resistance plays a minor role in this electrolysis mode.

1.2.2. ABO_3 Perovskite Oxides

Since the researchers have been seeking the ways to lower the operational temperature, the sufficient catalytic property of the electrode material to the oxygen must be maintained at the

lower temperature (600–800°C). Excluding precious metals such as Pt by their high cost, perovskite ceramics with particular catalytic activity and conductivity is the only kind of air electrode materials successfully applied in the SOCs [50].

A typical perovskites oxide material can be usually presented as ABO_3, which crystallizes in cubic close-packed lattice structure. The larger ions (e.g., La) occupy the 12 coordinated A-sites and the smaller ions (normally transition metal ions e.g., Mn) occupy the octahedral B-sites. The typical crystal structure of the ABO_3 perovskite oxide material is shown in Fig. 1-3 The crystial structure and the electronic structure of the metal ions make the perovskite oxide materials performing a great flexibility inherent in the structure and there are many different types of distortions which can occur from the ideal structure. The diversity of perovskite structure compounds which can be partly doped by other metal ions to introduce desired distortions, which provides the wide range of electrical, magnetic, optical and chemical (catalyst) properties over a wide temperature range [49,103-105].

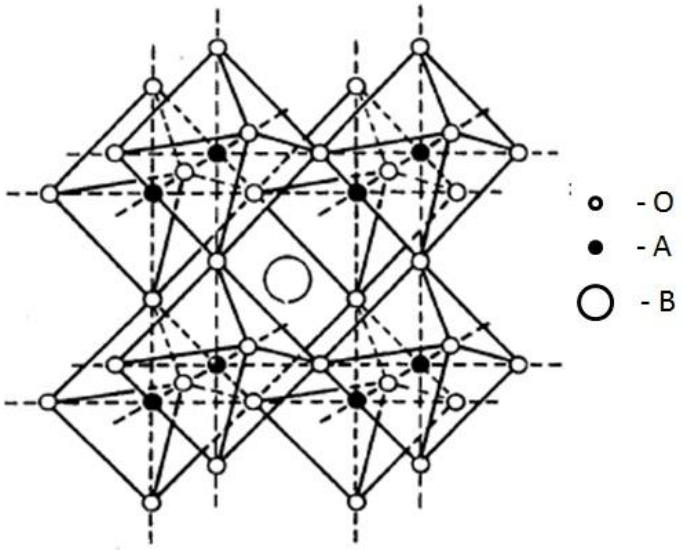

Fig. 1-3. Crystal structure of ABO_3 perovskite oxide [103]

As discussed above, some perovskite oxide ceramics provide the properties meeting the requirement of SOFC air electrode. The properties researchers concerning are the electric conductivity, the catalyst property to oxygen, and the ionic conductive (which is not necessary). The electric and catalyst properties are also affected by the temperature and the atmospheres (oxygen partial pressures). Of course the CTE must be pre-evaluated to choose the compatible electrolyte system. Many perovskite oxide materials have been tested [80]:

Table 1-2. Perovskite-type oxide materials for the air electrode of the SOCs: coefficient of thermal expansion, electronic (σ_e), and ionic conductivities (σ_i) in air [102].

Composition	CTE ($\times 10^{-6}$ K^{-1})	T (°C)	σ_e ($S \cdot cm^{-1}$)	σ_i ($S \cdot cm^{-1}$)	References
$La_{0.8}Sr_{0.2}MnO_3$	11.8	900	300	5.93×10^{-7}	[99]
$La_{0.7}Sr_{0.3}MnO_3$	11.7	800	240	–	[106]
$La_{0.6}Sr_{0.4}MnO_3$	13	800	130	–	[107]
$Pr_{0.6}Sr_{0.4}MnO_3$	12	950	220	–	[107]
$La_{0.8}Sr_{0.2}CoO_3$	19.1	800	1,220	_	[108,109]
$La_{0.6}Sr_{0.4}CoO_3$	20.5	800	1,600	0.22	[101]
$La_{0.8}Sr_{0.2}FeO_3$	12.2	750	155	–	[108,110]
$La_{0.5}Sr_{0.5}FeO_3$	–	550	352	–	[111]
	–	800	369	0.205	[112]
$La_{0.6}Sr_{0.4}FeO_3$	16.3	800	129	5.6×10^{-3}	[101]
$Pr_{0.5}Sr_{0.5}FeO_3$	13.2	550	300	–	[113]
$Pr_{0.8}Sr_{0.2}FeO_3$	12.1	800	78	–	[113]
$La_{0.7}Sr_{0.3}Fe_{0.8}Ni_{0.2}O_3$	13.7	750	290	–	[110]
$La_{0.8}Sr_{0.2}Co_{0.8}Fe_{0.2}O_3$	20.1	600	1,050	–	[113]
$La_{0.8}Sr_{0.2}Co_{0.2}Fe_{0.8}O_3$	15.4	600	125	–	[114,115]
$La_{0.6}Sr_{0.4}Co_{0.8}Mn_{0.2}O_3$	18.1	500	1,400	–	[116]
$La_{0.6}Sr_{0.4}Co_{0.8}Fe_{0.2}O_3$	21.4	800	269	0.058	[117]
$La_{0.6}Sr_{0.4}Co_{0.2}Fe_{0.8}O_3$	15.3	600	330	8×10^{-3}	[101,115]
$La_{0.4}Sr_{0.6}Co_{0.2}Fe_{0.8}O_3$	16.8	600	–	–	[115]
$La_{0.8}Sr_{0.2}Co_{0.2}Fe_{0.8}O_3$	14.8	800	87	2.2×10^{-3}	[101]
$La_{0.8}Sr_{0.2}Co_{0.8}Fe_{0.2}O_3$	19.3	800	1,000	4×10^{-2}	[101,117]
$La_{0.6}Sr_{0.4}Co_{0.9}Cu_{0.1}O_3$	19.2	700	1,400	–	[107]
$Pr_{0.8}Sr_{0.2}Co_{0.2}Fe_{0.8}O_3$	12.8	800	76	1.5×10^{-3}	[101]

$Pr_{0.7}Sr_{0.3}Co_{0.2}Mn_{0.8}O_3$	11.1	800	200	4.4×10^{-5}	[101]
$Pr_{0.6}Sr_{0.4}Co_{0.8}Fe_{0.2}O_3$	19.69	550	950	–	[109]
$Pr_{0.4}Sr_{0.6}Co_{0.8}Fe_{0.2}O_3$	21.33	550	600	–	[109]
$Pr_{0.7}Sr_{0.3}Co_{0.9}Cu_{0.1}O_3$	–	700	1236	–	[118]
$Ba_{0.5}Sr_{0.5}Co_{0.8}Fe_{0.2}O_3$	20	500	30	–	[119]
$Sm_{0.5}Sr_{0.5}CoO_3$	20.5	700 ~ 900	>1,000	–	[120,121]
$LaNi_{0.6}Fe_{0.4}O_3$	11.4	800	580	–	[122]
$Sr_{0.9}Ce_{0.1}Fe_{0.8}Ni_{0.2}O_3$	18.9	800	87	0.04	[101]

As shown above, the electronic and ionic conductivity are relatively simple and inert properties of the electrode materials. The electric conductivity is the required property, which all tested air electrode materials shows acceptable electronic conductivity. The electronic conductivity can also be significantly increased by thinner the cathode layer and optimized the porous structure.

The ionic conductivity is related to the atmosphere. In air, LSM shows very low ionic conductivity and make the oxygen ion diffusion path controlled by the surface and TPB. Many other perovskite materials with improved ionic conductivity can affect the performance by providing oxygen ion diffusion path through the bulk of the cathode. The investigation of ionic conductivity provide two different processes of the air electrode operations: surface diffusion of non-ionic conductors (e.g LSM), and mixed electronic/ionic conductors (e.g LSCF) [48].

The catalyst property with oxygen is much more complicated which is related with the stoichiometry and also strongly affected by the oxygen partial pressure in the atmosphere. The process of the oxygen reduction is even more complicated, the electron/ionic conductivity work together with the surface/interface catalyst and more than one steps are involving. Furthermore, the phase stability of the perovskite in the range of different partial oxygen pressure needs to be considered. The material properties, porous properties, and the atmosphere

Oxygen nonstoichiometry is critical to the performance of the perovskite materials. The major non-stoichiometric defects of this type of perovskite oxides are cation vacancies and the oxygen vacancies are also present [46]. The electronic conductivity is introduced by the cation

vacancies. The oxygen vacancies introduces considerable oxygen ionic conductivity in some materials which are called mixed conductors [123].

The typical oxygen stoichiometries of the representative air electrode materials is shown in Fig. 1-4. First of all, the $La_{1-x}Sr_xCo_{1-y}Fe_yO_{3-\sigma}$ (LSCF) shows oxygen-deficient nonstoichiometry. In comparison, $La_{1-x}Sr_xMnO_{3\pm\delta}$ (LSM) can have both the oxygen-excess as well as the oxygen-deficient nonstoichiometries. In the SOC air electrode environment, the oxygen partial pressure is high enough making the LSM in the oxygen-excess state. So the significant difference lead by the oxygen stoichiometry is the oxygen ion conductivity. The very large concentrations of oxygen vacancies in LSCF generated in these leads to rapid bulk oxygen ionic transport as well as increased rates [99].

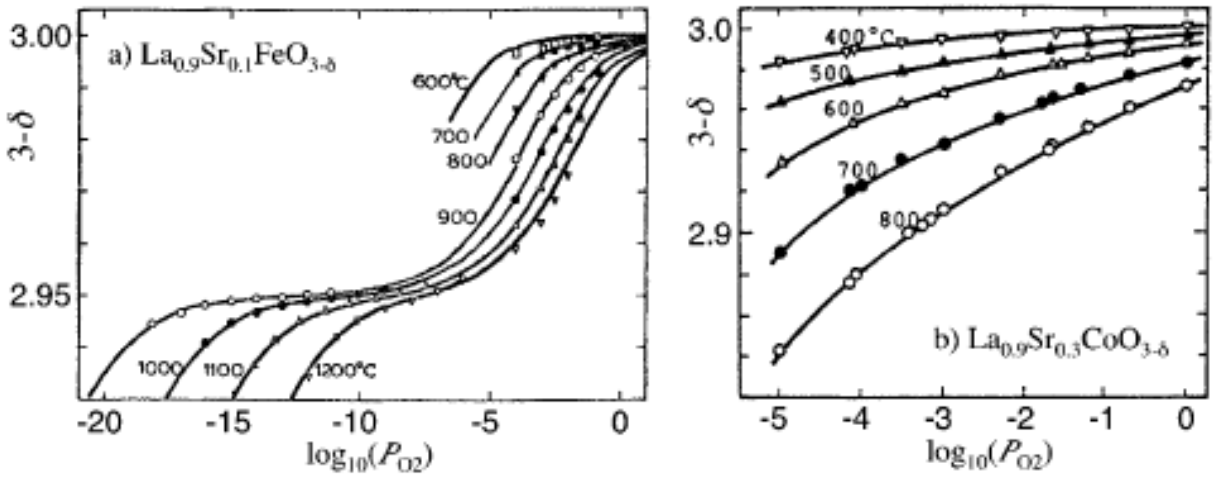

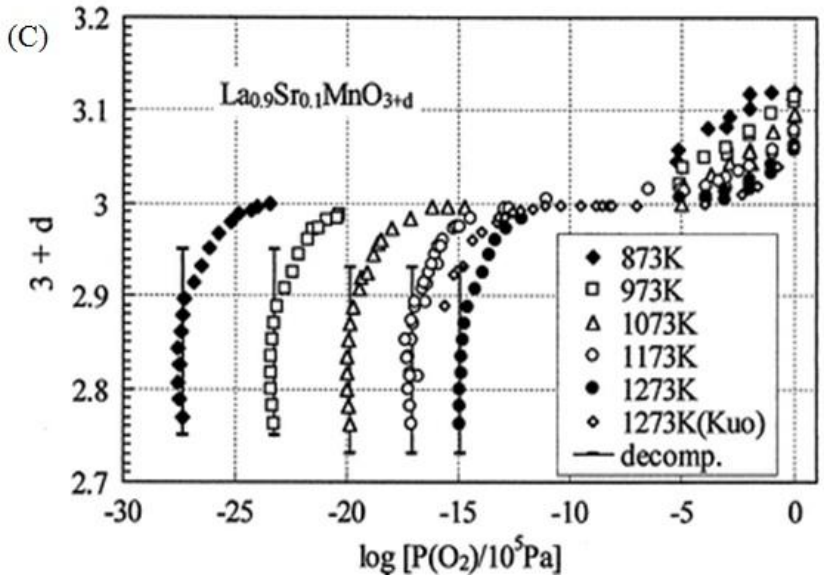

Fig. 1-4. Oxygen stoichiometry samples of LSF, LSC, and LSM [28,48].

Numbers of other perovskite oxide materials have been also applied for the air electrode of the SOFCs, such as $Ba_{0.5}Sr_{0.5}Co_{0.8}Fe_{0.2}O_3$ (BSCF) and $LaNi_{0.6}Fe_{0.4}O_3$ (LNF). BSCF has been investigated for the cathode of SOFC working at low temperature (600-650°C) and for the single chamber design. The performance of the BSCF is very high at that low temperature [124-127]. LNF is designed as an air electrode material with higher resistance to the Cr poisoning. However, more long term tests are needed for developing new perovskite oxides for the air electrode [28]. The thermal and chemical stability becomes very important in the long time tests. Mn is generally less reducible than other transition metals (Co, Fe) in a perovskite matrix, and thus LSM exhibits little or no chemical expansion [128]. Generally, LSM is that it is more thermodynamically stable than mixed conductors containing cobalt or iron (LSCF) [129].

As discussed above, many other perovskite materials show good properties and higher performance as the air electrode. However, the stability is not always good enough for many of the materials. In the temperature range 800-1000°C, LSM is still the state of the art air electrode material for SOFCs [102].

In SOEC mode, the available data is not sufficient and almost all the test has been done in LSM oxygen electrode [6,8-10,39]. Until now, LSM is the most well-investigated and promising air/oxygen electrode material for the SOCs.

1.2.3. Electrochemical Processes and Triple Phase Boundary

The electrochemical processes of the SOCs are fairly complicated for the materials for the gas catalyst reactions affected by many external conditions such as the atmospheres and electric polarization. Furthermore, the geometry parameters of the porous electrodes and the gas flow give more difficulties of the reaction condition control. On the aspect of SOFC efficiency, the cathode polarization causes the major voltage loss of the SOFC. The resistant loss from the air electrode/electrolyte interface cause by cathodic polarization has been investigated widely by the electric impedance spectroscopy (EIS) [47,130,131]. The cathode polarization is more significant in the LSM/YSZ system because the relatively poor ionic conductivity of LSM, which can contribute 60% of voltage loss of the whole SOFC [130]. For the SOEC mode, there is lack of detailed result to analyze the polarization loss.

In order to clarify the electrochemical reaction on the air electrode side of the SOFC, the basic concepts such as chemical reaction, electron/ion diffusion path, and materials and conditions of the process must be carefully defined and classified to study the mechanism.

First of all, the electrochemical reducing reaction of oxygen in the air electrode of SOFC is:

$$O_2\ (gas) + 2e^-\ (cathode) \rightarrow O^{2-}\ (electrolyte) \qquad (1\text{-}3)$$

where three reaction path can be listed below [47]:

1. The electrode surface path includes oxygen gas diffusion, adsorption of oxygen on the electrode surface, diffusion of (possibly dissociated and partly ionized) oxygen species along the surface toward the TPB where electrolyte, electrode, and gas phase meet, followed by complete ionization and ionic transfer into the electrolyte. The incorporation into the electrolyte does not necessarily occur directly at the TPB; surface or interface diffusion of the ionized species could lead to a certain broadening of the incorporation zone.
2. The bulk path consists of oxygen gas diffusion, adsorption on the air electrode surface, dissociation and ionization, incorporation into the air electrode, oxide ion transport through the electrode, and the transfer of the ion into the electrolyte.

3. The electrolyte surface path includes oxygen gas diffusion, adsorption, and ionization on the electrolyte surface (with electrons being provided by the electrolyte), followed by a direct incorporation into the electrolyte. The very low electronic conductivity of most relevant electrolytes (particularly of zirconia) can be expected to restrict the active zone to a region very close to the TPB. Hence, this path is, from a geometrical point of view, similar to the electrode surface path discussed above.

The three possible reaction paths briefly demonstrate the locations where oxygen reducing reactions occur which helps the investigation of geometric parameters. However, for each path, excluding the geometric parameters, the more detailed reaction mechanism should be analyzed [48]. Also, modifications of the paths (e.g., adsorption of a molecular rather than an atomic species or diffusion along the air electrode/electrolyte interface) and a combination of electrode and electrolyte surface paths (adsorption on air electrode and surface diffusion onto the electrolyte surface) are also possible [47,132].

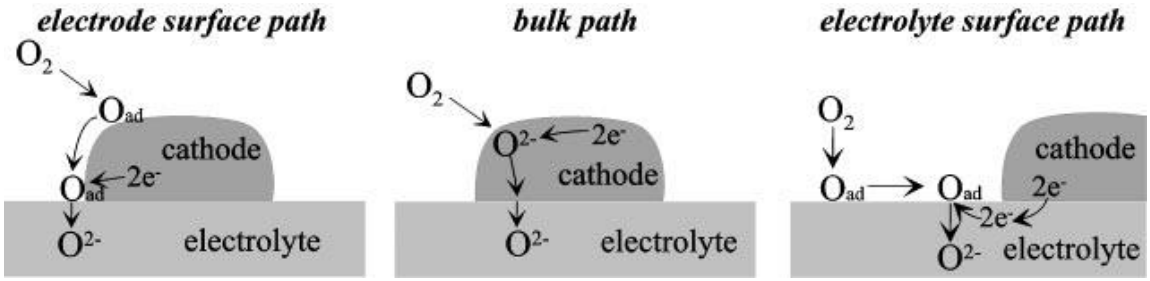

Fig. 1-5. Sketches of three reaction paths of the oxygen reduction and incorporation reaction and some possible rate-determining steps [47].

Second, in order to analyze the reaction detail of the air electrode, parameters influencing the corresponding reaction or transport rate and thus the polarization resistance can be divided into three groups [47]:

1. Independent of the material properties, the external parameters oxygen partial pressure $p(O_2)$ (or, more general, gas composition), overpotential, and temperature explicitly enter the reaction rates and thus the polarization resistance.

2. Reaction or transport rates depend on materials properties. For a given material, these properties are determined by the structure and composition of the bulk air electrode material (and thus also by factors such as doping level, impurities, number and microstructure of grain boundaries) and the structure and composition of the surfaces/interfaces (i.e., termination, orientation, segregated species, nonequilibrium interface defects, etc.). The materials properties usually depend on temperature and can also be affected by $p(O_2)$ and overpotential/bias voltage.
3. Geometrical parameters such as TPB length, surface area, interface area, porosity, electrode thickness, and exact distribution of all phases constitute a third group of parameters that strongly affect the reaction rate.

The strategies to study the oxygen reducing reaction mechanism are based on carefully control the parameters and analyze the EIS characterization. The complexity of the three groups of internal and external parameters and their interferences (for example, atmosphere and electric current can easily change the vacancy structure of the perovskite materials [49,104]) give extensive difficulties to analyze the contribution of each particular parameter.

In the early works of SOFC air electrode material selection, many perovskite materials have been investigated in different atmospheres ($p(O_2)$). As listed above, the effects of parameters group 1 (external: temperature, atmosphere and electric current) to parameter group 2 (internal properties: conductivity) has been studied. There are many useful results of the important internal material properties, such as ionic/electronic conductivity have been provided. The major representative perovskite air electrode materials are divided into two groups: LSM family (electronic conductors) and LSCF family (electronic/ionic mixed conductors) [48]. The dependences of materials properties with temperature and atmosphere are relatively simple. The electric current brings the most complex effects to the air electrode.

For LSM, the electronic conductivity is dependent to temperature, which is about 100-300 $S \cdot cm^{-1}$. And the ionic conductivity is as low as 10^{-7} $S \cdot cm^{-1}$.[99,106,107,133,134]. Due to the very low ionic conductivity of LSM phases, the oxygen reduction is thought to be located at the TPB between air electrode, electrolyte and gas. However, the oxygen diffusion path makes the overall process far more complex than the reaction happens only on the TPB.

Comprising with the LSM family, the LSCF family with much higher ionic conductivity attracts considerable attention. The bulk path of oxygen ion diffusion becomes a considerable mechanism. The oxygen reducing mechanism on the mixed conductor air electrode has been identified as the combination of bulk and surface transport paths [99,114,115,135]. The LSM is more interesting in this work. The process of oxygen reducing in the LSM air electrode will be briefly reviewed below.

As discussed above, the air electrode materials can be classified as electronic conductor and electronic and ionic mixed conductor, which give out the different oxygen diffusion paths and makes different electrochemical processes (Fig. 1-6) [48,132].

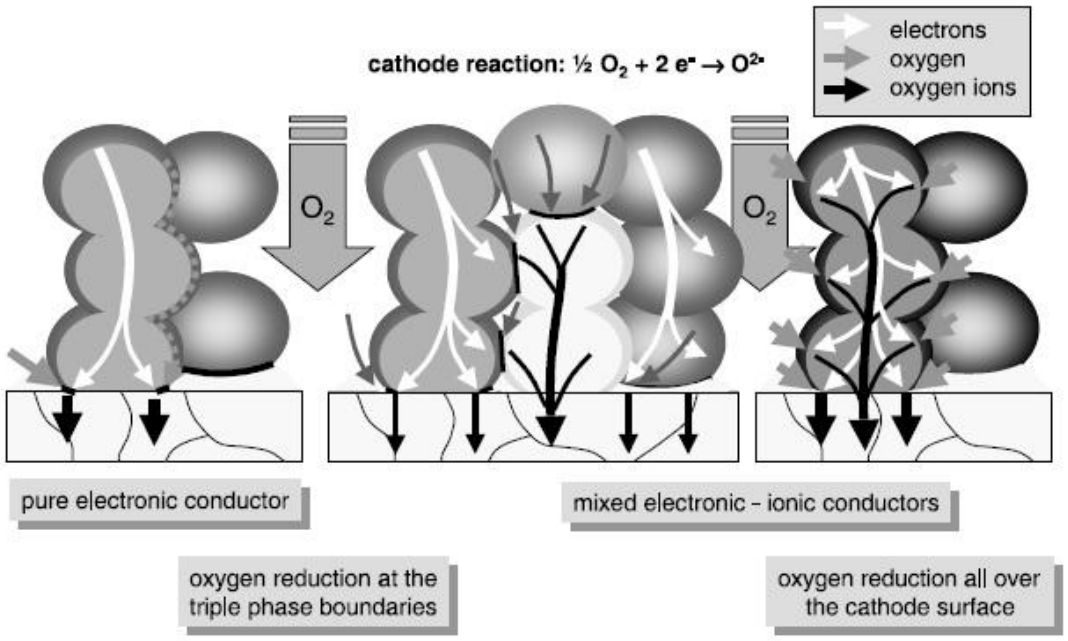

Fig. 1-6. Electrochemical processes of different air electrode materials of SOFC [136].

Among the steps for the oxygen reduction reaction, there are at least two steps associated with oxygen diffusion: oxygen surface exchange between the electrode and gaseous phase, and surface and/or bulk diffusion of oxygen species. In the LSM air electrode, the TPB is not the only effect of the reaction. The surface diffusion path has been found by the $^{16}O/^{18}O$ isotope exchange measurement. A gradual decrease of isotope oxygen concentration was observed in the LSM layer followed by a flat profile at the interface. This shows that the oxygen diffusion in the LSM layer is slow [137,138]. The result indicates that the oxygen can be reduced on the LSM

surface and diffuses to the TPB. There is also some work proves that the bulk diffusion path is also present in some case with polarization.

The term “three phase boundaries (TPB)” is where electrolyte and electrode contacts, and gases are feed on. The SOCs must obtain proper gas flow designs for their electrochemical processes of generating electrical power from fuel gas and oxygen (SOFC mode) or producing hydrogen (SOEC mode). So the porous electrodes are employed for the gas feeding. In order to investigate the processes of fuel gases/oxygen, the TPB is considered playing an important role in the electrochemical catalysis and ion/electron diffusion [48,138-140].

First of all, in order to figure out the behavior of the TPB and achieved the quantitative result, the geometry of the porous electrode must be well controlled to obtain the length of the TPB. The early research of Fukunaga et al quantitatively calculates the length of TPB of porous LSM air electrode, revealing that the cathode overpotential of the SOFC can be effectively decreased by increasing of the TPB length [139,141]. Furthermore, new technology such as laser deposition technique has been used to make micro-electrodes with regular shape to quantify the geometry parameters and obtain the precise controlled TPB [97,142,143]. The impedance results show the electric current plays a very important role in the oxygen diffusion. As shown in Fig. 1-7, the bulk path and surface path are coexist when the current is applied on the LSM electrode [143].

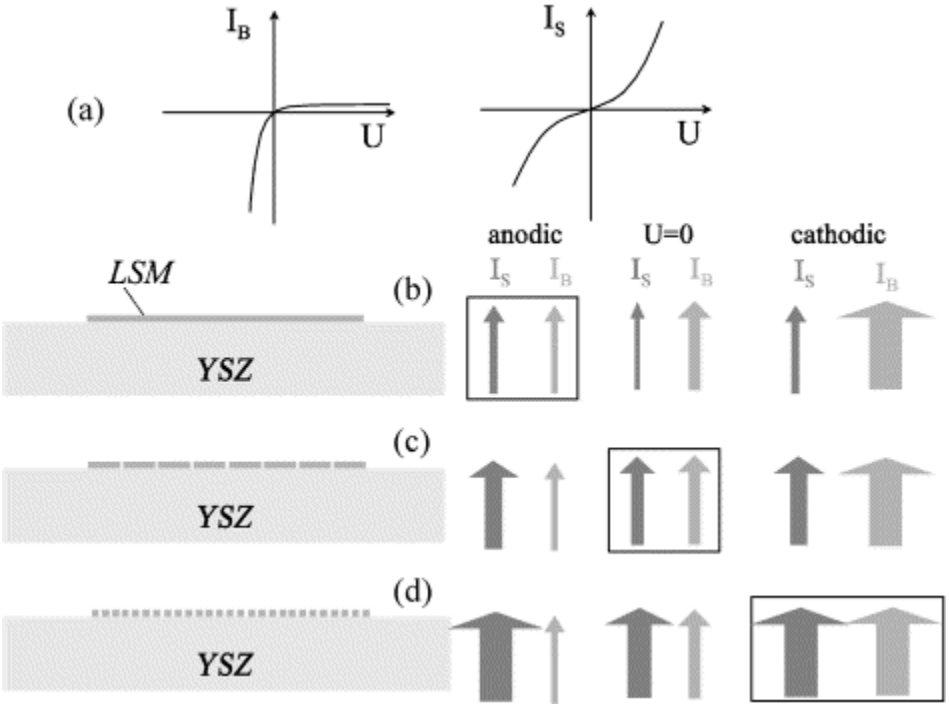

Fig. 1-7. Sketch to illustrate that the electrode geometry influences the "weight" of the current via bulk path I_B and via surface path I_S and, therefore, the transition from dominating bulk to dominating surface path. (a) Sketch of the two current–voltage characteristics assumed in these qualitative considerations. (b–d) Sketch of the corresponding current via bulk and surface path. The thickness of the arrows indicates the value of the current via bulk and via surface path. The three boxes correspond to $I_B=I_S$ and, hence, to the transition from surface path to bulk path. Obviously, the voltage at which this transition occurs depends on the electrode geometry [143].

After all, the mechanism of the oxygen reducing on the air electrode of the SOFC (both LSCF and LSM) is not well defined yet. The bulk/surface transport of oxygen ion is competing and strongly dependent to the electric current. Furthermore, fabrication is another famous factor affecting the performance [28,48].

Significant advances have been made in recent years in the development of air electrode materials and it is now essential that efforts are directed toward the optimization of the air electrode fabrication and structure.Although there are still issues not clear for the oxygen reducing mechanism in the porous air electrode especially with the polarization, some general agreements have been achieved. For the LSM porous electrode, increasing the TPB and surface area improves the performance contributed by the active surface area. The functional layer thickness is confirmed as several μm to about twenty μm. On the technology side, LSM/YSZ composite air electrode has been widely applied to improve the air electrode performance by increasing the TPB area.

1.3. Metallic Interconnect

1.3.1. Requirements of Interconnect

To connect multiple cells together, an interconnection is used in SOC stacks [52-61]. As stated above, the purpose of the interconnect materials is to electrically and physically connect each cell in series, so that the electricity each cell generates can be combined. The metallic interconnect can also supply mechanical support for the SOC stacks. The requirements of the interconnection are the most severe of all cell components and include:

1. Nearly 100 percent electronic conductivity: to maintain the current in the stacks and minimized the loss from the internal resistance.
2. Stability in both oxidizing and reducing atmospheres at the cell operating temperature: since it is exposed to air (or oxygen) on the air electrode side and fuel on the anode side, it is important to keep the electric conductivity and mechanical properties, avoiding degradation and failure during long-term operation.
3. Low permeability for oxygen and hydrogen: to minimize direct combination of oxidant and fuel during cell operation.
4. A thermal expansion coefficient close to that of the air electrode and the electrolyte; and non-reactivity with other cell materials: the thermal and chemical compatibilities with the ceramic cells are critical to the long term performance of the whole stack.

To satisfy these requirements, the ceramic interconnect materials have been employed in the earlier researches [53,54]. The most well-known ceramic interconnect material, doped lanthanum chromite ($LaCrO_3$, LSC) is used as the interconnection for cells intended for operation at 900-1000°C [54,144-146]. The ceramic interconnects generally shows matching CTE with ceramic cells and good chemical stability in the different atmospheres [54,60]. However, there are some disadvantages of the ceramic interconnects. The conductivity of ceramic interconnect is not high, such as doped LSC with electric conductivity of 40-60 S cm^{-1} at 1000°C. The conductivity of LSC at lower temperature and in lower oxygen partial pressure is even lower, which is harmful to the power generation efficiency and restricts the application of the ceramic interconnect (especially in lower temperature such as 600-800°C). Furthermore, the material cost of ceramic interconnect such as LSC is high and the fabrication of ceramic interconnect is more complicated than metallic interconnect which also lead to a higher cost [74]. The interconnect, which in some case also works as the bipolar plate and support of the stacks, needs larger amount of materials. The higher cost also makes ceramic interconnect less favorable.

In SOC cells intended for operation at lower temperatures (<900°C), it is possible to use oxidation-resistant metallic materials for the interconnection. Compared to ceramic interconnects (LSC), metallic alloys offer advantages such as improved manufacturability, significantly lower raw material and fabrication costs, and higher electrical and thermal conductivity [2,53,57-61,147]. But to be useful for the interconnect application, the metallic alloys must satisfy

additional requirements, including resistance to surface oxidation and corrosion in a dual atmosphere (simultaneous exposure to oxidizing and reducing atmospheres), high electrical conductivity not only through the bulk material but also in in-situ-formed oxide scales, mechanical reliability and durability at the cell operating temperature, and strong adhesion between the as-formed oxide scale and the underlying alloy substrate [44,60]. Ni based, Cr based, and ferritic alloy haven been tested for the metallic interconnect material [57].

For the metallic interconnect, most studies are focused on ferritic stainless steel. Chromium is the necessary ingredient in the interconnect to reduce oxidation under SOFC/SOEC operating conditions [56]. Compared with nickel-based and chromium based alloys, ferritic stainless steels are the most promising candidates for its low cost. Some specially designed alloys in the stainless steel family offer a protective and conductive chromium-based oxide scale, appropriate thermal expansion behavior, ease of manufacturing. Although these alloys demonstrate improved performance over traditional compositions, several critical issues remain; among these are chromium oxide scale evaporation and subsequent poisoning of air electrodes; scale electrical resistivity in the long term; corrosion under interconnect exposure conditions; and compatibility with the adjacent components such as seals and electrical contact layers. To overcome some of these problems, some surface coatings can be applied onto metallic interconnects to minimize scale growth, electrical resistance and chromium volatility [57,58].

1.3.2. Oxidization and Evaporation of Cr-containing Alloys

A variety of alloy systems have been investigated as interconnect materials, such as Fe-Cr, Ni-Cr, and Fe-Ni-Cr alloys [56-58]. The common trait of these systems is that they all form a surface layer of Cr_2O_3, or chomia, under the oxidizing atmosphere, and this layer provides high temperature oxidation resistance. The surface scale growing is considered as a method to resist the high temperature corrosion. Si, Al and Cr oxide scales are normally designed as the oxidation resistant scale on the alloy surface. Si and Al scales show better oxidation resistance than Cr scale, but for the interconnect of the e SOCs; the electric conductivity of the oxidization scale is necessary. So Cr-containing alloys forming Cr oxidation surface scale (sometimes including other elements such as Mn) become the choice of the SOC interconnect material [59]. Among the Fe-Cr, Ni-Cr, and Fe-Ni-Cr alloys, ferritic stainless steel (Fe-Cr alloy, with 10-30 wt% Cr and other minor components) is more promising for its low cost [58].

Chomia (from the oxide scale on the surface of Cr-containing alloys) evaporates at high temperatures and forms gaseous CrO_3 species. The pressure of the gaseous CrO_3 increases with oxygen partial pressure. The moisture in the oxidizing environment can cause chomia to evaporate as well, in the form of $CrO_2(OH)_2$. Water contents above 0.1% in air result in the partial pressure of $CrO_2(OH)_2$ to exceed the partial pressure of CrO_3 [23,56,148,149]:

$$Cr_2O_3+3/2O_2 \rightarrow 2CrO_3 \quad (1\text{-}4)$$

$$Cr_2O_3+3/2O_2+2H_2O \rightarrow 2CrO_2(OH)_2 \quad (1\text{-}5)$$

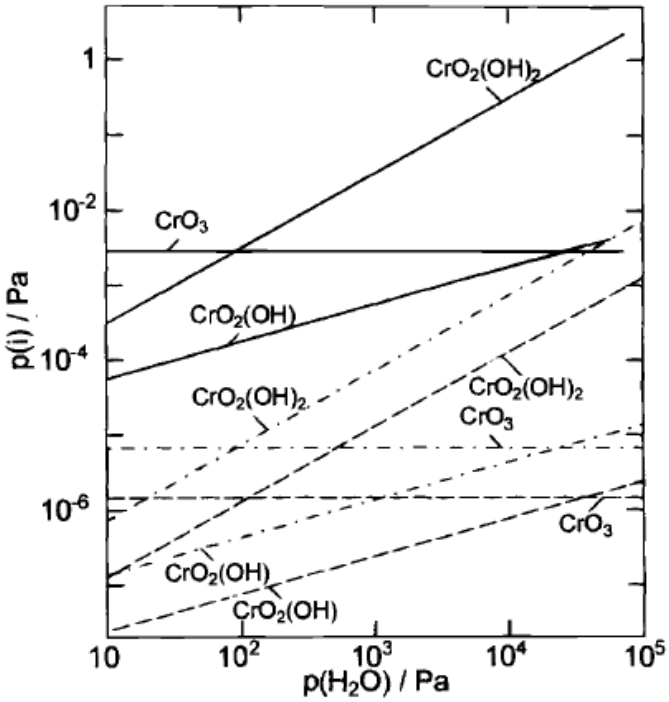

Fig. 1-8. vapor pressure of the Cr volatile species in different water vapor containing air at 1223K [23].

There are many alloys (all of them contain considerable chromium) have been applied as the interconnect materials for the SOCs [57,150]. The chromium-based alloys and nickel-based alloys have been considered by their capability of working in high temperature. Also, ferritic stainless steel was designed for SOC applications after the working temperature is lower than

900°C. Stanislowski et al. and Fergus [57,150-152] compared the component of different metallic interconnect materials and the amount of Cr evaporation of each sample.

Table 1-3. Nominal compositions of alloys for the SOC interconnect [57,150-152].

Alloy	Concentration (wt%)		
	Cr	**Fe**	**Y_2O_3**
Ducrolloy ($Cr5FeY_2O_3$)	Bal	5	1.0

	Concentration (wt%)								
	Ni	**Fe**	**Cr**	**Mo**	**Mn**	**Co**	**Si**	**Al**	**Zr**
Haynes 242	Bal	<2	8	25	<0.8	<2.5	<0.8	<0.5	

	Concentration (wt%)								
	Fe	**Cr**	**Ni**	**Al**	**Si**	**Mn**	**Ti**	**Mo**	**Nb**
AISI 441	Bal	17.6	0.20	0.045	0.47	0.33	0.18		0.46
E-Brite	Bal	24.1	o.11		1.7	1.3	0.05	0.96	
Crofer 22 APU	Bal	22.7	0.02	0.02	0.02	0.38	0.07		

In Table 1-3, Ducrolloy (also referred as $Cr5FeY_2O_3$) is a representative Cr based alloy, which has been tested in many early researches [153-156]. Haynes 242 is a representative Ni based alloy, which shows good conductivity and CTE close to YSZ [151,157-160]. And all others are Fe based alloy. In the chosen alloys, the requirements of CTE and electric conductivity at high operating temperature of SOCs mostly have been matched. The CTE of the alloys is controlled by the composition to be $10.0\text{-}12.0\times10^{-6}\cdot K^{-1}$ which is a little higher than YSZ [55,57]. The acceptable resistance is 25-50 $m\Omega\ cm^2$ [55]. The primary different between the Cr and Ni based alloy and the Fe based alloy is the surface oxidization. Cr and Ni based alloys such as Ducrolloy and Haynes 242 mainly form Cr_2O_3 on their surface during oxidization at SOC operational temperature. For ferritic stainless steel with small content of Mn (< 0.5 wt%) can form a $(Mn,Cr)_3O_4$ spinel top layer on the surface. Although the volatile Cr species are still released, the evaporation rate is slower. Some works investigated the $(Mn,Cr)_3O_4$ spinel top layer

[56,160,161]. Crofer 22 APU is one of the ferritic stainless steel designed to form spinel layer for the SOC application and E-Brite forms Cr_2O_3 on the oxidized surface. For Crofer 22 APU and E-Brite are widely investigated metallic interconnect materials [56,62,162-165]. The Cr vaporization rates of different high-temperature steels were measured directly [150]. It was shown that the Cr vaporization rates of the ferritic stainless steels, specifically developed for application as interconnector materials in SOFCs, such as Crofer 22 APU are very similar. These alloys form a well-adhered $(Cr, Mn)_3O_4$ spinel top layer that reduces Cr vaporization rates in humid air at 800°C by 61–75% when compared to alloys that form pure chromia scales like Ducrolloy and E-Brite [150].

AISI 441 (also referred as T 441), a similar ferritic stainless steel alloy with higher yield strength and lower cost, is also being considered as an alternative interconnect material [147,166-169]. Like Crofer 22 APU the surface scale growth is also $(Cr, Mn)_3O_4$ spinel layer [160]. The CTE of AISI 441 matches the other SOF components [170]. The AISI 441 alloy is considered as an economical and promising interconnect material for the SOCs, the long term test in SOC stacks is no going [152,169].

From the previous quantitative measurements of Cr volatile species vaporization rate, the release rates of Cr volatile species from ferritic stainless steel (with similar Cr content) are similar [30,150]. However, the reduced Cr evaporation rate still cannot inhibit the Cr poisoning in SOC application [30,156,160]. So coating on the metallic interconnect is an effective way to reduce the Cr evaporation [59]. The coating materials mainly include spinel and perovskite oxide materials for their similar structure and CTE to the air electrode materials obtaining the thermal and chemical compatibility. The electric conductive of the coating is also need to be high enough to avoid the extra ohmic resistance. $(La,Sr)CrO_3$ and $(La,Sr)FeO_3$ perovskite oxides was tested as the coating for the interconnect. $(La,Sr)CrO_3$ shows better conductivity and the Cr-containing coating need to be further evaluated to make sure it can effectively reduce the Cr evaporation [171]. $(Mn,Co)_3O_4$ oxide is the most common spinel coating, which can be fabricated by slurry method, sol-gel technique, and electro deposition method [172,173]. Some tests have been delivered, which shows the Co, Cu and Ni-containing metal oxide coatings can reduce the Cr evaporation rate in 1000 h test [174]. More long-term test of coated interconnect needs to be provide to further evaluate the stability. Another solution was reported by Konysheva et al. In this work, the thickness of LSM contact layer between the LSM/YSZ composite air electrode

and the Cr-containing interconnect is controlled between 0-50 μm. The contact layer is also working as a "coating" or "buffer layer" which probably adsorbs Cr on the surface and reduces the Cr diffusion. The result shows that the thick LSM contact layer can reduce the amount of Cr volatile species. The concentration of the gaseous Cr species could be diminished due to their adsorption in the thick porous LSM contact layer at 800°C in over 1000 h [29].

1.4. Interactions between Cell Components on the Air Electrode Side

Due to the high operational temperature of the SOCs, the interactions between the cell components including sealing and interconnect materials must be considered for the long term durability of the whole system. Degradation of the SOC performance along the time is almost entirely caused by the degradation of the materials. For the porous fuel electrode and air electrode, the aging or over-sintering of the porous microstructure leads to decrease of the active site of the electrochemical reaction [84]. The interfacial interactions between the electrodes, electrolyte, and also the sealing/interconnect materials is also the major factor of materials degradation under the SOC operation. Beside the solid state interfacial reactions, the catalyst poisoning caused by volatile Cr species from the interconnect plays another important role of the degradation. For some long term stack experiments from 2000–6000 h, the degradation is attributed to the interaction between the electrolyte and the air electrode, the Cr deposition at the air electrode, and the interaction of glass-ceramic sealant with metallic interconnect [136,175-177]. Understanding the interaction and compatibility of the SOC components is critical to choose the materials and improve the long term stability.

1.4.1. Interactions between Air Electrode and Electrolyte

One single SOC cell contains three layers: fuel/hydrogen electrode, electrolyte and air/oxygen electrode, which are generally thin ceramic layers. Both of the electrodes are porous to maintain the gas flow. On the air electrode side, the electrolyte/electrode interaction is a well-known issue affecting the contact resistance of the cell. For the commonly used YSZ/LSM system, the $La_2Zr_2O_7$ and $SrZrO_3$ are the phases formed in the interfacial interaction. Obviously, these undesired phases are formed predominantly at the TPB area causing an increase of the resistance [13,178-181]. The interaction is affected by temperature and chemical composition, as

well as cathodic polarization. Higher temperature is beneficial to the formation of $La_2Zr_2O_7$ phase. For LSM, a larger amount of La and Sr in the stoichiometry leads to easier formation of $La_2Zr_2O_7$ and $SrZrO_3$ [178,180]. In some reports, the polarization accelerates the formation of the foreign phases, but the effects are not very clear, which is because the undesired phases forms and change the resistance and the polarization accordingly [182].

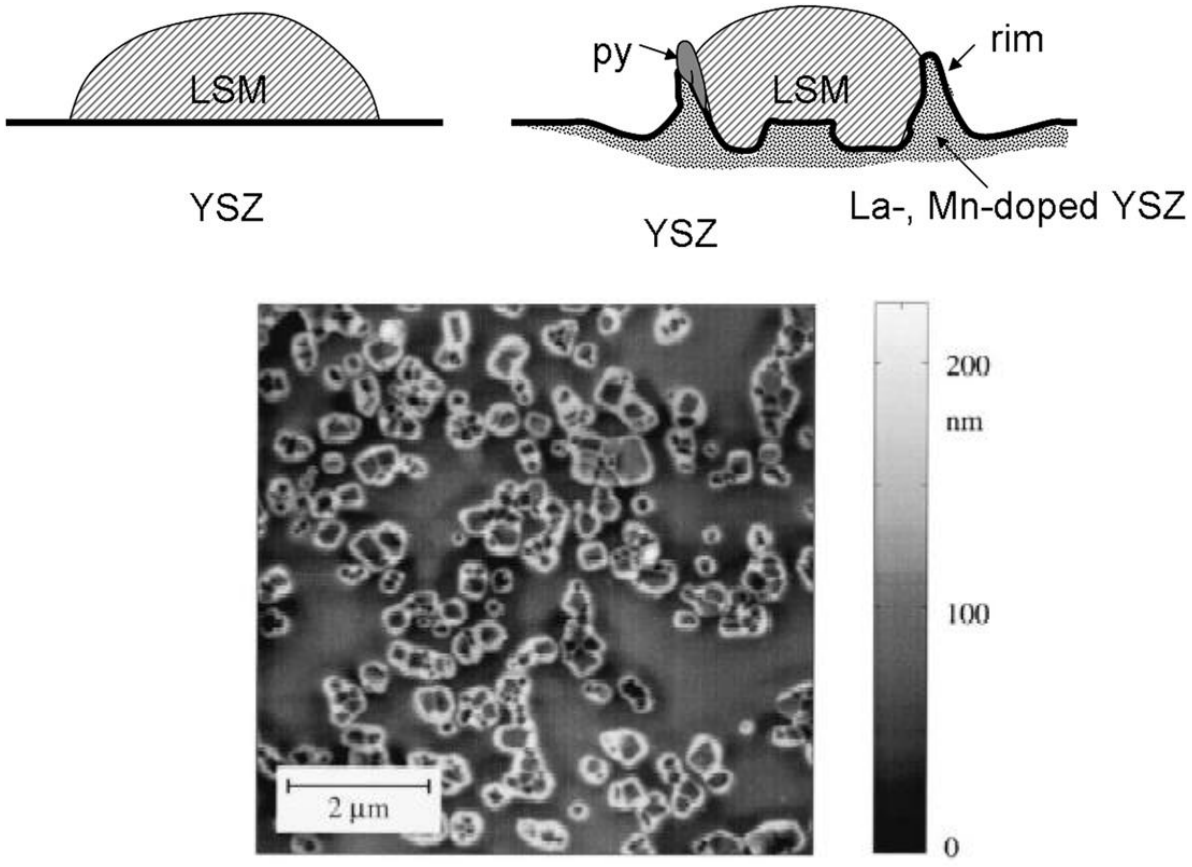

Fig. 1-9. Formation of $La_2Zr_2O_7$ [178,179].

For the ferric based air electrode such as $La_{1-x}Sr_xCo_{1-y}Fe_yO_3$ (LSCF), the chemical compatibility with YSZ electrolyte is much worse than the LSM air electrode, where the $SrZrO_3$ formation is extensive [131]. Gadolinium doped ceria (GDC) is generally applied as the barrier layer in between the LSCF air electrode and the YSZ electrolyte (Fig. 1-10) [183-185]. The diffusion of Sr can be inhibited. However, the GDC barrier layer leads to complex structure and higher manufacturing cost, and the long term stability needs to be tested.

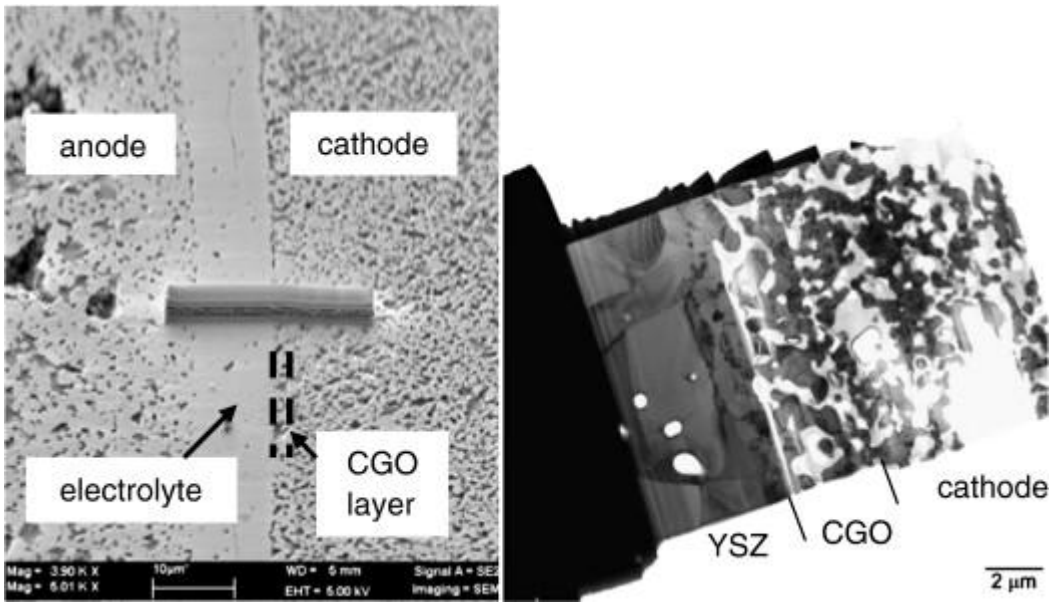

Fig. 1-10. Cross section of a single cell with an anode (fuel electrode)/YSZ electrolye/ CGO (GDC) barrier layer/LSCF cathode (air electrode) structure [185].

1.4.2. Interactions between Other Components

Besides the electrolyte and the electrodes, sealant and interconnect materials are critical for the SOC stacks. Glass or glass-ceramic sealant and metallic interconnect are the main-stream materials for the planar SOCs [63,66,186,187]. The interactions related to the sealant and interconnect are also very important. For their application, different cell components need to be hermetically sealed at all times in order to prevent gas mixing, leakage, or internal combustion. This requirement places extreme demands on a seal glass to perform in severe environments involving high temperatures, thermal stress, and chemically aggressive conditions [22,188-190]. Undesirable interaction at the metal/glass interface can lead to cracking of the glass seal and mixing of fuel and oxygen containing gases [57,62,191,192]. The interconnect/glass sealant interfacial behavior is also affected by different atmospheres. These issues are often exacerbated by long term operation (>40,000 hrs), high temperatures (750-900°C), and corrosive atmospheres (wet reducing), which frequently drive materials into regimes where conventional understanding of material behaviors and transport processes is not sufficient.

The sealing must be chemically and structurally stable in SOFC/SOEC high temperature reactive environments (moist reducing and/or oxidizing conditions), and demonstrate chemical

compatibility with interconnect materials [64,193-198]. Also, seals should have good bonding with the cell components that they seal. In addition, a seal glass must have high devitrification resistance. Volatile constituents (e.g., alkaline oxides) should be avoided. If there are any volatile species, they should not have a deleterious effect on cell performance.

The vapor phase deposition happens in the porous air electrode layer as well as the solid state interfacial interactions. When the low-cost Cr-containing ferritic alloy is used as the interconnect to collect the current and support the stacks, the volatile Cr species can cause serious poisoning to the air electrode, which is one of the major degradation mechanisms. Furthermore, other impurities such as Si from the sealant and S or P from the contaminated air flow are also found to be related to some deposition [199,200]. The Cr poisoning behavior will be discussed in detail in the following section.

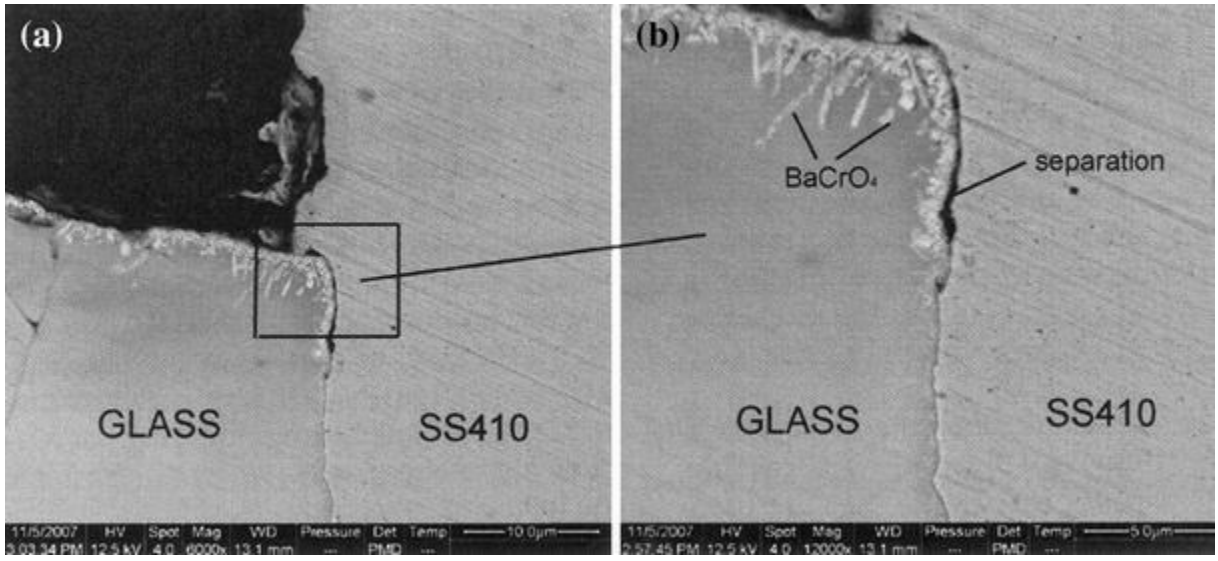

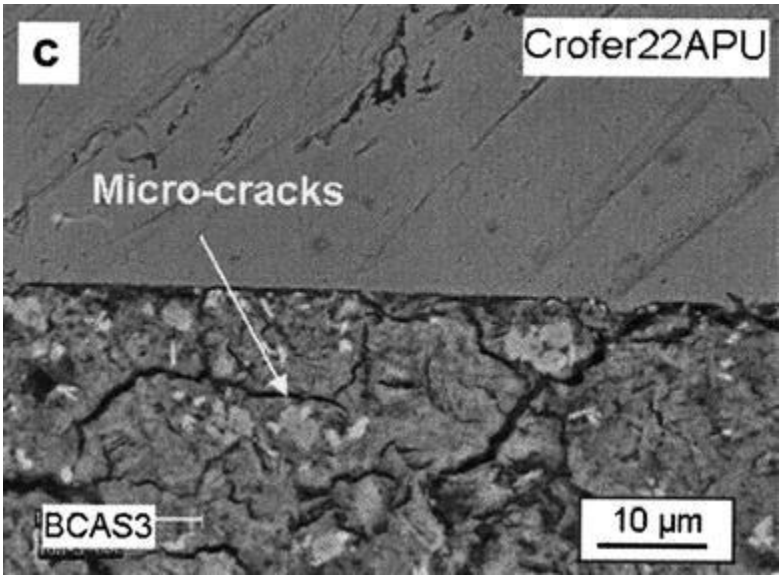

Fig. 1-11. Some possible leaking of the sealant/interconnect area [201,202].

1.5. Chromia Poisoning

1.5.1. Cr Deposition Behavior on the Air Electrode Side of SOCs

The Cr volatile species generated by the Cr-containing alloy interconnect of the SOCs lead to degradation of the cell stack. Chromium poisoning of SOC air electrodes occurs by gas-phase transport of chromium from the interconnect material to the air electrode [23,149]. The chromium transport occurs primarily through the formation of Cr^{6+}-containing species, such as CrO_3 or $CrO_2(OH)_2$, from oxidation of chromium oxide in the interconnect [22-27,29-33].

Hilpert et al [23]. used thermodynamic calculations to investigate the Cr evaporation and deposition processes, and claimed that the Cr volatile species are sensitive to the water vapor content, even the water vapor was over 0.1%, the major gaseous Cr phase becomes $CrO_2(OH)_2$ instead of CrO_3 in dry air. Also, Hilpert et al. [23] pedicted the electrochemical and chemical Cr deposition reactions [23].

Cr evaporation:

$$Cr_2O_3+3/2O_2 \rightarrow 2CrO_3 \quad (1\text{-}4)$$

$$Cr_2O_3+3/2O_2+2H_2O \rightarrow 2CrO_2(OH)_2 \quad (1\text{-}5)$$

Cr depostion:

1) Electrochemical reaction

$CrO_3\ (g) + 3e^- = 1/2Cr_2O_3\ (s) + 3/2O^{2-}$ (1-6)

$CrO_2(OH)_2\ (g) + 3e^- = 1/2Cr_2O_3\ (s) + H_2O(g) + 3/2O^{2-}$ (1-7)

2) Chemical reaction

$La_{1-x}Sr_xMnO_3(s) + 1/2Cr_2O_3(s) = La_{1-x}Sr_xMn_{1-y}Cr_yO_3(s) + (Cr_{1-y}Mn_y)O_{1.5-\delta}(s) + \delta/2O_2(g)$ (1-8)

$La_{1-x}Sr_xMnO_3(s) + yZrO_2(s) + (1-y)/2Cr_2O_3(s) = La_{1-x}Sr_xMn_{1-y}Zr_yO_3(s) + (Cr_{1-y}Mn_y)O_{1.5-\delta}(s) + 1/2(\delta + 0.5y)O_2(g)$ (1-9)

The Cr vaporation mechanisms have been confirmed by experimental work [149]. After metal interconnects started to be applied in SOCs, chromium poisoning on the air electrode leading to degradation was recognized and the behaviors were detailed studied. Based on the early research by Taniguchi et al. [33] and Hilpert et al. [23] fifteen years ago, more work has been done. The proposed Cr deposition mechanisms are more clearly understood based on new experimental results yet the controversy of polarization effect is still going on.

Considering the mechanism research, there are two parts which need to be evaluated: the degradation of the electrical performance and the Cr species deposition on the porous air electrode and the electrolyte.

Chromium poisoning in SOFC (LSM/YSZ based) was first investigated by Taniguchi et al. [33]. The SOFC with LSM air electrode working with Cr volatile species showed a rapid voltage drop of over 60% in 200 h at 1000°C. The polarization resistance increase accordingly. Large amounts of Cr were found on the LSM air electrode layer and close to the LSM air electrode/YSZ electrolyte interface in the test conditions [33]. Significant degradation of the cell performance indicated the interaction mechanism of Cr species on the air electrode side needed to be clarified. Badwal et al. [17] tested the SOFC (LSM/YSZ based) with chromium-based interconnect material at 900-1000°C. The cell voltage dropped 50% in 16 h in the operation with high current density (250 $mA \cdot cm^{-2}$). The most noticeable phenomenon was the current density strongly affected the degradation rate, while the effect of current loading time was that much smaller (Fig. 1-12). With a current density of 125 $mA \cdot cm^{-2}$ and lower, the decrease of the cell voltage was much slower. In the condition of high current density and fast degradation, the Cr

deposition (identified as Cr_2O_3 and spinel Cr, Mn oxides) were found to fill the pores of the porous LSM electrode close to the YSZ electrolyte. Quadakkers et al. [32] reported the solid phase interaction between the air electrode or contact layer (LSM) with the Cr-containing metallic interconnect forming oxides such as $MnCr_2O_4$. However, the Cr volatile species were considered as the main cause of the cell degradation, while the solid phase interaction just affected the interfacial resistance.

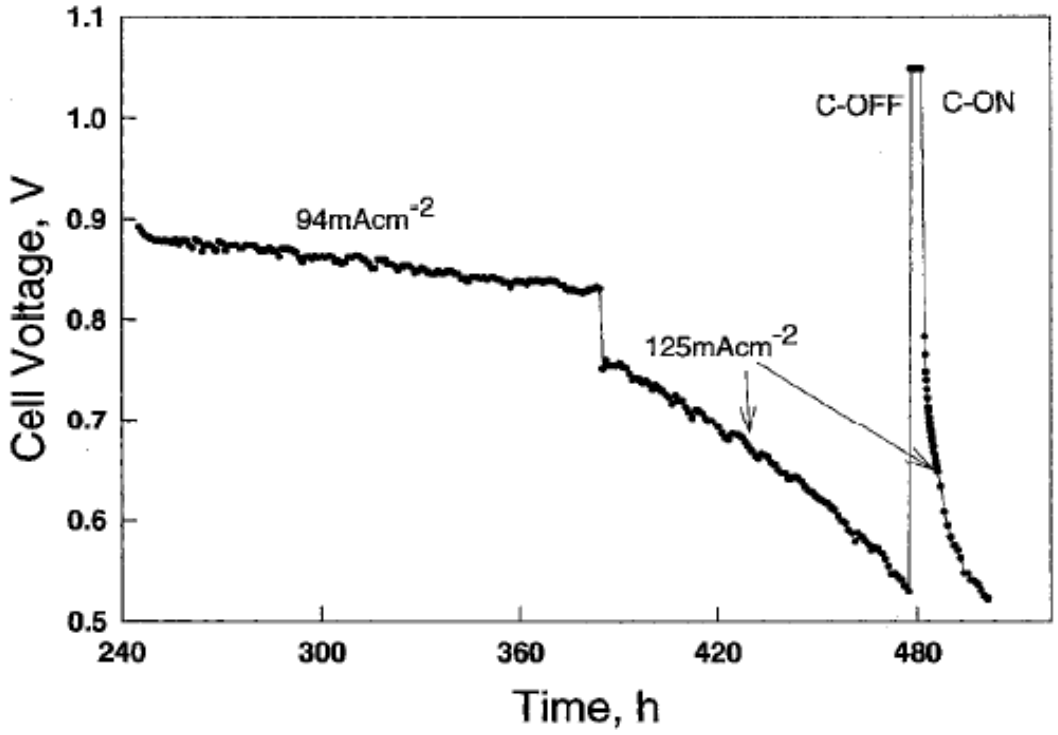

Fig. 1-12. A plot showing dependence of cell degradation as a function of the current density [17].

The early works discussed above are about the experiments carried out at high temperature, which causes large amounts of Cr deposition in the electrode and at electrode/electrolyte interface [17,33]. However, even working at lower temperature and reduced Cr deposition, Cr poisoning still happened [203-206]. The degradation of the cell voltage becomes a critical problem of using metallic interconnect materials. Mostly, the cathodic polarization was considered as the driving force of Cr deposition.

In order to address the problem, more detailed tests have been carried out to clarify the mechanism. The researchers focus on how the Cr species deposits and distributes on the air electrode and electrolyte. The simulated cell environment with external electric power to supply the current has been used. Jiang et al. [25-28,207,208] investigated the Cr deposition of the LSM/YSZ simulated cell in different conditions, and published a series of papers in which the Cr deposition behavior was characterized. First of all, it should be noticed that Cr can deposit not only on the TPB like the electrochemical reaction proposed by Badwal et al. [17] as Eq. 6 and 7. The crystals indentified by EDS as Cr_2O_3 and $(Cr, Mn)_3O_4$ deposit on all the YSZ surface, which is more favorable than the LSM surface with the cathodic polarization. Second, the effects of polarization show that the Cr species deposited on the YSZ surface when both cathodic polarization (oxygen reducing reaction) and anodic polarization (oxygen ion oxidization reaction) applied. When there is no electric current, the Cr deposition is minimized. These results indicated that at least the electrochemical reaction of Cr (VI) gaseous species reducing and depositing on the TPB is not the only reaction of Cr deposition. Furthermore, observation of the early stage polarization showed that the Cr deposits randomly on the YSZ surface first without preference of depositing on the TPB [208].

Paulson et al. [31] also characterized the Cr deposition in a LSM/YSZ half cell with cathodic polarization. The LSM porous air electrode layer partly covered the YSZ electrolyte disc. The Cr deposition was found on the YSZ surface outside the LSM layer as far as 500 μm. The Cr deposition of this case was not random, which extended from the edge during the polarization. The deposition process proposed is that of deposition on the extended TPB of the Cr_2O_3/YSZ. Wang et al. [209,210] investigated the behaviors of Cr deposition of the YSZ surface using a Mn, Co and Fe doped and undoped YSZ surface with a Pt electrode. The result showed that the Cr species rarely deposited on the undoped YSZ surface while the doping of Mn, Co and Fe accelerated the Cr deposition under cathodic polarization. However, Cr deposition was hard to detected clear the same condition of the doped and undoped YSZ without polarization.

For the Cr distribution in the porous LSM air electrode layer, many researches analyzing the Cr distribution have shown that the Cr deposition on the LSM electrode/YSZ electrolyte interface and porous LSM layer occurred simultaneously [21,29,30,206,211,212]. The interfacial deposition was strongly promoted by the current density, while the deposition on the LSM layer

was likely to be independent of the polarization and current density [30]. Liu et al. [212] analyzed the Cr deposited species by a microfocused synchrotron X-ray scattering and radiographic experiment. The result showed that there were about 10% $MnCr_2O_4$ and 90% Cr_2O_3 in the LSM/YSZ interfacial layer, and almost 100% $MnCr_2O_4$ in the LSM layer far away from the interface. It should be noticed that in different experiments, the amounts of Cr deposition were hard to compare because the different porous layer microstructures and the different evaporation rate from the Cr-containing alloys led to variations in the concentration of the volatile Cr species.

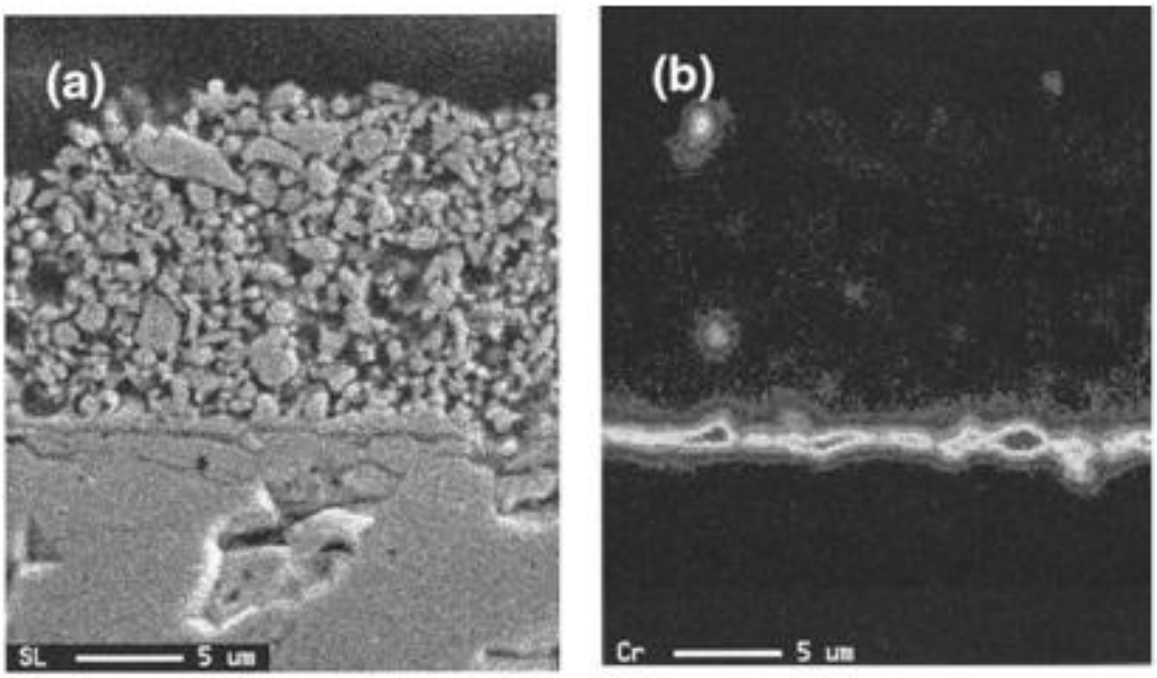

Fig. 1-13. LSM/8YSZ interface after a polarization for 100 h with a current density of 0.3 A cm^{-2} with the alloy current collector at 1073 K: (a) cross-sectional SEM photograph and (b)distribution of Cr element obtained by electron probe micro-analyzer (EPMA) [203].

Beside the LSM air electrode, other materials such as $La_{1-x}Sr_xCo_{1-y}Fe_yO_{3-\sigma}$ (LSCF) have been tested in the condition of volatile Cr species [18,24,30,213-218]. Unlike LSM/YSZ, the LSCF/GDC cell did not show the Cr deposition on the interface and TPB. The Cr deposition was more likely to deposit on the surface of LSCF forming $SrCrO_4$ which also led to cell degradation. Some newly developed air electrode materials without Mn and Sr (which can form compounds with Cr) are considered as Cr-tolerant electrode materials such as $LaNi_{1-y}Fe_yO_3$ (LNF) and

$(La_{0.6}Sr_{0.4-x}Ba_x)$ $(Co_{0.2}Fe_{0.8})O_3$ (LSBCF) have been developed and more evaluation work needs to be carried out to evaluate their tolerance to Cr poisoning [219,220].

For SOEC mode, Cr evaporation and deposition have also been observed in a SOEC stack test [177]. It confirmed that Cr deposition can happen under the anodic polarization condition (the electrochemical or non-electrochemical process is not clear) [25]. The Cr deposition was also suspected to affect the electrically active sites and led to the degradation of the SOEC stacks.

In summary, for the most widely studied LSM/YSZ cell components, Cr poisoning behavior comes from the deposition of volatile Cr species and leads to cell degradation. The Cr deposition contains interfacial deposition and surface deposition on the LSM. External conditions affecting Cr deposition mainly include temperature, polarization, and type of atmosphere. Higher temperature causes a higher Cr evaporation rate and volatile Cr species concentration which lead to large amounts of Cr deposition. The polarization condition is the main factor, which promotes interfacial Cr deposition. The atmosphere determines the volatile Cr species, especially with water vapor in the atmosphere. However, the above external factors must be considered carefully because they also play important roles in other aspects of cell operation. The temperature determines the conductivities and activities of electrolyte and electrode. The water content of the atmosphere also accelerates the electrode degradation [18,200]. So the external conditions affecting Cr poisoning must be comprehensively evaluated.

In addition, the internal factors such as the chemical composition of the cell components and the microstructure of the porous layer can be designed to improve tolerance to Cr poisoning. As discussed above, new air electrode materials have been tested, and surface coating of the Cr-containing alloy can effectively reduce Cr evaporation. Also, the microstructure of the porous air electrode layer can help to minimize Cr poisoning. For example, a thicker interconnect layer made of porous LSM or similar provskite materials can work as a “filter” to slow the diffusion of Cr species and inhibit the Cr poisoning [29].

Theoretically, further understanding of Cr diffusion and deposition processes would be helpful to develop SOC stacks with a high tolerance to Cr poisoning. However, there are still controversies with regard to the Cr deposition process, such as is the interfacial deposition a competitive process with the oxygen reducing reaction or a nuclei growth process related to Mn^{2+}. The porous electrode microstructure and the difficulties of quantitative analysis of Cr

make the mechanism of Cr species deposition/interaction in the SOC air electrode not totally clear.

1.5.2. Electrochemical and Non-electrochemical Mechanism

Based on the Cr deposition behavior discussed in the last section, there are three scenarios for deposition of the volatile Cr species:

1. Cr species deposit on the TPB.
2. Cr species deposit on the surface of the electrolyte.
3. Cr species directly deposit on the surface of the porous air electrode layer.

Scenarios 1 and 2 are believed to happened mainly in the presence of polarization and scenario 3 is considered independent of the polarization [1,25,30,31,33,203]. Disagreements over the electrochemical and non-electrochemical mechanisms occur in scenarios 1 and 2 (with polarization). The proposed electrochemical and non-electrochemical (chemical) mechanisms are demonstrated in Figs. 1-14, 1-15, and 1-16.

Badwal et al. [17] proposes that the deposition of the Cr volatile species competes with oxygen in the air electrode of the SOFC (the TPB sites, scenario 1).

$$2Cr(OH)O_2(g) + 6e^- \rightarrow Cr_2O_3(s) + 2H_2O(g) + 3O^{2-} \text{ (electrolyte)} \quad (1\text{-}10)$$

$$2CrO_3(g) + 6e^- \rightarrow Cr_2O_3(s) + 3O^{2-} \text{ (electrolyte)} \quad (1\text{-}11)$$

The electrochemical mechanism of Cr poisoning is shown above, where the Cr volatile species are reduced by the electrochemical process on the air electrode (mostly considered as the TPB).There are additional researchers who support the mechanism of electrochemical reaction of Cr reduction [18,24,29,30,203-206].

Some of the most convincing evidence for this assumption is that the Cr deposition is dependent on the cathodic polarization. The observation of Cr deposition on the air electrode layer close to the electrolyte is affected significantly by the polarization voltage. At the same temperature and under other test conditions, for the case of no electric current applied, the Cr

deposition is hardly seen. When the voltage gets higher, more Cr species can be seen by the SEM/TEM [204].

Another important phenomenon is that all the experimental results show that the Cr deposition on the LSM porous electrode is close to the LSM/YSZ interface and considered to block the TPB active sites (Fig. 1-14(a)).

In many cases, especially in long-term operation samples, the Cr deposition is observed not only at the TPB sites (scenario 2). The Cr species can be found in the porous air electrode, layer several microns away from the interface, and as far as 500 μm away from the porous electrode depositing on the uncovered electrolyte surface [30,31,203]. The Cr deposition in this case is not considered as a random deposition process, which extended from the TPB during the polarization. The deposition process proposed was that of deposition on the extended TPB of the Cr_2O_3/YSZ [31] (Fig. 1-14(b)) .

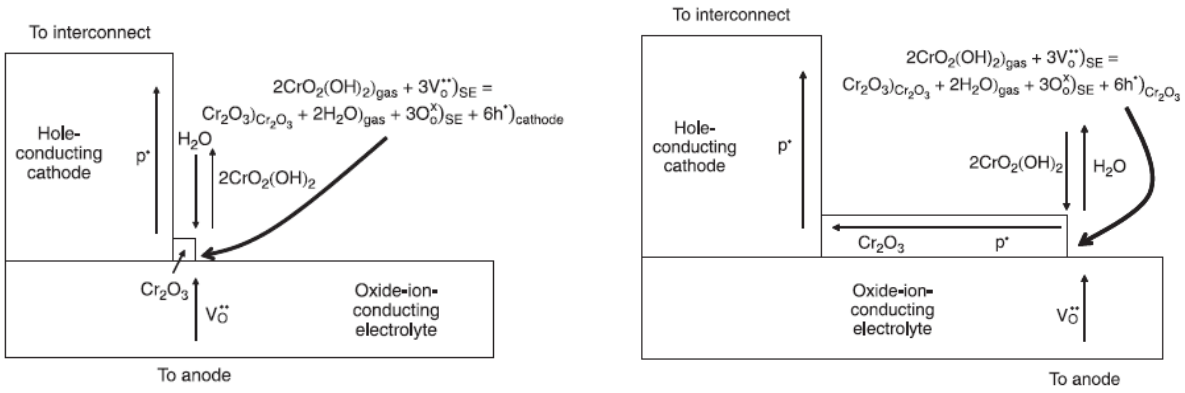

(a) (b)

Fig.1-14. Electrochemical mechanism of scenario 1 and 2: (a), Cr depositon in TPB; (b), the extending of Cr_2O_3 TPB [22].

On the other hand, Jiang et al. [25-28,35,99,208] propose that the deposition of Cr is not dominated by electrochemical reduction of the high valence Cr volatile species. The driving force of the Cr deposition is suggested to be related to the Mn species. The equations are [25,208]:

$$Mn^{2+} + CrO_3 \rightarrow \text{Cr-Mn-O (nuclei)} \quad (1\text{-}12)$$

$$\text{Cr-Mn-O (nuclei)} + CrO_3 \rightarrow Cr_2O_3 \quad (1\text{-}13)$$

$$\text{Cr-Mn-O (nuclei)} + Mn^{2+} + CrO_3 \rightarrow (Cr,Mn)_3O_4 \quad (1\text{-}14)$$

Experimental evidence supporting the non-electrochemical mechanism are [28]:

1. Cr deposition on the YSZ electrolyte occurs under cathodic as well as anodic polarization.
2. the initial polarization behavior is reversible, indicating no blocking effect of the active sites for the oxygen reduction as a consequence of the deposition of the Cr_2O_3 solid phase at the early stage of the reaction.
3. no preferential deposition of Cr at the LSM air electrode and YSZ electrolyte TPB area.
4. deposition of Cr can occur on the YSZ electrolyte surface far away from the LSM electrode that is not directly in contact with the Cr-containing alloy.

The non-electrochemical mechanism above considers the deposition on the YSZ is a chemical process and driven by thermodynamics and that the Cr deposition on the LSM is not an electrochemical process itself. Mn acts as the nuclei for the volatile Cr species deposition which is a chemical process. It should be pointed out that even the non-electrochemical mechanism considers that the polarization causes the Cr deposition of scenarios 1 and 2. The non-electrochemical explanation is that the polarization causes the valence change of a particular element (Mn) on the electrolyte surface which becomes the nuclei of the volatile species deposition [28,208]. The Mn species are affected by the polarization, which can be used to explain the dependence of the deposition rate on the polarization voltage.

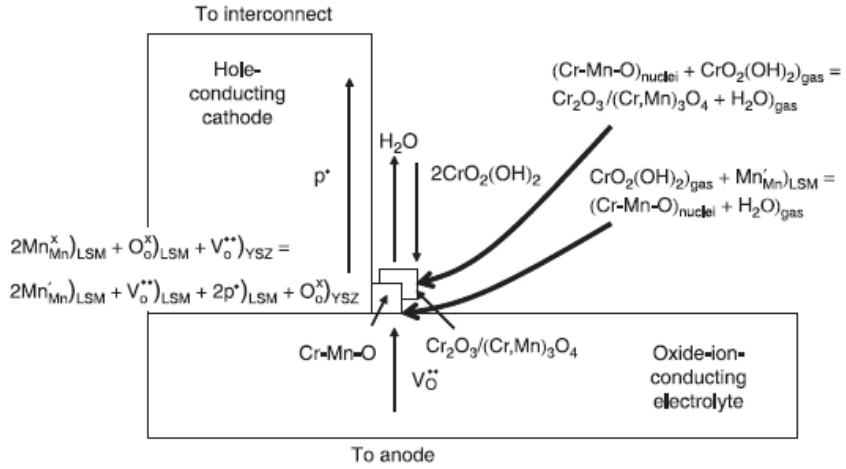

Fig. 3. Chemical deposition of Cr_2O_3 on LSM [31].

Fig. 1-15. Non-electrochemical mechanism of scenario 1 and 2 [22].

For scenario 3, the formation of the $(Cr,Mn)_3O_4$ spine1 phase is also reported in the LSM cathode[17,33]. It should be noted that in the early work reviewed above [17,23,33], the test temperature is relatively high (900-1000°C) for the large amount of Cr_2O_3 found on the LSM air electrode/YSZ electrolyte interface. When the temperature decreases to around 800°C, the Cr deposition becomes not so obvious which makes the characterization more difficult [18,221].

Furthermore, some researchers also proposed that scenario 3 generally occurrs at the same time with scenarios 1 and 2 and is showed independent to the polarization. Konysheva et al. [29] analyzed both LSM surface deposition and deposition close to the TPB as causing cell degradation. With cathodic polarization, the deposition on the electrode/electrolyte interface is fast, and the LSM surface deposition is the minor process. Because the contribution of scenario 3 is likely minor in Cr poisoning; however, there is no detailed research of this process.

It should be noticed that the LSM/YSZ system is a combination of an electron-conductive air electrode and an ion-conductive electrolyte. When using other materials such as LSCF/LSGM (mixed conductive materials), the mechanisms will be different. Horita et al. [24] compared the elemental distribution of LSM/GDC and LSF/GDC. The results also show that the deposition on the LSM/GDC interface (TPB area) is the major Cr poisoning process in SOFC operation (Fig. 1-16).

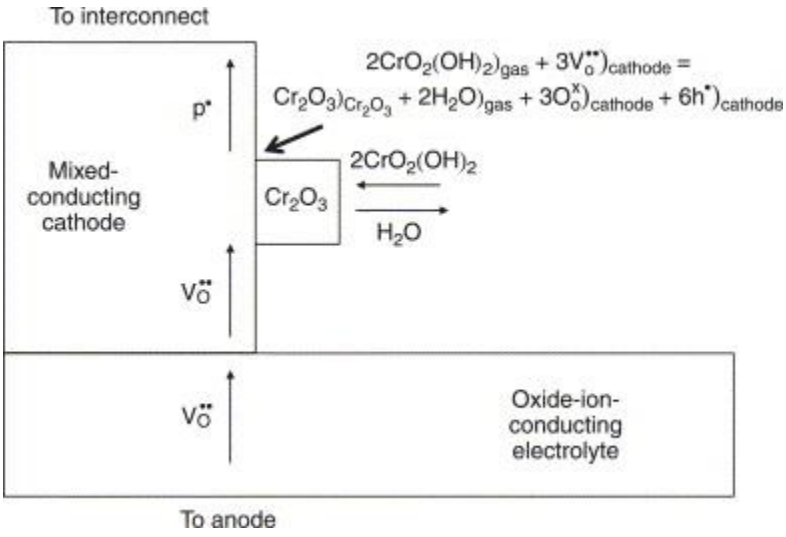

Fig. 1-16. Cr species deposition on the surface of LSCF [22].

Considering the Cr poisoning of the LSM/YSZ air electrode/electrolyte system, the main controversies of the Cr deposition mechanism have been discussed above. There are also some disagreements with regard to the experimental results. In a LSM/YSZ half cell with polarization, Jiang et al. [208] found that the Cr deposited particles formed on the YSZ surface randomly even far away from the LSM/YSZ interface (TPB) in a few minutes. Jiang et al. proposed that the Mn^{2+} on the YSZ surface reacted with the volatile Cr species. However, Wang et al. [209] used a Mn doped YSZ and Pt/YSZ half cell to study the same process and observed that the Cr only deposited on the Pt/YSZ interface (TPB) but not randomly on the YSZ surface. Although the experimental conditions are different in this comparison of results, the disagreement reveals the complexity of the Cr deposition process. More work should be done to improve the understanding of this problem.

1.6. Characterization Issues

As discussed above, the controversies surrounding interaction of the SOCs during long term operation is partly from the lack of a detailed and precise characterization technique. In the older work, the chemical composition analysis of the Cr deposition is qualitative and rough, which leads to problems in explaining the mechanism [25,33]. Improving the characterization technique will help to clarify the interactions affecting \SOC long-term operation.

For the porous air electrode layer, the definition of the microstructural parameters is a key point to studying microstructure changes during operation. Traditionally, scanning electron microscopy (SEM) has been the most popular method for observing the porous microstructure. However, the disadvantage of SEM is that it cannot supply quantitative results. Many new techniques and statistical methods are used for microstructure characterization. Focused ion beam (FIB) is the most notable technology in recent years. FIB tomography uses an ion beam to perform nanoscale sectioning of a sample; subsequent imaging can be performed using an electron beam. Repeating the milling and imaging procedure can build up a sequence of two-dimensional images that can be effectively reconstructed in three-dimensional space, affording access to a wide range of microstructural parameters [222-224]. The "reconstruction" is a great improvement for microstructure analysis, where all the parameters such as porosity pore size distribution and topology, even the special parameter such as TPB lengh for the SOC electrodes, can be clearly measured.

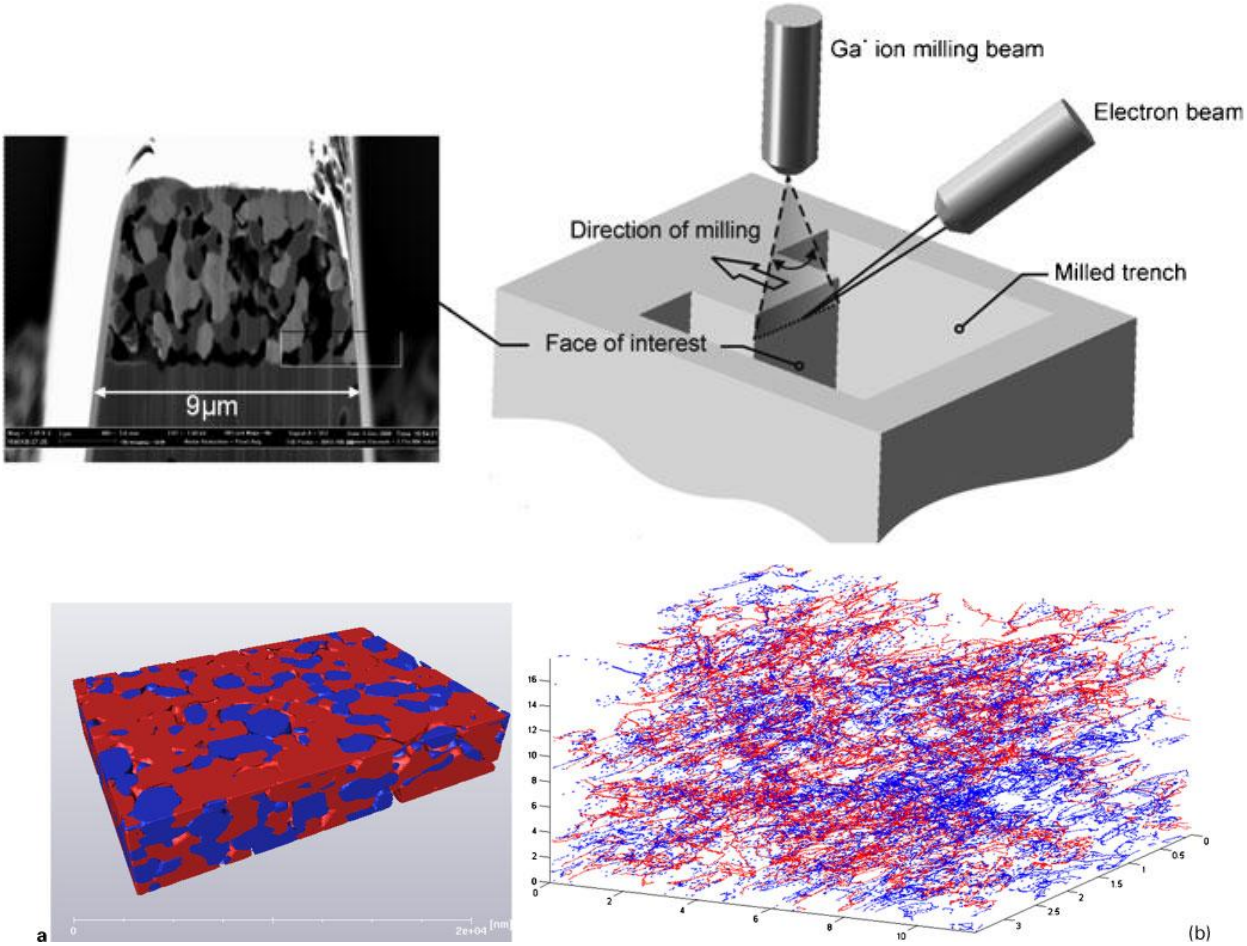

Fig. 1-17. Schematic of FIB milling with combined SEM imaging and the reconstruction and TPB analysis [222]

Chemical composition analysis is another important part to studying the interactions including the diffusion of the elements. The space resolution (probe size) and detect limit of the chemical analysis must be improved to match the requirement. For example, the SOC air electrode layer is generally tens of micrometers in length. The interaction zone at the electrolyte/electrode interface and at the electrolyte surface is normally on a nanometer scale. The detection must have enough resolution for these purposes. On the other hand, the lower the detection limit is, the better the results for the low amount element that can be achieved.

Energy dispersive spectroscopy (EDS) is a widely used method for elemental analysis. When EDS is used for Cr deposition analysis, the small amount of Cr is close to the detection limit (0.1 atom %) and the Cr EDS peaks are found overlapping with La, the major element in many electrode materials. These issues make Cr analysis hard and most of the early work just used EDS in a qualitative analysis [30,35,203]. Schule et al. [221,225] used La peaks to calibrate the Cr amount. A thin slice of the sample can also be used to improve the space resolution of the EDS with transmission electron microscopy (TEM) [226,227]. EDS is a fast and easy way for the elemental analysis of the SOCs. However, the quantitative results need to be carefully analyzed.

For SOC research, surface analysis has attracted more and more attention in recent years. Air electrode materials such as perovskite LSM have shown that surface segregation and surface chemistry are critical for oxygen reduction activity [132,228-230]. Furthermore, the surface is also sensitive to foreign phases which promote the catalyst poisoning [230]. Surface analysis is generally done by X-ray photoelectron spectroscopy (XPS) and Auger electron spectroscopy. Surface chemistry and the interaction have not been widely studied, particularly with regard to some surface behaviors such as time relaxation, which remain open questions.

Many other new techniques are used to improve SOC characterization. For the phase analysis in the interaction research, high resolution XRD is used and greatly increases the resolution. TEM is also applied more for the nanometer scale phase and elemental analysis. Another improvement in characterization is in situ analysis during operation by advanced equipment [231,232]. These novel characterization techniques nowadays give us opportunities to

go further in dealing with old issues and clarifying the controversies in the SOC research which have existed for over forty years.

1.7. Objectives and Outline of This Dissertation

As introduced in the literature review, the interactions of the air electrode with electrolyte and Cr-containing ferritic stainless steel interconnect material are critical to the performance and long-term stability for the SOCs. The interactions include the solid phase reaction and vapor phase transport in the SOC operating conditions, which cause the Cr poisoning of the air electrode and interface degradations.

These degradation issues have been extensively investigated. However, there is considerable disagreements on the mechanism of Cr-containing species interaction with and deposition on the air electrode. Some studies suggested that the deposition of Cr species is closely related to the oxygen activity at the electrode/electrolyte interface (TPB) [17,33]. In contrast, others believed that the interfacial degradation by Cr poisoning could be caused by (i) blocking of electrochemically active sites by electrochemical reduction of Cr-containing species, and (ii) decomposition of the air electrode by the formation of Cr-containing mixed oxide, driven by the thermodynamics without influence of the electrical potentials [233]. There were also claims that the deposition of Cr species depends strongly on the nature of the air electrode materials and that Cr species deposition at the air electrode is most likely controlled by a non-electrochemical process [22,28,208]

Besides the polarization status, other factors discussed above must be considered. In the operation environment of the air electrode side of the SOCs, the material interactions are complicated. The external factors such as atmosphere also affect the interactions as well as the chemical composition and microstructure (porosity and thickness of the porous air electrode). The atmosphere and microstructure affect the Cr deposition by affecting the concentration and transport path of the volatile Cr species. The different composition of LSM air electrode will cause different interface interaction with the YSZ electrolyte. Particularly, Mn in the LSM will be beneficial to the Cr deposition. The polarization will accelerate the Cr deposition at the TPB. By analyzing the factors during the thermal treatment, the mechanism of the interactions will be clarified for the SOC application.

This research is to reveal the materials interaction behaviors and their contribution to the material degradation of the SOCs. The material degradation mechanisms can contribute to develop new materials with better stability and compatibility and help to design new SOC stack structures to reduce materials degradation and increase the life time. Furthermore, the long-term operating performance can be better evaluated based on the understanding of the materials degradation.

Based on these motivations, the objectives of this study are to understand the material interactions in the SOC operating conditions. The contents in this dissertation are outlined:

1. Simulated samples including SOC electrolyte, air electrode, and interconnect will be developed in this research. The configuration of the samples with the different components should be well designed and assembled for the thermal treatment and characterization. The thickness effect of the porous air electrode layer will be investigated.
2. Water vapor leads to an increase of volatile Cr species from the Cr-containing interconnect. The electrolyte/air electrode/interconnect tri-layer samples will be thermally treated in atmospheres with different moist level to investigate the atmosphere effect.
3. Stoichiomtry effect of the LSM air electrode will be studied by using different LSM compositions in the thermal treatment. The mechanism of the interaction and Cr deposition will be discussed.
4. A cathodic polarization will be applied on the tri-layer sample during the thermal treatment to study the polarization effect in the SOFC mode.

The potential issues to be investigated in this research are:

1. Cr deposition on the LSM electrode surface. The direct deposition of the volatile Cr species on the LSM surface is considered as a non-electrochemical process or chemical process. The phase formed by the Cr-LSM interaction on the LSM surface and the affects of the different volatile Cr species (Cr_2O_3 or $CrO_2(OH)_2$) are not clear. Furthermore, the distribution of Cr in the porous LSM layer also needs to be addressed, which is important to understand the transport of the volatile Cr species.
2. The Cr deposition on (or close to) the LSM/YSZ interface under polarization is a controversial issue. How the Cr deposition forms on the particular region is not solved.

More detailed elemental analysis needs to be carried out to clarify the relation between the geometry of TPB and the deposition of Cr species.

3. The characterization of elements in this work is another issue. Cr and Mn are the critical elements in the interaction. However, Cr is present in small amounts on the air electrode surface, and one of the major elements of LSM, La, strongly interferences with Cr defection. It is hard to quantify the Cr distribution in the porous LSM layer [35,221]. Mn on the YSZ surface is the key of the non-electrochemical mechanism, which has not been clearly analyzed. By improving the surface characterization and quantitative elemental analysis procedure, the interactions can be better understood.

References

1. Badwal, S.P.S. and Foger, K., Solid oxide electrolyte fuel cell review. Ceramics International, 1996. 22(3): p. 257-265.
2. Singhal, S.C., Advances in solid oxide fuel cell technology. Solid State Ionics, 2000. 135(1-4): p. 305-313.
3. Singhal, S.C. and Kendall, K., High temperature solid oxide fuel cells. 2003, Oxford, UK: Elsevier.
4. Huang, K. and Goodenough, J.B., Solid oxide fuel cell technology: Principles, Performance and Operations. CRC, Cambrige, UK, 2009.
5. Minh, N.Q., Solid oxide fuel cell technology-features and applications. Solid State Ionics, 2004. 174(1-4): p. 271-277.
6. Eguchi, K., Hatagishi, T., and Arai, H., Power generation and steam electrolysis characteristics of an electrochemical cell with a zirconia- or ceria-based electrolyte. Solid State Ionics, 1996. 86-8: p. 1245-1249.
7. Isenberg, A.O., Energy-conversion via solid oxide electrolyte electrochemical-cells at high-temperatures. Solid State Ionics, 1981. 3-4(AUG): p. 431-437.
8. Jensen, S.H., Larsen, P.H., and Mogensen, M., Hydrogen and synthetic fuel production from renewable energy sources. International Journal of Hydrogen Energy, 2007. 32(15): p. 3253-3257.

9. Ni, M., Leung, M.K.H., and Leung, D.Y.C., Technological development of hydrogen production by solid oxide electrolyzer cell (SOEC). International Journal of Hydrogen Energy, 2008. 33(9): p. 2337-2354.
10. Hauch, A., Ebbesen, S.D., Jensen, S.H., and Mogensen, M., Highly efficient high temperature electrolysis. Journal of Materials Chemistry, 2008. 18(20): p. 2331-2340.
11. Steele, B.C.H., Middleton, P.H., and Rudkin, R.A., Material science aspects of SOFC technology with special reference to anode development. Solid State Ionics, 1990. 40-41(Part 1): p. 388-393.
12. Sigurvinsson, J., Mansilla, C., Lovera, P., and Werkoff, F., Can high temperature steam electrolysis function with geothermal heat? International Journal of Hydrogen Energy, 2007. 32(9): p. 1174-1182.
13. Yokokawa, H., Tu, H.Y., Iwanschitz, B., and Mai, A., Fundamental mechanisms limiting solid oxide fuel cell durability. Journal of Power Sources, 2008. 182(2): p. 400-412.
14. Ebbesen, S.D. and Mogensen, M., Exceptional Durability of Solid Oxide Cells. Electrochemical and Solid State Letters, 2010. 13(9): p. D106-D108.
15. Gemmen, R.S., Williams, M.C., and Gerdes, K., Degradation measurement and analysis for cells and stacks. Journal of Power Sources, 2008. 184(1): p. 251-259.
16. Hagen, A., Liu, Y.L., Barfod, R., and Hendriksen, P.V., Assessment of the cathode contribution to the degradation of anode-supported solid oxide fuel cells. Journal of the Electrochemical Society, 2008. 155(10): p. B1047-B1052.
17. Badwal, S.P.S., Deller, R., Foger, K., Ramprakash, Y., and Zhang, J.P., Interaction between chromia forming alloy interconnects and air electrode of solid oxide fuel cells. Solid State Ionics, 1997. 99(3-4): p. 297-310.
18. Bentzen, J.J., Hogh, J.V.T., Barfod, R., and Hagen, A., Chromium poisoning of LSM/YSZ and LSCF/CGO composite cathodes. Fuel Cells, 2009. 9(6): p. 823-832.
19. Brylewski, T., Nanko, M., Maruyama, T., and Przybylski, K., Application of Fe-16Cr ferritic alloy to interconnector for a solid oxide fuel cell. Solid State Ionics, 2001. 143(2): p. 131-150.
20. Chen, X.B., Hua, B., Pu, J., Li, J., Zhang, L., and Jiang, S.P., Interaction between (La, Sr)MnO_3 cathode and Ni-Mo-Cr metallic interconnect with suppressed chromium

vaporization for solid oxide fuel cells. International Journal of Hydrogen Energy, 2009. 34(14): p. 5737-5748.

21. Cruse, T.A., Ingram, B.J., Liu, D.-J., and Krumpelt, M., Chromium reactions and transport in solid oxide fuel cells. ECS Transactions, 2007. 5(1): p. 335-346.
22. Fergus, J.W., Effect of cathode and electrolyte transport properties on chromium poisoning in solid oxide fuel cells. International Journal of Hydrogen Energy, 2007. 32(16): p. 3664-3671.
23. Hilpert, K., Das, D., Miller, M., Peck, D.H., and Weiss, R., Chromium vapor species over solid oxide fuel cell interconnect materials and their potential for degradation processes. Journal of the Electrochemical Society, 1996. 143(11): p. 3642-3647.
24. Horita, T., Xiong, Y.P., Kishimoto, H., Yamaji, K., Brito, M.E., and Yokokawa, H., Chromium poisoning and degradation at (La,Sr)MnO_3 and (La,Sr)FeO_3 cathodes for solid oxide fuel cells. Journal of the Electrochemical Society, 2010. 157(5): p. B614-B620.
25. Jiang, S.P., Zhang, J.P., Apateanu, L., and Foger, K., Deposition of chromium species at Sr-doped $LaMnO_3$ electrodes in solid oxide fuel cells I. Mechanism and kinetics. Journal of the Electrochemical Society, 2000. 147(11): p. 4013-4022.
26. Jiang, S.P., Zhang, J.P., and Foger, K., Deposition of chromium species at Sr-doped $LaMnO_3$ electrodes in solid oxide fuel cells - II. Effect on O-2 reduction reaction. Journal of the Electrochemical Society, 2000. 147(9): p. 3195-3205.
27. Jiang, S.P., Zhang, J.P., and Foger, K., Deposition of chromium species at Sr-doped $LaMnO_3$ electrodes in solid oxide fuel cells - III. Effect of air flow. Journal of the Electrochemical Society, 2001. 148(7): p. C447-C455.
28. Jiang, S.P. and Zhen, Y.D., Mechanism of Cr deposition and its application in the development of Cr-tolerant cathodes of solid oxide fuel cells. Solid State Ionics, 2008. 179(27-32): p. 1459-1464.
29. Konysheva, E., Mertens, J., Penkalla, H., Singheiser, L., and Hilpert, K., Chromium poisoning of the porous composite cathode effect of cathode thickness and current density. Journal of the Electrochemical Society, 2007. 154(12): p. B1252-B1264.
30. Konysheva, E., Penkalla, H., Wessel, E., Mertens, J., Seeling, U., Singheiser, L., and Hilpert, K., Chromium poisoning of perovskite cathodes by the ODS alloy Cr5Fe1Y_2O_3

and the high chromium ferritic steel Crofer22APU. Journal of the Electrochemical Society, 2006. 153(4): p. A765-A773.

31. Paulson, S.C. and Birss, V.I., Chromium poisoning of LSM-YSZ SOFC cathodes - I. Detailed study of the distribution of chromium species at a porous, single-phase cathode. Journal of the Electrochemical Society, 2004. 151(11): p. A1961-A1968.
32. Quadakkers, W.J., Greiner, H., Hansel, M., Pattanaik, A., Khanna, A.S., and Mallener, W., Compatibility of perovskite contact layers between cathode and metallic interconnector plates of SOFCs. Solid State Ionics, 1996. 91(1-2): p. 55-67.
33. Taniguchi, S., Kadowaki, M., Kawamura, H., Yasuo, T., Akiyama, Y., Miyake, Y., and Saitoh, T., Degradation phenomena in the cathode of a solid oxide fuel cell with an alloy separator. Journal of Power Sources, 1995. 55(1): p. 73-79.
34. Tietz, F. and Sebold, D., Interface reactions between electrically conductive ceramics and ferritic steel-I. The system Cr-22Fe-0.5Mn/Mn_2O_3/(La,Ca)(Cr,Co,Cu)O_3. Materials Science and Engineering B-Advanced Functional Solid-State Materials, 2008. 150(2): p. 135-140.
35. Zhen, Y.D., Jiang, S.P., Zhang, S., and Tan, V., Interaction between metallic interconnect and constituent oxides of (La, Sr)MnO_3 coating of solid oxide fuel cells. Journal of the European Ceramic Society, 2006. 26(15): p. 3253-3264.
36. Steele, B.C.H. and Heinzel, A., Materials for fuel-cell technologies. Nature, 2001. 414(6861): p. 345-352.
37. Hassmann, K., SOFC power plants, the Siemens-Westinghouse approach. Fuel Cells, 2001. 1(1): p. 78-84.
38. 2006 office of fossil energy fuel cell program annual report, 2006.
39. O'Brien, J.E., Stoots, C.M., Herring, J.S., and Hartvigsen, J.J., Performance of planar high-temperature electrolysis stacks for hydrogen production from nuclear energy. Nuclear Technology, 2007. 158(2): p. 118-131.
40. Goodenough, J.B., Manthiram, A., Paranthaman, M., and Zhen, Y.S., Oxide ion electrolytes. Materials Science and Engineering B-Solid State Materials for Advanced Technology, 1992. 12(4): p. 357-364.
41. Brandon, N.P., Skinner, S., and Steele, B.C.H., Recent advances in materials for fuel cells. Annual Review of Materials Research, 2003. 33: p. 183-213.

42. Brett, D.J.L., Atkinson, A., Brandon, N.P., and Skinner, S.J., Intermediate temperature solid oxide fuel cells. Chemical Society Reviews, 2008. 37(8): p. 1568-1578.
43. Sun, C.W. and Stimming, U., Recent anode advances in solid oxide fuel cells. Journal of Power Sources, 2007. 171(2): p. 247-260.
44. Zhu, W.Z. and Deevi, S.C., A review on the status of anode materials for solid oxide fuel cells. Materials Science and Engineering a-Structural Materials Properties Microstructure and Processing, 2003. 362(1-2): p. 228-239.
45. Jiang, S.P. and Chan, S.H., A review of anode materials development in solid oxide fuel cells. Journal of Materials Science, 2004. 39(14): p. 4405-4439.
46. Anderson, H.U., Review of p-type doped perovskite materials for SOFC and other applications. Solid State Ionics, 1992. 52(1-3): p. 33-41.
47. Fleig, J., Solid oxide fuel cell cathodes: Polarization mechanisms and modeling of the electrochemical performance. Annual Review of Materials Research, 2003. 33: p. 361-382.
48. Adler, S.B., Factors governing oxygen reduction in solid oxide fuel cell cathodes. Chemical Reviews, 2004. 104(10): p. 4791-4843.
49. Islam, M.S., Cherry, M., and Winch, L.J., Defect chemistry of $LaBO_3$ (B=Al, Mn or Co) perovskite-type oxides - Relevance to catalytic and transport behaviour. Journal of the Chemical Society-Faraday Transactions, 1996. 92(3): p. 479-482.
50. Skinner, S.J., Recent advances in Perovskite-type materials for solid oxide fuel cell cathodes. International Journal of Inorganic Materials, 2001. 3(2): p. 113-121.
51. Stoots, C., O'Brien, J., and Hartvigsen, J., Results of recent high temperature coelectrolysis studies at the Idaho National Laboratory. International Journal of Hydrogen Energy, 2009. 34(9): p. 4208-4215.
52. Huang, K., Wan, J., and Goodenough, J.B., Oxide-ion conducting ceramics for solid oxide fuel cells. Journal of Materials Science, 2001. 36(5): p. 1093-1098.
53. Zhu, W.Z. and Deevi, S.C., Development of interconnect materials for solid oxide fuel cells. Materials Science and Engineering A, 2003. 348(1-2): p. 227-243.
54. Fergus, J.W., Lanthanum chromite-based materials for solid oxide fuel cell interconnects. Solid State Ionics, 2004. 171(1-2): p. 1-15.

55. Yang, Z.G., Weil, K.S., Paxton, D.M., and Stevenson, J.W., Selection and evaluation of heat-resistant alloys for SOFC interconnect applications. Journal of the Electrochemical Society, 2003. 150(9): p. A1188-A1201.
56. Simner, S.P., Anderson, M.D., Xia, G.G., Yang, Z., Pederson, L.R., and Stevenson, J.W., SOFC performance with Fe-Cr-Mn alloy interconnect. Journal of the Electrochemical Society, 2005. 152(4): p. A740-A745.
57. Fergus, J.W., Metallic interconnects for solid oxide fuel cells. Materials Science and Engineering a-Structural Materials Properties Microstructure and Processing, 2005. 397(1-2): p. 271-283.
58. Yang, Z.G., Recent advances in metallic interconnects for solid oxide fuel cells. International Materials Reviews, 2008. 53(1): p. 39-54.
59. Shaigan, N., Qu, W., Ivey, D.G., and Chen, W.X., A review of recent progress in coatings, surface modifications and alloy developments for solid oxide fuel cell ferritic stainless steel interconnects. Journal of Power Sources, 2010. 195(6): p. 1529-1542.
60. Wu, J.W. and Liu, X.B., Recent development of SOFC metallic interconnect. Journal of Materials Science & Technology, 2010. 26(4): p. 293-305.
61. Quadakkers, W.J., Piron-Abellan, J., Shemet, V., and Singheiser, L., Metallic interconnectors for solid oxide fuel cells - a review. Materials at High Temperatures, 2003. 20(2): p. 115-127.
62. Batfalsky, P., Haanappel, V.A.C., Malzbender, J., Menzler, N.H., Shemet, V., Vinke, I.C., and Steinbrech, R.W., Chemical interaction between glass-ceramic sealants and interconnect steels in SOFC stacks. Journal of Power Sources, 2006. 155(2): p. 128-137.
63. Weil, K.S., The state-of-the-art in sealing technology for solid oxide fuel cells. Jom, 2006. 58(8): p. 37-44.
64. Fergus, J.W., Sealants for solid oxide fuel cells. Journal of Power Sources, 2005. 147(1-2): p. 46-57.
65. Singh, R.N., Sealing technology for solid oxide fuel cells (SOFC). International Journal of Applied Ceramic Technology, 2007. 4(2): p. 134-144.
66. Mahapatra, M.K. and Lu, K., Seal glass for solid oxide fuel cells. Journal of Power Sources, 2010. 195(21): p. 7129-7139.

67. Mahapatra, M.K. and Lu, K., Glass-based seals for solid oxide fuel and electrolyzer cells - A review. Materials Science & Engineering R-Reports, 2010. 67(5-6): p. 65-85.
68. Mahapatra, M.K., Lu, K., and Reynolds, W.T., Thermophysical properties and devitrification of SrO-La_2O_3-Al_2O_3-B_2O_3-SiO_2-based glass sealant for solid oxide fuel/electrolyzer cells. Journal of Power Sources, 2008. 179(1): p. 106-112.
69. Hauch, A., Jensen, S.H., Ramousse, S., and Mogensen, M., Performance and durability of solid oxide electrolysis cells. Journal of the Electrochemical Society, 2006. 153(9): p. A1741-A1747.
70. Marina, O.A., Pederson, L.R., Williams, M.C., Coffey, G.W., Meinhardt, K.D., Nguyen, C.D., and Thomsen, E.C., Electrode performance in reversible solid oxide fuel cells. Journal of the Electrochemical Society, 2007. 154(5): p. B452-B459.
71. Mogensen, M., Jensen, S.H., Hauch, A., Chorkendorff, I., and Jacobsen, T., Performance of reversible solid oxide cells: A review. Proceedings of the 7th European SOFC Forum, Lucerne; 2006.
72. Dokiya, M., SOFC system and technology. Solid State Ionics, 2002. 152: p. 383-392.
73. Menzler, N.H., Tietz, F., Uhlenbruck, S., Buchkremer, H.P., and Stover, D., Materials and manufacturing technologies for solid oxide fuel cells. Journal of Materials Science, 2010. 45(12): p. 3109-3135.
74. Tietz, F., Buchkremer, H.P., and Stover, D., Components manufacturing for solid oxide fuel cells. Solid State Ionics, 2002. 152: p. 373-381.
75. Kharton, V.V., Marques, F.M.B., and Atkinson, A., Transport properties of solid oxide electrolyte ceramics: a brief review. Solid State Ionics, 2004. 174(1-4): p. 135-149.
76. Maricle, D.L., Swarr, T.E., and Karavolis, S., Enhanced ceria - A low-temperature SOFC electrolyte. Solid State Ionics, 1992. 52(1-3): p. 173-182.
77. Song, H.Z., Wang, H.B., Zha, S.W., Peng, D.K., and Meng, G.Y., Aerosol-assisted MOCVD growth of Gd_2O_3-doped CeO_2 thin SOFC electrolyte film on anode substrate. Solid State Ionics, 2003. 156(3): p. 249-254.
78. Chen, F.L. and Liu, M.L., Study of transition metal oxide doped $LaGaO_3$ as electrode materials for LSGM-based solid oxide fuel cells. Journal of Solid State Electrochemistry, 1998. 3(1): p. 7-14.

79. Wan, J.H., Yan, J.Q., and Goodenough, J.B., LSGM-based solid oxide fuel cell with 1.4 W/cm^2 power density and 30 day long-term stability. Journal of the Electrochemical Society, 2005. 152(8): p. A1511-A1515.
80. Sun, C.W., Hui, R., and Roller, J., Cathode materials for solid oxide fuel cells: a review. Journal of Solid State Electrochemistry, 2010. 14(7): p. 1125-1144.
81. McIntosh, S. and Gorte, R.J., Direct hydrocarbon solid oxide fuel cells. Chemical Reviews, 2004. 104(10): p. 4845-4865.
82. Gorte, R.J., Kim, H., and Vohs, J.M., Novel SOFC anodes for the direct electrochemical oxidation of hydrocarbon. Journal of Power Sources, 2002. 106(1-2): p. 10-15.
83. Drennan, J., Zelizko, V., Hay, D., Ciacchi, F.T., Rajendran, S., and Badwal, S.P.S., Characterisation, conductivity and mechanical properties of the oxygen-ion conductor $La_{0.9}Sr_{0.1}Ga_{0.8}Mg_{0.2}O_{3-x}$. Journal of Materials Chemistry, 1997. 7(1): p. 79-83.
84. Tu, H.Y. and Stimming, U., Advances, aging mechanisms and lifetime in solid-oxide fuel cells. Journal of Power Sources, 2004. 127(1-2): p. 284-293.
85. Blum, L., Meulenberg, W.A., Nabielek, H., and Steinberger-Wilckens, R., Worldwide SOFC technology overview and benchmark. International Journal of Applied Ceramic Technology, 2005. 2(6): p. 482-492.
86. Yamamoto, O., Solid oxide fuel cells: fundamental aspects and prospects. Electrochimica Acta, 2000. 45(15-16): p. 2423-2435.
87. Tietz, F., Fu, Q., Haanappel, V.A.C., Mai, A., Menzler, N.H., and Uhlenbruck, S., Materials development for advanced planar solid oxide fuel cells. International Journal of Applied Ceramic Technology, 2007. 4(5): p. 436-445.
88. Richter, J., Holtappels, P., Graule, T., Nakamura, T., and Gauckler, L.J., Materials design for perovskite SOFC cathodes. Monatshefte Fur Chemie, 2009. 140(9): p. 985-999.
89. Hammouche, A., Schouler, E.J.L., and Henault, M., Electrical and thermal properties of Sr-doped lanthanum manganites. Solid State Ionics, 1988. 28-30(Part 2): p. 1205-1207.
90. Kuo, J.H., Anderson, H.U., and Sparlin, D.M., Oxidation reduction behavior of undoped and Sr-doped $LaMnO_3$ - defect structure, electrical-conductivity, and thermoelectric-power. Journal of Solid State Chemistry, 1990. 87(1): p. 55-63.
91. Haanappel, V.A.C., Mertens, J., Rutenbeck, D., Tropartz, C., Herzhof, W., Sebold, D., and Tietz, F., Optimisation of processing and microstructural parameters of LSM

cathodes to improve the electrochemical performance of anode-supported SOFCs. Journal of Power Sources, 2005. 141(2): p. 216-226.

92. Jorgensen, M.J., Primdahl, S., Bagger, C., and Mogensen, M., Effect of sintering temperature on microstructure and performance of LSM-YSZ composite cathodes. Solid State Ionics, 2001. 139(1-2): p. 1-11.

93. Liu, Y.L., Hagen, A., Barfod, R., Chen, M., Wang, H.J., Poulsen, F.W., and Hendriksen, P.V., Microstructural studies on degradation of interface between LSM-YSZ cathode and YSZ electrolyte in SOFCs. Solid State Ionics, 2009. 180(23-25): p. 1298-1304.

94. Meixner, D.L. and Cutler, R.A., Sintering and mechanical characteristics of lanthanum strontium manganite. Solid State Ionics, 2002. 146(3-4): p. 273-284.

95. Virkar, A.V., Chen, J., Tanner, C.W., and Kim, J.W., The role of electrode microstructure on activation and concentration polarizations in solid oxide fuel cells. Solid State Ionics, 2000. 131(1-2): p. 189-198.

96. Cha, S.W., O'Hayre, R., and Prinz, F.B., The influence of size scale on the performance of fuel cells. Solid State Ionics, 2004. 175(1-4): p. 789-795.

97. Brichzin, V., Fleig, J., Habermeier, H.U., and Maier, J., Geometry dependence of cathode polarization in solid oxide fuel cells investigated by defined Sr-doped $LaMnO_3$ microelectrodes. Electrochemical and Solid State Letters, 2000. 3(9): p. 403-406.

98. Tietz, F., Thermal expansion of SOFC materials Ionics Volume 5, Numbers 1-2, 129-139, DOI: 10.1007/BF02375916, 1999.

99. Jiang, S.P., A comparison of O_2 reduction reactions on porous $(La,Sr)MnO_3$ and $(La,Sr)(Co,Fe)O_3$ electrodes. Solid State Ionics, 2002. 146(1-2): p. 1-22.

100. Tietz, F., Thermal expansion of SOFC materials. Ionics, 1999. 5(1-2): p. 129-139.

101. Ullmann, H., Trofimenko, N., Tietz, F., Stover, D., and Ahmad-Khanlou, A., Correlation between thermal expansion and oxide ion transport in mixed conducting perovskite-type oxides for SOFC cathodes. Solid State Ionics, 2000. 138(1-2): p. 79-90.

102. Jiang, S.P., Development of lanthanum strontium manganite perovskite cathode materials of solid oxide fuel cells: a review. Journal of Materials Science, 2008. 43(21): p. 6799-6833.

103. Bhalla, A.S., Guo, R.Y., and Roy, R., The perovskite structure - a review of its role in ceramic science and technology. Materials Research Innovations, 2000. 4(1): p. 3-26.

104. Pena, M.A. and Fierro, J.L.G., Chemical structures and performance of perovskite oxides. Chemical Reviews, 2001. 101(7): p. 1981-2017.

105. Davies, P.K., Wu, H., Borisevich, A.Y., Molodetsky, I.E., and Farber, L., Crystal chemistry of complex perovskites: New cation-ordered dielectric oxides. Annual Review of Materials Research, 2008. 38: p. 369-401.

106. Yamamoto, O., Takeda, Y., Kanno, R., and Noda, M., Perovskite-type oxides as oxygen electrodes for high-temperature oxide fuel-cells. Solid State Ionics, 1987. 22(2-3): p. 241-246.

107. Yasumoto, K., Inagaki, Y., Shiono, M., and Dokiya, M., An (La,Sr)(Co,Cu)$O_{3-\delta}$ cathode for reduced temperature SOFCs. Solid State Ionics, 2002. 148(3-4): p. 545-549.

108. Tietz, F., Raj, I.A., Zahid, M., and Stover, D., Electrical conductivity and thermal expansion of $La_{0.8}Sr_{0.2(}$Mn,Fe,Co)$O_{3-\delta}$ perovskites. Solid State Ionics, 2006. 177(19-25): p. 1753-1756.

109. Meng, X.W., Lu, S.Q., Ji, Y., Wei, T., and Zhang, Y.L., Characterization of $Pr_{1-x}Sr_xCo_{0.8}Fe_{0.2}O_{3-\delta}$ ($0.2 <= x <= 0.6$) cathode materials for intermediate-temperature solid oxide fuel cells. Journal of Power Sources, 2008. 183(2): p. 581-585.

110. Simner, S.P., Bonnett, J.F., Canfield, N.L., Meinhardt, K.D., Sprenkle, V.L., and Stevenson, J.W., Optimized lanthanum ferrite-based cathodes for anode-supported SOFCs. Electrochemical and Solid State Letters, 2002. 5(7): p. A173-A175.

111. Bongio, E.V., Black, H., Raszewski, F.C., Edwards, D., McConville, C.J., and Amarakoon, V.R.W., Microstructural and high-temperature electrical characterization of $La_{1-x}Sr_xFeO_{3-\delta}$. Journal of Electroceramics, 2005. 14(3): p. 193-198.

112. Patrakeev, M.V., Bahteeva, J.A., Mitberg, E.B., Leonidova, I.A., Kozhevnikov, V.L., and Poeppelmeier, K.R., Electron/hole and ion transport in $La_{1-x}Sr_xFeO_{3-\delta}$. Journal of Solid State Chemistry, 2003. 172(1): p. 219-231.

113. Piao, J.H., Sun, K.N., Zhang, N.Q., Chen, X.B., Xu, S., and Zhou, D.R., Preparation and characterization of $Pr_{1-x}Sr_xFeO_3$ cathode material for intermediate temperature solid oxide fuel cells. Journal of Power Sources, 2007. 172: p. 633-640.

114. Tai, L.W., Nasrallah, M.M., Anderson, H.U., Sparlin, D.M., and Sehlin, S.R., Structure and electrical-properties of $La_{1-x}Sr_xCo_{1-y}Fe_yO_3$ .1. the system $La_{0.8}Sr_{0.2}Co_{1-y}Fe_yO_3$. Solid State Ionics, 1995. 76(3-4): p. 259-271.

115. Tai, L.W., Nasrallah, M.M., Anderson, H.U., Sparlin, D.M., and Sehlin, S.R., Structure and electrical-properties of $La_{1-x}Sr_xCo_{1-y}Fe_yO_3$ .2. the system La1-xSrxCo0.2Fe0.8O3. Solid State Ionics, 1995. 76(3-4): p. 273-283.

116. Chen, W.X., Wen, T.L., Nie, H.W., and Zheng, R., Study of $Ln_{0.6}Sr_{0.4}CO_{0.8}Mn_{0.2}O_{3-\delta}$ (Ln = La, Gd, Sm or Nd) as the cathode materials for intermediate temperature SOFC. Materials Research Bulletin, 2003. 38(8): p. 1319-1328.

117. Petric, A., Huang, P., and Tietz, F., Evaluation of La-Sr-Co-Fe-O perovskites for solid oxide fuel cells and gas separation membranes. Solid State Ionics, 2000. 135(1-4): p. 719-725.

118. Zhu, C.J., Liu, X.M., Xu, D., Yan, D.T., Wang, D.Y., and Su, W.H., Preparation and performance of $Pr_{0.7}Sr_{0.3}Co_{1-y}Cu_yO_{3-\delta}$ as cathode material of IT-SOFCs. Solid State Ionics, 2008. 179(27-32): p. 1470-1473.

119. Wei, B., Lu, Z., Huang, X.Q., Miao, J.P., Sha, X.Q., Xin, X.S., and Su, W.H., Crystal structure, thermal expansion and electrical conductivity of perovskite oxides $Ba_xSr_{1-x}Co_{0.8}Fe_{0.2}O_{3-\delta}$ ($0.3 <= x <= 0.7$). Journal of the European Ceramic Society, 2006. 26(13): p. 2827-2832.

120. Ishihara, T., Honda, M., Shibayama, T., Minami, H., Nishiguchi, H., and Takita, Y., Intermediate temperature solid oxide fuel cells using a new LaGaO3 based oxide ion conductor - I. Doped $SmCoO_3$ as a new cathode material. Journal of the Electrochemical Society, 1998. 145(9): p. 3177-3183.

121. Xia, C.R., Rauch, W., Chen, F.L., and Liu, M.L., $Sm_{0.5}Sr_{0.5}CoO_3$ cathodes for low-temperature SOFCs. Solid State Ionics, 2002. 149(1-2): p. 11-19.

122. Chiba, R., Yoshimura, F., and Sakurai, Y., An investigation of $LaNi_{1-x}Fe_xO3$ as a cathode material for solid oxide fuel cells. Solid State Ionics, 1999. 124(3-4): p. 281-288.

123. Carter, S., Selcuk, A., Chater, R.J., Kajda, J., Kilner, J.A., and Steele, B.C.H., Oxygen-transport in selected nonstoichiometric perovskite-structure oxides. Solid State Ionics, 1992. 53: p. 597-605.

124. Zhou, W., Ran, R., and Shao, Z.P., Progress in understanding and development of $Ba_{0.5}Sr_{0.5}Co_{0.8}Fe_{0.2}O_{3-\delta}$-based cathodes for intermediate-temperature solid-oxide fuel cells: A review. Journal of Power Sources, 2009. 192(2): p. 231-246.

125. Shao, Z.P., Haile, S.M., Ahn, J., Ronney, P.D., Zhan, Z.L., and Barnett, S.A., A thermally self-sustained micro solid-oxide fuel-cell stack with high power density. Nature, 2005. 435(7043): p. 795-798.
126. Shao, Z.P. and Haile, S.M., A high-performance cathode for the next generation of solid-oxide fuel cells. Nature, 2004. 431(7005): p. 170-173.
127. Zhu, Q.S., Jin, T.A., and Wang, Y., Thermal expansion behavior and chemical compatibility of $Ba_xSr_{1-x}Co_{1-y}Fe_yO_{3-\delta}$ with 8YSZ and 20GDC. Solid State Ionics, 2006. 177(13-14): p. 1199-1204.
128. Atkinson, A. and Ramos, T., Chemically-induced stresses in ceramic oxygen ion-conducting membranes. Solid State Ionics, 2000. 129(1-4): p. 259-269.
129. Mizusaki, J., Tagawa, H., Tsuneyoshi, K., and Sawata, A., Reaction-kinetics and microstructure of the solid oxide fuel-cells air electrode $La_{0.6}Ca_{0.4}MnO_3$/YSZ. Journal of the Electrochemical Society, 1991. 138(7): p. 1867-1873.
130. Huang, K., Zampieri, A., and Ise, M., Cathode polarizations of a cathode-supported solid oxide fuel cell. Journal of the Electrochemical Society, 2010. 157(10): p. B1471-B1478.
131. Wang, W.G. and Mogensen, M., High-performance lanthanum-ferrite-based cathode for SOFC. Solid State Ionics, 2005. 176(5-6): p. 457-462.
132. Caillol, N., Pijolat, M., and Siebert, E., Investigation of chemisorbed oxygen, surface segregation and effect of post-treatments on $La_{0.8}Sr_{0.2}MnO_3$ powder and screen-printed layers for solid oxide fuel cell cathodes. Applied Surface Science, 2007. 253(10): p. 4641-4648.
133. Rotureau, D., Viricelle, J.P., Pijolat, C., Caillol, N., and Pijolat, M., Development of a planar SOFC device using screen-printing technology. Journal of the European Ceramic Society, 2005. 25(12): p. 2633-2636.
134. Kuharuangrong, S., Effects of Ni on the electrical conductivity and microstructure of $La_{0.82}Sr_{0.16}MnO_3$. Ceramics International, 2004. 30(2): p. 273-277.
135. Fu, C.Y., Chang, C.L., Hsu, C.S., and Hwang, B.H., Electrostatic spray deposition of $La_{0.8}Sr_{0.2}Co_{0.2}Fe_{0.8}O_3$ films. Materials Chemistry and Physics, 2005. 91(1): p. 28-35.
136. Weber, A. and Ivers-Tiffee, E., Materials and concepts for solid oxide fuel cells (SOFCs) in stationary and mobile applications. Journal of Power Sources, 2004. 127(1-2): p. 273-283.

137. Horita, T., Tsunoda, T., Yamaji, K., Sakai, N., Kato, T., and Yokokawa, H., Microstructures and oxygen diffusion at the $LaMnO_3$ film/yttria-stabilized zirconia interface. Solid State Ionics, 2002. 152-153: p. 439-446.

138. Horita, T., Yamaji, K., Ishikawa, M., Sakai, N., Yokokawa, H., Kawada, T., and Kato, T., Active sites imaging for oxygen reduction at the $La_{0.9}Sr_{0.1}MnO_{3-x}$/yttria-stabilized zirconia interface by secondary-ion mass spectrometry. Journal of the Electrochemical Society, 1998. 145(9): p. 3196-3202.

139. Fukunaga, H., Ihara, M., Sakaki, K., and Yamada, K., The relationship between overpotential and the three phase boundary length. Solid State Ionics, 1996. 86-8: p. 1179-1185.

140. vanHeuveln, F.H., Bouwmeester, H.J.M., and vanBerkel, F.P.F., Electrode properties of Sr-doped $LaMnO_3$ on yttria-stabilized zirconia .1. Three-phase boundary area. Journal of the Electrochemical Society, 1997. 144(1): p. 126-133.

141. Fukunaga, H., Wen, C., and Yamada, K., Change of three-phase-boundary length of $La_{1-x}Sr_xMnO_3$-yttria stabilized zirconia-air by sintering. Journal of the Ceramic Society of Japan, 1999. 107(3): p. 229-236.

142. Fleig, J., Microelectrodes in solid state ionics. Solid State Ionics, 2003. 161(3-4): p. 279-289.

143. Brichzin, V., Fleig, J., Habermeier, H.U., Cristiani, G., and Maier, J., The geometry dependence of the polarization resistance of Sr-doped $LaMnO_3$ microelectrodes on yttria-stabilized zirconia. Solid State Ionics, 2002. 152: p. 499-507.

144. Schoonman, J., Dekker, J.P., Broers, J.W., and Kiwiet, N.J., Electrochemical vapor-deposition of stabilized zirconia and interconnection materials for solid oxide fuel-cells. Solid State Ionics, 1991. 46(3-4): p. 299-308.

145. Sakai, N., Yokokawa, H., Horita, T., and Yamaji, K., Lanthanum chromite-based interconnects as key materials for SOFC stack development. International Journal of Applied Ceramic Technology, 2004. 1(1): p. 23-30.

146. Suzuki, M., Sasaki, H., and Kajimura, A., Oxide ionic conductivity of doped lanthanum chromite thin film interconnectors. Solid State Ionics, 1997. 96(1-2): p. 83-88.

147. Yang, Z.G., Xia, G.G., Wang, C.M., Nie, Z.M., Templeton, J., Stevenson, J.W., and Singh, P., Investigation of iron-chromium-niobium-titanium ferritic stainless steel for

solid oxide fuel cell interconnect applications. Journal of Power Sources, 2008. 183(2): p. 660-667.

148. Kurokawa, H., Jacobson, C.P., DeJonghe, L.C., and Visco, S.J., Chromium vaporization of bare and of coated iron-chromium alloys at 1073 K. Solid State Ionics, 2007. 178(3-4): p. 287-296.

149. Opila, E.J., Myers, D.L., Jacobson, N.S., Nielsen, I.M.B., Johnson, D.F., Olminsky, J.K., and Allendorf, M.D., Theoretical and experimental investigation of the thermochemistry of $CrO_2(OH)_2(g)$. Journal of Physical Chemistry A, 2007. 111(10): p. 1971-1980.

150. Stanislowski, M., Wessel, E., Hilpert, K., Markus, T., and Singheiser, L., Chromium vaporization from high-temperature alloys I. Chromia-forming steels and the influence of outer oxide layers. Journal of the Electrochemical Society, 2007. 154(4): p. A295-A306.

151. Geng, S.J., Zhu, J.H., and Lu, Z.G., Evaluation of Haynes 242 alloy as SOFC interconnect material. Solid State Ionics, 2006. 177(5-6): p. 559-568.

152. Mahapatra, M.K., Lu, K., Liu, X.B., and Wu, J.W., Compatibility of a seal glass with $(Mn,Co)_3O_4$ coated interconnects: Effect of atmosphere. International Journal of Hydrogen Energy, 2010. 35(15): p. 7945-7956.

153. Gindorf, C., Singheiser, L., and Hilpert, K., Chromium vaporisation from Fe,Cr base alloys used as interconnect in fuel cells. Steel Research, 2001. 72(11-12): p. 528-533.

154. Hatchwell, C., Sammes, N.M., Brown, I.W.M., and Kendall, K., Current collectors for a novel tubular design of solid oxide fuel cell. Journal of Power Sources, 1999. 77(1): p. 64-68.

155. Martinz, H.P., Kock, W., and Sakaki, T., Ducropur, Ducrolloy - new chromium materials. Journal De Physique Iv, 1993. 3(C9): p. 205-213.

156. Konysheva, E., Seeling, U., Besmehn, A., Singheiser, L., and Hilpert, K., Chromium vaporization of the ferritic steel Crofer22APU and ODS $Cr5Fe1Y_2O_3$ alloy. Journal of Materials Science, 2007. 42(14): p. 5778-5784.

157. Krupp, U., Trindade, V.B., Schmidt, P., Christ, H.J., Buschmann, U., and Wiechert, W., Oxidation mechanisms of Cr-containing steels and Ni-base alloys at high temperatures. Part II: Computer-based simulation. Materials and Corrosion-Werkstoffe Und Korrosion, 2006. 57(3): p. 263-268.

158. Liu, Y. and Zhu, J., Stability of Haynes 242 as metallic interconnects of solid oxide fuel cells (SOFCs). International Journal of Hydrogen Energy, 2010. 35(15): p. 7936-7944.
159. Trindade, V.B., Krupp, U., Wagenhuber, P.E.G., and Christ, H.J., Oxidation mechanisms of Cr-containing steels and Ni-base alloys at high-temperatures - Part I: The different role of alloy grain boundaries. Materials and Corrosion-Werkstoffe Und Korrosion, 2005. 56(11): p. 785-790.
160. Yang, Z.G., Xia, G.G., and Stevenson, J.W., Evaluation of Ni-Cr-base alloys for SOFC interconnect applications. Journal of Power Sources, 2006. 160(2): p. 1104-1110.
161. Huang, W.H., Gopalan, S., Pal, U.B., and Basu, S.N., Evaluation of electrophoretically deposited CuMn1.8O4 spinel coatings on Crofer 22 APU for solid oxide fuel cell interconnects. Journal of the Electrochemical Society, 2008. 155(11): p. B1161-B1167.
162. Haanappel, V.A.C., Shemet, V., Vinke, I.C., Gross, S.M., Koppitz, T., Menzler, N.H., Zahid, M., and Quadakkers, W.J., Evaluation of the suitability of various glass sealant-alloy combinations under SOFC stack conditions. Journal of Materials Science, 2005. 40(7): p. 1583-1592.
163. Menzler, N.H., Sebold, D., Zahid, M., Gross, S.M., and Koppitz, T., Interaction of metallic SOFC interconnect materials with glass-ceramic sealant in various atmospheres. Journal of Power Sources, 2005. 152(1): p. 156-167.
164. Montero, X., Fischer, W., Tietz, F., Stover, D., Cassir, M., and Villarreal, I., Development and characterization of a quasi-ternary diagram based on $La_{0.8}Sr_{0.2}(Co,Cu,Fe)O_3$ oxides in view of application as a cathode contact material for solid oxide fuel cells. Solid State Ionics, 2009. 180(9-10): p. 731-737.
165. Montero, X., Tietz, F., Stover, D., Cassir, M., and Villarreal, I., Comparative study of perovskites as cathode contact materials between an $La_{0.8}Sr_{0.2}FeO_3$ cathode and a Crofer22APU interconnect in solid oxide fuel cells. Journal of Power Sources, 2009. 188(1): p. 148-155.
166. Chandra-Ambhorn, S., Wouters, Y., Antoni, L., Toscan, F., and Galerie, A., Adhesion of oxide scales grown on ferritic stainless steels in solid oxide fuel cells temperature and atmosphere conditions. Journal of Power Sources, 2007. 171(2): p. 688-695.

167. Oliver, D.C., External corrosion resistance of steel and ferritic stainless steel exhaust systems. Journal of the South African Institute of Mining and Metallurgy, 2003. 103(2): p. 93-100.

168. Srisrual, A., Coindeau, S., Galerie, A., Petit, J.P., and Wouters, Y., Identification by photoelectrochemistry of oxide phases grown during the initial stages of thermal oxidation of AISI 441 ferritic stainless steel in air or in water vapour. Corrosion Science, 2009. 51(3): p. 562-568.

169. Jablonski, P.D., Cowen, C.J., and Sears, J.S., Exploration of alloy 441 chemistry for solid oxide fuel cell interconnect application. Journal of Power Sources, 2010. 195(3): p. 813-820.

170. Jin, T. and Lu, K., Compatibility between AISI441 alloy interconnect and representative seal glasses in solid oxide fuel/electrolyzer cells. Journal of Power Sources, 2010. 195(15): p. 4853-4864.

171. Yang, Z.G., Xia, G.G., Maupin, G.D., and Stevenson, J.W., Conductive protection layers on oxidation resistant alloys for SOFC interconnect applications. Surface & Coatings Technology, 2006. 201(7): p. 4476-4483.

172. Chen, X., Hou, P.Y., Jacobson, C.P., Visco, S.J., and De Jonghe, L.C., Protective coating on stainless steel interconnect for SOFCs: oxidation kinetics and electrical properties. Solid State Ionics, 2005. 176(5-6): p. 425-433.

173. Wu, J.W., Jiang, Y.L., Johnson, C., and Liu, X.B., DC electrodeposition of Mn-Co alloys on stainless steels for SOFC interconnect application. Journal of Power Sources, 2008. 177(2): p. 376-385.

174. Stanislowski, M., Froitzheim, J., Niewolak, L., Quadakkers, W.J., Hilpert, K., Markus, T., and Singheiser, L., Reduction of chromium vaporization from SOFC interconnectors by highly effective coatings. Journal of Power Sources, 2007. 164(2): p. 578-589.

175. Konysheva, E., Laatsch, J., Wessel, E., Tietz, F., Christiansen, N., Singheiser, L., and Hilpert, K., Influence of different perovskite interlayers on the electrical conductivity between $La_{0.65}Sr_{0.3}MnO_3$ and Fe/Cr-based steels. Solid State Ionics, 2006. 177(9-10): p. 923-930.

176. Menzler, N.H., Batfalsky, P., Blum, L., Bram, M., Gross, S.M., Haanappel, V.A.C., Malzbender, J., Shemet, V., Steinbrech, R.W., and Vinke, I., Studies of material interaction after long-term stack operation. Fuel Cells, 2007. 7(5): p. 356-363.

177. Mawdsley, J.R., Carter, J.D., Kropf, A.J., Yildiz, B., and Maroni, V.A., Post-test evaluation of oxygen electrodes from solid oxide electrolysis stacks. International Journal of Hydrogen Energy, 2009. 34(9): p. 4198-4207.

178. Mitterdorfer, A. and Gauckler, L.J., $La_2Zr_2O_7$ formation and oxygen reduction kinetics of the $La_{0.85}Sr_{0.15}Mn_yO_3$, O-2(g) - YSZ system. Solid State Ionics, 1998. 111(3-4): p. 185-218.

179. Backhaus-Ricoult, M., SOFC - A playground for solid state chemistry. Solid State Sciences, 2008. 10(6): p. 670-688.

180. Levy, C., Zhong, Y., Morel, C., and Marlin, S., Thermodynamic stabilities of $La_2Zr_2O_7$ and $SrZrO_3$ in SOFC and their relationship with LSM synthesis processes. Journal of the Electrochemical Society, 2010. 157(11): p. B1597-B1601.

181. Taimatsu, H., Wada, K., Kaneko, H., and Yamamura, H., Mechanism of reaction between lanthanum manganite and yttria-stabilized zirconia. Journal of the American Ceramic Society, 1992. 75(2): p. 401-405.

182. Jiang, S.P., Activation, microstructure, and polarization of solid oxide fuel cell cathodes. Journal of Solid State Electrochemistry, 2007. 11(1): p. 93-102.

183. Kharton, V.V., Figueiredo, F.M., Navarro, L., Naumovich, E.N., Kovalevsky, A.V., Yaremchenko, A.A., Viskup, A.P., Carneiro, A., Marques, F.M.B., and Frade, J.R., Ceria-based materials for solid oxide fuel cells. Journal of Materials Science, 2001. 36(5): p. 1105-1117.

184. Fergus, J.W., Electrolytes for solid oxide fuel cells. Journal of Power Sources, 2006. 162(1): p. 30-40.

185. Uhlenbruck, S., Moskalewicz, T., Jordan, N., Penkalla, H.J., and Buchkremer, H.P., Element interdiffusion at electrolyte-cathode interfaces in ceramic high-temperature fuel cells. Solid State Ionics, 2009. 180(4-5): p. 418-423.

186. Donald, I., Mallinson, P., Metcalfe, B., Gerrard, L., and Fernie, J., Recent developments in the preparation, characterization and applications of glass- and glass–ceramic-to-metal seals and coatings. Journal of Materials Science, 2011. 46(7): p. 1975-2000.

187. Jin, T. and Lu, K., Thermal stability of a new solid oxide fuel/electrolyzer cell seal glass. Journal of Power Sources, 2010. 195(1): p. 195-203.
188. Schafer, W., Koch, A., HeroldSchmidt, U., and Stolten, D., Materials, interfaces and production techniques for planar solid oxide fuel cells. Solid State Ionics, 1996. 86-8: p. 1235-1239.
189. Akikusa, J., Adachi, K., Hoshino, K., Ishihara, T., and Takita, Y., Development of a low temperature operation solid oxide fuel cell. Journal of the Electrochemical Society, 2001. 148(11): p. A1275-A1278.
190. Singh, P. and Minh, N.Q., Solid oxide fuel cells: Technology status. International Journal of Applied Ceramic Technology, 2004. 1(1): p. 5-15.
191. Chu, C.L., Lee, J., and Lee, S.Y., Evaluation of glass composites for sealing solid oxide fuel cells. Journal of Ceramic Processing Research, 2008. 9(4): p. 338-342.
192. Yang, Z.G., Meinhardt, K.D., and Stevenson, J.W., Chemical compatibility of barium-calcium-aluminosilicate-based sealing glasses with the ferritic stainless steel interconnect in SOFCs. Journal of the Electrochemical Society, 2003. 150(8): p. A1095-A1101.
193. Bahadur, D., Lahl, N., Singh, K., Singheiser, L., and Hilpert, K., Influence of nucleating agents on the chemical interaction of MgO-Al_2O_3-SiO_2-B_2O_3 glass sealants with components of SOFCs. Journal of the Electrochemical Society, 2004. 151(4): p. A558-A562.
194. Bram, M., Reckers, S., Drinovac, P., Monch, J., Steinbrech, R.W., Buchkremer, H.P., and Stover, D., Deformation behavior and leakage tests of alternate sealing materials for SOFC stacks. Journal of Power Sources, 2004. 138(1-2): p. 111-119.
195. Zheng, R., Wang, S.R., Nie, H.W., and Wen, T.L., SiO_2-CaO-B_2O_3-Al_2O_3 ceramic glaze as sealant for planar ITSOFC. Journal of Power Sources, 2004. 128(2): p. 165-172.
196. Bansal, N.P. and Gamble, E.A., Crystallization kinetics of a solid oxide fuel cell seal glass by differential thermal analysis. Journal of Power Sources, 2005. 147(1-2): p. 107-115.
197. Flugel, A., Dolan, M.D., Varshneya, A.K., Zheng, Y., Coleman, N., Hall, M., Earl, D., and Misture, S.T., Development of an improved devitrifiable fuel cell sealing glass I. Bulk properties. Journal of the Electrochemical Society, 2007. 154(6): p. B601-B608.

198. Story, C., Lu, K., Reynolds, W.T., and Brown, D., Shape memory alloy/glass composite seal for solid oxide electrolyzer and fuel cells. International Journal of Hydrogen Energy, 2008. 33(14): p. 3970-3975.
199. Zhang, T., Fahrenholtz, W.G., Reis, S.T., and Brow, R.K., Borate volatility from SOFC sealing glasses. Journal of the American Ceramic Society, 2008. 91(8): p. 2564-2569.
200. Nielsen, J., Hagen, A., and Liu, Y.L., Effect of cathode gas humidification on performance and durability of Solid Oxide Fuel Cells. Solid State Ionics, 2010. 181(11-12): p. 517-524.
201. Peng, L. and Zhu, Q.S., Thermal cycle stability of $BaO-B_2O_3-SiO_2$ sealing glass. Journal of Power Sources, 2009. 194(2): p. 880-885.
202. Ghosh, S., Das Sharma, A., Kundu, P., Mahanty, S., and Basu, R.N., Development and characterizations of $BaO-CaO-Al_2O_3-SiO_2$ glass-ceramic sealants for intermediate temperature solid oxide fuel cell application. Journal of Non-Crystalline Solids, 2008. 354(34): p. 4081-4088.
203. Matsuzaki, Y. and Yasuda, I., Dependence of SOFC cathode degradation by chromium-containing alloy on compositions of electrodes and electrolytes. Journal of the Electrochemical Society, 2001. 148(2): p. A126-A131.
204. Cruse, T.A., Krumpelt, M., Ingram, B.J., Wang, S., and Salvador, P.A., Examination of chromium's effects on a LSM/YSZ solid oxide fuel cell cathode, in Advances in Solid Oxide Fuel Cells IV, Prabhakar Singh, N.P.B.T.O.A.W., Editor. 2009. p. 147-158.
205. Menzler, N.H., Tietz, F., Bram, M., Vinke, I.C., and Haart, L.G.J.B.d., Degradation phenomena in SOFCs with metallic interconnects, in Advances in Solid Oxide Fuel Cells IV, Prabhakar Singh, N.P.B.T.O.A.W., Editor. 2009. p. 93-104.
206. Neumann, A., Menzler, N.H., Vinke, I., and Lippert, H., Systematic study of chromium poisoning of LSM cathodes - single cell tests. ECS Transactions, 2009. 25(2): p. 2889-2898.
207. Jiang, S.P., Zhang, J.P., Apateanu, L., and Foger, K., Deposition of chromium species on Sr-doped $LaMnO_3$ cathodes in solid oxide fuel cells. Electrochemistry Communications, 1999. 1(9): p. 394-397.

208. Jiang, S.P., Zhang, S., and Zhen, Y.D., Early interaction between Fe-Cr alloy metallic interconnect and Sr-doped $LaMnO_3$ cathodes of solid oxide fuel cells. Journal of Materials Research, 2005. 20(3): p. 747-758.

209. Wang, K. and Fergus, J.W., The effect of manganese doping on chromium deposition at Pt/YSZ cathode interfaces. Electrochemical and Solid State Letters, 2008. 11(8): p. B156-B160.

210. Wang, K.L. and Fergus, J.W., The effect of transition-metal doping on chromium deposition at Pt/YSZ cathode interfaces. Journal of the Electrochemical Society, 2010. 157(7): p. B1008-B1011.

211. Liu, D.J. and Almer, J., Phase and strain distributions associated with reactive contaminants inside of a solid oxide fuel cell. Applied Physics Letters, 2009. 94(22).

212. Liu, D.J., Almer, J., and Cruse, T., Characterization of Cr poisoning in a solid oxide fuel cell cathode using a high energy X-ray microbeam. Journal of the Electrochemical Society, 2010. 157(5): p. B744-B750.

213. Jiang, S.P., Zhang, S., and Zhen, Y.D., Deposition of Cr species at $(La,Sr)(Co,Fe)O_3$ cathodes of solid oxide fuel cells. Journal of the Electrochemical Society, 2006. 153(1): p. A127-A134.

214. Kim, J.Y., Sprenkle, V.L., Canfield, N.L., Meinhardt, K.D., and Chick, L.A., Effects of chrome contamination on the performance of $La_{0.6}Sr_{0.4}Co_{0.2}Fe_{0.8}O_3$ cathode used in solid oxide fuel cells. Journal of the Electrochemical Society, 2006. 153(5): p. A880-A886.

215. Tucker, M.C., Kurokawa, H., Jacobson, C.P., De Jonghe, L.C., and Visco, S.J., A fundamental study of chromium deposition on solid oxide fuel cell cathode materials. Journal of Power Sources, 2006. 160(1): p. 130-138.

216. Yokokawa, H., Horita, T., Sakai, N., Yamaji, K., Brito, M.E., Xiong, Y.P., and Kishimoto, H., Thermodynamic considerations on Cr poisoning in SOFC cathodes. Solid State Ionics, 2006. 177(35-36): p. 3193-3198.

217. Chen, X.B., Zhang, L., and Jiang, S.P., Chromium deposition and poisoning on $(La_{0.6}Sr_{0.4-x}Ba_x)$ $(Co_{0.2}Fe_{0.8})O_3$ ($0 <= x <= 0.4$) cathodes of solid oxide fuel cells. Journal of the Electrochemical Society, 2008. 155(11): p. B1093-B1101.

218. Komatsua, T., Chiba, R., Arai, H., and Sato, K., Chemical compatibility and electrochemical property of intermediate-temperature SOFC cathodes under Cr poisoning condition. Journal of Power Sources, 2008. 176(1): p. 132-137.
219. Zhen, Y.D., Jiang, S.P., and Tok, A.I.Y., Strategy for the development of Cr-tolerant cathodes for solid oxide fuel cells, in Solid Oxide Fuel Cells 10, Eguchi, K., Singhai, S.C., Yokokawa, H., and Mizusaki, H., Editors. 2007, Electrochemical Society Inc: Pennington. p. 263-269.
220. Zhen, Y.D., Tok, A.I.Y., Jiang, S.P., and Boey, F.Y.C., La(Ni,Fe)O_3 as a cathode material with high tolerance to chromium poisoning for solid oxide fuel cells. Journal of Power Sources, 2007. 170(1): p. 61-66.
221. Schuler, J.A., Tanasini, P., Hessler-Wyser, A., and Van Herle, J., Rapid chromium quantification in solid oxide fuel cell cathodes. Scripta Materialia, 2010. 63(8): p. 895-898.
222. Shearing, P.R., Brett, D.J.L., and Brandon, N.P., Towards intelligent engineering of SOFC electrodes: a review of advanced microstructural characterisation techniques. International Materials Reviews, 2010. 55(6): p. 347-363.
223. Van Gestel, T., Han, F., Sebold, D., Buchkremer, H.P., and Stover, D., Nano-structured solid oxide fuel cell design with superior power output at high and intermediate operation temperatures. Microsystem Technologies-Micro-and Nanosystems-Information Storage and Processing Systems, 2011. 17(2): p. 233-242.
224. Grew, K.N., Chu, Y.S., Yi, J., Peracchio, A.A., Izzo, J.R., Hwu, Y., De Carlo, F., and Chiu, W.K.S., Nondestructive nanoscale 3D elemental mapping and analysis of a solid oxide fuel cell anode. Journal of the Electrochemical Society, 2010. 157(6): p. B783-B792.
225. Schuler, J.A., Tanasini, P., Hessler-Wyser, A., Comninellis, C., and Van Herle, J., Cathode thickness-dependent tolerance to Cr-poisoning in solid oxide fuel cells. Electrochemistry Communications, 2010. 12(12): p. 1682-1685.
226. Sato, K., Kinoshita, T., and Abe, H., Performance and durability of nanostructured $(La_{0.85}Sr_{0.15})_{0.98}MnO_3$/yttria-stabilized zirconia cathodes for intermediate-temperature solid oxide fuel cells. Journal of Power Sources, 2010. 195(13): p. 4114-4118.

227. Hessler-Wyser, A., Wuillemin, Z., Schuler, J.A., Faes, A., and Van Herle, J., TEM investigation on zirconate formation and chromium poisoning in LSM/YSZ cathode. Journal of Materials Science, 2011. 46(13): p. 4532-4539.

228. Kan, C.C. and Wachsman, E.D., Identifying drivers of catalytic activity through systematic surface modification of cathode materials. Journal of the Electrochemical Society, 2009. 156(6): p. B695-B702.

229. la O, G.J., Savinell, R.F., and Shao-Horn, Y., Activity enhancement of dense strontium-doped lanthanum manganite thin films under cathodic polarization: A combined AES and XPS study. Journal of the Electrochemical Society, 2009. 156(6): p. B771-B781.

230. Sharma, V.I. and Yildiz, B., Degradation mechanism in $La_{0.8}Sr_{0.2}CoO_3$ as contact Layer on the solid oxide electrolysis cell anode. Journal of the Electrochemical Society, 2010. 157(3): p. B441-B448.

231. Brett, D.J.L., Kucernak, A.R., Aguiar, P., Atkins, S.C., Brandon, N.P., Clague, R., Cohen, L.F., Hinds, G., Kalyvas, C., Offer, G.J., Ladewig, B., Maher, R., Marquis, A., Shearing, P., Vasileiadis, N., and Vesovic, V., What happens inside a fuel cell? Developing an experimental functional map of fuel cell performance. Chemphyschem, 2010. 11(13): p. 2714-2731.

232. Zhang, C.J., Grass, M.E., McDaniel, A.H., DeCaluwe, S.C., El Gabaly, F., Liu, Z., McCarty, K.F., Farrow, R.L., Linne, M.A., Hussain, Z., Jackson, G.S., Bluhm, H., and Eichhorn, B.W., Measuring fundamental properties in operating solid oxide electrochemical cells by using in situ X-ray photoelectron spectroscopy. Nature Materials, 2010. 9(11): p. 944-949.

233. Konysheva, E., Penkalla, H., Wessel, E., Mertens, J., Seeling, U., Singheiser, L., and Hilpert, K., Chromium poisoning of perovskite cathodes by the ODS alloy Cr5Fe1Y(2)O(3) and the high chromium ferritic steel Crofer22APU. Journal of the Electrochemical Society, 2006. 153(4): p. A765-A773.

Chapter 2

Chemical Compatibility between Sr-doped Lanthanum Manganite Air electrode and AISI 441 Interconnect

Abstract

Chromium poisoning in the air electrode of solid oxide fuel/electrolyzer cells is a critical issue when stainless steel with high Cr content is used as an interconnect material. The mechanism of the diffusion and deposition of the Cr species is not totally clear yet. In this work, an yttria-stabilized zirconia electrolyze (YSZ)/strontium-doped lanthanum manganite electrode (LSM)/AIS I441 alloy interconnect tri-layer structure has been fabricated by screen printing in order to simulate the working environment of a real cell. The samples are thermally treated in moist air atmosphere at 800°C for up to 500 h. The porous LSM layer thickness has been controlled to investigate the Cr distribution in the porous layer and the diffusion behaviors of the Cr species. The microstructure and elemental analysis show that Cr species diffuses into the porous LSM layer and deposits on the LSM surface. The deposition occurs simultaneously with the LSM grain growth.

2.1. Introduction

Solid oxide fuel cells (SOFCs) and solid oxide electrolyzer cells (SOECs) are electrochemical devices that produce electricity from fuel or hydrogen by splitting water [1,2]. In a SOFC/SOEC stack, an interconnect is placed between the air electrode and the fuel electrode in order to electrically connect single cells [3,4]. According to the planar stack design, the electrical resistance of the electrodes, the electrolyte, the interconnect, and their interfaces should be low enough to minimize the current loss and achieve a high energy conversion efficiency. High oxidation and corrosion resistance in oxidizing atmospheres, suitable coefficient of thermal expansion match with other cell components, good chemical compatibility with other cell materials, and long-term stability are also needed [5,6].

Conductive perovskite ceramics have been considered as air electrode materials, such as Sr-doped lanthanum manganite (LSM) and Sr-doped lanthanum ferrite (LSF) [7,8]. A variety of alloy systems have been investigated as interconnect materials, such as Fe-Cr, Fe-Ni, Ni-Cr, and Fe-Ni-Cr alloys. Ferritic stainless steel with high Cr content is widely studied as a more cost effective interconnect material [5,6,9].The common trait of these systems is that they all form a surface layer of Cr_2O_3, or chomia, under the oxidizing atmosphere, and this layer provides high temperature oxidation resistance. However, chomia evaporates at high temperatures and forms gaseous CrO_3 species. The pressure of the gaseous CrO_3 increases with oxygen partial pressure. The moisture in the oxidizing environment can cause chomia to evaporate as well, in the form of $CrO_2(OH)_2$. Water contents above 0.1% in air result in the partial pressure of $CrO_2(OH)_2$ to exceed the partial pressure of CrO_3 [10,11]:

$$Cr_2O_3+3/2O_2 \rightarrow 2CrO_3 \quad (2\text{-}1)$$

$$Cr_2O_3+3/2O_2+2H_2O \rightarrow 2CrO_2(OH)_2 \quad (2\text{-}2)$$

During the SOFC/SOEC operation, interconnect/air electrode interfacial evolution and structure/performance degradation encompass diffusion and reaction as well as the corresponding microstructure changes. The air electrode materials such as LSM show good durability in a single cell [12,13]. However, during the operation with Cr-containing metallic interconnect materials, the volatile Cr species transport to the air electrode and the air electrode/electrolyte interface. The interaction between the porous air electrode and the volatile Cr species is generally called Cr poisoning, which causes the major degradation on the air electrode side [14].When the porous LSM air electrode works with the interconnect forming volatile Cr species, the Cr poisoning leads to a dramatic increase of the cathode polarization resistance and a fast drop of the output voltage of the cell in several hundreds of hours [15-19]. In SOFCs, the Cr poisoning is undoubtedly the most serious problem. The atmosphere strongly affects the composition of the volatile Cr species [10,11]. The high humidity of the atmosphere in the air electrode of SOFCs can lead to large drop of the output cell voltage and degradation of the air electrode/electrolyte interface [20]. In SOECs, it is an even bigger problem because the interfacial degradation is 10 times faster than that in SOFCs due to the moist condition [21].

The interaction between the Cr-containing species from the interconnect and the air electrode has been investigated. However, there is considerable disagreements on the mechanism of Cr-containing species interaction with and deposition on the air electrode. Some studies

suggested that the deposition of Cr species is closely related to the oxygen activity at the electrode/electrolyte interface--triple phase boundaries (TPB) [15,19]. In contrast, others. believed that the interfacial degradation by Cr poisoning could be caused by (i) blocking of electrochemically active sites by electrochemical reduction of Cr-containing species, and (ii) decomposition of the air electrode by the formation of Cr-containing mixed oxide, driven by the thermodynamics without any influence of the electrical potentials [22]. There were also claims that the deposition of Cr species depends strongly on the nature of the air electrode materials and that Cr species deposition at the air electrode is most likely controlled by a non-electrochemical process [17,23,24].

As seen from the discussion, a fundamental issue is still in heated debate for the interconnect/air electrode interface: the location of the chemical reactions. The primary reasons for the disagreements is that to date there is no detailed knowledge of Cr species transport at the interface, interfacial reactions, and the corresponding electrode microstructure evolution. The accelerated interconnect/air electrode degradation in moist atmosphere and its relation to the reactions above need to be understood. Currently there is a lack of materials design, testing, and characterization efforts to systematically answer these questions.

In this work, $La_{0.8}Sr_{0.2}MnO_3$ (LSM) powder was made into air electrode and assembled with the AIS I441 alloy interconnect and yttria-stabilized zirconia (YSZ) electrolyte to simulate the air electrode side of SOFCs/SOECs. The microstructure and elemental distribution are investigated to evaluate the Cr poisoning of the porous air electrode layer. Focused ion beam (FIB) was used to assist the sample preparation for microstructure and surface analysis. The elemental analysis was carried out by energy dispersive spectroscopy (EDS). The EDS results were corrected to minimize the interferences of multiple elements. The effects of thickness and thermal treatment time on the Cr poisoning were investigated.

2.2. Experimental Procedures

2.2.1. Sample Preparation

LSM powder was prepared by conventional solid state reaction method [25]. $SrCO_3$ (99.9%, Sigma Aldrich, St. Louis, MO), La_2O_3 (99.98%, Alfa Aesar, Ward Hill, MA), and $MnCO_3$ (99.9%, Alfa Aesar, Ward Hill, MA) at designed composition ratios were mixed in a ball

mill for overnight. The mixed oxide and carbonates were calcined in a box furnace (Lindberg, Model No. 51314, Watertown, WI) at 1200°C for 20 h.The LSM powder was ground in a ball mill for 72 h after the calcination. The particle size of the LSM powder was measured by a laser light scattering analyzer (LA-750, Horiba Ltd., Japan). The particle size followed a normal distribution curve. The mean particle diameter of the LSM powder was 2.92 μm (based on three measurements, Fig. 2-1).

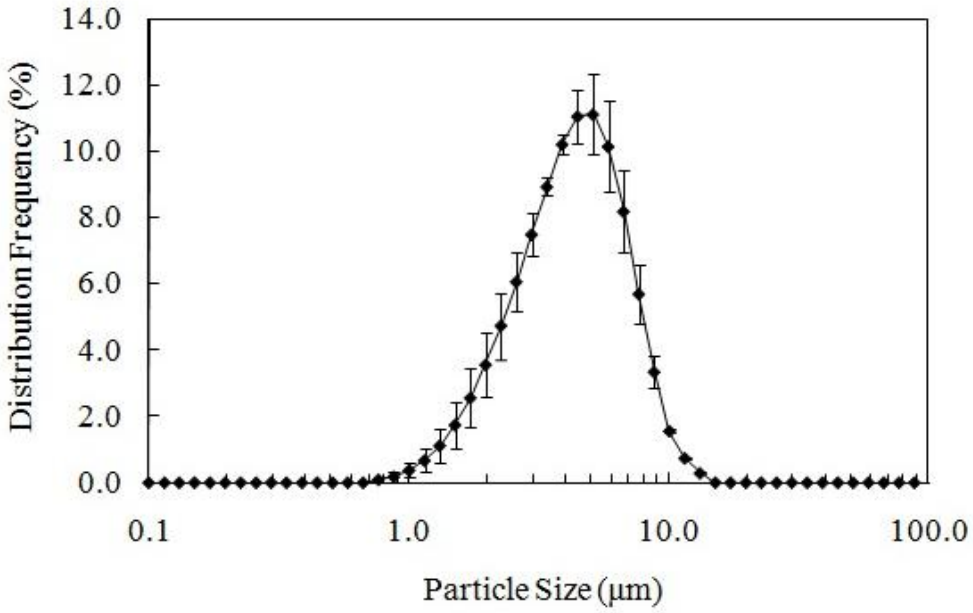

Fig. 2-1. Particle size distribution of the LSM powder.

AISI 441 ferritic stainless steel samples (ATI Allegheny Ludlum Corporation, Brackenridge, PA) were prepared as rectangular substrates (25.4 × 25.4 mm, thickness 2.08 mm). They were polished to optical finish to remove the oxidized layer, if any, and to obtain a scratch free flat surface. The polished samples were cleaned by ultrasound in water first and then in acetone.

The LSM air electrode was fabricated on the polished AISI 441 surface by screen printing. A polyvinyl butyral (PVB) based organic binder (B-73225, Ferro Co., Cleveland, OH) was used to make the LSM ink for the screen printing. The ink was obtained by mixing 52 wt% of the LSM powder, 30 wt% of the PVB binder, and 18 wt% of ethanol (99.5% purity, Sigma Aldrich, St. Louis, MO) and ball milling for over 12 h. 8 mol% yttria-stabilized zirconia (YSZ)

was chosen as the electrolyte material (Nextech Materials, Lewis Center, OH). The LSM ink was directly printed on the YSZ substrates (20 mm diameter, 250 -290 μm thickness) using a #120 mesh. Multiple prints were used in order to obtain different thickness for the air electrode layer. LSM/YSZ sample coupons were sintered at 1100°C for 2 h. The heating and cooling rates were 1°C/min. The bi-layer was kept at 200°C for 3 h and 400°C for 1 h to burn out the binder. After sintering, the thickness of the air electrode was measured by a micrometer.

The AISI 441 alloy coupon was placed on the LSM electrode side of the LSM/YSZ bi-layer as the interconnect. The configuration of the YSZ/LSM/AISI 441 tri-layer was shown in Fig. 2-2. A pressure of 450 Pa was applied on each tri-layer sample during the thermal treatment.

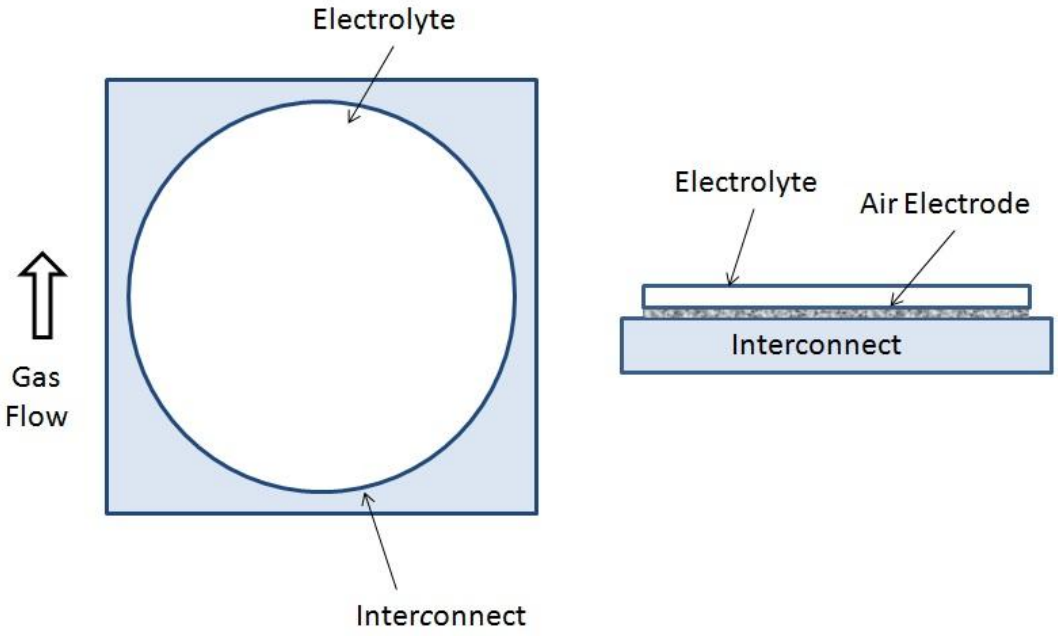

Fig. 2-2. Configuration of the YSZ/LSM/AISI 441 tri-layer.

2.2.2. Thermal Treatment

Thermal treatment was carried out in 25 vol% moist air at 800°C for 100, 200, and 500 h. The thermal treatment set-up was shown in Fig. 2-3. Water vapor was generated by heating a flask on a hot plate. The water vapor concentration in the gas flow was monitored by flowmeters #1 and #2 and controlled by the temperature of the water flask. The flow rates were 30 ml/s for air and 10 ml/s for water vapor, respectively.

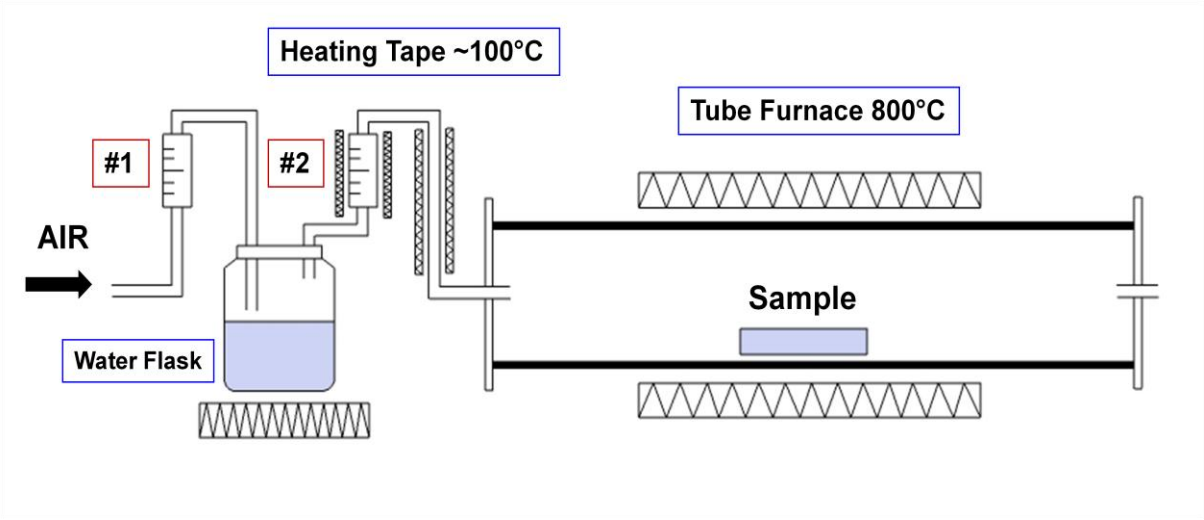

Fig. 2-3. Schematic drawing of the thermal treatment set-up.

2.2.3. Characterization

After the thermal treatment, the tri-layer samples were mounted into epoxy, and then cut, ground, and polished to obtain cross-sections. To study the microstructure, scanning electron microscopy (SEM, Quanta 600 FEG, FEI, Hillsboro, OR) was used to examine the cross-sections of the YSZ/LSM/AISI 441 samples. Backscattering electron images were used in order to obtain optimal contrast. The EDS module (Bruker AXS, MiKroanalysis Gmbh, Berlin, Germany) attached to the SEM was used for composition spot analysis, line scan, and elemental mapping across the interface. To improve the resolution of the composition analysis, FIB (FEI Helios 600 NanoLab, FEI, Hillsboro, OR) was used to cut a thin piece of a tri-layer sample.

2.3. Results and Discussion

2.3.1. Microstructure

Fig. 2-4 shows the microstructures of the as-sintered LSM/YSZ samples. For the 1 print, 2 prints, and 3 prints samples, the thicknesses are well controlled, which are 10-15 μm (Fig. 2-4(a)), 20-30 μm (Fig. 2-4(b)), and 30-45 μm (Fig. 2-4(c)), respectively. The air electrode layer shows good adhesion with the YSZ electrolyte. No visible cracks or voids in the porous air

electrode or at the interface are observed. There is some air electrode thickness variation but the darker color on the layer top is from the region farther into the air electrode. Based on the thickness, the surface area, and the weight of the air electrode layers, the relative density of the LSM air electrode is estimated to be 55-60%.

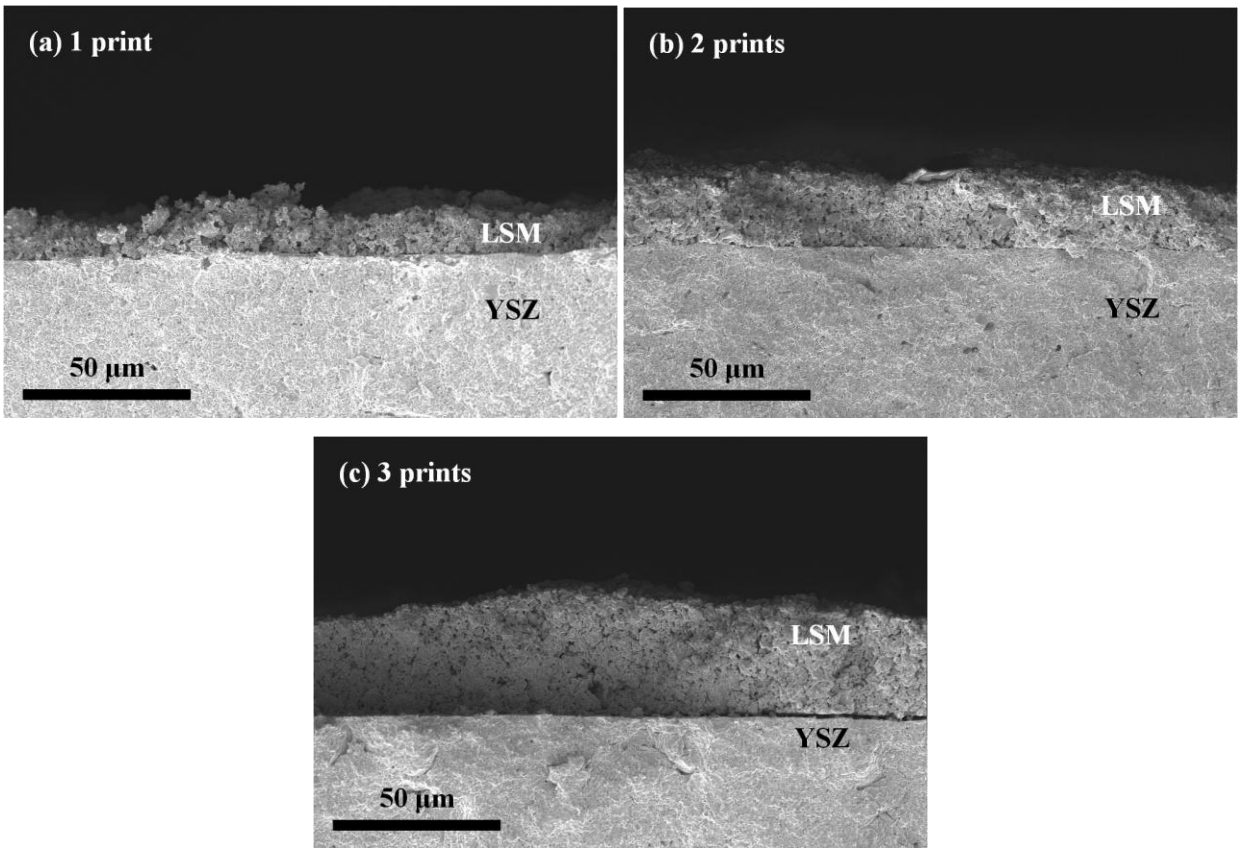

Fig. 2-4. SEM images of sintered LSM/YSZ bi-layers with different thicknesses.

The SEM images of the YSZ/LSM/AISI 441 tri-layer samples are shown in Fig. 2-5. The LSM electrode is in direct contact with the YSZ electrolyte and the AISI 441 interconnect. Before the thermal treatment, the microstructure of the porous LSM layer shows grain sizes around 3 μm (Figs. 2-5(a), (d), and (g)). After the thermal treatment for 200 h, the LSM grains grow larger (Figs. 2-5(b), (e), and (h)), some grains show sizes over 5 μm. After the thermal treatment for 500 h (Fig. 2-5(c), (f), and (i)), many of the grains grow to 5-10 μm in size.

After being thermally treated at high temperature, the grain growth of the porous LSM air electrode is caused by diffusion. The ionic diffusion is mainly influenced by defect chemistry [26]. The microstructure strongly affects the performance of the air electrode. Generally, in

SOFC mode, the polarization resistance increases with the grain growth of the air electrode, because the decrease in surface area caused by the grain growth simply decreases the active sites for oxygen reducing [27]. However, the effect of grain size is always hard address separately because the gas flow paths are also changed as a consequence. In this work, in order to investigate the surface deposition of the Cr species, the grain growth caused by ionic diffusion of the LSM must also be considered.

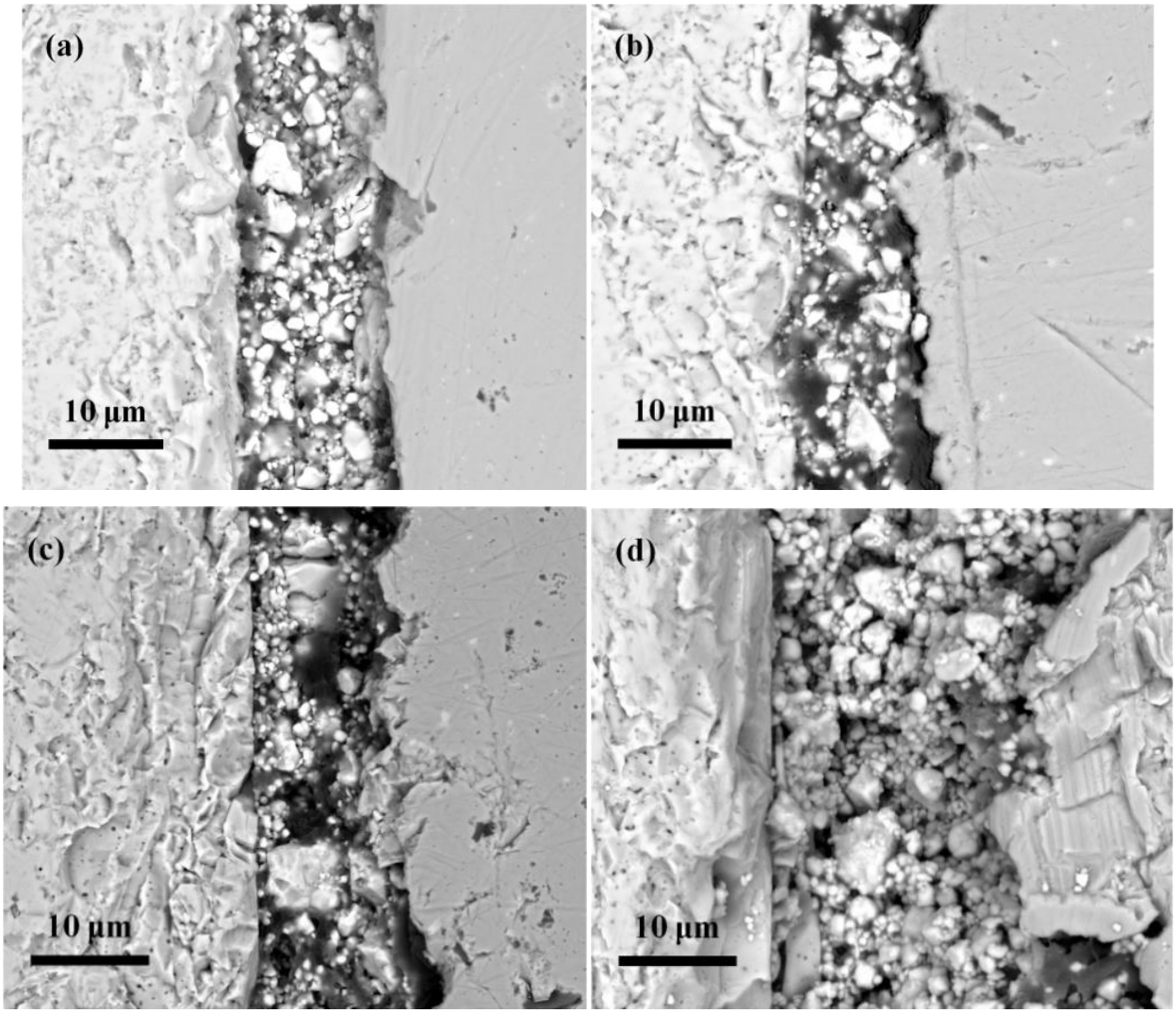

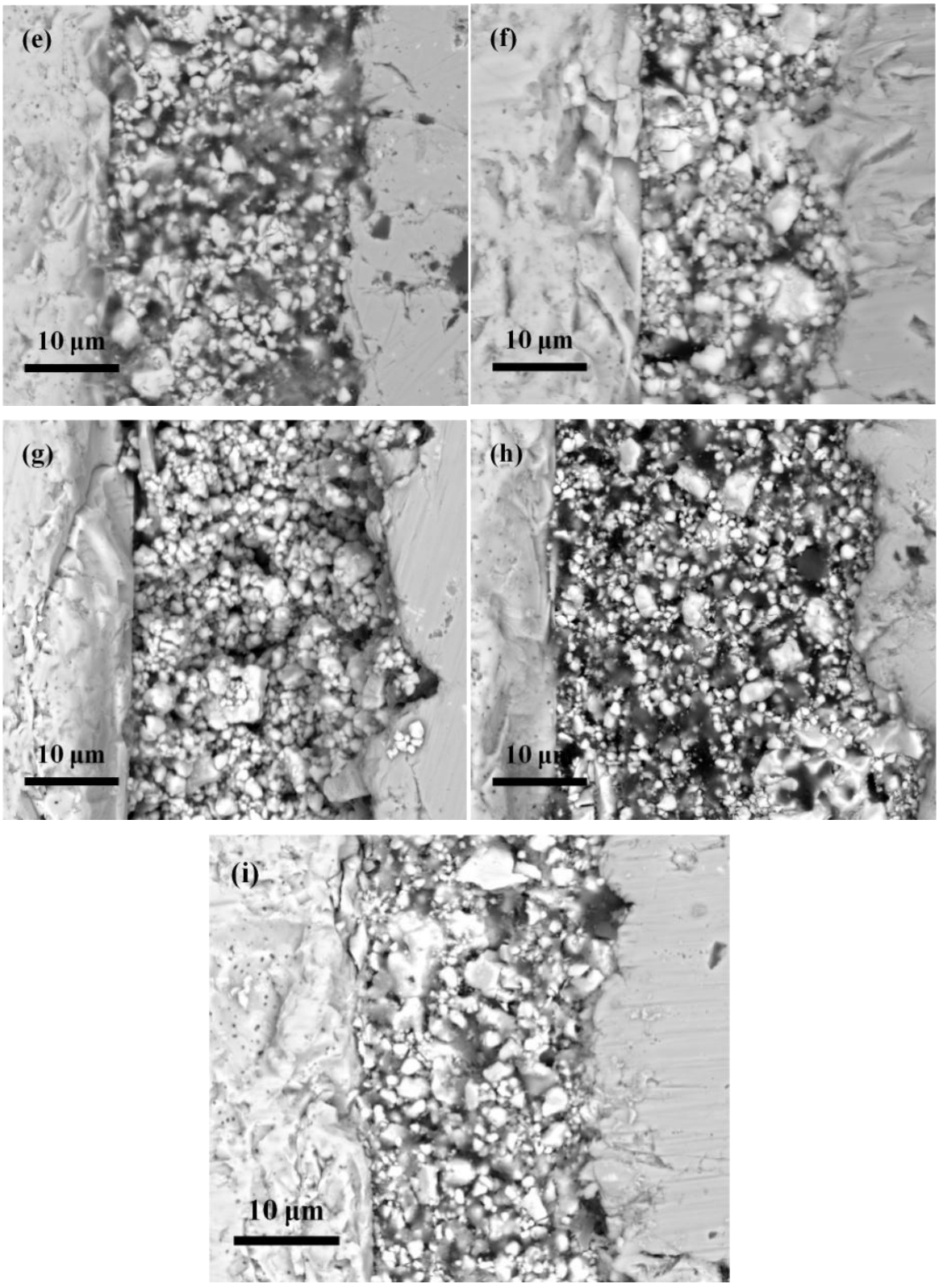
(e)
10 µm
(f)
10 µm
(g)
10 µm
(h)
10 µm
(i)
10 µm

Fig. 2-5. SEM images of YSZ/LSM/AISI 441 tri-layer before and after thermal treatment in air with 25 vol% water vapor at 800°C: (a) 1 print as-prepared, (b) 1 print 200 h, (c) 1 print 500 h, (d) 2 prints as-prepared, (e) 2 prints 200 h, (f) 2 prints 500 h, (g) 3 prints as-prepared, (h) 3 prints 200 h, and (i) 3 prints 500 h. The three layers are YSZ, LSM, and AISI 441 from left to right.

2.3.2. Elemental Analysis

In order to analyze the elemental distribution across the porous LSM layer, an EDS quantitative analysis is carried out. However, the sample surface obtained by mechanical polishing is uneven. This is because the porous LSM layer is sandwiched in-between the YSZ and the AISI 441 layers and the dense YSZ and AISI 441 have a much higher hardness than the porous LSM. During the polishing process, the porous LSM layer is preferentially removed over that of the YSZ and AISI 441 layers on the sides. The unevenness of the tri-layer cross-section leads to variations in the EDS analysis, especially for the line scan and elemental mapping. To address the issue and obtain an even tri-layer cross-section, a FIB is used to cut a thin slice of the tri-layer sample that has 2 prints of the air electrode thickness which have been thermally treated for 200 h.

Fig. 2-6 shows a cross-section of the 200 h thermally treated sample with 2 prints obtained by the FIB. The thickness of the slice is ~2 μm. Pt has been deposited on the cross sectional surface before the FIB cutting in order to keep the porous LSM electrode intact and provide electrical conductivity. Through this ~25 μm thick sample, a very even surface is obtained and the data scattering because of the sample surface unevenness can be effectively minimized.

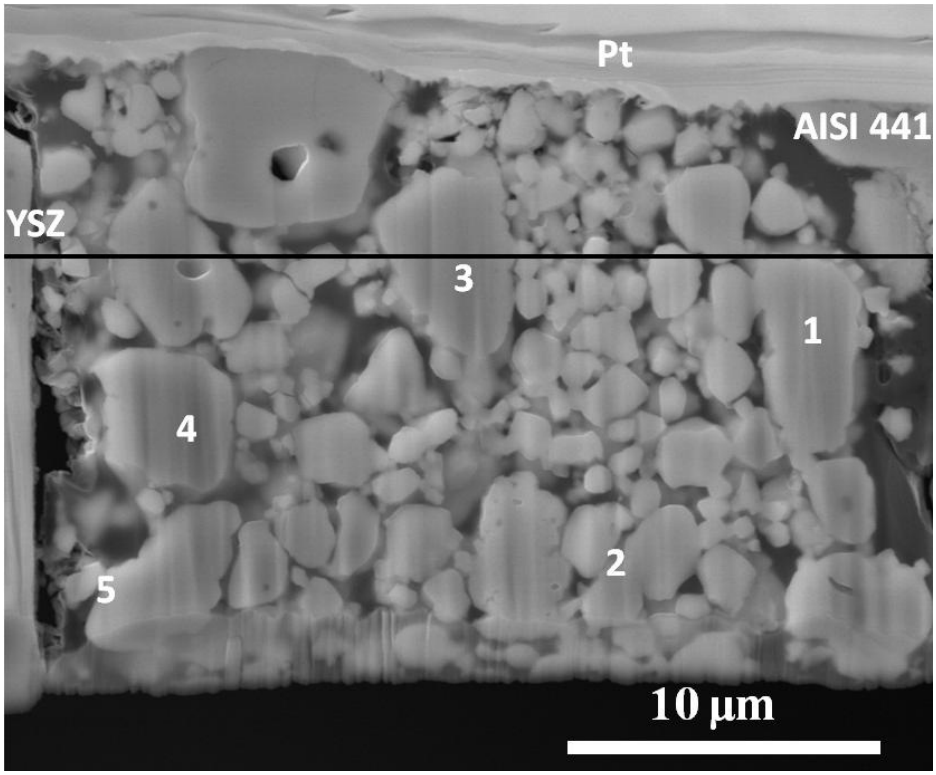

Fig. 2-6. SEM image of a thin layer across the YSZ/LSM/AISI 441 tri-layer by FIB cutting. The tri-layer has 2 prints and is thermally treated for 200 h.

The EDS spot analysis for the LSM electrode of the as-prepared and 200 h thermally treated YSZ/LSM/AISI 441 tri-layer with 2 prints is shown in Fig. 2-7. For the as-prepared LSM sample, the L lines of La and the K_α line of Mn are in the energy range of 4.0-7.0 keV. After the thermal treatment, unfortunately the K lines of Cr overlap with the lines from other elements: $Cr_{K\alpha}$(5.415 keV)/$La_{L\beta2}$(5.484 keV) and $Cr_{K\beta}$(5.989 keV)/$Mn_{K\alpha}$(5.899 keV). Because $Cr_{K\beta}$ is a minor line of Cr and $Mn_{K\alpha}$ is a major line of Mn and Mn is a major component of the LSM electrode, it is hard to estimate the Cr content by the overlapping $Cr_{K\beta}$/$Mn_{K\alpha}$ line. The $Cr_{K\alpha}$ line that overlaps with the $La_{L\beta2}$ line (a minor line of La) is used to analyze the presence of the Cr species. In the EDS pattern of the 200 h thermally treated sample, the relative height of the $Cr_{K\alpha}$/$La_{L\beta2}$ line is higher than the one in the EDS pattern of the as-prepared LSM, indicating that Cr diffusion into the air electrode and deposition on its surface occur during the thermal treatment. However, the amount of Cr is small based on the peak height difference.

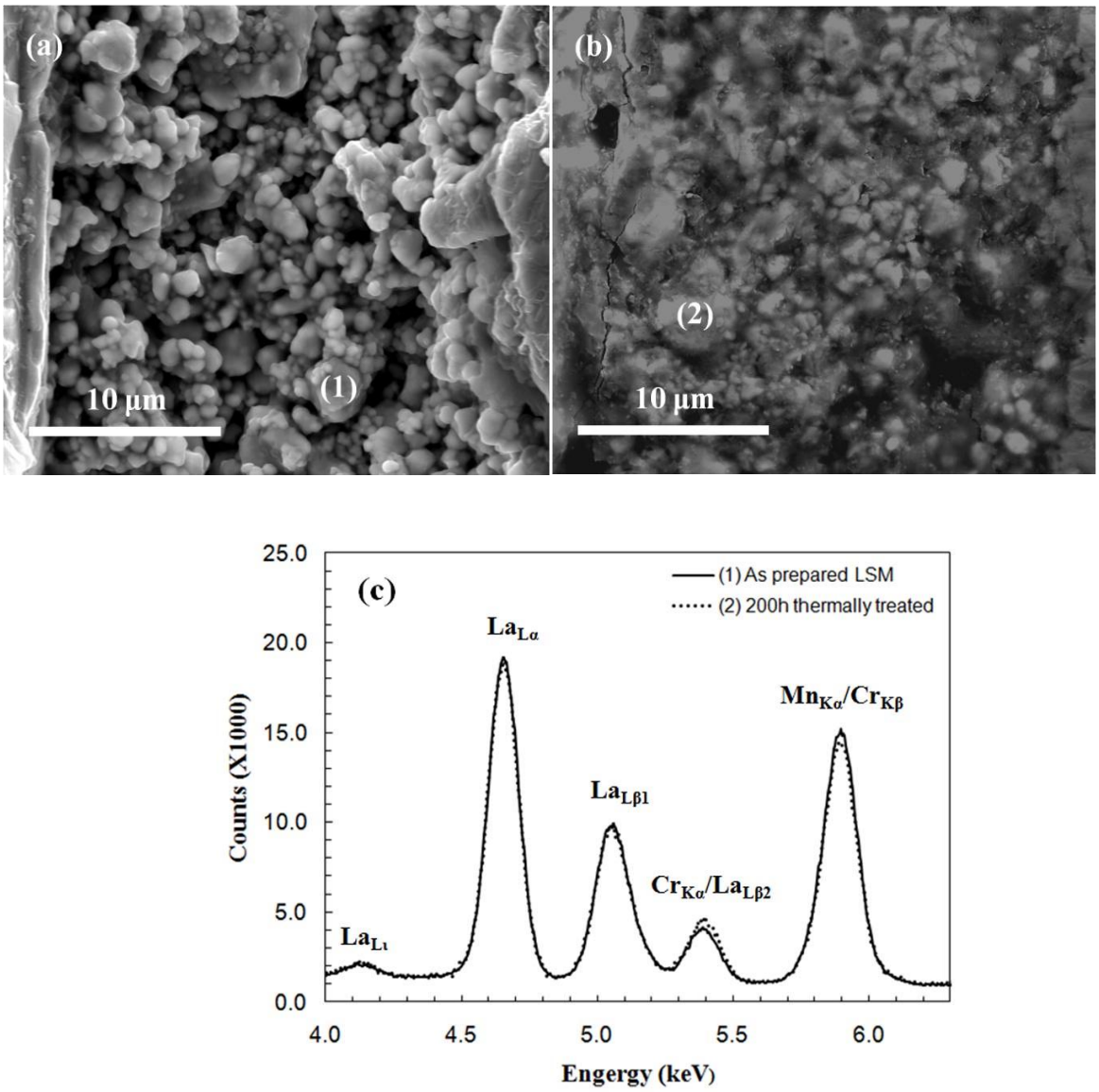

Fig. 2-7. EDS profiles of the as-prepared the LSM and LSM after 200 h of thermal treatment. The numbers in (a) and (b) show the data point locations in (c).

In this study, the quantitative EDS analysis of different species is corrected based on the equation [28]:

$$\frac{C_i}{C_{(i)}} = [ZAF]_i \frac{I_i}{I} \tag{2-3}$$

where C_i and $C_{(i)}$ are the weight fractions of the element i in the sample and in the standard sample respectively; I_i and $I_{(i)}$ are the line intensities of the element i in the examined sample and the standard sample, respectively; Z, A, and F are the factors related to atomic number, x-ray

absorption, and x-ray fluorescence. ZAF in combination can be called correction factor. Since the conversion from the mass fraction to the atomic fraction is linear, the correction factor from the standard LSM sample (the as-prepared sample) can be used to correct the Cr content in the thermally treated samples. When the Cr content is zero (the case for the as-prepared sample), the correction factor $a = \frac{A_{La}}{A_{Cr}{}^{pseudo}} = 25.87$ (A_{La} and $A_{Cr}{}^{pseudo}$ are the atomic fractions of La and Cr obtained in the as-prepared LSM sample where the actual Cr atomic fraction is zero). In the sample with La and Cr coexisting (the thermally treated sample):

$$A_{Cr} = A_{Cr}{}' - aA_{La} \tag{2-4}$$

A_{La} and $A_{Cr}{}'$ are the atomic fractions of La and Cr obtained in the Cr-containing LSM sample, and A_{Cr} is the corrected Cr atomic fraction. It should be mentioned that the correction process does not consider the change of the ZAF factors during the conversion from the mass fraction to the atomic fraction, because for the standardless EDS analysis, the ZAF factors of the weight fraction are easier to apply in the calculation. Furthermore, the ZAF factors are close to 1 leading to very small errors for the approximate quantitative analysis. Thus, equations 2-3 and 2-4 can help to estimate the error from the overlapping lines in the EDS analysis.

Fig. 2-6 shows the 5 spots analyzed by the EDS. Table 2-1 shows the quantitative EDS analysis results of the spots in Fig. 2-6. In Table 2-1, the as-prepared LSM sample is used as a reference. By considering Cr (which does not exist in the sample) in the quantitative calculation, a pseudo-Cr content of 0.53 atom% and a correction factor of La/Cr = 25.87 are obtained to correct the EDS line overlapping error.

Table 2-1. Quantitative EDS spot analysis, #1-5 corresponds to spots 1-5 in Fig. 2-6.

Atomic %	La	Sr	Mn	Cr	O
As-prepared*	13.63	8.41	17.40	0.53	60.04
#1	11.85	3.37	14,76	0.44	69.58
#2	14.88	6.29	17.23	1.14	60.47
#3	11.76	3.75	14.89	0.41	69.19
#4	11.91	3.46	14.94	0.44	69.26
#5	11.57	7.49	13.91	1.14	65.89

*Average of 3 spots

In Fig. 2-6, spots 1, 3, and 4 are from large LSM grains with over 2 μm size. These spots show the Cr content at 0.41-0.44 atom% and the ratio of La/Cr close to 25.87, which means the actual Cr content is zero. Also, the La/Mn ratio for these three spots is ~ 0.8, which indicates the chemical composition maintains the initial LSM stoichiometry. On the other hand, spots 2 and 5 are chosen along the edges of the LSM grains. The Cr atom percents calculated are significantly higher. After the correction, the Cr content on spots 2 and 5 are 0.56% and 0.69%, respectively.

The Cr content difference between the LSM grain centers and edges shows that the Cr species mainly reacts with the LSM grain surface by vapor diffusion instead of by solid state diffusion, leading to a surface deposition of Cr of less than 1%. Furthermore, the La/Sr ratios in the tested spots show large variations. In spots 1, 3, and 4, the La/Sr atomic ratio is 3.0-3.5, which is less than the original ratio of 4. In spots 2 and 5, the La/Sr atomic ratio is much lower, around 1.5-2.5. In the as-prepared LSM sample, the La/Sr ratio is 1.6. The different La/Sr ratios show that the Sr content is lower inside the LSM grains (spots 1, 3, and 4 are the cross-sections of large size LSM grains). For the as-prepared LSM in Table 2-1, the sample is not cut by the FIB, so the EDS spot analysis represents more of the surface La/Sr ratio, which matches with the results of spots 2 and 5 from the surface of the LSM grains. Sr segregation on the LSM surface has been investigated for the sintered LSM electrode [29]. The spot analysis of the FIB cut sample shows that after the thermal treatment in the moist air atmosphere, the surface Sr enrichment remains.

Fig. 2-8 shows the line scan result from the FIB cut sample along the line shown in Fig. 2-6 and the content of Cr is corrected by a factor of 25.87 based on the discussion related to the spot analysis. The La and Mn contents are mostly determined by the morphology of the porous layer. When the scan goes across the particle cross-section (dense LSM), La and Mn maintain their ratio in the LSM and show high atomic fractions. When the scan goes across the pores between the LSM grains, La and Mn show low atomic fractions, since the EDS detects more signals from the polish mounting material epoxy. The Sr/La ratio shows the same Sr surface segregation as from the spot analysis. Cr shows very low content across the porous LSM layer. There is no significant difference of Cr content along the porous LSM layer from the left to the right, which means the Cr vapor species diffuses fast and deposits on the LSM surface simultaneously across the porous layer. Also, there is a Cr concentrated region on the AISI 441 surface, which is believed to be the Cr_2O_3 oxide scale formed on the AISI 441 interconnect.

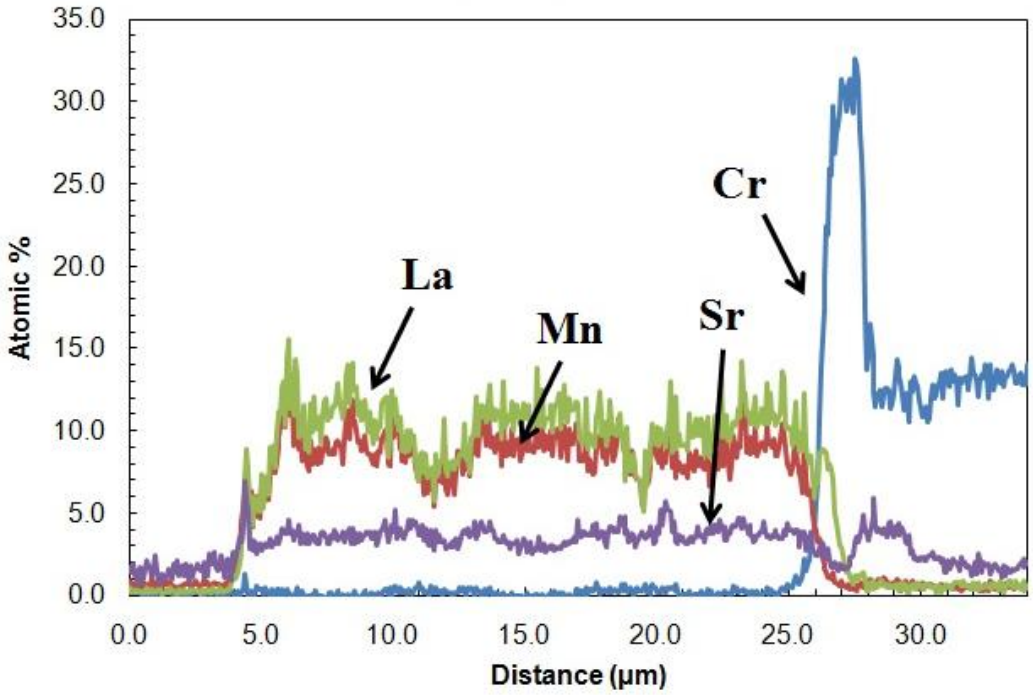

Fig. 2-8. EDS line scan of Cr , La, Mn, and Sr atom fractions across the YSZ/LSM/AISI 441 tri-layer sample with ~ 25 μm thickness and thermally treated for 200 h. The microstructure is shown in Fig. 2-6. The three layers are YSZ, LSM, and AISI 441 from left to right.

2.3.3. Thickness Effect and Distribution of Cr Species

The LSM electrode thickness also affects the Cr species diffusion and deposition on the porous LSM electrode. The elemental distribution profiles for the YSZ/LSM/AISI 441 tri-layers with different LSM thicknesses are shown in Fig. 2-9 before and after the thermal treatment. The Cr atomic fraction for the line scan is corrected by a factor of 25.87 based on the discussion related to the spot analysis. It should be pointed out that the tri-layers are from mechanical polishing only and uneven sample surfaces cause larger data variation for the line scan results. Fig. 2-9 is more suited for a qualitative trend analysis on Cr diffusion. For each figure, the Cr atomic fraction shows insignificant change from left to right across the porous LSM electrode, which means the Cr species diffuse into the LSM layer from the interconnect and distribute randomly on the porous air electrode layer. In air atmosphere and at 800°C, the vapor phase

diffusion of the volatile Cr species can reach hundreds of microns across the porous air electrode [30]. That means through the 10–40 μm thick air electrodes in this study, the Cr content through the porous layer is not obviously different regardless of the LSM thickness.

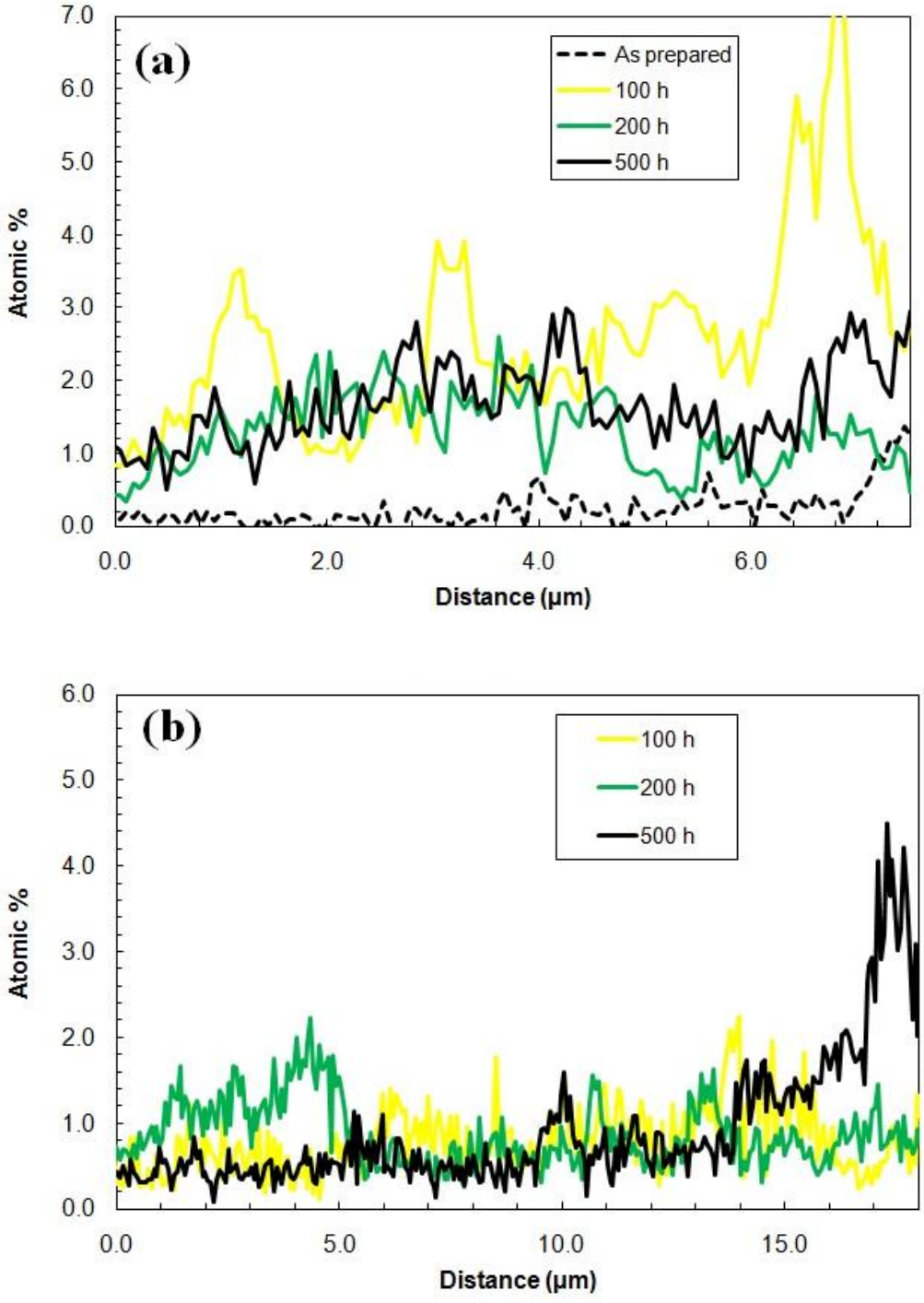

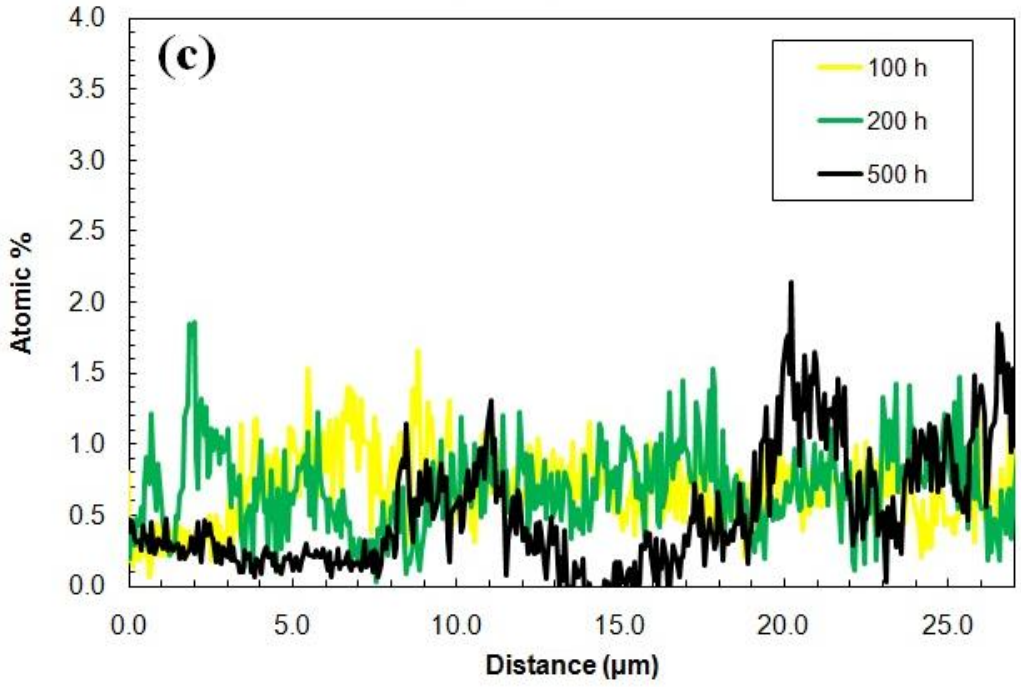

Fig. 2-9. EDS line scan of Cr content across the YSZ/LSM/AISI 441 tri-layer samples with different LSM thicknesses. (a) 1 print, 10-15 μm thick, (b) 2 prints, 20-30 μm thick, (c) 3 print, 30-45 μm thich. The three layers are YSZ, LSM, and AISI 441 from left to right. Each curve is averaged by 3 random scans.

In SOFCs, a thicker air electrode layer is proved to be beneficial for decreasing Cr poisoning. The reason is that there are more active sites not blocked by the Cr deposition [19]. Fig. 2-9 shows that in the thicker porous LSM layer (2 prints and 3 prints), the Cr atomic fraction is lower. That means the surface Cr deposition can be reduced by increasing the total surface area of the porous air electrode layer. Furthermore, the pathway of the gas flow affects the vapor phase diffusion and Cr deposition. Investigation of the morphological effects on Cr poisoning in the porous air electrode will provide useful information. It should also be noticed that the Cr fraction in the LSM layer does not significantly increase with the thermal treatment time. Thermodynamically, increasing the thermal treatment time should increase the Cr species diffusion. However, the current result occurs because that the deposition of the Cr species on the surface of the LSM electrode diminishes over time because of the reduced sites availability. In addition, the LSM electrode surface area also decreases with the thermal treatment time because of LSM grain growth. More experiments need to be carried out to clearly answer these questions.

2.4. Conclusions

LSM electrodes with different thicknesses are made and assembled with YSZ electrolyte and AISI 441 interconnect into a tri-layer configuration using screen printing. The tri-layer samples are thermally treated in air with 25 vol% water vapor at 800°C for up to 500 hrs. The porous LSM air electrode show grain growth during the thermal treatment. EDS elemental analysis shows that Cr species generated from the AISI 441 interconnect diffuses into the porous LSM layer and deposits on the LSM grain surface, mainly through vapor diffusion. Sr segregation on the LSM surface is also found for the as-sintered and thermally treated electrodes. The EDS line scan shows that the Cr atomic fraction decreases with LSM layer thickness increase but is not significantly affected by with thermal treatment time.

References

1. S.C. Singhal, K.K., High Temperature Solid Oxide Fuel Cells. 2003, Oxford, UK: Elsevier.
2. Jensen, S.H., Larsen, P.H., and Mogensen, M., Hydrogen and synthetic fuel production from renewable energy sources. International Journal of Hydrogen Energy, 2007. 32(15): p. 3253-3257.
3. Minh, N.Q., Solid oxide fuel cell technology-features and applications. Solid State Ionics, 2004. 174(1-4): p. 271-277.
4. O'Brien, J.E., Stoots, C.M., Herring, J.S., and Hartvigsen, J.J., Performance of planar high-temperature electrolysis stacks for hydrogen production from nuclear energy. Nuclear Technology, 2007. 158(2): p. 118-131.
5. Yang, Z.G., Recent advances in metallic interconnects for solid oxide fuel cells. International Materials Reviews, 2008. 53(1): p. 39-54.
6. Fergus, J.W., Metallic interconnects for solid oxide fuel cells. Materials Science and Engineering a-Structural Materials Properties Microstructure and Processing, 2005. 397(1-2): p. 271-283.
7. Jiang, S.P., Development of lanthanum strontium manganite perovskite cathode materials of solid oxide fuel cells: a review. Journal of Materials Science, 2008. 43(21): p. 6799-6833.

8. Simner, S.P., Bonnett, J.R., Canfield, N.L., Meinhardt, K.D., Shelton, J.P., Sprenkle, V.L., and Stevenson, J.W., Development of lanthanum ferrite SOFC cathodes. Journal of Power Sources, 2003. 113(1): p. 1-10.
9. Yang, Z.G., Xia, G.G., Wang, C.M., Nie, Z.M., Templeton, J., Stevenson, J.W., and Singh, P., Investigation of iron-chromium-niobium-titanium ferritic stainless steel for solid oxide fuel cell interconnect applications. Journal of Power Sources, 2008. 183(2): p. 660-667.
10. Hilpert, K., Das, D., Miller, M., Peck, D.H., and Weiss, R., Chromium vapor species over solid oxide fuel cell interconnect materials and their potential for degradation processes. Journal of the Electrochemical Society, 1996. 143(11): p. 3642-3647.
11. Opila, E.J., Myers, D.L., Jacobson, N.S., Nielsen, I.M.B., Johnson, D.F., Olminsky, J.K., and Allendorf, M.D., Theoretical and experimental investigation of the thermochemistry of $CrO_2(OH)_2(g)$. Journal of Physical Chemistry A, 2007. 111(10): p. 1971-1980.
12. Gemmen, R.S., Williams, M.C., and Gerdes, K., Degradation measurement and analysis for cells and stacks. Journal of Power Sources, 2008. 184(1): p. 251-259.
13. Yokokawa, H., Tu, H.Y., Iwanschitz, B., and Mai, A., Fundamental mechanisms limiting solid oxide fuel cell durability. Journal of Power Sources, 2008. 182(2): p. 400-412.
14. Fergus, J.W., Effect of cathode and electrolyte transport properties on chromium poisoning in solid oxide fuel cells. International Journal of Hydrogen Energy, 2007. 32(16): p. 3664-3671.
15. Taniguchi, S., Kadowaki, M., Kawamura, H., Yasuo, T., Akiyama, Y., Miyake, Y., and Saitoh, T., Degradation phenomena in the cathode of a solid oxide fuel cell with an alloy separator. Journal of Power Sources, 1995. 55(1): p. 73-79.
16. Matsuzaki, Y. and Yasuda, I., Dependence of SOFC cathode degradation by chromium-containing alloy on compositions of electrodes and electrolytes. Journal of the Electrochemical Society, 2001. 148(2): p. A126-A131.
17. Bentzen, J.J., Hogh, J.V.T., Barfod, R., and Hagen, A., Chromium poisoning of LSM/YSZ and LSCF/CGO composite cathodes. Fuel Cells, 2009. 9(6): p. 823-832.
18. Konysheva, E., Mertens, J., Penkalla, H., Singheiser, L., and Hilpert, K., Chromium poisoning of the porous composite cathode effect of cathode thickness and current density. Journal of the Electrochemical Society, 2007. 154(12): p. B1252-B1264.

19. Badwal, S.P.S., Deller, R., Foger, K., Ramprakash, Y., and Zhang, J.P., Interaction between chromia forming alloy interconnects and air electrode of solid oxide fuel cells. Solid State Ionics, 1997. 99(3-4): p. 297-310.
20. Nielsen, J., Hagen, A., and Liu, Y.L., Effect of cathode gas humidification on performance and durability of Solid Oxide Fuel Cells. Solid State Ionics, 2010. 181(11-12): p. 517-524.
21. Rufner, J., Gannon, P., White, P., Deibert, M., Teintze, S., Smith, R., and Chen, H., Oxidation behavior of stainless steel 430 and 441 at 800 degrees C in single (air/air) and dual atmosphere (air/hydrogen) exposures. International Journal of Hydrogen Energy, 2008. 33(4): p. 1392-1398.
22. Konysheva, E., Penkalla, H., Wessel, E., Mertens, J., Seeling, U., Singheiser, L., and Hilpert, K., Chromium poisoning of perovskite cathodes by the ODS alloy Cr5Fe1Y_2O_3 and the high chromium ferritic steel Crofer22APU. Journal of the Electrochemical Society, 2006. 153(4): p. A765-A773.
23. Jiang, S.P., Zhang, S., and Zhen, Y.D., Early interaction between Fe-Cr alloy metallic interconnect and Sr-doped $LaMnO_3$ cathodes of solid oxide fuel cells. Journal of Materials Research, 2005. 20(3): p. 747-758.
24. Jiang, S.P. and Zhen, Y.D., Mechanism of Cr deposition and its application in the development of Cr-tolerant cathodes of solid oxide fuel cells. Solid State Ionics, 2008. 179(27-32): p. 1459-1464.
25. Hammouche, A., Siebert, E., and Hammou, A., Crystallographic, thermal and electrochemical properties of the system $La_{1-x}Sr_xMnO_3$ for high temperature solid electrolyte fuel cells. Materials Research Bulletin, 1989. 24(3): p. 367-380.
26. Meixner, D.L. and Cutler, R.A., Sintering and mechanical characteristics of lanthanum strontium manganite. Solid State Ionics, 2002. 146(3-4): p. 273-284.
27. Jorgensen, M.J., Primdahl, S., Bagger, C., and Mogensen, M., Effect of sintering temperature on microstructure and performance of LSM-YSZ composite cathodes. Solid State Ionics, 2001. 139(1-2): p. 1-11.
28. Minh, N.Q., CERAMIC FUEL-CELLS. Journal of the American Ceramic Society, 1993. 76(3): p. 563-588.

29. Caillol, N., Pijolat, M., and Siebert, E., Investigation of chemisorbed oxygen, surface segregation and effect of post-treatments on $La_{0.8}Sr_{0.2}MnO_3$ powder and screen-printed layers for solid oxide fuel cell cathodes. Applied Surface Science, 2007. 253(10): p. 4641-4648.
30. Paulson, S.C. and Birss, V.I., Chromium poisoning of LSM-YSZ SOFC cathodes - I. Detailed study of the distribution of chromium species at a porous, single-phase cathode. Journal of the Electrochemical Society, 2004. 151(11): p. A1961-A1968.

Chapter 3

Surface and Interface Behaviors of Sr-doped Lanthanum Manganite Air Electrode in Different Moisture Atmospheres

Abstract

Surface and interface reactions of the air electrode with the contacting components of solid oxide cells are essential for the long term operation stability and performance. In this work, an yttria-stabilized zirconia electrolyte (YSZ)/strontium-doped lanthanum manganite electrode (LSM)/AISI 441 alloy interconnect tri-layer structure has been fabricated in order to simulate the working environment of a real cell with Cr-containing interconnect. The samples are thermally treated in moist air atmospheres (0 vol%, 10 vol%, and 25 vol% moistures) at 800°C for up to 500 h. The interactions among different cell components are characterized. The LSM air electrode shows slight grain growth but the growth is less in moist atmospheres. High moisture level affects the bonding between the LSM and the YSZ and leads to formation of small particles on the YSZ surface. The amount of Cr deposition on the LSM surface is slightly more for the samples thermally treated in the moist atmospheres and shows no significant difference between the 10 vol% and 25 vol% moist air. At the YSZ/LSM interface, La enrichment is significant and facilitates the Cr deposition while Mn depletion occurs. The YSZ surface composition is not strongly affected by the atmosphere.

3.1. Introduction

Solid oxide cells (SOCs), including solid oxide fuel cells (SOFCs) and solid oxide electrolyzer cells (SOECs), are promising electrochemical devices that generate electricity from fuel or produce hydrogen by splitting water. In order to obtain desired power output or hydrogen production, SOC stacks of planar geometry is widely investigated [1-5].

Ferritic stainless steel with a high Cr content has been intensively studied as a cost effective interconnect material for SOC stacks working at 700-900°C [6-8]. Perovskite materials have been widely investigated as air electrode materials, such as Sr-doped lanthanum manganite

(LSM) and Sr-doped lanthanum ferrite [9-11]. The air electrode is fabricated on the electrolyte, such as yttria-stabilized zirconia (YSZ), to reduce the oxygen molecules into oxygen ions (in the SOFC mode) or oxidize the oxygen ions to oxygen molecules (in the SOEC mode):

$$\text{SOFC: } \tfrac{1}{2}\,O_2\,(\text{gas}) + 2e^-\,(\text{cathode}) \rightarrow O^{2-} \tag{3-1}$$

$$\text{SOEC: } O^{2-}\,(\text{electrolyte}) \rightarrow \tfrac{1}{2}\,O_2\,(\text{gas}) + 2e^- \tag{3-2}$$

The ceramic air electrode of SOCs sintered with the electrolyte should have certain porosity and thickness in order to provide gas flow route and active sites for the above electrochemical reactions. At the contact between the electrolyte and the air electrode, the triple phase boundary (TPB) is the active area for the oxygen reduction/oxidation reactions, which is essential to the cell performance and determined by the microstructure of the electrolyte/air electrode interface [12]. For the long term operation, the air electrode should be stable in the high temperature oxidizing environment and chemically compatible with other contacting cell components [13,14]. Undesirable interactions can cause the degradation of the cell stacks. For the air electrode, grain size and porosity as well as TPB structure influence the cell performance [15-17]. Foreign phases formed at the interface due to the solid state reactions can also affect the active sites. For example, $La_2Zr_2O_7$ and $SrZrO_3$ formed at the YSZ/LSM interface block the TPBs and cause an increase in the ohmic resistance [18-20]. Furthermore, the deposition of poisoning species such as Cr species from the ferritic stainless steel across the air electrode and at the TPBs is a critical issue in cell degradation [21-25].

The degradation of the air electrode caused by the Cr-containing alloy interconnects (chromium poisoning) [26,27] includes three steps: oxidation and vaporization of Cr species from the surface of the interconnect, the diffusion of the Cr species, and the interaction between the vapor phase Cr species and the air electrode. Formation of the vapor phase Cr species is believed to be strongly dependent on the atmosphere. CrO_3 and $CrO_2(OH)_2$ are the two major compounds of the volatile Cr species, and $CrO_2(OH)_2$ is the dominant phase when water vapor is present in the atmosphere [28,29].

$$Cr_2O_3 + 3/2O_2 \rightarrow 2CrO_3 \tag{3-3}$$

$$Cr_2O_3 + 3/2O_2 + 2H_2O \rightarrow 2CrO_2(OH)_2 \tag{3-4}$$

Besides that the volatile Cr species are strongly affected by the water vapor in the atmosphere, Nielsen et al. observed that the SOFC voltage dropped 70% in 12.8 mol% moist air and small particles appear on the YSZ surface [30]. Kim et al. observed ~25% cell voltage drop

when using a 40 vol% moisture content. Composition analysis showed that La_2O_3 forms on the LSM air electrode surface and decreases conductivity [31].

AISI 441 is a promising stainless steel interconnect material that shows good stability in the SOFC working environment, forms a $(Mn,Cr)_3O_4$ layer, and decreases the Cr evaporation [7,32]. The composition of the alloy is shown in Table 3-1. As seen, AISI 441 has a high content of Fe (80.7 wt%) followed by Cr (17.6 wt%). However, the stability of AISI 441 with the air electrode in high moisture atmosphere has not been reported.

Table 3-1. Nominal composition of AISI 441 alloy (wt%). [7,33]

Cr	**Fe**	**Mn**	**Ti**	**Si**	**Al**	**C**	**S**	**P**	**Ni**	**Nb**	**Re**
17.6	80.68	0.33	0.18	0.47	0.045	0.01	0.001	0.024	0.20	0.46	-

In order to improve the understanding of the Cr species interaction with the air electrode, different moisture atmospheres are introduced in this study through the electrolyte/air electrode/interconnect tri-layer configuration (8% yttria-stabilized zirconia (YSZ) /$La_{0.8}Sr_{0.2}MnO_3$ (LSM)/AISI 441). The samples are thermally treated at 800°C for up to 500 h in dry air, 10 vol% moist air, and 25 vol% moist air, respectively. Scanning electron microscopy (SEM) is used to characterize the morphology changes of the LSM porous air electrode and the YSZ/LSM interface.

After the thermal treatment, the tri-layer samples were broken to examine the cross-sections. Some samples were mounted into epoxy, and then cut and ground to detect different positions (distances away from the AISI 441 layer) in the porous LSM air electrode. Along the 30 μm thick LSM layer, the examined locations were shown in Fig. 3-1. They were labeled as YSZ/LSM, LSM left, LSM middle, LSM right, and LSM/AISI 441 from the YSZ to the AISI 441. X-ray photoelectron spectroscopy (XPS) is used to obtain surface chemistry and elemental distribution across the LSM layer. X-ray diffraction (XRD) and energy dispersive spectroscopy (EDS) are used to investigate the Cr deposition difference in the different atmospheres.

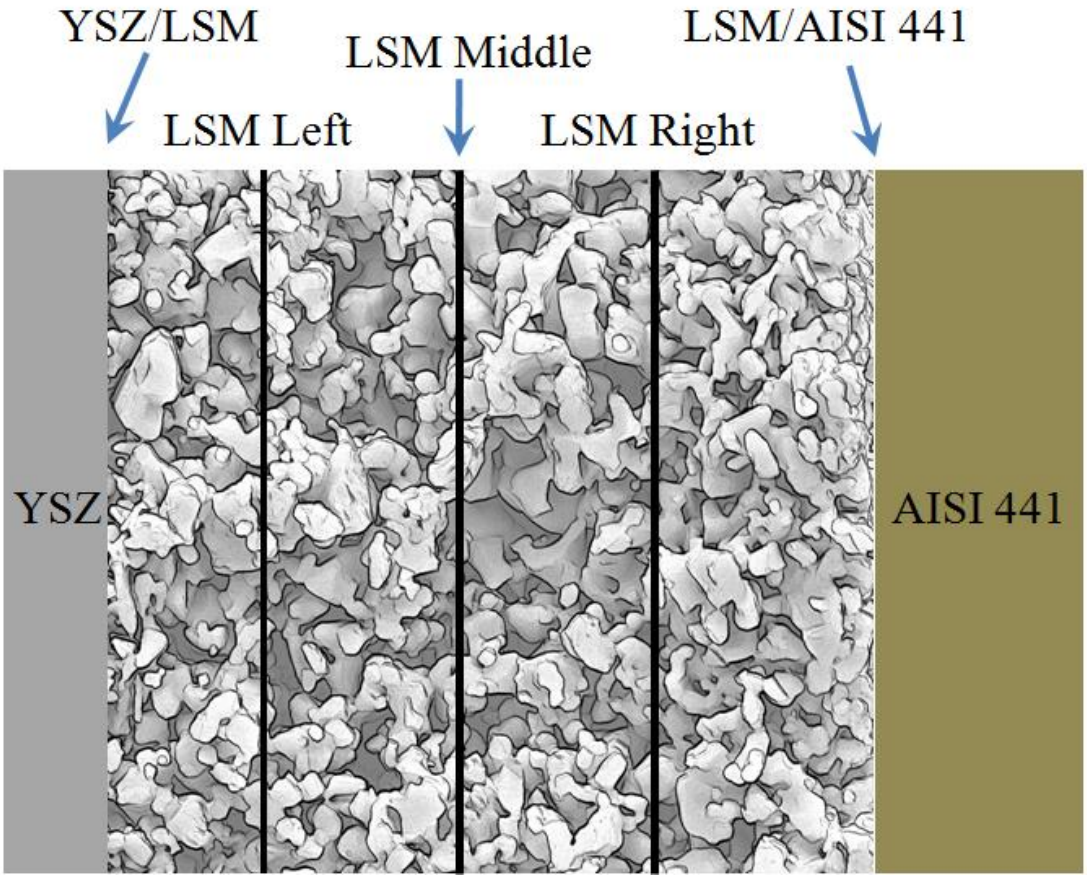

Fig. 3-1. The examination locations of the porous LSM air electrode. XPS is carried out at five locations: YSZ/LSM, LSM Left, LSM Middle, LSM Right, and LSM/AISI 441.

3.2. Experimental Procedures

3.2.1. Sample Preparation

LSM powder was prepared by conventional solid state reaction method [34]. AISI 441 ferritic stainless steel samples (ATI Allegheny Ludlum Corporation, Brackenridge, PA) were prepared as rectangular substrates (25.4 × 25.4 mm, thickness 2.08 mm). They were polished to optical finish to remove the oxidized layer, if any, and to obtain a scratch free flat surface. The polished samples were cleaned by ultrasound in water first and then in acetone.

The LSM air electrode was fabricated on the polished AISI 441 surface by screen printing [35]. The LSM layer on the YSZ substrates (20 mm diameter, 250–290 μm thickness, Nextech Materials, Lewis Center, OH) was 20-30 μm thick after being sintered at 1100°C for 2 h.

After the sintering of the LSM/YSZ bi-layer, the AISI 441 alloy was placed on the LSM electrode side as the interconnect. The details of the tri-layer sample configuration can be found in the previous chapter.

Thermal treatment was carried out in dry air (compressed air), 10 vol% and 25 vol% moist air at 800°C for 500 h. The thermal treatment set-up was given in Chapter 2. The flow rates were 10 $ml \cdot s^{-1}$ for the dry air, 10 $ml \cdot s^{-1}$ air/1.1 $ml \cdot s^{-1}$ water vapor for the 10 vol% moist air, and 30 $ml \cdot s^{-1}$ air/10 $ml \cdot s^{-1}$ water vapor for the 25 vol% moist air, respectively.

3.2.2. Characterization

After the thermal treatment, the tri-layer samples were broken to examine the cross-sections. SEM (Quanta 600 FEG, FEI, Hillsboro, OR) was used to study the microstructure. The EDS module (Bruker AXS, MiKroanalysis Gmbh, Berlin, Germany) attached to the SEM was used for compositional spot analysis. Some samples were mounted into epoxy, and then cut and ground to detect different positions (distances away from the AISI 441 layer) in the porous LSM air electrode by an X-ray photoelectron spectrometer (XPS, PHI Quantera SXM-03, Physical Electronics Inc., Chanhassen, MN). An Al Kα radiation (1486.6 eV) was used as the X-ray source. Along the 30 μm thick LSM layer, the examined locations were shown in Fig. 3-1. They were labeled as YSZ/LSM, LSM Left, LSM Middle, LSM Right, and LSM/AISI 441 from the YSZ to the AISI 441. In order to identify the phases, X-ray diffraction (XRD) studies were carried out in an X'Pert PRO diffractometer (PANalytical B.V., EA Almelo, The Netherlands). The step size was 0.030° s^{-1} with Cu Kα radiation (λ= 1.5406 Å).

3.3. Results

3.3.1. Microstructure

Fig. 3-2(a) shows the microstructure of the LSM layer at the LSM/AISI 441 interface before and after the thermal treatment in the different atmospheres. The AISI 441 interconnect was removed after the thermal treatment; the SEM images in Fig. 3-2(a) are taken at the LSM "top" surface, which is directly in contact with the AISI 441 polished surface. Before the thermal treatment, the microstructure of the porous LSM layer shows grain sizes around 3 μm (Fig. 3-

2(a)). After the thermal treatment in dry air for 500 h, the grains grow larger, whereas some small grains adhere together and form large grains with about 5 μm size. Also, the grains become more roundish compared with those before the thermal treatment. The air electrode looks dense. For the samples thermally treated in 10 vol% and 25 vol% moist air atmospheres, the microstructures are almost the same, with the latter having more roundish grains. The grain growth and morphology change are both relatively less than those of the dry air treated sample. Based on this observation, it can be concluded that dry air induces more sintering than moist atmospheres during the thermal treatment.

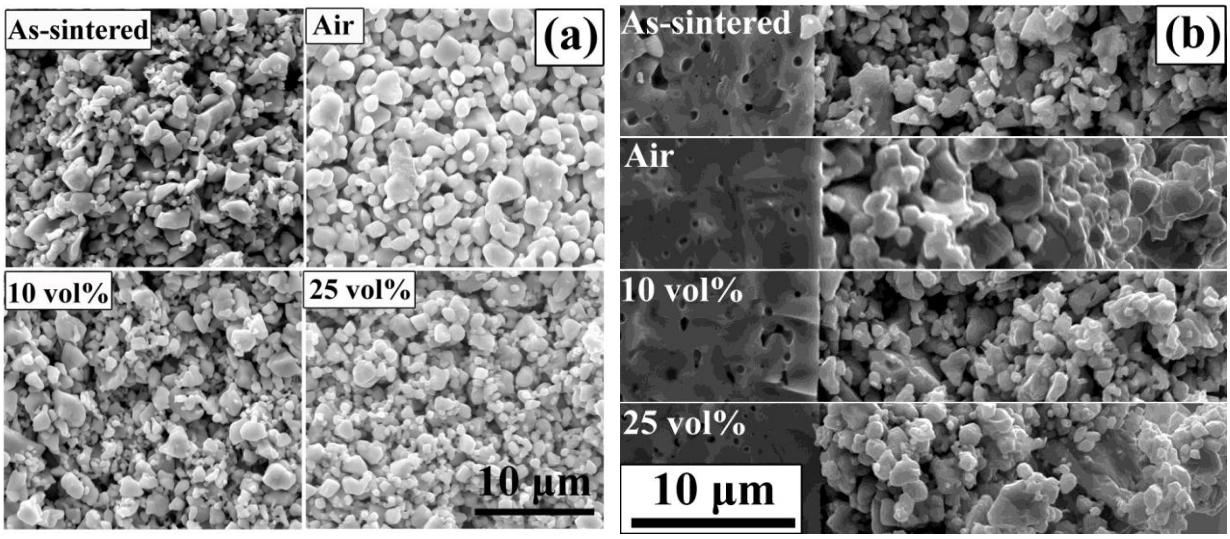

Fig. 3-2. SEM images of the LSM porous layer before and after the thermal treatment in the different moisture atmospheres at 800°C for 500 h: (a) the LSM side in contact with the AISI 441 interconnect, (b) fractured cross section, the dense YSZ electrolyte is on the left.

The cross sections of the LSM layer and the YSZ/LSM interface are shown in Fig. 3-2(b). The YSZ/LSM samples were fractured to obtain the cross sections and avoid morphological alteration from polishing. The LSM air electrode layer shows good adhesion with the YSZ electrolyte after sintering and after the thermal treatment. No visible cracks in the porous air electrode or at the interface are observed. The microstructure of the LSM porous air electrode is homogeneous across the LSM thickness, where no differences are seen from the left (YSZ/LSM interface) to the right (LSM/AISI 441 interface). The microstructure of each sample is consistent with the LSM "top" surface. The sample thermally treated in dry air shows the most significant

grain growth among all the samples, where small grains adhere together and form large grains over 5 μm. For the samples thermally treated in 10 vol% and 25 vol% moist air, the grain growth and bonding are observed but less than those for the dry air treated sample. The 25% moisture sample shows more sintering than the 10 vol% moisture sample.

The YSZ/LSM interfacial behaviors of the thermally treated samples are also examined (Fig. 3-3). Fig. 3-3(a) is the original surface of the YSZ substrate (without any LSM layer) after sintering, which shows clear grain boundaries. Figs. 3-3(b)–3-3(e) are the SEM images taken from the YSZ surface after the LSM layer being mechanically peeled off. In order to preserve the morphologies at the interfaces, the LSM layers were carefully scratched off and no further disturbance was involved. Bonding spots and some remaining LSM grains can be seen on the YSZ surface. For the YSZ/LSM interface after sintering, small contact spots with mostly less than 500 nm sizes are observed on the YSZ surface (Fig. 3-3(b), pointed by the arrows). The YSZ grain boundaries are still visible. After the thermal treatment at 800°C for 500 h in dry air (Fig. 3-3(c)), the bonding spots substantially increase and the spot size increases to ~1 μm (pointed by the arrows). No YSZ grain boundaries can be seen. This means more extensive contacts are formed during the thermal treatment. This result is consistent with the microstructure of the LSM layer (Fig. 3-2(b)). The bonding spots for the sample thermally treated in dry air, however, are clean. For the sample thermally treated in 10 vol% moist air (Fig. 3-3(d)), individual bonding spots are flatter but harder to distinguish. On the YSZ surface, the grain boundaries are hard to be seen and many small particles with less than 50 nm size are observed. These small particles tend to distribute along the boundaries of the YSZ grains. For the sample thermally treated in 25 vol% moist air, the bonding merges into a continuous layer and the YSZ grain boundaries are invisible (Fig. 3-3(e)). More small particles are seen with larger sizes (~100 nm and more scattering over the interface).

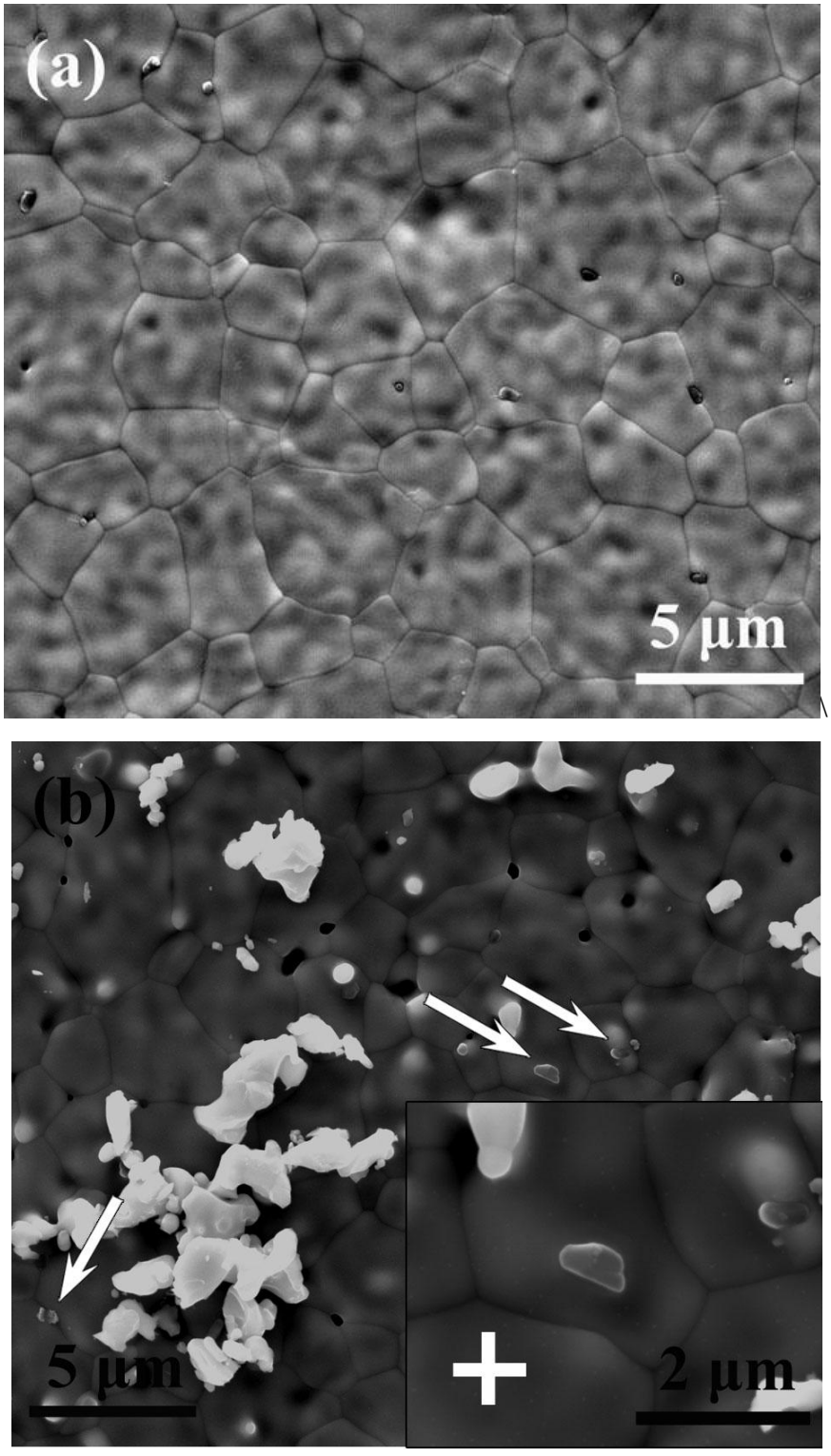
(a)
5 µm
(b)
5 µm
2 µm

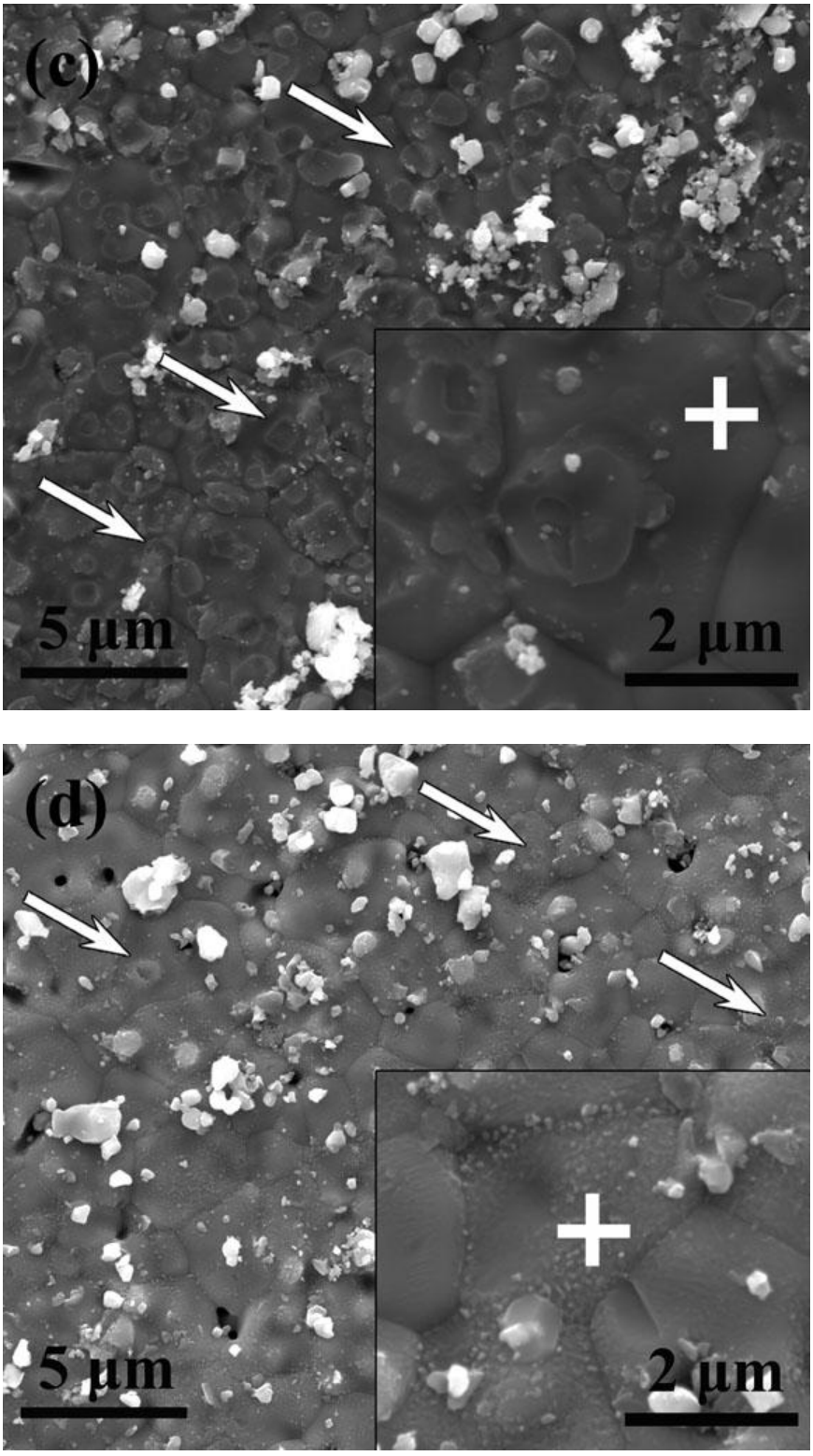
(c)
5 µm
2 µm
(d)
5 µm
2 µm

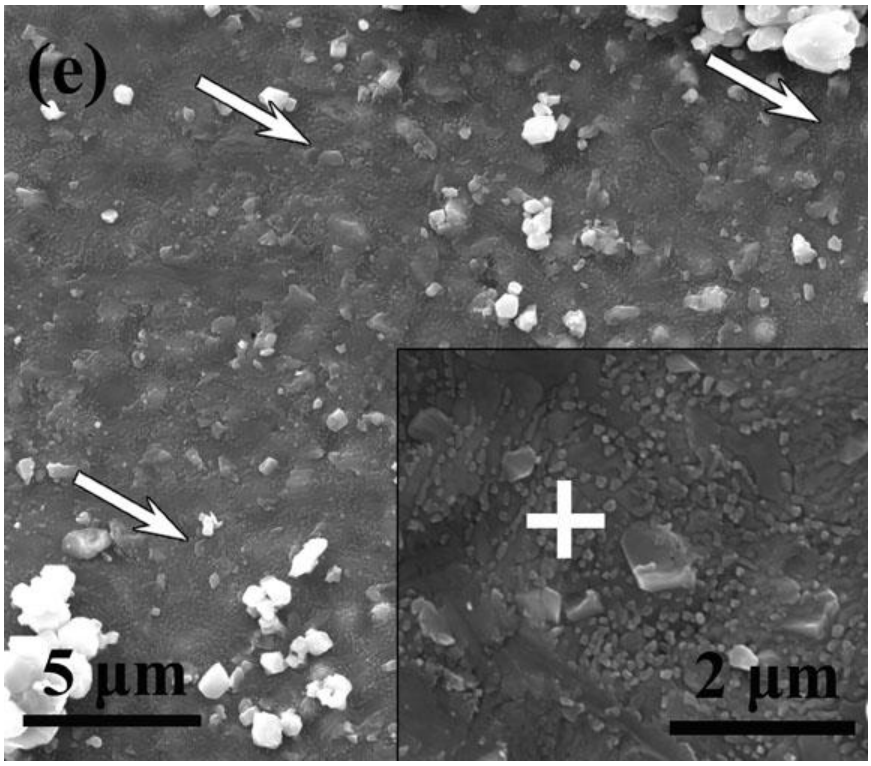

Fig. 3-3. SEM images of the YSZ/LSM interface after the LSM porous layer removal: (a) YSZ surface, (b) as-sintered, (c) thermally treated in dry air, (d) thermally treated in 10 vol% moist air, and (e) thermally treated in 25 vol% moist air.

EDS spot analysis is used to determine the composition of the YSZ surface after the LSM layer removal (Fig. 3-4). The examination locations are marked as "+" in Fig. 3-3. The results show that the main elements are Zr and Y (the peaks are very strong and not shown in Fig. 3-4). This is expected because of the presence of the YSZ substrate. The minor elements are La and Mn (approximately less than 1 atom%), which means the analyzed spots contain small amounts of La and Mn. Cr deposition on the surface is of a very small amount and the main EDS peak $Cr_{K\alpha}$ overlaps with $La_{L\beta2}$, one of the minor peak of La; and $Mn_{K\alpha}$, the main peak of Mn, overlaps with a minor Cr peak $Cr_{K\beta}$ (Chapter 2). Since La shows relatively strong peaks, for comparison purposes, the $La_{L\alpha}$ peak is used as a reference to compare other elements. Fig. 3-4 is rescaled to obtain approximately the same intensity for the $La_{L\alpha}$ peaks. The as-sintered sample shows a very small $Mn_{K\alpha}/Cr_{K\beta}$ peak. After the thermal treatment, the peak height increases for all the samples. However, the $Mn_{K\alpha}/Cr_{K\beta}$ peak increases the most for the sample thermally treated in dry air and the least for the samples thermally treated in the 25 vol% moist air. Compared with the main

$La_{L\alpha}$ peak, the $Cr_{K\alpha}/La_{L\beta2}$ peak shows no significant difference between the as-sintered state (no Cr deposition) and the thermally treated samples (with Cr deposition), which means the $Cr_{K\alpha}$ peak is very weak. From this, it can be deduced that the contribution of the $Cr_{K\beta}$ peak is very weak and the $Mn_{K\alpha}/Cr_{K\beta}$ peak intensity represents the Mn content. This result means using La as a reference, Mn deposits relatively less in the high moisture atmosphere.

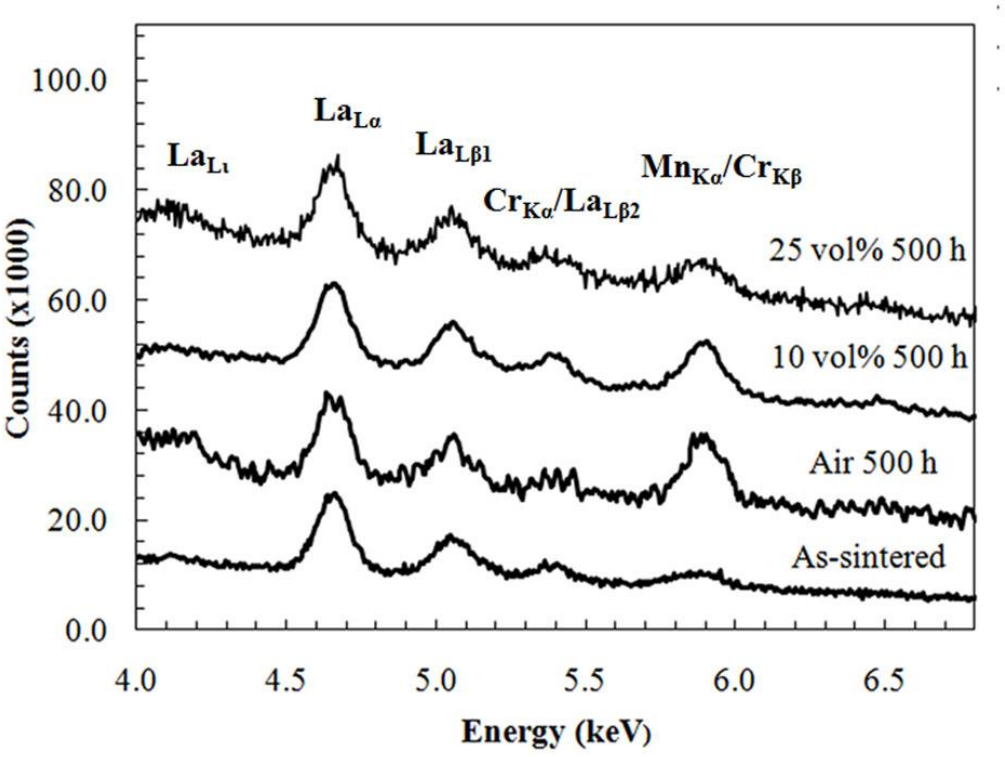

Fig. 3-4. EDS spot analysis of YSZ/LSM interface after the LSM porous layer removal. The analyzed spots are on the YSZ surface. The corresponding locations are shown in Figs. 3-3(b), (c), (d), and (e), marked by crosses.

3.3.2. Deposition and Distribution of Different Species

After the thermal treatment at 800°C for 500 h in different atmospheres, the AISI 441 interconnects were removed and XPS analysis was carried out at different locations across the LSM layer. Along the porous LSM air electrode layer (~30 μm thick), five different locations are obtained for the XPS analysis (Fig. 3-5). The thickness of each layer is controlled by a micrometer at ~8 μm. The results are normalized to 100% by considering La, Sr, Mn, and Cr

only in order to avoid errors by oxygen from the mounting epoxy. The elemental concentrations are averaged by three measurements at each location.

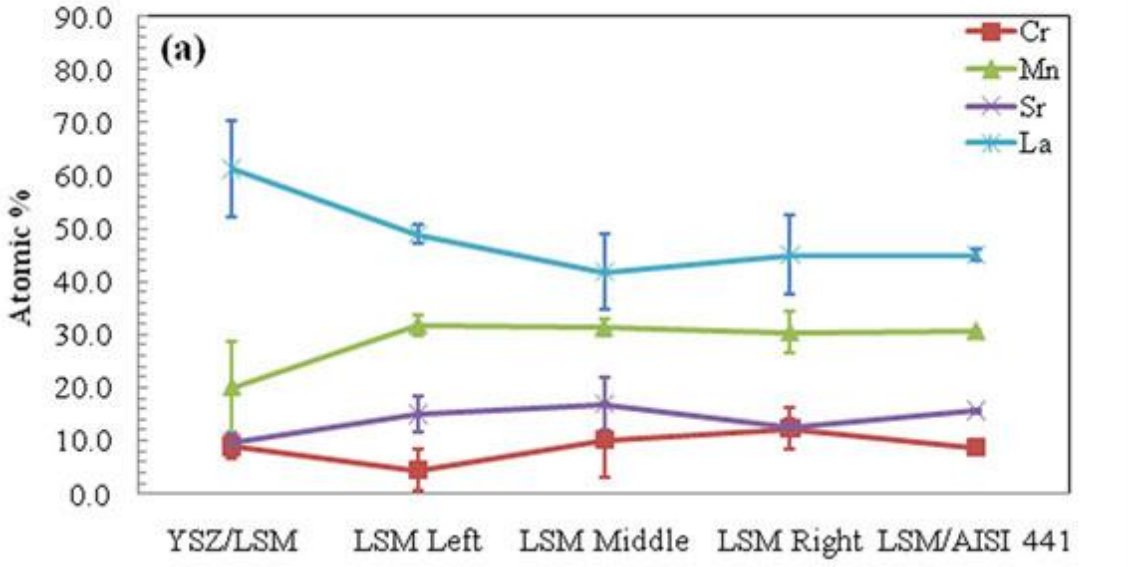

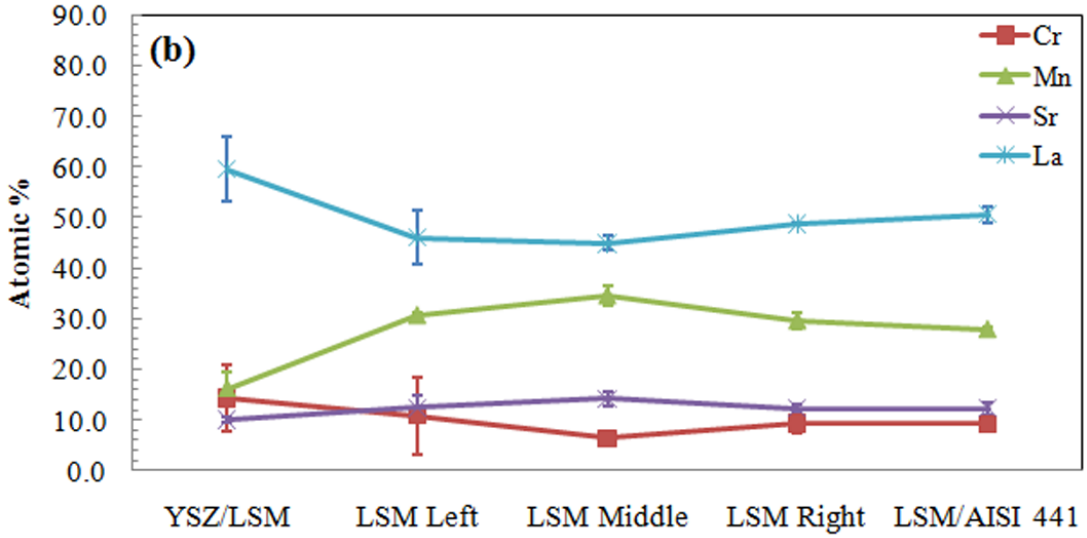

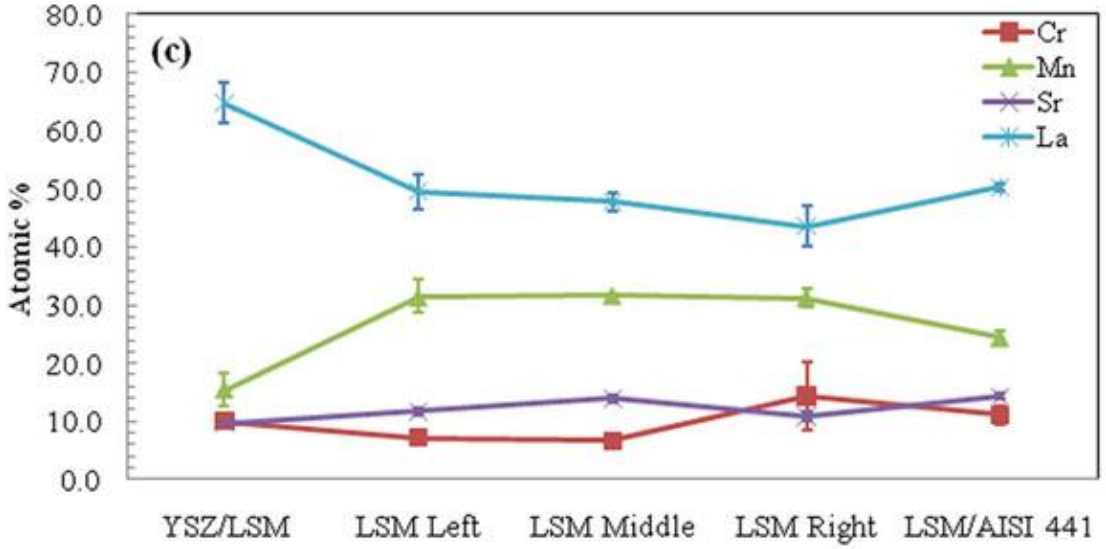
(c)
Cr
Mn
Sr
La
Atomic %
80.0
70.0
60.0
50.0
40.0
30.0
20.0
10.0
0.0
YSZ/LSM
LSM Left
LSM Middle
LSM Right
LSM/AISI 441

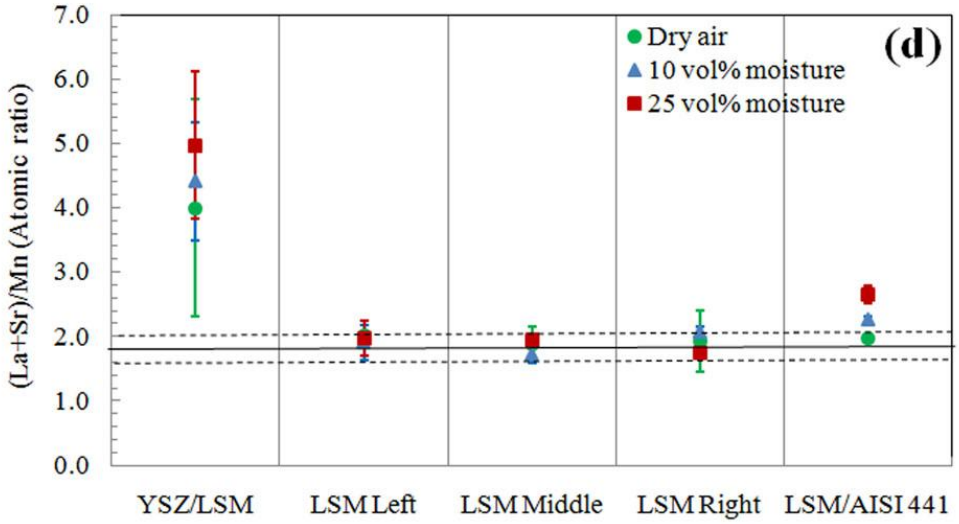
(d)
Dry air
10 vol% moisture
25 vol% moisture
(La+Sr)/Mn (Atomic ratio)
7.0
6.0
5.0
4.0
3.0
2.0
1.0
0.0
YSZ/LSM
LSM Left
LSM Middle
LSM Right
LSM/AISI 441

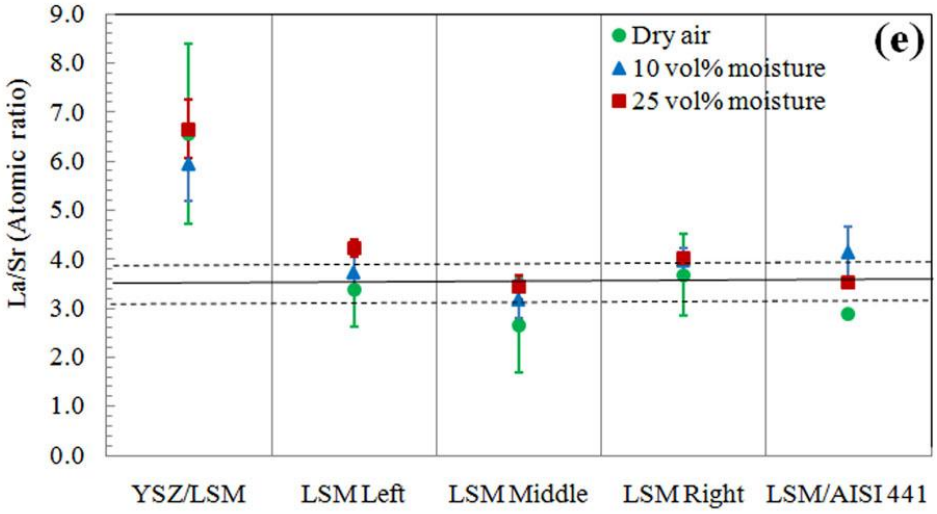

Fig. 3-5. Composition of the LSM layer before and after the thermal treatment at 800°C for 500 h in different atmospheres: (a) dry air, (b) 10 vol% moist air, and (c) 25 vol% moist air. All the concentrations are normalized to 100% by considering La, Sr, Mn, and Cr only. Atomic ratios: (d) (La+Sr)/Mn ratio, (e) La/Sr ratio. The solid and dash lines mark the values and standard deviations of the ratios before the thermal treatment.

The surface compositions of the LSM "top" layer after sintering at 1100°C for 2 h (shown in Fig. 3-2(a), "As-sintered") show significant enrichments of La and Sr (not shown in Figs. 3-5(a)–3-5(c)). The content of La, Sr, and Mn is 49.6%, 14.3%, and 36.1%, which is very different from the designed 40% La, 10% Sr, and 50% Mn (It should be mentioned that all the elemental analysis data in this paper are presented in atomic percent). La and Sr increase by 24% and 42%, respectively, and Mn decreases by 28%. This means that the surface composition has changed after sintering, where Sr enriches the most, La enriches less than Sr, and Mn content depletes accordingly at the LSM surface. Such Sr and La surface segregation and the Mn depletion have been observed before and are believed to result from the strain energy driven re-distribution of the ions.

After the thermal treatment in dry air, at the LSM/AISI 441 interface, the content of La, Sr, Mn, and Cr is 45.0 ± 1.0%, 15.6 ± 0.3%, 30.7 ± 0.3%, and 8.7 ± 1.3%, respectively. The surface composition is very close to that of the as-sintered state if Cr is excluded. In the 10 vol% moist air, the content of La, Sr, Mn, and Cr is 50.6 ± 1.5%, 12.3 ± 1.2%, 27.9 ± 0.5%, and 9.2 ±

0.2%, respectively. In the 25 vol% moist air, the content is 50.3 ± 0.7%, 14.3 ± 0.5%, 24.4 ± 1.1%, and 11.1 ± 1.5%, respectively. This indicates that the thermal treatment leads to Cr deposition. As the moisture content increases, La enrichment increases, Sr enrichment decreases, and Mn depletion worsens. For the samples treated in the 10 vol% and 25 vol% moist air, La surface enrichment is ~10% higher than that for the dry air treated sample. At the same time, Cr deposition increases monotonically with the water content, from 8.7% to 9.2% to 11.1%, which is a considerable amount and reflects the Cr deposition on the air electrode.

Across the LSM porous layer, the contents of La, Sr, and Mn show different changes from right to left of the tri-layer assembly. For the LSM sample thermally treated in dry air, the La, Sr, and Mn content is almost the same as that at the LSM/AISI 441 interface. For the sample thermally treated in 10 vol% moist air, the composition is also fairly consistent with some random variations such as the higher Mn content in the LSM Middle location. For the sample thermally treated in 25 vol% moist air, the content of La and Sr decreases by about 10% and 20%, respectively, and Mn increases by about 20% at the LSM Right location compared with those at the LSM/AISI 441 interface. These results indicate that higher water vapor content in the atmosphere causes more La and Sr composition segregation at the LSM/AISI 441 interface, but the segregation is limited to the interface.

At the YSZ/LSM interface, a much higher La content is detected at 61.3 ± 9.0% in dry air, 59.5 ± 6.3% in 10 vol% moist air, and 64.8 ± 3.5% in 25 vol% moist air. On the other hand, the Mn content is lower than those across the LSM layer and at the LSM/AISI 441 interface, are 20.1 ± 8.4% in dry air, 16.2 ± 3.2% in 10 vol% moist air, and 15.4 ± 2.7% in 25 vol% moist air. Sr content also decreases compared with that across the LSM layer at 9.6 ± 1.8% in dry air, 10.0 ± 0.6% in 10 vol% moist air, and 9.8 ± 0.5% in 25 vol% moist air, even though the content is close to that for the samples thermally treated in dry and moisture atmospheres. This means that La is more favorable to interacting with the YSZ electrolyte and likely forms La-containing compounds at the interface. Sr and Mn segregate inwards to the LSM layer. Water vapor in the atmosphere increases the La enrichment and Mn depletion, while having negligible effect on the Sr composition at the YSZ/LSM interface.

After the thermal treatment, Cr is detected in all the locations of the tri-layers for all three conditions. At LSM Right (close to the AISI 441), the Cr contents are 12.2 ± 3.9% in dry air, 9.4 ± 2.1% in 10 vol% moist air, and 14.4 ± 5.9% in 25 vol% moist air, which are similar to the Cr

contents at the LSM/AISI 441 interface and show no clear impact from moisture. The lowest Cr contents of the samples are 4.4 ± 3.9% shown in LSM Right in dry air, 6.4 ± 1.0% shown in LSM Middle in 10 vol% moist air, and 6.6 ± 1.2% shown in LSM Middle in 25 vol% moist air, respectively. This means that the high moisture leads to higher Cr deposition at the "deeper" locations close to the YSZ, which is probably because of the different concentration of the volatile Cr species. According to the work of Opila et al. [29], compared with dry air, the Cr evaporation rate could be ten times higher in moist air with less than 5 vol% water vapor. This is because the gas phase $CrO_2(OH)_2$ has lower formation energy than CrO_3 (in equation 3-3 and 3-4). In the present work, at the YSZ/LSM interface, the Cr content increases to 9.0 ± 2.5% in dry air, 14.4 ± 8.6% in 10 vol% moist air, and 10.0 ± 1.7% in 25 vol% moist air. Thus, here as well, high moisture content aggravates Cr deposition at the YSZ/LSM interface. For all the thermal treatment conditions, the Cr content first decreases from right to left along the cross section of the LSM layer and then increases, which shows the preferential deposition of Cr at the YSZ/LSM interface, i.e., at the TPBs. For the samples thermally treated in 10 vol% and 25 vol% moist air, the Cr content increases at the LSM Left location compared with that of the LSM Middle location. Cr accumulates at the YSZ/LSM interface and shows even higher concentration, as much as over 50% compared with the lower values at LSM Middle or LSM Left. The higher Cr content at the LSM Left location for the moist air conditions is a propagation of the high Cr content at the YSZ/LSM interface. This means high water vapor not only accelerates Cr accumulation at the YSZ/LSM interface but also causes a larger extent of Cr deposition in the adjacent region.

That the surface composition changes for the thermally treated samples at different conditions can be more clearly seen from the atomic ratios of the elements involved (Figs. 3-5(d) and (e)). The solid and dashed lines mark the values and standard deviations of the (La+Sr)/Mn and La/Sr ratios of the LSM layer before the thermal treatment. At this condition, the (La+Sr)/Mn ratio is 1.8±0.2, which is much higher than the designed ratio of 1.0 and shows the surface enrichment of La and Sr and the depletion of Mn; and the La/Sr ratio is 3.5±0.4, which is less than the designed ratio of 4.0 and indicates that the Sr surface enrichment is more significant. After the thermal treatment in different atmospheres, these two ratios do not show significant changes across the LSM porous layer (LSM Left, LSM Middle, and LSM Right in Figs. 3-5(d)

and (e)). These results mean that the composition of the LSM layer does not change significantly during the thermal treatment in the different atmospheres.

At the LSM/AISI 441 interface, the (La+Sr)/Mn ratios are all higher than that of the as-sintered state, and the moist air treated samples show higher values than the dry air treated sample. This means that water vapor leads to more La and Sr enrichments on the LSM "top" surface. The chemical composition at the YSZ/LSM interface shows more remarkable enrichment of La (Fig. 3-5(e)), which is consistent with the microstructure (Fig. 3-3) and the EDS results (Fig. 3-4). At the YSZ surface, the (La+Sr)/Mn ratios are 4.0 ± 1.7% in dry air, 4.4 ± 0.9% in 10 vol% moist air, and 5.0 ± 1.1% in 25 vol% moist air; the La/Sr ratios are 6.5 ± 1.8% in dry air, 5.9 ± 0.7% in 10 vol% moist air, and 6.7 ± 0.6% in 25 vol% moist air. La accumulates and forms new species such as $La_2Zr_2O_7$ with YSZ (Figs. 3-3 and 3-4) [18,36].

3.3.3. LSM/AISI 441 Interfacial Phase Evolution

XRD is used to analyze the phases of the LSM porous layer in contact with the AISI 441 interconnect (the LSM "top" surface as shown in Fig. 3-2(a)) after the interconnect is removed (Fig. 3-6). Before the thermal treatment, the LSM air electrode shows a pure perovskite phase. After the thermal treatment at 800°C for 500 h in dry and moist air, some minor new phases are indentified. They are $Mn_{1.5}Cr_{1.5}O_4$ and $SrMn_3O_{6-x}$. The main LSM phase maintains and all the other phases show very weak peak intensities, which mean the new compounds formed during the thermal treatment are in small amounts. It should be noted that the YSZ phase shown in some of the XRD patterns is from the electrolyte, which is not considered in the phase analysis of the LSM layer.

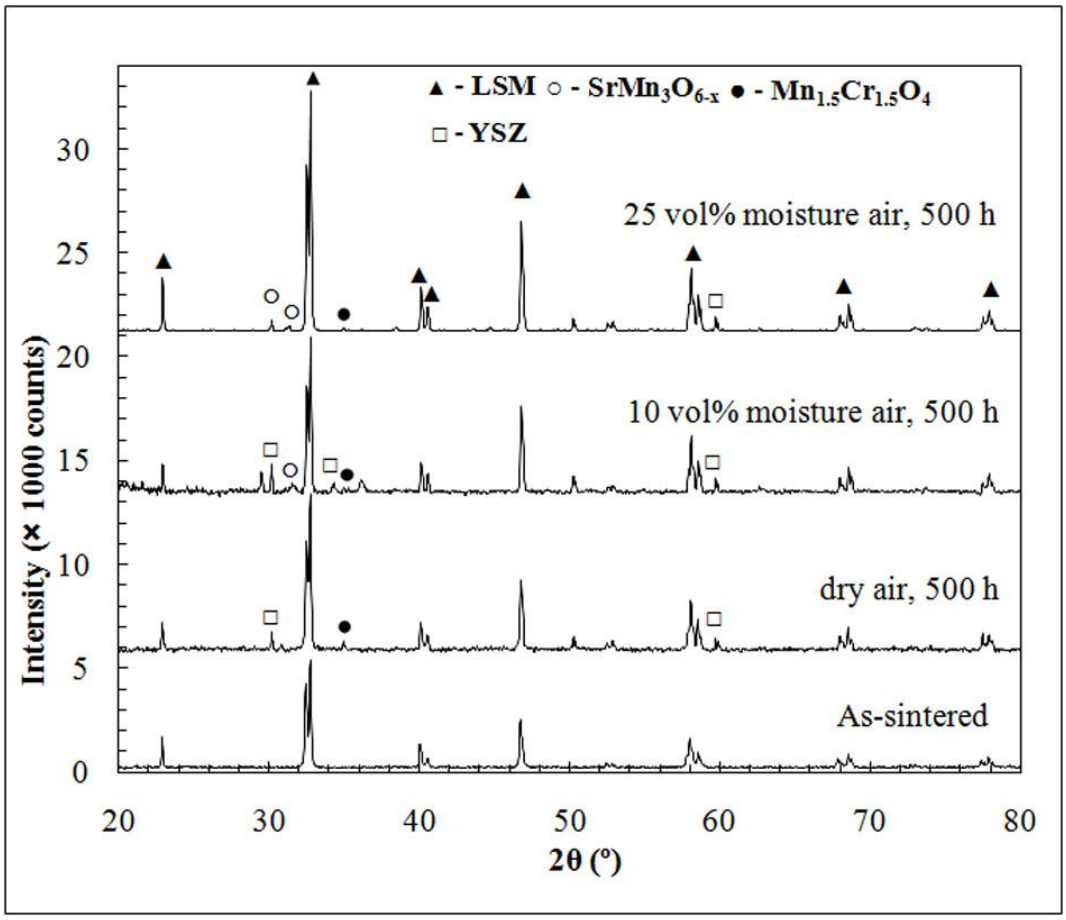

Fig. 3-6. XRD patterns of the LSM surface in contact with the AISI 441 interconnect before and after the thermal treatment at 800°C in different atmospheres for 500 h.

For the LSM sample thermally treated in dry air, only $Mn_{1.5}Cr_{1.5}O_4$ is indentified. For the samples thermally treated in moist air (10 vol% and 25 vol% moisture), both $Mn_{1.5}Cr_{1.5}O_4$ and $SrMn_3O_{6-x}$ are detected. $Mn_{1.5}Cr_{1.5}O_4$ formation is due to the surface deposition of the volatile Cr species and the interaction on the LSM surface. For the samples thermally treated in 10 vol% and 25 vol% moist air, the formation of $SrMn_3O_{6-x}$ should be caused by the Sr surface segregation, as indicated by the XPS results in Fig. 3-5. This result means that the Sr surface segregation is more significant in the wet air atmosphere. However, the amount of $SrMn_3O_{6-x}$ is too small to be compared between the 10 vol% and 25 vol% moisture conditions.

3.4. Discussion

3.4.1. LSM Grain Growth and Sintering

From the SEM images, the microstructure of the porous LSM air electrode changes during the thermal treatment. For the as-sintered samples, the LSM particles bond with each other, forming a homogeneous network structure. During the thermal treatment at 800°C, the grain growth and bonding continue. The LSM grains grow and bond more extensively for the sample treated in dry air, while the extent is less for the samples treated in moist air, even though the sample treated in 25 vol% moist air exhibits more sintering than the 10 vol% moist air sample. Overall, the samples thermally treated in 10 vol% and 25 vol% moist air show significantly less sintering than that in dry air with a slight difference of grain size. This means that the LSM sintering is likely to be suppressed by the water vapor in the atmosphere. Also, the atmosphere has no significant influence on the surface composition of the LSM grains. The increase in the contact between the LSM grains in the porous layer after the thermal treatment should be beneficial for reducing the ohmic resistance [15]. However, the activation polarization increase is generally much larger than the ohmic resistance from the materials and the microstructure effects have not been well established [13,37,38]. There is more work needed to correlate the microstructure to the cell performance. On the other hand, at the LSM/AISI 441 interface, the microstructure of the LSM is the same as that across the LSM porous layer. This means that the thermal treatment temperature of 800°C is not high enough to lead to extensive morphological changes between the LSM and the AISI 441.

3.4.2. Interfacial Behaviors of the Cell Components

The LSM air electrode porous layer is in direct contact with two other cell components: the YSZ electrolyte and the AISI 441 interconnect, during the thermal treatment. For the YSZ/LSM interface, bonding forms during the sintering at 1100°C. The bonding spot size enlarges after being treated in dry air but stays about the same after being treated in moisture atmospheres, which is consistent with the grain growth (Figs. 3-2 and 3-3). This result can be explained as the influence of the atmosphere on the diffusion during the thermal treatment. A dry atmosphere likely facilitates the diffusion and bonding between the LSM grains while the

moisture atmosphere induces the formation of substantially higher amounts of the volatile Cr species, which suppress the diffusion of other elements such as La and Mn. Mn deposition at the YSZ surface is much less than that of La, and is further inhibited in the moisture atmospheres. Cr shows significant enrichment at the YSZ/LSM interface in different atmospheres. More detailed elemental analysis should help to understand the YSZ/LSM interface interaction process.

Small particles appear on the YSZ surface after being thermally treated in moist air and the size and number of the particles are larger for the higher moisture condition (Fig. 3-3). Both EDS spot analysis and XPS surface analysis show that La compounds form on the YSZ surface at the as-sintered state and after the thermal treatment. Similar microstructure change has been observed in the work of Nielsen et al. [30] and Hagen et al.'s work [39]. Nielsen et al. [30] observed small particles on the YSZ surface when the cell was treated in moisture atmosphere; while the YSZ surface was clean when thermally treated in dry air. Hagen et al. [39] proposed that the microstructure change is attributed to the enhanced diffusion of Mn and the impurity elements such as Si, Ca, and S. In our elemental analysis, no impurity elements are detected and La is considered the major component causing the particle-like feature on the YSZ surface. The EDS spot analysis has better lateral resolution of a few μm^2; the XPS, on the other hand, shows the average composition in tens of nanometers of depth on the surface. For both the EDS and XPS analyses on the YSZ surface, Zr and Y are still the dominant elements and La is less than 1% for the EDS and less than 10% for the XPS, respectively (the La atomic percent at the YSZ/LSM interface in Fig. 3-5 is the value after excluding Zr and Y). Additionally, the quantitative result of the surface concentration of La does not show a significant difference caused by the atmosphere. La is concentrated at the YSZ surface. Combining the EDS and XPS results, the particles are likely La-containing species such as $La_2Zr_2O_7$ [18,40].

At the LSM surface, the deposition of Cr is considerable for all the three samples, but there are no visible Cr-containing particles. It is believed that the Cr-containing phases form a thin layer at the LSM surface. The surface chemistry is critical to the electrochemical reaction in the air electrode; however, the surface reaction mechanism has not been well-established [41,42]. Detailed investigation of the air electrode surface reactions involving Cr deposition will be needed to improve our understanding. On the other hand, it is believed that the TPBs are the major area to determine the performance of the porous LSM air electrode; and Cr deposition can block the TPB area, causing cell performance degradation [43]. In our work, the different

atmospheres cause variable YSZ/LSM interfacial bonding; the stronger bonding in dry air should be beneficial for increasing the active sites (TPB length) and reducing the ohmic resistance of the interface. However, there is no evidence that the Cr deposition at the YSZ/LSM interface is related to the TPB area.

3.4.3. Elemental Diffusion and Distribution

The distribution of La, Sr, and Mn across the LSM layer is fairly uniform except for at the YSZ/LSM interface. For the Cr, the amount decreases from the right side, where the Cr source from the AISI 441 interconnect is located, to the left side, which is further away from the AISI 441 interconnect. The surface deposition of Cr is considerable. However, it does not cause a significant difference in LSM surface composition across the LSM porous layer. There is no visible morphological change at the LSM grain surface for all the thermal treatment conditions (Figs. 3-2 and 3-3). $Mn_{1.5}Cr_{1.5}O_4$ and $SrMn_3O_{6-x}$ phases are detected by XRD. Cr also deposits on the YSZ surface. $(Cr,Mn)_3O_4$ spinel is generally believed to be the phase [44,45]. Current density can significantly accelerate this process [46] and will be reported in future work. In the present work, no visible Cr-containing particles are found and the Cr deposition amount is small. This could be due to the following: (i) without polarization the driving force for Cr deposition at TPBs is not strong enough; (ii) the AISI 441 is designed to form a Mn-Cr spinel protection layer on its own surface to inhibit the release of the volatile Cr species.

At 800°C, the volatile Cr species are affected by the water vapor in air. In moist air, the amount of the volatile $CrO_2(OH)_2$ phase is higher than that of the CrO_3 [29]. In this study, the Cr content is slightly higher for the moist air conditions after the thermal treatment. This reflects the moisture effect. However, the deposition process without current is slow in both dry and moisture atmospheres, and the deposition amount is small.

3.5. Conclusions

The YSZ/LSM/AISI 441 tri-layer is thermally treated at 800°C for 500 h to investigate the interaction between different SOC components in dry air, 10 vol% moist air, and 25 vol% moist air. The LSM microstructure shows more grain growth and bonding in dry air than in the moisture atmospheres. The bonding between the YSZ and the LSM is more extensive as the

moisture content increases. At the YSZ/LSM interface, moisture leads to La-containing particle formation on the YSZ surface. Higher moisture leads to more extensive particle formation and Mn depletion at the YSZ surface. Cr deposition is detected across the porous LSM layer where the deposition amount decreases from the AISI 441 side to the YSZ side and shows accumulation at the YSZ/LSM interface. The Cr deposition amount is slightly higher for the samples thermally treated in the moisture atmosphere. A small amount of $Cr_{1.5}Mn_{1.5}O_4$ is detected on the LSM surface for all the samples, and $SrMn_3O_{6-x}$ is identified for the samples thermally treated in the moisture atmospheres.

References

1. Minh, N.Q., Ceramic fuel cells. Journal of the American Ceramic Society, 1993. 76(3): p. 563-588.
2. Brandon, N.P., Skinner, S., and Steele, B.C.H., Recent advances in materials for fuel cells. Annual Review of Materials Research, 2003. 33: p. 183-213.
3. Ni, M., Leung, M.K.H., and Leung, D.Y.C., Technological development of hydrogen production by solid oxide electrolyzer cell (SOEC). International Journal of Hydrogen Energy, 2008. 33(9): p. 2337-2354.
4. Jensen, S.H., Larsen, P.H., and Mogensen, M., Hydrogen and synthetic fuel production from renewable energy sources. International Journal of Hydrogen Energy, 2007. 32(15): p. 3253-3257.
5. Hauch, A., Ebbesen, S.D., Jensen, S.H., and Mogensen, M., Highly efficient high temperature electrolysis. Journal of Materials Chemistry, 2008. 18(20): p. 2331-2340.
6. Fergus, J.W., Metallic interconnects for solid oxide fuel cells. Materials Science and Engineering a-Structural Materials Properties Microstructure and Processing, 2005. 397(1-2): p. 271-283.
7. Yang, Z.G., Recent advances in metallic interconnects for solid oxide fuel cells. International Materials Reviews, 2008. 53(1): p. 39-54.
8. Wu, J.W. and Liu, X.B., Recent development of SOFC metallic interconnect. Journal of Materials Science & Technology, 2010. 26(4): p. 293-305.

9. Simner, S.P., Bonnett, J.F., Canfield, N.L., Meinhardt, K.D., Shelton, J.P., Sprenkle, V.L., and Stevenson, J.W., Development of lanthanum ferrite SOFC cathodes. Journal of Power Sources, 2003. 113(1): p. 1-10.
10. Jiang, S.P., Development of lanthanum strontium manganite perovskite cathode materials of solid oxide fuel cells: a review. Journal of Materials Science, 2008. 43(21): p. 6799-6833.
11. Haanappel, V.A.C., Mertens, J., Rutenbeck, D., Tropartz, C., Herzhof, W., Sebold, D., and Tietz, F., Optimisation of processing and microstructural parameters of LSM cathodes to improve the electrochemical performance of anode-supported SOFCs. Journal of Power Sources, 2005. 141(2): p. 216-226.
12. Adler, S.B., Factors governing oxygen reduction in solid oxide fuel cell cathodes. Chemical Reviews, 2004. 104(10): p. 4791-4843.
13. Fleig, J., Solid oxide fuel cell cathodes: Polarization mechanisms and modeling of the electrochemical performance. Annual Review of Materials Research, 2003. 33: p. 361-382.
14. Laguna-Bercero, M.A., Kilner, J.A., and Skinner, S.J., Performance and Characterization of (La, Sr)MnO_3/YSZ and $La_{0.6}Sr_{0.4}Co_{0.2}Fe_{0.8}O_3$ Electrodes for Solid Oxide Electrolysis Cells. Chemistry of Materials, 2010. 22(3): p. 1134-1141.
15. Sasaki, K., Wurth, J.P., Gschwend, R., Godickemeier, M., and Gauckler, L.J., Microstructure-property relations of solid oxide fuel cell cathodes and current collectors - Cathodic polarization and ohmic resistance. Journal of the Electrochemical Society, 1996. 143(2): p. 530-543.
16. Jorgensen, M.J., Primdahl, S., Bagger, C., and Mogensen, M., Effect of sintering temperature on microstructure and performance of LSM-YSZ composite cathodes. Solid State Ionics, 2001. 139(1-2): p. 1-11.
17. Jiang, S.P. and Wang, W., Sintering and grain growth of (La,Sr)MnO_3 electrodes of solid oxide fuel cells under polarization. Solid State Ionics, 2005. 176(13-14): p. 1185-1191.
18. Mitterdorfer, A. and Gauckler, L.J., $La_2Zr_2O_7$ formation and oxygen reduction kinetics of the $La_{0.85}Sr_{0.15}Mn_yO_3$, O_2(g)vertical bar YSZ system. Solid State Ionics, 1998. 111(3-4): p. 185-218.

19. Tsipis, E.V. and Kharton, V.V., Electrode materials and reaction mechanisms in solid oxide fuel cells: a brief review. Journal of Solid State Electrochemistry, 2008. 12(11): p. 1367-1391.
20. Levy, C., Zhong, Y., Morel, C., and Marlin, S., Thermodynamic stabilities of $La_2Zr_2O_7$ and $SrZrO_3$ in SOFC and their relationship with LSM synthesis processes. Journal of the Electrochemical Society, 2010. 157(11): p. B1597-B1601.
21. Taniguchi, S., Kadowaki, M., Kawamura, H., Yasuo, T., Akiyama, Y., Miyake, Y., and Saitoh, T., Degradation phenomena in the cathode of a solid oxide fuel cell with an alloy separator. Journal of Power Sources, 1995. 55(1): p. 73-79.
22. Badwal, S.P.S., Deller, R., Foger, K., Ramprakash, Y., and Zhang, J.P., Interaction between chromia forming alloy interconnects and air electrode of solid oxide fuel cells. Solid State Ionics, 1997. 99(3-4): p. 297-310.
23. Matsuzaki, Y. and Yasuda, I., Electrochemical properties of a SOFC cathode in contact with a chromium-containing alloy separator. Solid State Ionics, 2000. 132(3-4): p. 271-278.
24. Jiang, S.P. and Love, J.G., Origin of the initial polarization behavior of Sr-doped $LaMnO_3$ for O_2 reduction in solid oxide fuel cells. Solid State Ionics, 2001. 138(3-4): p. 183-190.
25. Simner, S.P., Anderson, M.D., Xia, G.G., Yang, Z., Pederson, L.R., and Stevenson, J.W., SOFC performance with Fe-Cr-Mn alloy interconnect. Journal of the Electrochemical Society, 2005. 152(4): p. A740-A745.
26. de Haart, L.G.J., Mougin, J., Posdziech, O., Kiviaho, J., and Menzler, N.H., Stack Degradation in Dependence of Operation Parameters; the Real-SOFC Sensitivity Analysis. Fuel Cells, 2009. 9(6): p. 794-804.
27. Horita, T., Xiong, Y.P., Kishimoto, H., Yamaji, K., Brito, M.E., and Yokokawa, H., Chromium poisoning and degradation at $(La,Sr)MnO_3$ and $(La,Sr)FeO_3$ cathodes for solid oxide fuel cells. Journal of the Electrochemical Society, 2010. 157(5): p. B614-B620.
28. Hilpert, K., Das, D., Miller, M., Peck, D.H., and Weiss, R., Chromium vapor species over solid oxide fuel cell interconnect materials and their potential for degradation processes. Journal of the Electrochemical Society, 1996. 143(11): p. 3642-3647.

29. Opila, E.J., Myers, D.L., Jacobson, N.S., Nielsen, I.M.B., Johnson, D.F., Olminsky, J.K., and Allendorf, M.D., Theoretical and experimental investigation of the thermochemistry of $CrO_2(OH)_2$(g). Journal of Physical Chemistry A, 2007. 111(10): p. 1971-1980.
30. Nielsen, J., Hagen, A., and Liu, Y.L., Effect of cathode gas humidification on performance and durability of Solid Oxide Fuel Cells. Solid State Ionics, 2010. 181(11-12): p. 517-524.
31. Kim, S.H., Shim, K.B., Kim, C.S., Chou, J.T., Oshima, T., Shiratori, Y., Ito, K., and Sasaki, K., Degradation of solid oxide fuel cell cathodes accelerated at a figh water vapor concentration. Journal of Fuel Cell Science and Technology, 2010. 7(2): p. 021011.
32. Srisrual, A., Coindeau, S., Galerie, A., Petit, J.P., and Wouters, Y., Identification by photoelectrochemistry of oxide phases grown during the initial stages of thermal oxidation of AISI 441 ferritic stainless steel in air or in water vapour. Corrosion Science, 2009. 51(3): p. 562-568.
33. Mahapatra, M.K. and Lu, K., Effect of atmosphere on interconnect-seal glass interaction for solid oxide fuel/electrolyzer cells. Journal of the American Ceramic Society, 2011. 94(3): p. 875-885.
34. Hammouche, A., Schouler, E.J.L., and Henault, M., Electrical and thermal properties of Sr-doped lanthanum manganites. Solid State Ionics, 1988. 28-30(Part 2): p. 1205-1207.
35. Jin, T. and Lu, K., Chemical compatibility between Sr-doped lanthanum manganite air electrode and AISI 441 interconnect. International Journal of Hydrogen Energy, 2011. 36(7): p. 4440-4448.
36. Brugnoni, C., Ducati, U., and Scagliotti, M., SOFC cathode/electrolyte interface .1. Reactivity between $La_{0.85}Sr_{0.15}MnO_3$ and ZrO_2-Y_2O_3. Solid State Ionics, 1995. 76(3-4): p. 177-182.
37. Jiang, S.P. and Love, J.G., Observation of structural change induced by cathodic polarization on (La,Sr)MnO_3 electrodes of solid oxide fuel cells. Solid State Ionics, 2003. 158(1-2): p. 45-53.
38. Shearing, P.R., Brett, D.J.L., and Brandon, N.P., Towards intelligent engineering of SOFC electrodes: a review of advanced microstructural characterisation techniques. International Materials Reviews, 2010. 55(6): p. 347-363.

39. Hagen, A., Neufeld, K., and Liu, Y.L., Effect of humidity in air on performance and long-term durability of SOFCs. Journal of the Electrochemical Society, 2010. 157(10): p. B1343-B1348.
40. Chen, M., Liu, Y.L., Hagen, A., Hendriksen, P.V., and Poulsen, F.W., LSM-YSZ Reactions in Different Atmospheres. Fuel Cells, 2009. 9(6): p. 833-840.
41. Horita, T., Yamaji, K., Ishikawa, M., Sakai, N., Yokokawa, H., Kawada, T., and Kato, T., Active sites imaging for oxygen reduction at the $La_{0.9}Sr_{0.1}MnO_{3-x}$/yttria-stabilized zirconia interface by secondary-ion mass spectrometry. Journal of the Electrochemical Society, 1998. 145(9): p. 3196-3202.
42. la O, G.J., Savinell, R.F., and Shao-Horn, Y., Activity enhancement of dense strontium-doped lanthanum manganite thin films under cathodic polarization: A combined AES and XPS study. Journal of the Electrochemical Society, 2009. 156(6): p. B771-B781.
43. Konysheva, E., Penkalla, H., Wessel, E., Mertens, J., Seeling, U., Singheiser, L., and Hilpert, K., Chromium poisoning of perovskite cathodes by the ODS alloy Cr5Fe1Y_2O_3 and the high chromium ferritic steel Crofer22APU. Journal of the Electrochemical Society, 2006. 153(4): p. A765-A773.
44. Jiang, S.P., Zhang, S., and Zhen, Y.D., Early interaction between Fe-Cr alloy metallic interconnect and Sr-doped $LaMnO_3$ cathodes of solid oxide fuel cells. Journal of Materials Research, 2005. 20(3): p. 747-758.
45. Wang, S., Cruse, T.A., Krumpelt, M., Ingram, B.J., and Salvador, P.A., Microstructural Degradation of (La,Sr)MnO[sub 3]/YSZ Cathodes in Solid Oxide Fuel Cells with Uncoated E-Brite Interconnects. Journal of the Electrochemical Society, 2011. 158(2): p. B152-B158.
46. Krumpelt, M., Cruse, T.A., Ingram, B.J., Routbort, J.L., Wang, S.L., Salvador, P.A., and Chen, G., The Effect of Chromium Oxyhydroxide on Solid Oxide Fuel Cells. Journal of the Electrochemical Society, 2010. 157(2): p. B228-B233.

Chapter 4

Surface and Interface Behaviors of $(La_{0.8}Sr_{0.2})_xMnO_3$ Air Electrode for Solid Oxide Cells

Abstract

In solid oxide cell operation, the stoichiometry of the air electrode is an important factor for its interaction with electrolyte and interconnect and long-term cell performance. In this study, tri-layer samples of yttria-stabilized zirconia (YSZ)/$(La_{0.8}Sr_{0.2})_xMnO_3$ (LSM)/AISI 441 stainless steel are made and thermally treated in dry air atmosphere at 800°C for 500 h. The air electrode composition is varied by changing the x value in $(La_{0.8}Sr_{0.2})_xMnO_3$ from 0.95 to 1.05 (LSM95, LSM100, and LSM105). The LSM composition segregation, YSZ/LSM/AISI 441 interfacial interaction, and the reaction of volatile chromium species with the LSM surface are characterized by scanning electron microscopy (SEM), X-ray photoelectron spectroscopy (XPS), and X-ray diffraction (XRD). Surface segregation of Sr and La is detected for all the LSM samples. Cr deposition is found across the LSM surface under the same thermal treatment condition. For the LSM95 sample, Sr-containing compound leads to a high Cr content at the YSZ/LSM interface. On the other hand, for the LSM105 sample, the enrichment of La at the YSZ/LSM interface inhibits the Cr deposition, leading to a very low Cr content. The mechanisms of Cr poisoning and LSM elemental surface segregation are discussed.

4.1. Introduction

Solid oxide cells (SOCs), including solid oxide fuel cells (SOFCs) and solid oxide electrolyzer cells (SOECs), are promising electrochemical devices in high efficiency electricity generation and novel hydrogen production technologies [1-5]. In order to obtain desired power output or hydrogen production, single cells are connected together by the interconnect. In recent years, lowering the operating temperature of SOCs to 700-900°C has attracted attention because a reduction in operating temperature means less material degradation such as coarsening of the porous electrodes, stresses and failures caused by mismatches of coefficient of thermal

expansion (CTE), and sealing problems, and enables replacement of ceramic interconnects by cheaper metallic materials [6,7]. In this temperature range, ferritic alloy (stainless steel) containing 15-25 wt% chromium becomes the choice of interconnect material because it is more cost effective and easier to fabricate [8-12].

However, the degradation of the SOC air electrode has been a challenging problem when the Cr-containing alloy is employed as the interconnect material. This is often caused by Cr-containing species evaporation and transport to the air electrode, which is also called Cr poisoning [13]. Cr poisoning has been observed in both SOFC and SOEC stacks, leading to fast decreases in power output (SOFC) [14,15] or hydrogen production (SOEC) [16,17]. At 700-900°C, a chromia oxide scale forms on the surface of Cr-containing alloys, which evaporates and forms volatile Cr species. In the oxidizing atmosphere, the volatile Cr species are Cr(VI) compounds and the composition is dependent on the moisture level in the atmosphere. The evaporation occurs as [18] :

$$Cr_2O_3 + 3/2O_2 \rightarrow 2CrO_3 \quad (4\text{-}1)$$

$$Cr_2O_3 + 3/2O_2 + 2H_2O \rightarrow 2CrO_2(OH)_2 \quad (4\text{-}2)$$

When the water content is more than 0.1 mol%, $CrO_2(OH)_2$ becomes the dominant volatile Cr species in the atmosphere [18,19].

The volatile Cr species diffuse through the porous air electrode and deposit on the electrolyte/air electrode/air triple phase boundaries (TPB) and the interface of electrolyte and air electrode materials. For different provskite air electrode materials, Cr poisoning is observed in the widely used strontium-doped lanthanum manganite (LSM) and lanthanum strontium cobaltite ferrite (LSCF) for SOFCs [20,21]. In the SOEC mode, Cr deposition on the LSM oxygen electrode is also believed to cause the degradation of SOEC stacks [17]. However, the mechanism of Cr-containing species interaction with and deposition on the air electrode remains controversial. For the extensively investigated yttria-stabilized zirconia (YSZ)/LSM half cell, the Cr deposition concentrates on the YSZ/LSM interface and blocks the pores of the air electrode under cathodic polarization in the SOFC mode [15,22]. Some studies suggest that the deposition of the Cr species is closely related to the oxygen activity at the electrode/electrolyte interface (TPB) and competes with the oxygen reduction [15]. In contrast, others believe that the interfacial degradation by Cr poisoning is caused by the blocking of electrochemically active sites by electrochemical reduction of Cr-containing species, which is driven by the

thermodynamics without direct influence of the electrical potentials [23,24]. In some further studies, the Cr deposition is observed not only at the TPBs, but also in the porous air electrode layer several microns away from the interface [25,26]. Overall, the surface interaction between the LSM air electrode and the volatile Cr species has not been well defined. First, the overall Cr poisoning process is complicated, and there are many different parameters, such as temperature, atmosphere, and cell structure, leading to varying results. Second, the Cr species deposition on TPBs, electrolyte, and electrode surface have different but convoluted mechanisms. Third, the Cr species have very low concentrations in both gaseous and solid phases, which make the characterization difficult. The interference of different elements during the characterization also presents problems.

The resulting phases of the Cr species interaction with the LSM air electrode have not been well defined [26]. Although $MnCr_2O_4$ and $(Mn,Cr)_3O_4$ spinel phases as well as Cr_2O_3 have been identified in the LSM air electrode and contact layer [27,28], the surface chemistry of the Cr poisoning and the degradation mechanism of the LSM electrode are not clear. Previous work indicates that Mn is an important factor for the reactions between the volatile Cr species and the LSM electrode [23]. Different LSM stoichiometry such as excessive or deficient Mn can lead to differences in such surface reactions. Detailed study of the interactions of the electrolyte/air electrode/interconnect tri-layer can improve the understanding of the Cr poisoning process and the interaction at the interfaces.

In this chapter, LSM air electrodes with different stoichiometry ($(La_{0.8}Sr_{0.2})MnO_3$, $(La_{0.8}Sr_{0.2})_{0.95}\ MnO_3$, and $(La_{0.8}Sr_{0.2})_{1.05}MnO_3$ (LSM100, LSM95, and LSM105)) are prepared on YSZ electrolyte. AISI 441, a stainless steel, is applied on the YSZ/LSM bi-layer as a SOC interconnect material. The tri-layered samples are thermally treated at 800°C for 500 h. The LSM electrode composition and the Cr distribution in the porous air electrode are analyzed to examine the LSM stoichiometry effect on the Cr deposition and the interface reactions. The phases at the interfaces are determined.

4.2. Experimental Procedures

4.2.1. Sample Preparation

LSM powders with different stoichiometry were prepared with a conventional solid state reaction method [29]. $SrCO_3$ (99.9%, Sigma Aldrich, St. Louis, MO), La_2O_3 (99.98%, Alfa Aesar, Ward Hill, MA), and $MnCO_3$ (99.9%, Alfa Aesar, Ward Hill, MA) at designed composition ratios (LSM95, LSM100, and LSM105) were mixed in a ball mill overnight. The mixed oxide and carbonates were calcined in a box furnace (DelTech, Model DT-31-Fl-8-C, Denver, CO) at 1200°C for 20 hrs. The LSM air electrode was fabricated on the YSZ surface by screen printing [30]. The LSM layer on the YSZ substrate (8 mol% yttria-stabilized zirconia, 20 mm diameter, 250 -290 μm thickness, NexTech Materials, Lewis Center, OH) was 20-30 μm thick after being sintered at 1100°C for 2 h.

After the sintering of the YSZ/LSM bi-layer, the AISI 441 alloy was placed on the LSM electrode as the interconnect. The configuration of the YSZ/LSM/AISI 441 tri-layer was given in chapter 3. Also, some YSZ/LSM bi-layer samples were prepared without the AISI 441 interconnect layer. All the tri-layer (with AISI 441) and bi-layer (without AISI 441) samples were thermally treated in a tube furnace (1730-20 HT Furnace, CM Furnace Inc. Bloomfield, NJ). The thermal treatment was carried out in dry air (compressed air) at 800°C for 500 h. The thermal treatment set-up was also shown in chapter 3. In order to observe the TPB region, the LSM porous layers were peeled off to show the YSZ/LSM interface for the 500 h thermally treated samples.

4.2.2. Characterization

After the thermal treatment, the tri-layer samples were broken to examine the cross-sections. Some samples were mounted into epoxy, and then cut and ground to detect different positions (distances away from the AISI 441 layer) in the porous LSM air electrode. Along the 30 μm thick LSM layer, the examined locations were shown in Fig. 4-1. They were labeled as YSZ/LSM, LSM left, LSM middle, LSM right, and LSM/AISI 441 from the YSZ to the AISI 441. To study the microstructure, both secondary electron images and backscattered electron images of scanning electron microscopy (SEM, Quanta 600 FEG, FEI, Hillsboro, OR) were used.

Surface analysis was carried out in an X-ray photoelectron spectrometer (XPS, PHI Quantera SXM-03, Physical Electronics Inc., Chanhassen, MN). An Al Kα radiation (1486.6 eV) was used as the X-ray source. In order to identify the phases, X-ray diffraction (XRD) studies were carried out in an X'Pert PRO diffractometer (PANalytical B.V., EA Almelo, The Netherlands). The step size was 0.030° s^{-1} with Cu Kα radiation (λ= 1.5406 Å).

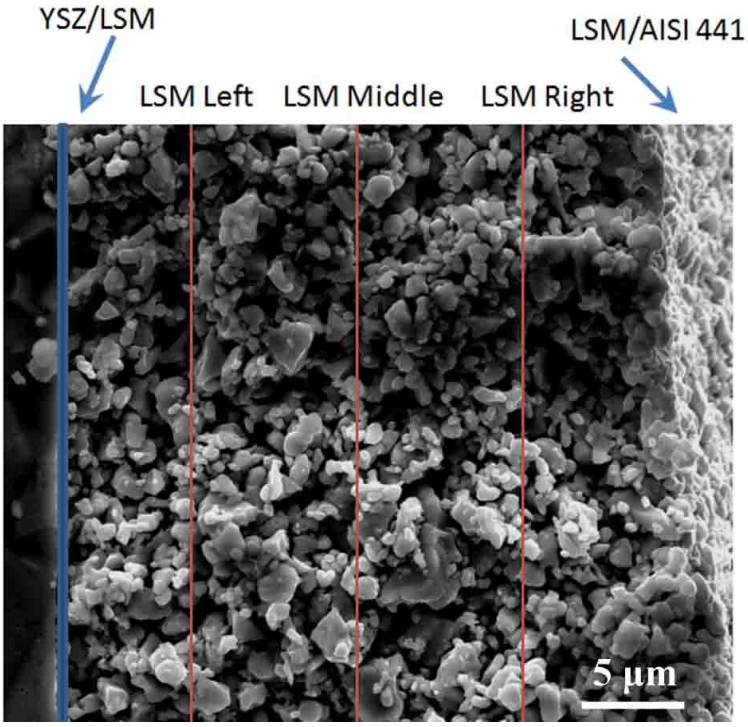

Fig. 4-1. The examination locations of the porous LSM air electrode. XPS is carried out at five locations: YSZ/LSM, LSM left, LSM middle, LSM right, and LSM/AISI 441.

4.3. Results

4.3.1. Microstructure

The SEM images of the YSZ electrolyte/LSM air electrode/AISI 441 interconnect cross sections are shown in Fig. 4-2. The top images are before the thermal treatment and the bottom images are after that. The images are taken from the polished tri-layer samples mounted in epoxy. The thickness of the LSM porous layer is 25-30 µm. Fig. 4-2 shows that the tri-layer configuration is maintained. Before the thermal treatment, the LSM grains appear to have been sintered (top of Figs. 4-2(a), (b), and (c)). The porous LSM air electrode layer is homogeneous

for all the three different compositions (LSM95, LSM100, and LSM105). The grain size distribution of the LSM electrode increases from LSM95 to LSM105. For the LSM95 sample, the grains are 2-4 μm and almost no small grains below 1 μm can be seen. For the LSM100 and LSM105 samples, smaller grain sizes below 1 μm are apparent and some large grains of ~5 μm are observed. The grain size of the LSM100 sample is slightly larger than that of the LSM105 samples. The LSM95 sample shows the most compact network among the three samples. For the other two samples, local porous regions are more prevalent. Also, the grains in the LSM100 and LSM105 samples do not bond well.

Fig. 4-3 shows the SEM images of the unmounted, fractured YSZ/LSM bi-layer cross sections, before (top) and after (bottom) the thermal treatment. The porous LSM layer can be observed without the possible damage from grinding and polishing. In the SEM images, the YSZ electrolyte is dense although small closed pores are present. Among the three studied samples, all the interfaces show good contact between the YSZ electrolyte and the LSM electrode before the thermal treatment (top of Figs. 4-3(a), (b), and (c)). The LSM grain size difference is consistent with that in Fig. 4-2. The LSM95 sample has more uniform grain sizes. The LSM100 and LSM105 samples show a larger grain size distribution, especially for the LSM100 sample. For the LSM95 sample, the LSM grains and the YSZ surface seem to form a better contact. For the LSM100 and LSM105 samples, the contact of the LSM grains with the YSZ surface may be slightly less. These different microstructures indicate that the Mn-excessive sample (LSM95) is easier to sinter and forms a better contact with the YSZ electrolyte.

After the thermal treatment of the tri-layer and bi-layer samples in air at 800°C for 500 h, the microstructure (bottom of Figs. 4-2(a) and 4-3(a)) of the LSM95 layer becomes more porous without singnificant change in the LSM grain size. This is mainly because the sintering process at 1100ºC has consumed the excess surface energy and the LSM microstructures such as porosity, pore size, and pore structure are mostly determined by the sintering process. The thermal treatment at 800°C causes no substantial change. For the LSM100 sample, however, microstructure changes after 500 h of thermal treatment are more visible (bottom of Figs. 4-2(b) and 4-3(b)). Some small LSM grains (< 1 μm) disappear and large grains connect and form a continuous network. The grain size is about 2–5 μm after 500 h of thermal treatment. For the LSM105 sample, the microstructure shows the smallest sintered grain sizes (bottom of Figs. 4-2(c) and 4-3(c)) and there is no fundamental grain size change after the thermal treatment. For

the YSZ/LSM interfaces, after the thermal treatment, the LSM105 sample shows the most contact with the YSZ followed by the LSM100 sample and then the LSM95 sample. However, the bonding between the YSZ and the LSM does not necessarily follow the contact trend, as seen in 4.3.2.

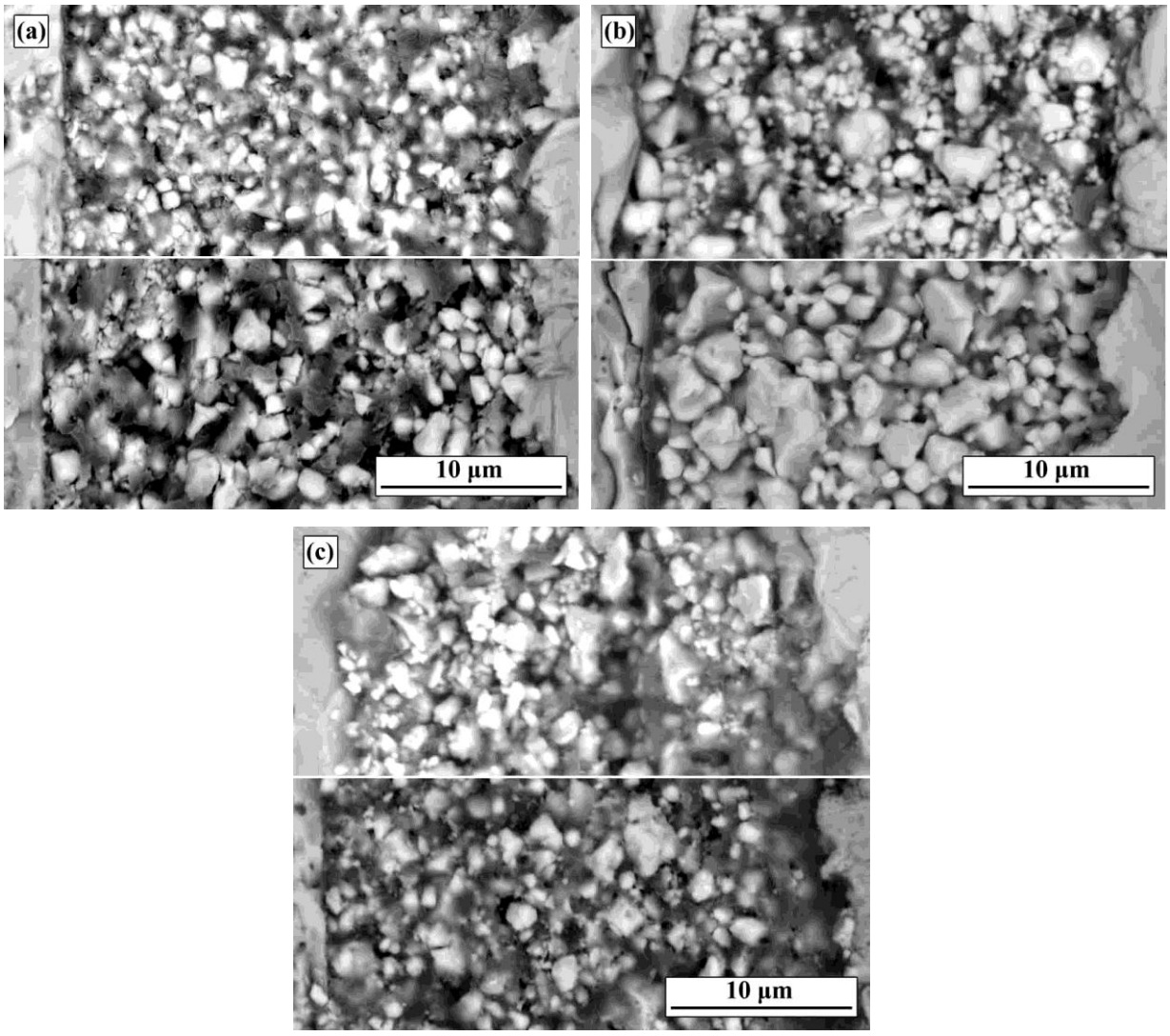

Fig. 4-2. SEM images of YSZ/LSM/AISI 441 tri-layer cross-sections before and after thermal treatment in air at 800°C for 500 h: (a) LSM95, (b) LSM100, and (c) LSM105. For each figure, the top is before the thermal treatment and the bottom is after the thermal treatment. The samples are mounted in epoxy and polished.

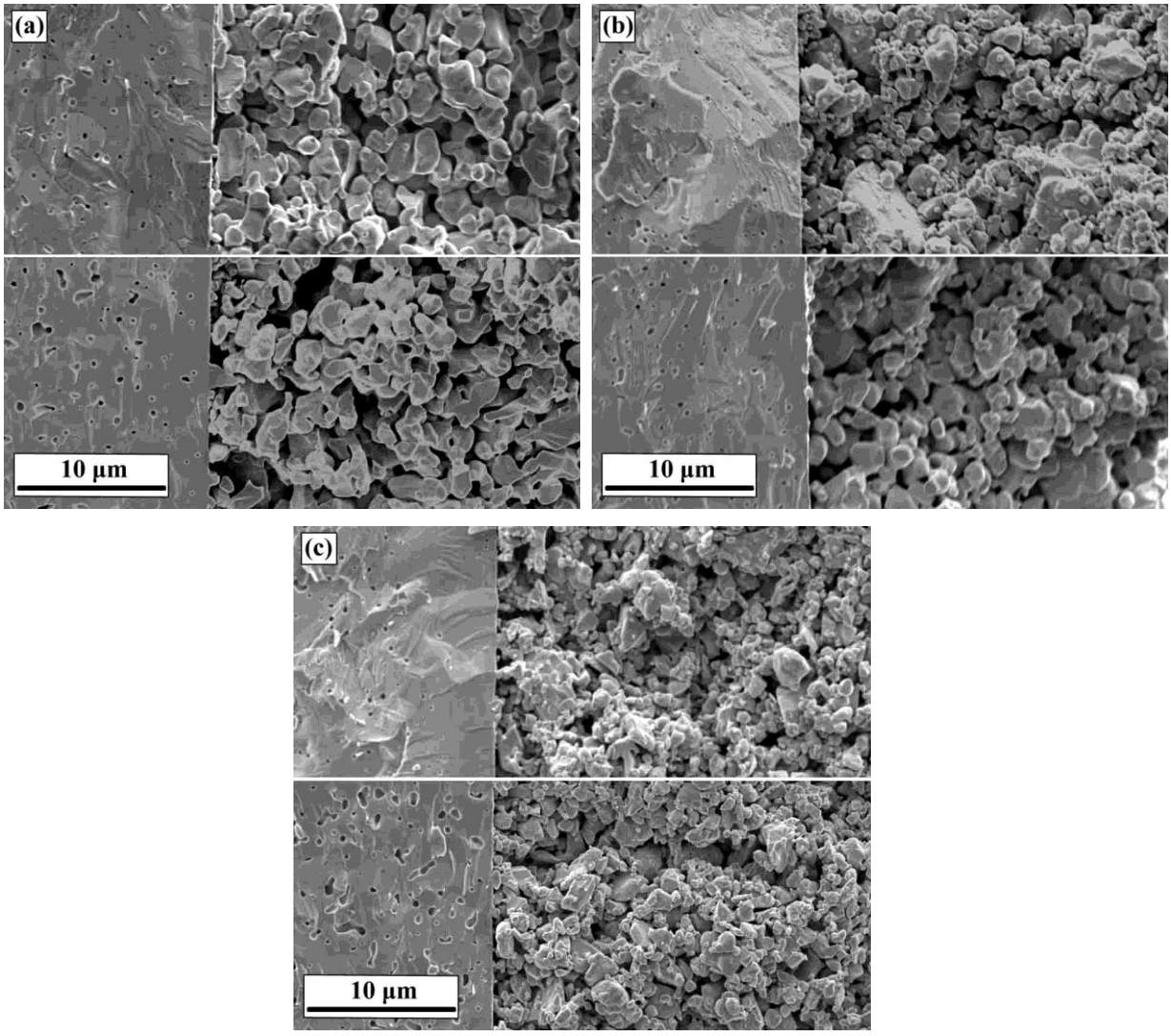

Fig. 4-3. SEM images of YSZ/LSM bi-layers before and after thermal treatment in air at 800°C for 500 h (unpolished cross section): (a) LSM95, (b) LSM100, and (c) LSM105. For each figure, the top is before the thermal treatment and the bottom is after the thermal treatment.

4.3.2. YSZ/LSM interface Analysis

To examine the microstructure at the YSZ/LSM interface, the LSM porous layer was mechanically peeled off from the YSZ substrate. The resulting YSZ surface morphologies are shown in Fig. 4-4 for different conditions. Fig. 4-4(a) is the surface of the YSZ substrate, which shows no change during the sintering and the thermal treatment. The grain boundaries of the YSZ are shown and the grain size is about 5 μm. For the LSM95 sample, the LSM layer forms

extensive bonding spots with the YSZ layer even before the thermal treatment (Fig. 4-4(b) top). For the LSM100 and LSM105 samples, the bonding with the YSZ diminishes at the as-sintered state (top of Figs. 4-4(c) and (d)). This result is different from the interface contact trend discussed in 3.1. After the thermal treatment, the LSM95 sample still shows extensive bonding with the YSZ; the YSZ surface is almost totally covered with LSM. Fig. 4-4(b) bottom shows the low and high magnification images respectively. The YSZ grain boundaries cannot be seen. For the LSM100 and LSM105 samples (Figs. 4-4(c) and (d) bottom, also with low and high magnification images), the bonding spots with the YSZ surface and the residual LSM on the YSZ surface diminish in the same order. For the LSM100 sample, the bonding spots increase compared to the as-sintered sample, which means more contacts are formed during the thermal treatment (Fig.4-4(c)). However, the grain boundaries of the YSZ surface are still visible and the high magnification image shows less extensive bonding struts. For the LSM105 sample (Fig. 4-4(d)), there are very few bonding spots after the thermal treatment and very little LSM residual is seen on the YSZ surface. The high magnification image clearly reveals the YSZ grain boundaries and very few weak bonding spots with negligible bonding struts. This trend is consistent with the adhesion strength observed between the LSM and the YSZ layer for the different samples.

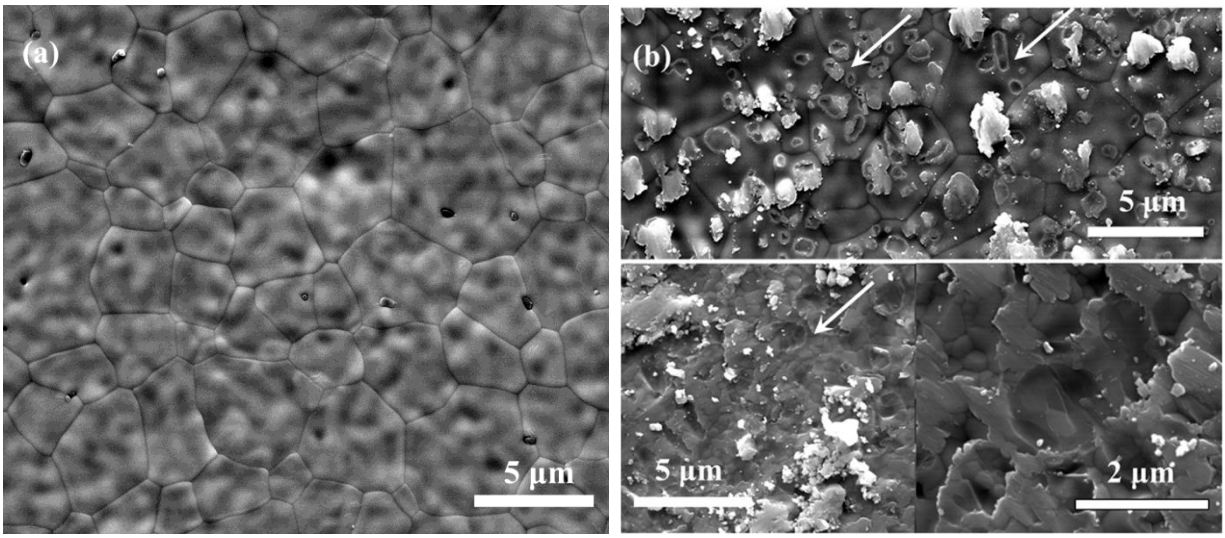

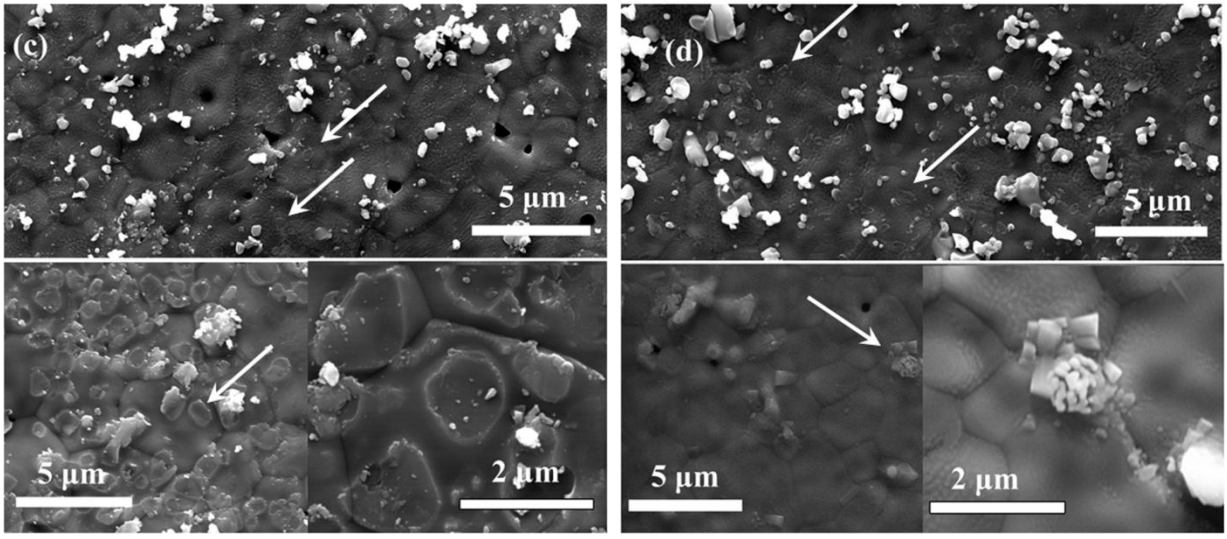

Fig. 4-4. SEM images of the YSZ/LSM interface after the LSM porous layer removal. (a) YSZ surface, (b) LSM95, (c) LSM100, (d) LSM105. For (b), (c), and (d), the top is the as-sintered sample and the bottom is the thermally treated sample with low and high magnifications.

4.3.3. LSM/AISI 441 Interfacial Composition Analysis

In order to examine the LSM layer chemical composition and understand the interfacial interaction between LSM and AISI 441, the AISI 441 interconnect is removed for the XPS analysis. The elemental compositions at the LSM/AISI 441 interface at different conditions are shown in Fig. 4-5. The scan area is 200 × 200 μm^2. Since the LSM samples are mounted in oxygen-containing epoxy, oxygen is excluded from the analysis. The atomic percentages of La, Sr, Mn, and Cr are normalized to 100%. Each atomic percentage result from the XPS analysis is averaged by three scans, the standard deviations are also shown in Fig. 4-5.

The initial composition of the LSM samples is shown in Fig. 4-5 as a reference. After being sintered at 1100°C for 2 h, the surface compositions of the LSM samples are different from the initial compositions (Fig. 4-5(a)). Sr and La show enrichment on the LSM surface. Sr increases by 46% in LSM95, 42% in LSM100, and 23% in LSM105; La increases by 31% in LSM95, 24% in LSM100, and 33% in LSM105. Accordingly, Mn decreases on the LSM surface by 32% in LSM95, 28% in LSM100, and 33% in LSM105. It should be noted that oxygen is excluded from the analysis and these changes are for the relative change of the respective metal elements only. The surface Sr and La segregation can be understood as follows. The crystal

structure of the LSM surface is different from that in the bulk. Broken bonds and strain energy drive composition re-distribution [31,32]. For LSM, Sr surface segregation is a well-known phenomenon [33-37]. La^{3+} (1.36Å) and Sr^{2+} (1.44 Å) have much larger ionic radii, whereas those for the Mn^{3+}/Mn^{4+} ions are relatively small (less than 1 Å) [38]. As a result, La and Sr are more likely to reside on the surface for size accommodation. Sr shows more surface enrichment than La for the LSM95 and LSM100 samples, which causes the La/Sr ratio to decrease to 3.5 from the initial ratio of 4 (Fig. 4-5(b)). For the LSM105 sample, the La/Sr ratio increases to 4.3. This is likely due to the excessive A sites of the LSM perovskite structure which offer more accommodation to La. Ar the same time, Mn ions decrease significantly (Fig. 4-5(a)), likely due to Mn migration to the LSM bulk as a result of its small size. The (La+Sr)/Mn ratio, thus, increases significantly. Initially the (La+Sr)/Mn ratios are 0.95, 1, and 1.05, respectively (Fig. 4-5(c)). At the as-sintered state, this ratio increases to 1.8-2.0. The significant change of the A/B site ratio in the LSM indicates that the LSM surface may not maintain the perovskite crystal structure.

For the YSZ/LSM bi-layers without the presence of the AISI 441 interconnect after the 500 h thermal treatment, the surface compositions of the LSM samples change continuously (Fig. 4-5(a)). La slightly decreases by 4% in LSM95 and LSM100, and 11% in LSM105. The surface segregation of Sr continues, increasing by 9% in LSM95, 19% in LSM100, and 46% in LSM105. The La/Sr ratios of LSM95, LSM100, and LSM105 are 3.1, 2.8, and 2.6, respectively (Fig. 4-5(b)). These values are drastically lower than the designed value of 4.0. Mn stays almost the same in all the LSM samples, where the Mn contents of the three samples are close to each other at 33-36%. As a result, the LSM95 and LSM100 samples show very similar surface compositions. For the LSM105 sample, the surface shows more Sr and less Mn contents. Since La decreases and Sr increases for all the LSM samples, the (La+Sr)/Mn ratios stay similar to the as-sintered samples at 1.8-2.0 (Fig. 4-5(c)). These values again are very different from the designed value of 0.95-1.05 and indicate likely crystal structure change on the LSM surface.

For the YSZ/LSM/AISI 441 tri-layers, after the thermal treatment for 500 h, Cr is detected on the LSM surface. For the LSM105 sample, the Cr concentration on the surface is 13.7%, which is higher than those for the LSM95 and LSM100 samples at 7.1% and 8.7%, respectively (normalized to 100% of La, Sr, Mn, and Cr). If oxygen were included in the atomic percent calculation, the Cr deposition amounts would be 2-5%, much higher than those from the

energy dispersive spectroscopy (EDS) analysis in Chapter 3. The reason is that XPS collects composition data from at most ~ 10 nm of depth while EDS collects composition data from ~ 1 μm of depth [39]. For the Cr deposition on the LSM surface, XPS surface analysis is a more sensitive technique.

After the tri-layer sample thermal treatment, La decreases for all the three samples compared to the as-sintered samples, i.e., by 21% in LSM95, 9% in LSM100, and 17% in LSM105, respectively. At the same time, Mn decreases by 5% in LSM95, 15% in LSM100, and 23% in LSM105; and Sr increases by 37% in LSM95, 10% in LSM100, and 28% in LSM105. The Sr enrichment and Mn depletion on the surface follow the same trends as the bi-layers. However, La decreases more significantly on the surfaces than for the bi-layer samples. This is believed to result from Cr^{3+} taking the place of La^{3+} in the surface structures and causing La^{3+} to diffuse into the LSM samples. For LSM95, Sr increases by 37% compared to the as-sintered state, which is much higher than the increase for the bi-layer sample (9%). For LSM100 and LSM105, the Sr increases are much less than those for the bi-layers. This is likely due to the fact that the Mn decreases in the opposite direction instead of remaining unchanged for the tri-layer samples, which provides more room for the Sr to resist segregation. Interestingly, after the tri-layer thermal treatment, the Mn surface concentrations of the LSM95 and LSM100 samples are very close, at 31% and 33%, respectively (Fig. 4-5(a)), whereas the LSM105 samples shows a lower Mn surface concentration at 25%. Apparently, higher La and Sr contents lead to more Mn segregation. Since the LSM95 sample has more Sr and less La, the La/Sr ratio of the LSM95 sample is 2.1 while those for the LSM100 and LSM105 samples are 2.8 and 2.9, respectively (Fig. 4-5(b)). In any case, these values are much lower than the designed ratio of 4.0 and indicate crystal structure instability. The (La+Sr)/Mn ratios of the LSM95 and LSM100 samples are very close to the same value of 1.9 (Fig. 4-5(c)) while for the LSM105 sample it is 2.4, still all much higher than 1. For the LSM95 sample, Cr leads to a 15% decrease in La and a slight decrease in Mn, while Sr increases more significantly than that of the no-Cr condition. For the LSM100 sample, both the La and Mn decrease and the Sr increase are less than those of the no-Cr condition. The final result shows similar (La+Sr)/Mn ratios. For the LSM95 and LSM100 samples, Cr likely froms Mn-Cr compounds with Mn. For the LSM105 sample, the Mn content is less than those of the LSM95 and LSM100 samples and the Cr is significantly higher; this result may be caused by the excessive La and Sr interaction with the Cr species, which also

increases the amount of Cr surface deposition. However, other analysis such as with XRD cannot verify this conjecture.

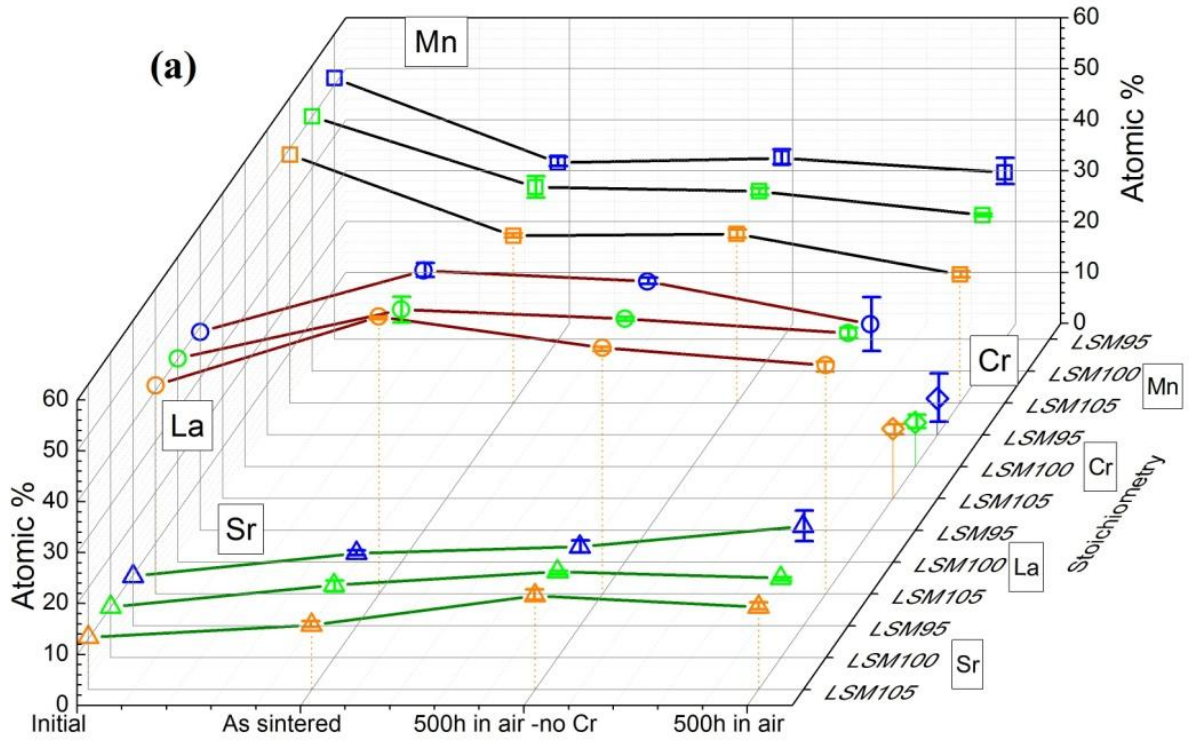

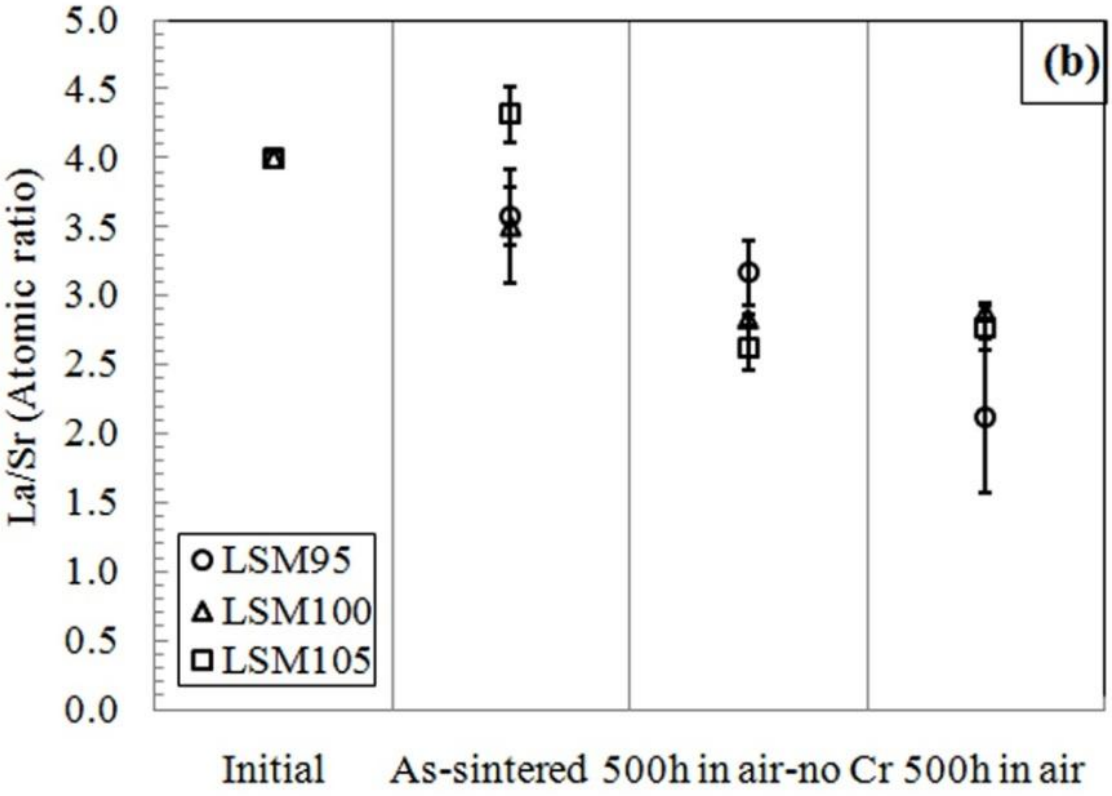
(b)
La/Sr (Atomic ratio)
5.0
4.5
4.0
3.5
3.0
2.5
2.0
1.5
1.0
0.5
0.0
LSM95
LSM100
LSM105
Initial
As-sintered
500h in air-no Cr
500h in air

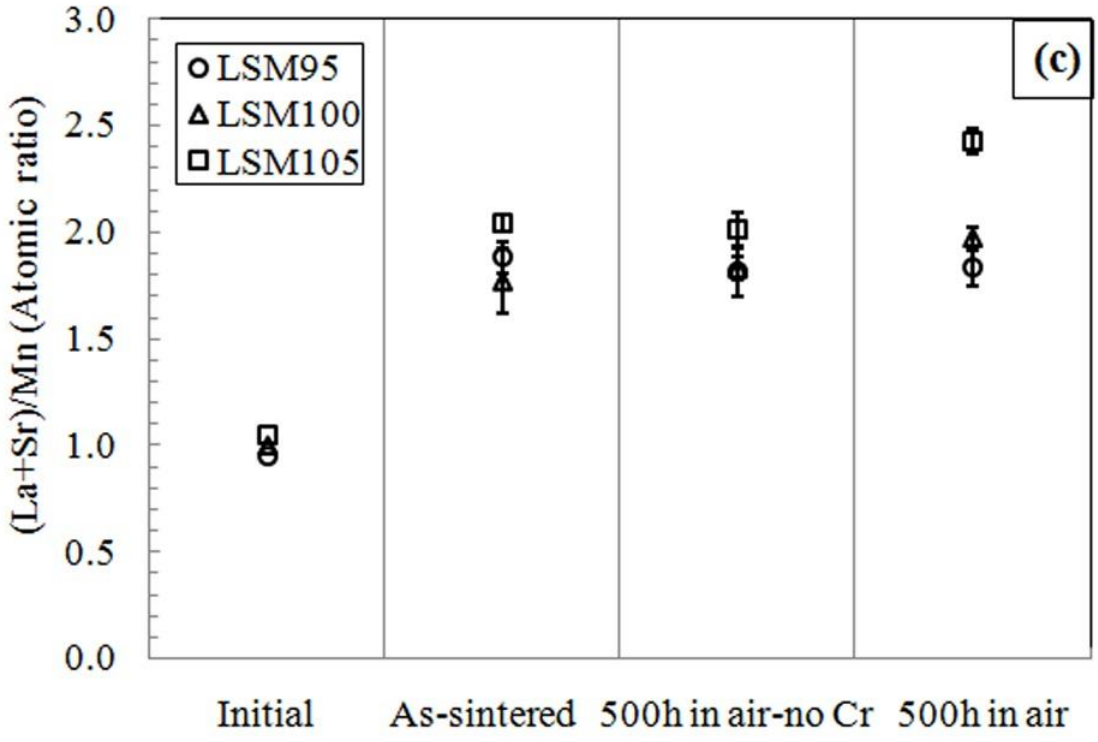
(c)
(La+Sr)/Mn (Atomic ratio)
3.0
2.5
2.0
1.5
1.0
0.5
0.0
LSM95
LSM100
LSM105
Initial
As-sintered
500h in air-no Cr
500h in air

Fig. 4-5. Elemental concentrations of the LSM samples: (a) atomic concentrations, (b) La/Sr ratio, (c) (La+Sr)/Mn ratio.

4.3.4. LSM/AISI 441 Phase Evolution

XRD patterns of the LSM with different stoichiometries (LSM95, LSM100, and LSM105) are shown in Fig. 4-6. Before the thermal treatment, the LSM95, LSM100, and LSM105 air electrodes show an almost pure perovskite phase. The excessive and deficient Mn contents in the non-stoichiometric samples (LSM95 and LSM105) do not lead to visible phase separation of the LSM. After the thermal treatment for 500 h at 800°C in air and without contact with the AISI 441 interconnect, the XRD patterns of all the three samples show no detectable change (not shown in Fig. 4-3). The surface segregation detected by the XPS analysis is located only on the very surface, which is beyond the detection limit of the XRD. The bulk phases of the LSM samples with different stoichiometries are stable during the thermal treatment. This also explains why the drastic LSM surface composition segregation has not been widely reported.

For the tri-layer samples, after the thermal treatment at 800°C for 500 h, the LSM layers with different stoichiometries mainly contain the same perovskite phase. However, some other phases are identified. $SrMnO_{3-x}$ is a minor phase identified in the LSM95 sample, which cannot be detected in the other two samples. The $SrMn_6O_{3-x}$ phase may correspond to the surface phase of the LSM95 sample with higher Sr concentration. A minor $Mn_{1.5}Cr_{1.5}O_4$ phase is detected in the LSM95 and LSM100 sample. For the LSM105 sample, no other phase can be identified besides the perovskite LSM. As indicated in 3.3, the Cr species may interact with La and Sr and form $(La,Sr)CrO_3$. However, no new phase is detected by the XRD because the possible phase should be at the very surface. This shows again that the XRD is more of a bulk detection technique and its result cannot be correlated with the XPS results. Other experiments such as high resolution X-ray technique and electron diffraction should be sought to confirm the phases related to the Cr surface deposition.

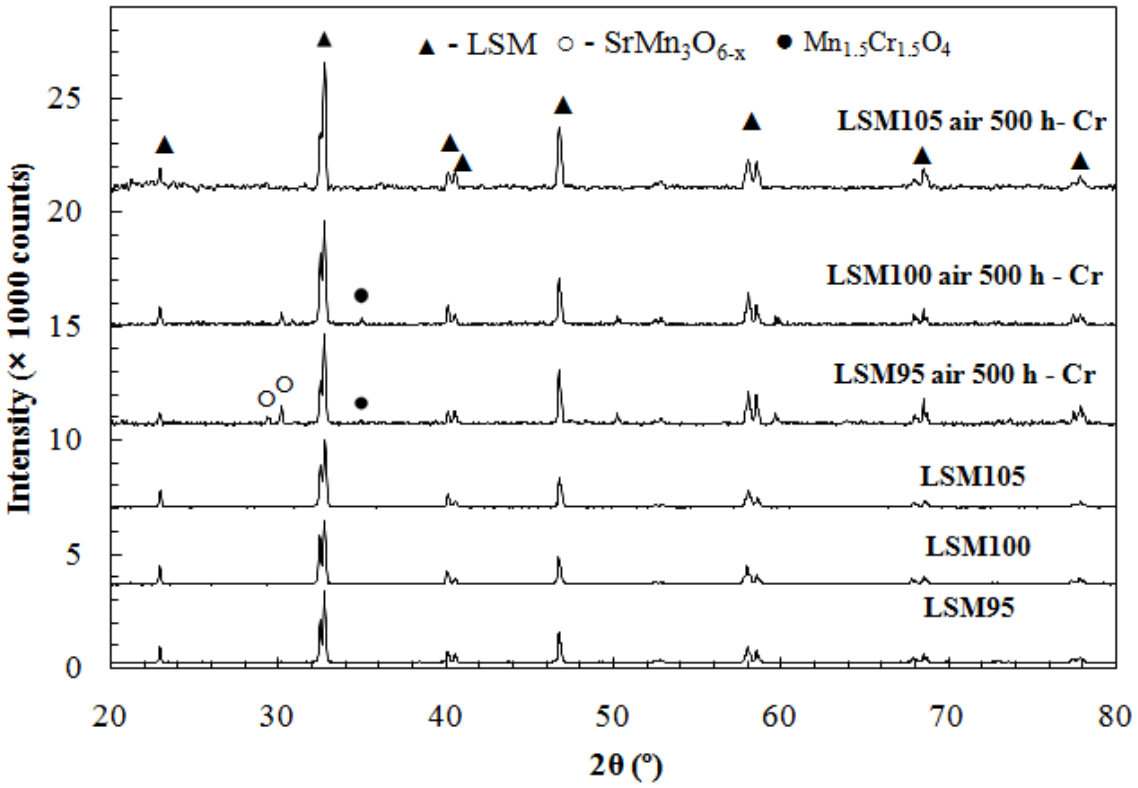

Fig. 4-6. XRD patterns of the LSM layer before and after the thermal treatment at 800°C for 500 h in air. The latter case is the tri-layer arrangement.

4.3.5. Cr Distribution

In order to investigate the Cr species diffusion through the porous LSM air electrode and deposition at both the LSM surface and the YSZ/LSM interface, XPS elemental analysis is employed at different locations along the LSM layer after the thermal treatment. Before the XPS analysis, the AISI 441 interconnect is removed and the porous LSM air electrode on the YSZ electrolyte is mounted in epoxy. The mounted LSM samples are carefully grinded layer by layer from the top (the surface in contact with the AISI 441 interconnect) to the bottom (the YSZ/LSM interface) as shown in Fig. 4-1. The results are normalized to 100% by considering La, Sr, Mn, and Cr only. Along the porous LSM air electrode layer (~30 μm thick), five different locations are obtained for the XPS analysis (Fig. 4-7). The thickness of each layer is controlled by a micrometer to 8-10 μm.

Along the cross sections of the LSM layer, from the LSM/AISI 441 interface to the locations close to the YSZ/LSM interface, the distribution of La, Sr, and Mn stay almost the same. There are some composition variations, but the differences are not significant. The Cr content, however, decreases from right to left for all the samples. The Cr amounts at the LSM/AISI 441 interface reflect the effect of the stoichiometry. The LSM95 sample shows the lowest Cr concentration at about 7.1%; the LSM100 sample shows about 8.7%, and the LSM105 sample shows 13.7%. Excessive A sites lead to more Cr deposition, consistent with the La replacement explanation. For all the samples, the Cr content shows a decrease from the AISI 441 side to the YSZ side through the porous LSM layer (except at the YSZ/LSM interface). Compared to the Cr content of 7-14% at the LSM right and the LSM/AISI 441 interface, the Cr content shows only 2-5% at the LSM left (Fig. 4-7).

At the YSZ/LSM interface, the Cr content shows an increase for the LSM95 and LSM100 samples but a decrease for the LSM105 sample. For the LSM95 sample, the Cr content at the YSZ/LSM interface is 12.7 %. For the LSM100 sample, it is 9.0%. For the LSM105 sample, the Cr content is only 2.4%, much less than those of LSM95 and LSM105, which is because the Cr deposition is affected by the La content in a manner, similar to the LSM surface Cr deposition. This La effect to the Cr deposition will be discussed more in the discussion section. Other than Cr, the Sr content is 16.4% for the LSM95 sample, much higher than those of 9.6% for the LSM100 sample and 11.5% for the LSM105 sample. La content increases to 51.9% for LSM95, 61.3% for LSM100, and 69.0% for LSM105. On the other hand, the Mn content stays almost the same (17.1-20.1%), even though they are all much lower than those across the LSM layers. The different extent of Cr deposition at the YSZ/LSM interface is related to the interactions between the LSM sample and the YSZ electrolyte. As shown in Fig. 4-4, LSM95 and LSM100 form stronger bonds with the YSZ electrolyte. The interfacial interactions likely lead to new species formation such as $SrZrO_3$ [40]. The Cr deposition at the YSZ/LSM95 interface is accelerated by the new Sr-containing phase, because the Sr content at the interface may create more sites for the volatile Cr species to deposit. From the LSM95 to the LSM105 sample (Figs. 4-7(a), (b) and (c)), La shows increasing enrichment while the amount of Cr deposition decreases. This means that the excessive La and likely La-containing phase (such as $La_2Zr_2O_7$ [41]) are not favorable for Cr deposition and bond formation with the YSZ surface. Mn does not participate in these interfacial interactions, but the overall depletion at the YSZ/LSM

interface will compromise TPB reactivity. However, XRD cannot identify the new phases suggested by the XPS analysis. This means that the amounts of these Sr-containing and La-containing phases are low and stay at the very interface.

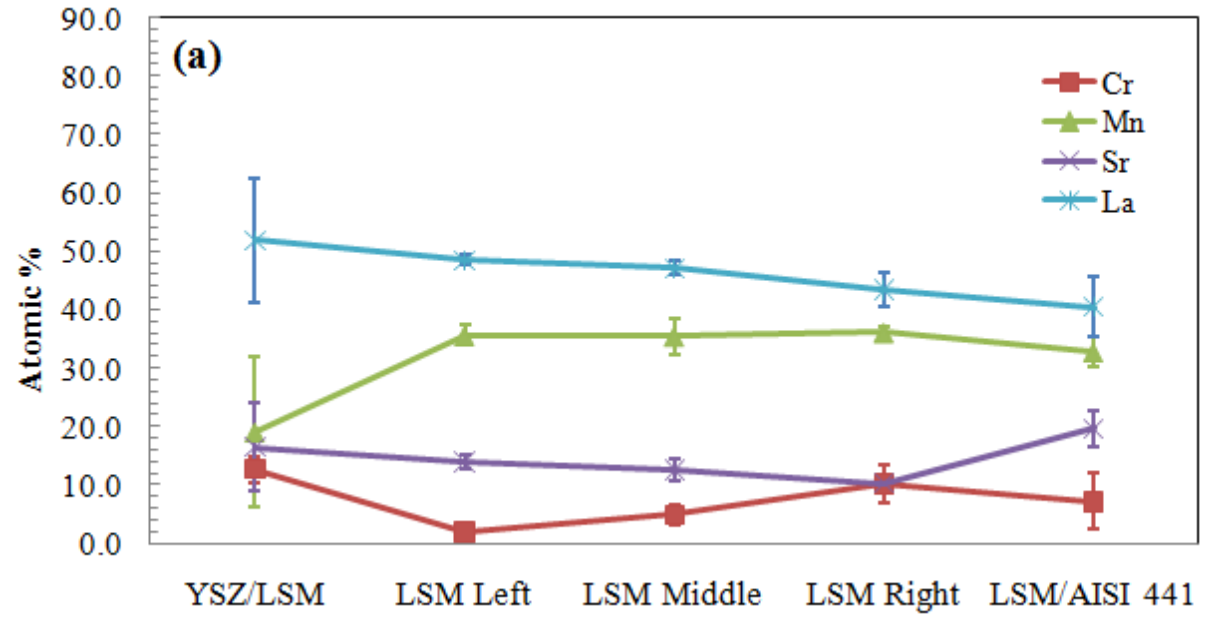

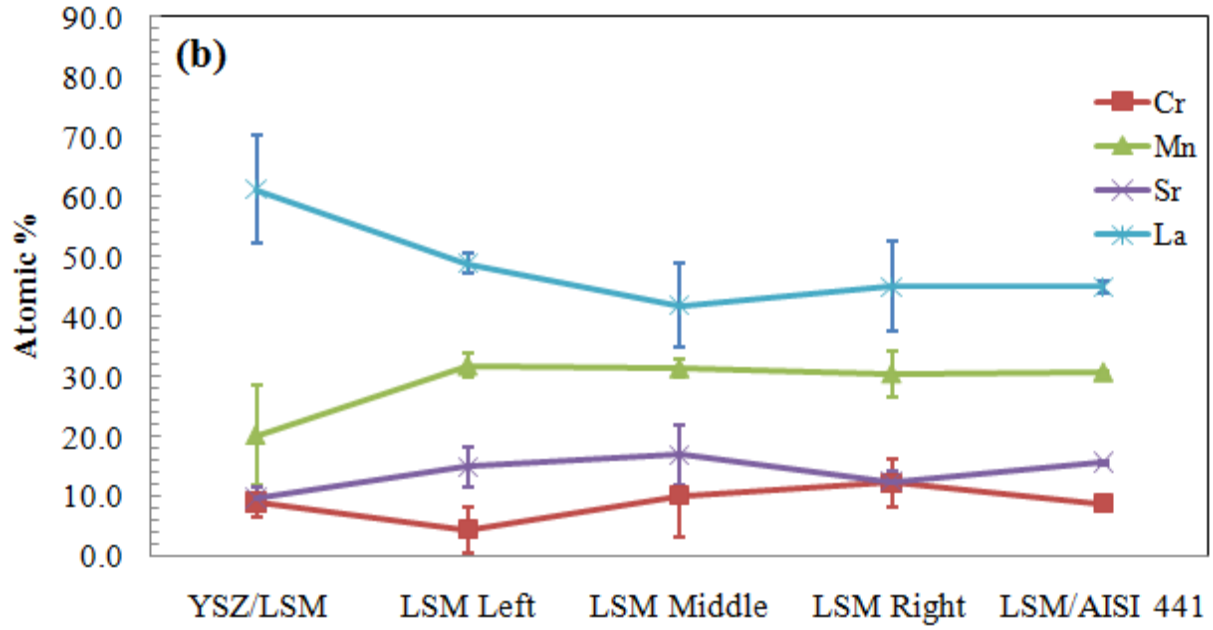

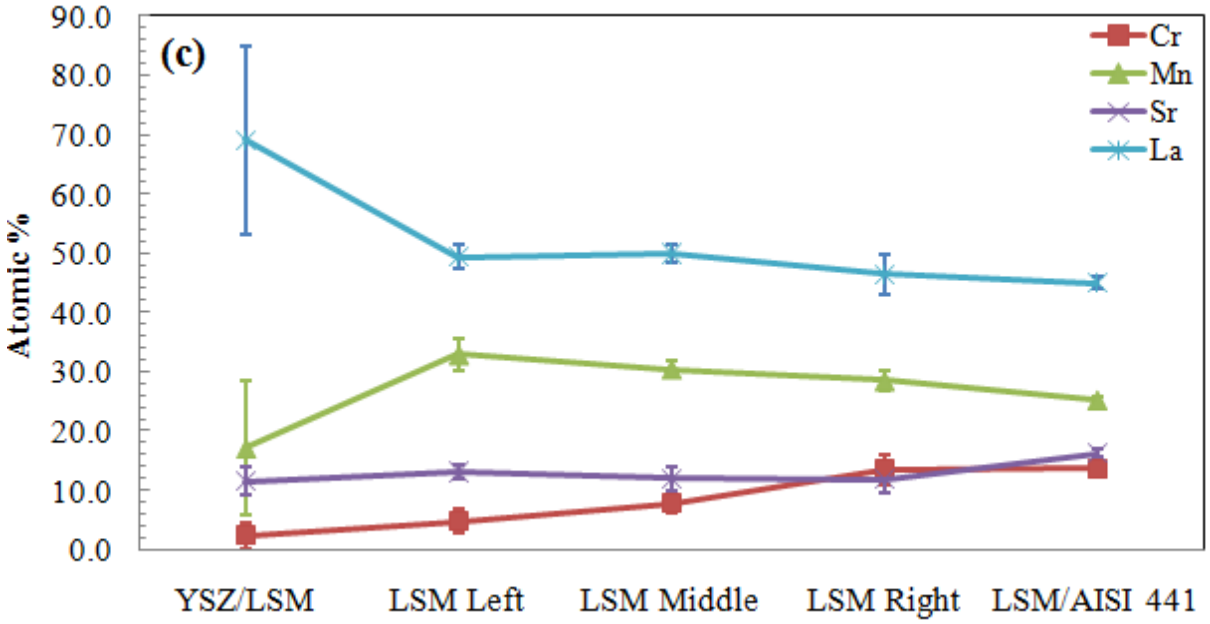

Fig. 4-7. Atomic concentrations along the LSM air electrode layer. The YSZ/LSM/AISI 441 samples are thermally treated in air at 800°C for 500 h: (a) LSM95, (b) LSM100, and (c) LSM105. All the concentrations are normalized to 100% by considering La, Sr, Mn, and Cr only.

4.4. Discussion

Because LSM with an ABO_3 perovskite structure consists of (La,Sr)O (A-site plane) and MnO_2 (B-site plane, consisting of MnO_6 octahedra) atomic layers alternatively stacked [42], the same XRD results for the as-synthesized LSM means that although the (La+Sr)/Mn ratio is slightly changed in LSM95 and LSM105, the MnO_2 layers maintain the same structure. For the as-sintered and the bi-layer samples (without Cr deposition) after the thermal treatment, the surface segregation of La and Sr fundamentally changes the (La+Sr)/Mn ratio. It is highly likely that the LSM surface cannot maintain the provskite structure and composition segregation occurs more easily. This La and Sr surface enrichment is mainly caused by their larger sizes. For the tri-layer samples, the Cr deposition inhibits the surface segregation of La for all the samples since it has a tendency to occupy the La sites. However, Cr can only inhibit the Sr surface segregation for the LSM100 and LSM105 samples. For the LSM95 sample, this inhibition is less effective, most likely because of the fewer A site species in the composition design. The $SrMn_3O_{6-x}$ phase

identified in the LSM95 sample means that in the Mn excessive situation, Sr interacts with the excessive Mn first instead of waiting for the diffusing Cr species to become available.

The presence of Cr across the LSM layer indicates the Cr distribution from the AISI 441 interconnect into the LSM air electrode layer, which in turn changes the surface structure of the LSM. The Cr-containing phase forms a very thin surface layer on the LSM since the microstructures do not show visible morphological changes and the XRD pattern shows very weak detectable peaks of the new phases. The interaction is schematically shown in Fig. 4-8. First of all, La and Sr surface segregation occurs. Then, Cr species deposit on the La-Sr enriched LSM surface, forming $Mn_{1.5}Cr_{1.5}O_4$ for the LSM95 and LSM100 samples and $(La,Sr)CrO_3$ for the LSM105 sample. The reaction equations can be expressed as:

$$(La_{0.8}Sr_{0.2})_xMnO_3 \xrightarrow{\text{La,Sr segregation}} (La,Sr)_{x+n}MnO_3 \text{ (surface)} \quad (4\text{-}3)$$

LSM95 and LSM100:

$$(La,Sr)_{x+n}MnO_3 \text{ (surface)} \xrightarrow{CrO_3} (La,Sr)_{x+n}Mn_{1-m}O_3 + \frac{2}{3}m\ Cr_{1.5}Mn_{1.5}O_4 \text{ (surface)} \quad (4\text{-}4)$$

LSM105:

$$(La,Sr)_{x+n}MnO_3 \text{ (surface)} \xrightarrow{CrO_3} (La,Sr)_{x+n-m}MnO_3 + m\ (La,Sr)\ CrO_3 \text{ (surface)} \quad (4\text{-}5)$$

At the same time, Cr diffuses to the YSZ/LSM interface. For the LSM95 sample, excessive Mn in the LSM95 is beneficial for forming a good bonding between the YSZ and the LSM and the interaction leads to a significant change of the microstructure (Fig. 4-4(b)). The Cr shows significant accumulation at the interface which means the interfacial interaction forms new compounds and leads to more Cr deposition. Sr shows a larger content compared with the other two samples, which shows the change from the original composition of the LSM95 (excessive Mn). Sr should be the main component of the formed phase during the thermal treatment. Thus, at the YSZ/LSM95 interface, $SrZrO_3$ may be the phase leading to more Cr accumulation. The LSM100 sample is similar to the LSM95, where Cr also shows accumulation at the interface. For the LSM105 sample, at the YSZ/LSM interface, a large amount of La is found and the Cr content is much smaller than those of the LSM95 and LSM100 samples. Apparently, the deficient Mn in the LSM105 leads to the $La_2Zr_2O_7$ formation at the TPBs causing poor interfacial bonding. Furthermore, the $La_2Zr_2O_7$ at the YSZ/LSM interface strongly inhibits Cr deposition.

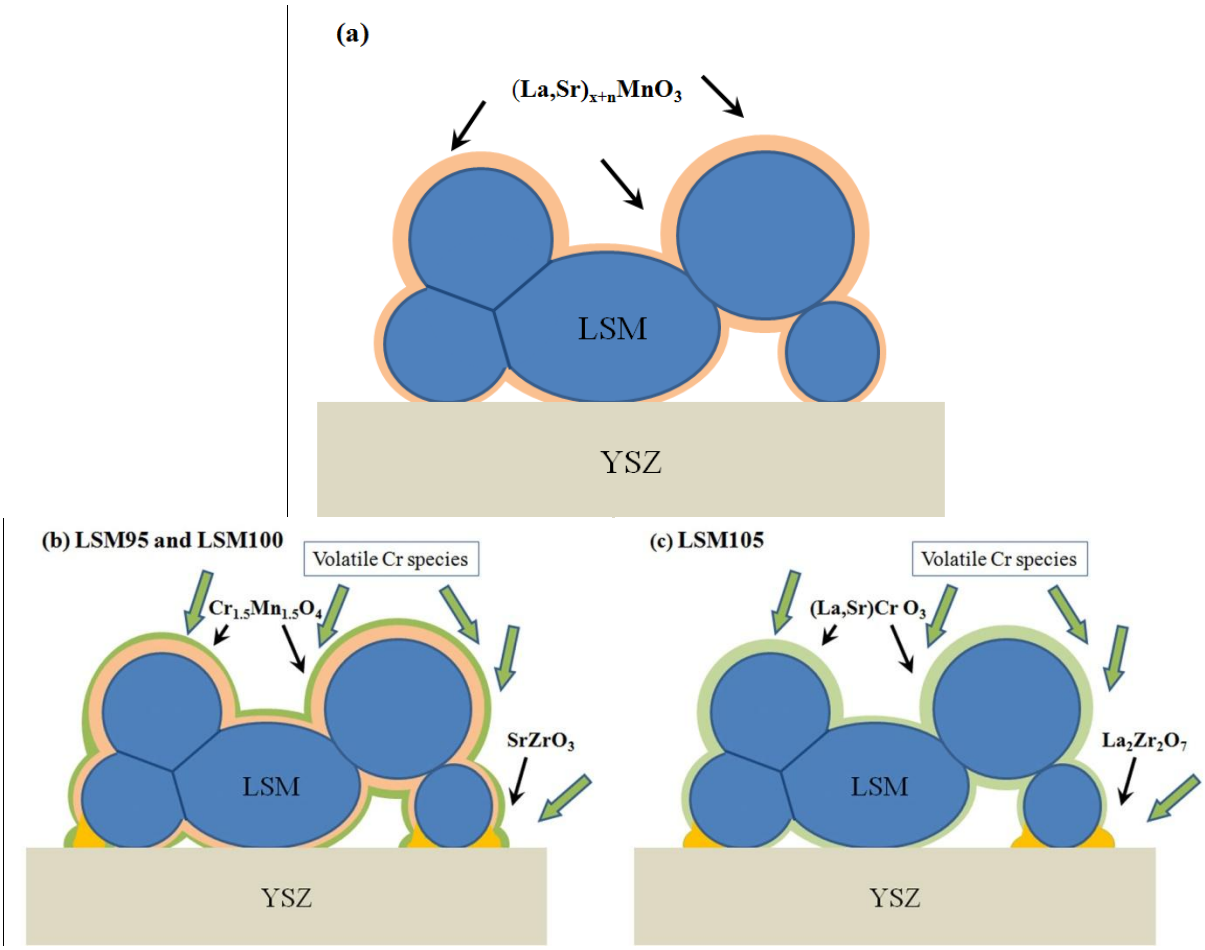

Fig. 4-8. Schematic of the surface and interfacial interactions of the LSM air electrode with Cr-containing species and YSZ: (a) thermally treated without Cr species, (b) LSM95 and LSM100 thermally treated with Cr species, (c) LSM105 thermally treated with Cr species.

As seen, LSM is highly unstable at the very surface. Sr and La surface segregation and Cr deposition on the LSM surface changes the surface chemistry and the bonding between the YSZ and the LSM, and compromises the activity for oxygen reduction. These interactions can impose serious constraints on the performance and long-term stability of SOFC/SOECs. Compared with the effects of Cr species deposition on the LSM surface, La and Sr surface segregation and the subsequent impact on YSZ/LSM bonding and the reaction with the TPBs should be more carefully considered.

4.5. Conclusions

In this study, YSZ/LSM/AISI 441 samples with different LSM stoichiometries are thermally treated to study the LSM composition effect on the interfacial interactions. All the LSM samples ($(La_{0.8}Sr_{0.2})_xMnO_3$, x= 0.95, 1, and 1.05) show Sr and La enrichment and Mn deficiency after being thermally treated in dry air at 800°C for 500 h. Cr surface deposition inhibits the surface segregation of La and Sr for the LSM100 and LSM105 samples. For the LSM95 sample, the Sr surface segregation is accelerated by the Cr deposition. $SrMn_3O_{6-x}$ is identified for LSM95 and $Cr_{1.5}Mn_{1.5}O_4$ is identified for both LSM95 and LSM100. Cr deposition decreases with increasing distance from the AISI 441 interconnect but increases again at the YSZ/LSM interface. The YSZ/LSM95 interface shows strong bonding; the XPS analysis shows a higher Sr concentration and Cr deposition. The YSZ/LSM105 interface shows poor bonding; the XPS analysis shows a higher La concentration and less Cr deposition. The fundamental mechanisms for these processes are proposed.

References

1. Minh, N.Q., Ceramic fuel cells. Journal of the American Ceramic Society, 1993. 76(3): p. 563-588.
2. Minh, N.Q., Solid oxide fuel cell technology-features and applications. Solid State Ionics, 2004. 174(1-4): p. 271-277.
3. Badwal, S.P.S. and Foger, K., Solid oxide electrolyte fuel cell review. Ceramics International, 1996. 22(3): p. 257-265.
4. Jensen, S.H., Larsen, P.H., and Mogensen, M., Hydrogen and synthetic fuel production from renewable energy sources. International Journal of Hydrogen Energy, 2007. 32(15): p. 3253-3257.
5. Ni, M., Leung, M.K.H., and Leung, D.Y.C., Technological development of hydrogen production by solid oxide electrolyzer cell (SOEC). International Journal of Hydrogen Energy, 2008. 33(9): p. 2337-2354.
6. Steele, B.C.H., Materials for IT-SOFC stacks 35 years R&D: the inevitability of gradualness? Solid State Ionics, 2000. 134(1-2): p. 3-20.

7. Brett, D.J.L., Atkinson, A., Brandon, N.P., and Skinner, S.J., Intermediate temperature solid oxide fuel cells. Chemical Society Reviews, 2008. 37(8): p. 1568-1578.
8. Yang, Z.G., Weil, K.S., Paxton, D.M., and Stevenson, J.W., Selection and evaluation of heat-resistant alloys for SOFC interconnect applications. Journal of the Electrochemical Society, 2003. 150(9): p. A1188-A1201.
9. Zhu, W.Z. and Deevi, S.C., Development of interconnect materials for solid oxide fuel cells. Materials Science and Engineering A, 2003. 348(1-2): p. 227-243.
10. Fergus, J.W., Metallic interconnects for solid oxide fuel cells. Materials Science and Engineering a-Structural Materials Properties Microstructure and Processing, 2005. 397(1-2): p. 271-283.
11. Yang, Z.G., Recent advances in metallic interconnects for solid oxide fuel cells. International Materials Reviews, 2008. 53(1): p. 39-54.
12. Wu, J.W. and Liu, X.B., Recent development of SOFC metallic interconnect. Journal of Materials Science & Technology, 2010. 26(4): p. 293-305.
13. Fergus, J.W., Effect of cathode and electrolyte transport properties on chromium poisoning in solid oxide fuel cells. International Journal of Hydrogen Energy, 2007. 32(16): p. 3664-3671.
14. Taniguchi, S., Kadowaki, M., Kawamura, H., Yasuo, T., Akiyama, Y., Miyake, Y., and Saitoh, T., Degradation phenomena in the cathode of a solid oxide fuel cell with an alloy separator. Journal of Power Sources, 1995. 55(1): p. 73-79.
15. Badwal, S.P.S., Deller, R., Foger, K., Ramprakash, Y., and Zhang, J.P., Interaction between chromia forming alloy interconnects and air electrode of solid oxide fuel cells. Solid State Ionics, 1997. 99(3-4): p. 297-310.
16. O'Brien, J.E., Stoots, C.M., Herring, J.S., and Hartvigsen, J.J., Performance of planar high-temperature electrolysis stacks for hydrogen production from nuclear energy. Nuclear Technology, 2007. 158(2): p. 118-131.
17. Mawdsley, J.R., Carter, J.D., Kropf, A.J., Yildiz, B., and Maroni, V.A., Post-test evaluation of oxygen electrodes from solid oxide electrolysis stacks. International Journal of Hydrogen Energy, 2009. 34(9): p. 4198-4207.

18. Hilpert, K., Das, D., Miller, M., Peck, D.H., and Weiss, R., Chromium vapor species over solid oxide fuel cell interconnect materials and their potential for degradation processes. Journal of the Electrochemical Society, 1996. 143(11): p. 3642-3647.
19. Opila, E.J., Myers, D.L., Jacobson, N.S., Nielsen, I.M.B., Johnson, D.F., Olminsky, J.K., and Allendorf, M.D., Theoretical and experimental investigation of the thermochemistry of CrO2(OH)(2)(g). Journal of Physical Chemistry A, 2007. 111(10): p. 1971-1980.
20. Zhen, Y.D., Jiang, S.P., Zhang, S., and Tan, V., Interaction between metallic interconnect and constituent oxides of (La, Sr)MnO_3 coating of solid oxide fuel cells. Journal of the European Ceramic Society, 2006. 26(15): p. 3253-3264.
21. Bentzen, J.J., Hogh, J.V.T., Barfod, R., and Hagen, A., Chromium poisoning of LSM/YSZ and LSCF/CGO composite cathodes. Fuel Cells, 2009. 9(6): p. 823-832.
22. Konysheva, E., Laatsch, J., Wessel, E., Tietz, F., Christiansen, N., Singheiser, L., and Hilpert, K., Influence of different perovskite interlayers on the electrical conductivity between $La_{0.65}Sr_{0.3}MnO_3$ and Fe/Cr-based steels. Solid State Ionics, 2006. 177(9-10): p. 923-930.
23. Jiang, S.P., Zhang, J.P., Apateanu, L., and Foger, K., Deposition of chromium species at Sr-doped $LaMnO_3$ electrodes in solid oxide fuel cells I. Mechanism and kinetics. Journal of the Electrochemical Society, 2000. 147(11): p. 4013-4022.
24. Jiang, S.P., Zhang, J.P., and Zheng, X.G., A comparative investigation of chromium deposition at air electrodes of solid oxide fuel cells. Journal of the European Ceramic Society, 2002. 22(3): p. 361-373.
25. Konysheva, E., Mertens, J., Penkalla, H., Singheiser, L., and Hilpert, K., Chromium poisoning of the porous composite cathode effect of cathode thickness and current density. Journal of the Electrochemical Society, 2007. 154(12): p. B1252-B1264.
26. Matsuzaki, Y. and Yasuda, I., Dependence of SOFC cathode degradation by chromium-containing alloy on compositions of electrodes and electrolytes. Journal of the Electrochemical Society, 2001. 148(2): p. A126-A131.
27. Komatsu, T., Chiba, R., Arai, H., and Sato, K., Chemical compatibility and electrochemical property of intermediate-temperature SOFC cathodes under Cr poisoning condition. Journal of Power Sources, 2008. 176(1): p. 132-137.

28. Liu, D.J., Almer, J., and Cruse, T., Characterization of Cr poisoning in a solid oxide fuel cell cathode using a high energy X-ray microbeam. Journal of the Electrochemical Society, 2010. 157(5): p. B744-B750.
29. Hammouche, A., Siebert, E., and Hammou, A., Crystallographic, thermal and electrochemical properties of the system $La_{1-x}Sr_xMnO_3$ for high temperature solid electrolyte fuel cells. Materials Research Bulletin, 1989. 24(3): p. 367-380.
30. Jin, T. and Lu, K., Chemical compatibility between Sr-doped lanthanum manganite air electrode and AISI 441 interconnect. International Journal of Hydrogen Energy, 2011. 36(7): p. 4440-4448.
31. la O, G.J., Savinell, R.F., and Shao-Horn, Y., Activity enhancement of dense strontium-doped lanthanum manganite thin films under cathodic polarization: A combined AES and XPS study. Journal of the Electrochemical Society, 2009. 156(6): p. B771-B781.
32. Sharma, V.I. and Yildiz, B., Degradation mechanism in $La_{0.8}Sr_{0.2}CoO_3$ as contact Layer on the solid oxide electrolysis cell anode. Journal of the Electrochemical Society, 2010. 157(3): p. B441-B448.
33. Abraham, F.F. and Brundle, C.R., Surface segregation in binary solid-solutions - A theoretical and experimental perspective. Journal of Vacuum Science & Technology, 1981. 18(2): p. 506-519.
34. Caillol, N., Pijolat, M., and Siebert, E., Investigation of chemisorbed oxygen, surface segregation and effect of post-treatments on $La_{0.8}Sr_{0.2}MnO_3$ powder and screen-printed layers for solid oxide fuel cell cathodes. Applied Surface Science, 2007. 253(10): p. 4641-4648.
35. Decorse, P., Caboche, G., and Dufour, L.-C., A comparative study of the surface and bulk properties of lanthanum-strontium-manganese oxides $La_{1-x}Sr_xMnO_{3\pm\delta}$ as a function of Sr-content, oxygen potential and temperature. Solid State Ionics, 1999. 117(1-2): p. 161-169.
36. Mannella, N., Rosenhahn, A., Nambu, A., Sell, B.C., Mun, B.S., Yang, S.H., Marchesini, S., Watanabe, M., Ibrahim, K., Ritchey, S.B., Tomioka, Y., and Fadley, C.S., Surface characterization of colossal magnetoresistive manganites $La_{1-x}Sr_xMnO_3$ using photoelectron spectroscopy. Journal of Electron Spectroscopy and Related Phenomena, 2006. 153(1-2): p. 37-57.

37. Dulli, H., Dowben, P.A., Liou, S.H., and Plummer, E.W., Surface segregation and restructuring of colossal-magnetoresistant manganese perovskites $La_{0.65}Sr_{0.35}MnO_3$. Physical Review B, 2000. 62(22): p. 14629-14632.
38. Sun, C.W. and Stimming, U., Recent anode advances in solid oxide fuel cells. Journal of Power Sources, 2007. 171(2): p. 247-260.
39. Yamamoto, O., Solid oxide fuel cells: fundamental aspects and prospects. Electrochimica Acta, 2000. 45(15-16): p. 2423-2435.
40. Liu, Y.L., Hagen, A., Barfod, R., Chen, M., Wang, H.J., Poulsen, F.W., and Hendriksen, P.V., Microstructural studies on degradation of interface between LSM-YSZ cathode and YSZ electrolyte in SOFCs. Solid State Ionics, 2009. 180(23-25): p. 1298-1304.
41. Mitterdorfer, A. and Gauckler, L.J., La_2Zr_2O7 formation and oxygen reduction kinetics of the $La_{0.85}Sr_{0.1}5Mn_yO_3$, O_2(g)/YSZ system. Solid State Ionics, 1998. 111(3-4): p. 185-218.
42. Kumigashira, H., Horiba, K., Ohguchi, H., Ono, K., Oshima, M., Nakagawa, N., Lippmaa, M., Kawasaki, M., and Koinuma, H., In situ photoemission characterization of terminating-layer-controlled La0.6Sr0.4MnO3 thin films. Applied Physics Letters, 2003. 82(20): p. 3430-3432.

Chapter 5

Chromium Deposition and Interfacial Interactions of an Electrolyte-Air Electrode-Interconnect Tri-layer for Solid Oxide Fuel Cells

Abstract

In solid oxide fuel cell operation, electrical current plays an important role in the air electrode interaction with electrolyte and interconnect and long-term cell performance. In this study, $(La_{0.8}Sr_{0.2})_xMnO_3$ (LSM) air electrodes with different stoichiometry (x = 0.95, 1, and 1.05) are fabricated on the surface of yttria stabilized zirconia (YSZ) and then sandwiched with AISI 441 stainless steel interconnect. The simulated half cells are thermally treated at 800°C for 500 h under a 200 $mA \cdot cm^{-2}$ current density in dry air. YSZ/LSM interfacial interaction and the reaction of volatile chromium species on the LSM surface are characterized. Different LSM stoichiometry leads to different interfacial reactions and Cr deposition amounts. Mn is a critical species for the Cr deposition under polarization. Excessive Mn in LSM lessens the formation of La-containing phase at the YSZ/LSM interface and accelerates Cr deposition. Deficient Mn in LSM leads to extensive interfacial reaction with YSZ, forming more La-containing phase and inhibiting Cr deposition.

5.1. Introduction

Solid oxide fuel cells (SOFCs) are composed of ceramic electrolyte and electrodes, metal interconnect, and glass seals [1-4]. Compared with other kinds of fuel cells, the high operation temperature (generally 600-1000°C) offers SOFCs advantages such as flexibility in different fuel gases including hydrocarbon fuels and much higher tolerance for fuel *impurities* [5-7]. In order to obtain desired electric power output, single cells are often fabricated together to form stacks. Interconnect and sealing materials are employed to join the unit cells and hold the stack together [8-10]. From material choice point of view, lowering the operation temperature of SOFCs is highly desired. At the reduced temperatures (700-900°C), material degradation issues such as coarsening of the porous electrodes, stresses and failures caused by coefficient of thermal

expansion (CTE) mismatches, and sealing problems can be lessened; metallic interconnects become feasible with cost and processability advantages [11-16].

When the Cr-containing alloys, especially the ferritic stainless steels, are employed as the interconnect in the SOFC stacks, Cr poisoning becomes a major degradation issue on the air electrode side. The Cr poisoning is caused by the diffusion of volatile Cr species evaporating from the Cr-containing metallic interconnect and deposition on the air electrode and the air electrode/electrolyte interface, leading to a fast degradation in cell and stack performance [17-22].

The Cr poisoning of SOFCs has been extensively investigated under different cell operating conditions. The Cr deposition is believed to be highly dependent on the polarization. For the most commonly used air electrode and electrolyte materials, strontium-doped lanthanum manganite (LSM) and yttria-stabilized zirconia electrolyte (YSZ), the Cr species accumulate on the LSM/YSZ interface (or described as triple phase boundary (TPB)) under cathodic polarization [23,24]. There is only a very small amount of Cr on the porous LSM air electrode [25]. When the polarization is absent, the Cr species in the TPB area are insignificant. There are considerable disagreements on the mechanism of Cr-containing species interaction with and deposition on the air electrode and electrolyte. On one hand, Konysheva et al. [26] believed that the Cr volatile species deposit by electrochemical reduction on the air electrode (mostly considered to happen in the TPB area). Cr-containing mixed oxide forms from the interaction with the air electrode and is driven by thermodynamics without an influence from the electrical potentials. On the other hand, Jiang et al. [27] proposed that the deposition of Cr is not dominated by electrochemical reduction of the high valence Cr volatile species; the driving force for the Cr deposition is related to the Mn species, and the Mn species are affected by the polarization, which explains the influence of the polarization on the Cr poisoning.

In light of the above disagreement, the stoichiometry of the LSM becomes an important factor to be evaluated for the Cr species interaction with other cell components. $(La_{0.8}Sr_{0.2})_xMnO_3$ is classified as an ABO_3 perovskite compound, where La and Sr are in the A sites and Mn is in the B sites. The A/B cation ratio has critical effects on the phase stability [28]. In the case of $x > 1$, the excessive La can lead to the formation of $La_2Zr_2O_7$ with YSZ, which is a non-conductive phase at the electrolyte/air electrode interface and undesirable for the SOFC

operation [29]. Because of this, most cells use Mn excessive (x <1) LSM as the air electrode. However, the effect of LSM stoichiomery on the Cr deposition has not been studied.

In order to clarify the mechanism of Cr deposition and related interactions in the TPB area and on the LSM surface, more detailed investigation on the interaction of electrolyte/air electrode/interconnect tri-layer is needed. Although Cr_2O_3 and $(Mn,Cr)_3O_4$ have been identified in the Cr deposition, the effect of Mn is not totally known [24,30]. Furthermore, the surface segregation of Sr and La from LSM affects the electrochemical oxygen reduction reaction in SOFCs [31,32]. Surface chemistry of the TPB area is also a poorly understood factor for the Cr deposition.

In this work, LSM samples with different stoichiometries $(La_{0.8}Sr_{0.2})_xMnO_3$ (x=0.95, 1, 1.05 notated as LSM95, LSM100, and LSM105) were made into air electrode on YSZ electrolyte. YSZ/LSM bi-layer samples were assembled with the AISI 441 alloy to simulate the air electrode side of SOFCs. A cathodic polarization current density of 200 $mA \cdot cm^{-2}$ was applied on the tri-layer samples. The samples were thermally treated in dry air at 800°C for 500 h. Microstructure examination, surface analysis, and phase analysis were carried out across the LSM porous layer and at the LSM/YSZ interface. The mechanism of the Cr deposition was discussed.

5.2. Experimental Procedures

5.2.1. Sample Preparation

LSM samples with different stoichiometries (LSM95, LSM100, and LSM105) were prepared with a conventional solid state reaction method and screen printed on the YSZ substrate (8 mol% yttria stabilized zirconia, 20 mm diameter, 250–290 μm thickness, NexTech Materials, Lewis Center, OH). AISI 441 alloy (ATI Allegheny Ludlum Corporation, Brackenridge, PA) was used as the interconnect material. A detailed experimental description can be found in the previous papers [33,34].

After the sintering of the YSZ/LSM bi-layer, the AISI 441 alloy was placed on the LSM electrode as the interconnect. A potentiostat (VersaSTAT 3, Princeton Applied Research, Oak Ridge, TN) was used to supply a current density of 200 $mA \cdot cm^{-2}$. Platinum meshes were placed in-between the LSM porous layer and the AISI 441 interconnect to optimize the current distribution. On the YSZ side, an electrical wire was attached through a Pd paste. The tri-layer

setup was shown in Fig. 5-1. The YSZ/LSM/AISI 441 tri-layer samples including a control group of LSM samples without any electric current were thermally treated in a tube furnace (1730-20 HT Furnace, CM Furnace Inc. Bloomfield, NJ). The thermal treatment was carried out in dry air (compressed air) at 800°C for 500 h. In order to observe the TPB regions, the LSM porous layers were peeled off to show the YSZ/LSM interface for the 500 h thermally treated samples.

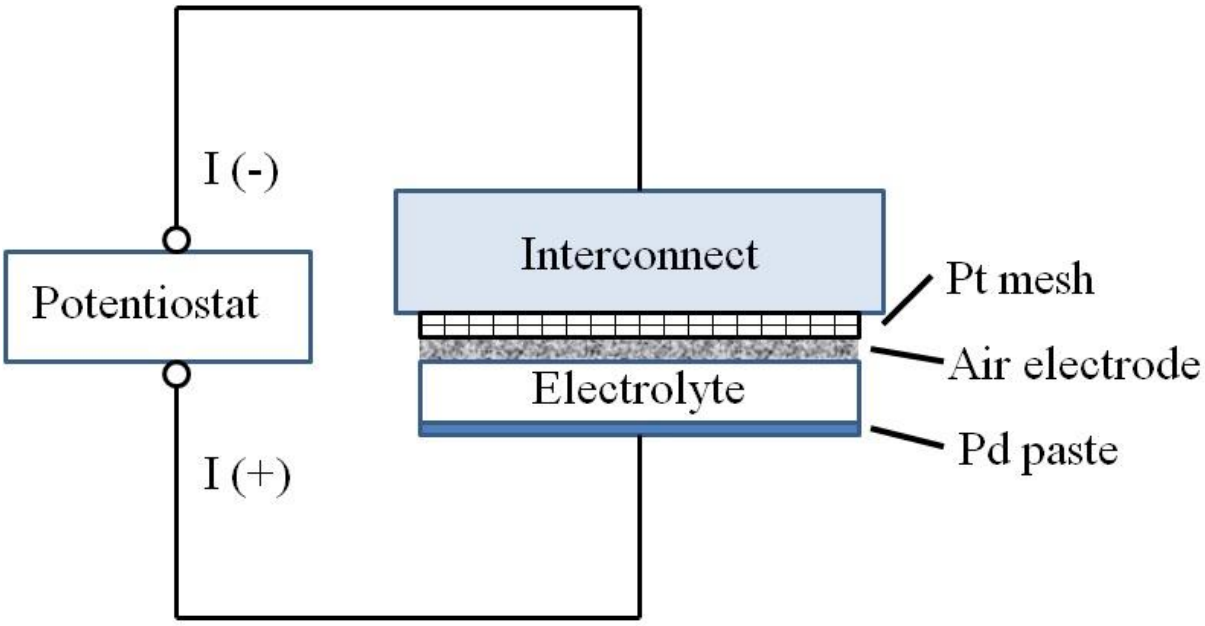

Fig. 5-1. Schematic representation of the tri-layer sample testing setup with an electric current applied.

5.2.2. Characterization

After the thermal treatment, the tri-layer samples were fractured to examine the cross-sections. Some samples were mounted into epoxy, and then cut and ground to detect different positions (distances away from the AISI 441 layer) in the porous LSM air electrode. The detailed experimental description can be found in the previous paper [33]. To study the microstructure, scanning electron images (SEM, Quanta 600 FEG, FEI, Hillsboro, OR) were obtained. An energy dispersive spectroscopy (EDS) module (Bruker AXS, MiKroanalysis Gmbh, Berlin, Germany) attached to the SEM was used for composition analysis. Surface analysis was also

carried out in an X-ray photoelectron spectrometer (XPS, PHI Quantera SXM-03, Physical Electronics Inc., Chanhassen, MN). An Al Kα radiation (1486.6 eV) was used as the X-ray source. In order to identify the phases, X-ray diffraction (XRD) studies were carried out in a Geigerflex D/max-B X-ray diffractometer (Rigaku Corporation,Tokyo, Japan). The step size was 0.01° s^{-1} with Cu Kα radiation (λ= 1.5406 Å).

5.3. Results

5.3.1. Microstructure

Fig. 5-2 shows the microstructures of the LSM layer before and after the thermal treatment. LSM95 shows more bonding and sintering between the grains at the as-sintered state (Fig. 5-2(a)).The pores form a 3D network structure with round grain shapes and corners. The grain size is about 1–3 μm. After the thermal treatment without an electric current (Fig. 5-2(b)), small grains grow larger to about 3 μm and the size distribution is narrower. More extensive bonding between the grains is observed and the porosity is lower. After the thermal treatment with the electric current (Fig. 5-2(c)), however, the grains actually become smaller and the decreased bonding between the grains is visible. For the LSM100 sample, before the thermal treatment without an electric current (Fig. 5-2(d)), the grains have a wide size distribution, ranging from 1–4 μm with irregular shapes and sharp corners/edges. Many small grains attach to the large LSM grain surfaces. The grain bonding is lower than the LSM95 sample. After the thermal treatment without an electric current (Fig. 5-2(e)), the grains grow larger and more roundish. However, the bonding between the grains shows no substantial change. After the thermal treatment with the electric current (Fig. 5-2(f)), grain growth and bonding increase are both observed. However, the grains show sharper corners and edges than those in the sample without an electric current. For the LSM105 sample before the thermal treatment (Fig. 5-2(g)), the grain size is much smaller with a narrower size distribution (0.5–2 μm). After the thermal treatment without an electric current (Fig. 5-2(h)), the grains grow larger and the bonding between the grains is more extensive. After the thermal treatment with the electric current (Fig. 5-2(i)), the grains maintain their small sizes. However, the large and small grains are slightly better bonded and the porosity is lower.

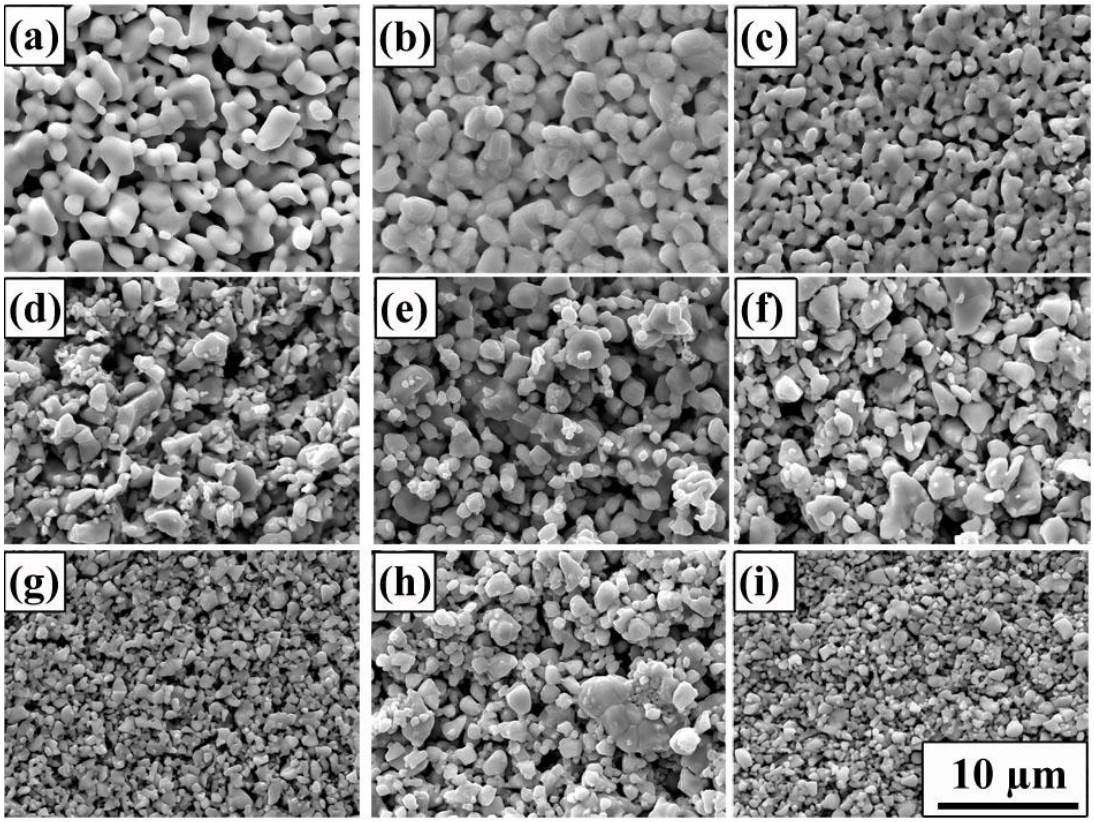

Fig. 5-2. SEM images of the LSM porous layer after the thermal treatment at 800°C for 500 h. The surface has been in contact with the AISI 441 alloy for the samples without an electric current, and with a Pt mesh (close to the AISI 441 alloy) for the samples with the electric current. (a)–(c), LSM95 as-sintered, thermally treated without and with an electric current; (d)–(f) LSM100 as-sintered, thermally treated without and with an electric current; and (g)–(i) LSM105 as-sintered, thermally treated without and with an electric current.

The above microstructure results show that for the three samples with different stoichiometries, the grain size and shape are different to start with. As the Mn content decreases in LSM, from LSM95 (Fig. 5-2(a)), to LSM100 (Fig. 5-2(d)), to LSM105 (Fig. 5-2(g)), the LSM grain sizes decrease and the angular shape is increasingly maintained. For all the three samples, grain growth during the thermal treatment without the electric current is obvious. The grain shapes all become roundish. However, the difference between LSM100 and LSM105 is small. This means that the thermal treatment without the current causes more grain growth especially for LSM105. After the thermal treatment with the current, surprisingly, the LSM95 shows grain size decrease (grain break-down). The LSM100 sample shows grain growth. The LSM105

sample shows no obvious grain size change. The phenomenon that cathodic polarization influences grain growth and bonding has been investigated by Wang and Jiang et al. [35,36]. They suggested that the Mn ions in the lattice and interstitial sites are electrochemically reduced under cathodic polarization, forming concomitant oxygen vacancies. The changes of LSM surface chemistry affect the cation diffusion rate during the thermal treatment. In this work, it shows that the Mn reduction/oxygen vacancy creation has a larger effect on the LSM95 sample (Mn excessive), even to the point of breaking down the LSM grains, possibly by oxygen vacancy generation. On the other hand, low Mn content (LSM105) has a desirable effect of resisting grain growth possibly because of the resistance of vacancy generation and ion diffusion.

To examine the YSZ/LSM interface, the LSM layer is peeled off from the YSZ surface after the thermal treatment where some bonding spots are marked by arrows (Fig. 5-3). The bright particles with irregular shapes are the LSM grains left on the YSZ electrolyte surface. For the LSM95 samples before the thermal treatment (Fig. 5-3(a)), extensive bonding spots about 1–2 μm in size are formed with the YSZ layer after the sintering. After the thermal treatment without an electric current (Fig. 5-3(b)), the bonding spots show that the LSM grains are embedded deeper in the YSZ substrate and the YSZ surface is cleaner. After the thermal treatment with the electric current (Fig. 5-3(c)), large areas of the YSZ surface are coved by small grains of 20–40 nm in size. The crystals show distinct facets with cubic shapes. The EDS spot analysis shows 1.2 ± 0.3 at% Cr (average of three measurements), which is a considerable amount of Cr deposition compared with the previous results, where the surface Cr deposition is hard to detect by EDS [34]. This means LSM reacts extensively with Cr-containing species under the electric current. For the LSM100 sample before the thermal treatment (Fig. 5-3(d)), the bonding spot sizes are less than 0.5 μm and shallow. The surface has some rough texture. After the thermal treatment without an electric current (Fig. 5-3(e)), the YSZ surface is also clean and the grain boundaries are visible. The bonding spots are much larger and deeper with sizes about 1 μm. After the thermal treatment with the electric current (Fig. 5-3(f)), the YSZ surface is still visible. The LSM bonding spots are larger than those at the as-sintered state, but smaller than those without the electric current, 1–2 μm in size. Some irregular-shaped deposits are at the peeled off bonding spots, which is likely the new phase formed from the interaction at the YSZ/LSM interface (Fig. 5-3(f)). There are some small particles adjacent to the bonding spots. For the LSM105 sample before the thermal treatment (Fig. 5-3(g)), the microstructure of the

YSZ surface is similar to that of the LSM100 sample, where small and shallow bonding spots are seen. The rough surface texture is visible with some roundish particles present. For the LSM105 sample after the thermal treatment without an electric current (Fig. 5-3(h)), the YSZ surface is clean. The bonding spots are over 1 μm in size. However, the shape of the bonding spots is not as roundish and concave as those of LSM95 and LSM100. After the thermal treatment with the electric current (Fig. 5-3(i)), the interfacial microstructure is similar to that of the LSM100 sample but to a more severe extent. Some irregular-shaped species are present at the bonding spots. Combing Figs. 5-3(f) and 5-3(i), it indicates that interfacial reaction(s) occurs for LSM100 and LSM105 under the electric current, but mainly around the bonding spots.

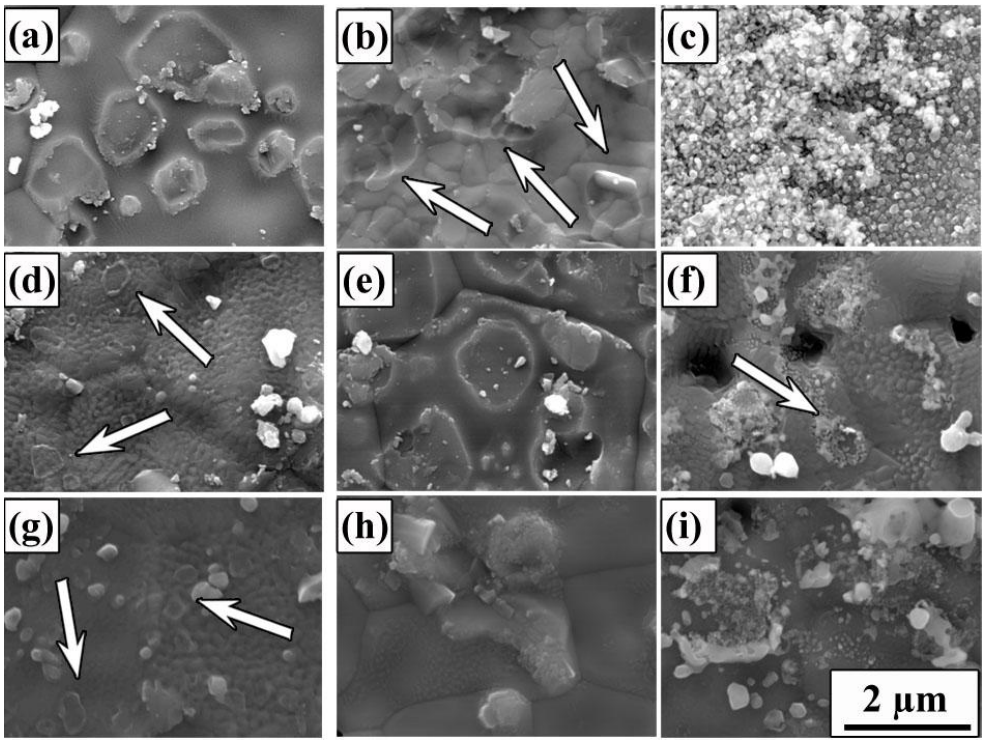

Fig. 5-3. SEM images of the YSZ/LSM interface after the LSM porous layer removal before and after the thermal treatment: (a)–(c) LSM95 as-sintered, thermally treated without and with an electric current; (d)–(f) LSM100 as-sintered, thermally treated without and with an electric current; and (g)–(i) LSM105 as-sintered, thermally treated without and with an electric current. The arrows point to the bonding spots.

Before the thermal treatment, the LSM samples with different stoichiometry show different interfacial microstructures and indicate that LSM95 has better bonding with the YSZ substrate than the LSM100 and LSM105 samples. For the LSM95 sample, extensive Mn

facilitates the bonding with YSZ. For LSM100 and LSM105, the rough surfaces and particle-like species mean that new compounds likely form. After the thermal treatment without an electric current, the bonding between the YSZ substrate and the LSM increases for all the samples. LSM95 (the composition with excessive Mn) leads to the strongest bonding, while the LSM105 sample seems to have the weakest bonding. The bonding spots for the latter are not concave-like. After the thermal treatment with an electric current, the microstructures show that the interfacial interaction is more extensive. For LSM95, small cubic crystals cover the YSZ surface, which is deduced as a Cr-containing phase based on the EDS analysis. For LSM100, the electric current leads to the formation of irregular-shaped species at the bonding spots. For LSM105, the bonding spots are larger but the new deposit is also more extensive. The newly formed phase at the interface for the LSM100 and LSM105 samples is believed to be a La-containing phase [29]. This will be discussed more in the following sections.

5.3.2. Elemental Analysis and Distribution

After the thermal treatment with a 200 $mA \cdot cm^{-2}$ current density, the AISI 441 interconnects were removed. The YSZ/LSM bi-layer samples were mounted into epoxy, and then cut and ground to examine different positions across the LSM layer by XPS analysis. Along the porous LSM air electrode layer (~30 μm thick), five different locations (labeled as YSZ/LSM, LSM Left, LSM Middle, LSM Right, and LSM/AISI 441 from the YSZ to the AISI 441) are studied (Fig. 5-4). The thickness of each layer is controlled by a micrometer at ~8 μm [33]. The results are presented by atomic percent and normalized to 100% by considering La, Sr, Mn, and Cr only in order to avoid errors by oxygen from the mounting epoxy. The elemental concentrations are averaged by three measurements at each location and the standard deviation of each examination point is shown by an error bar.

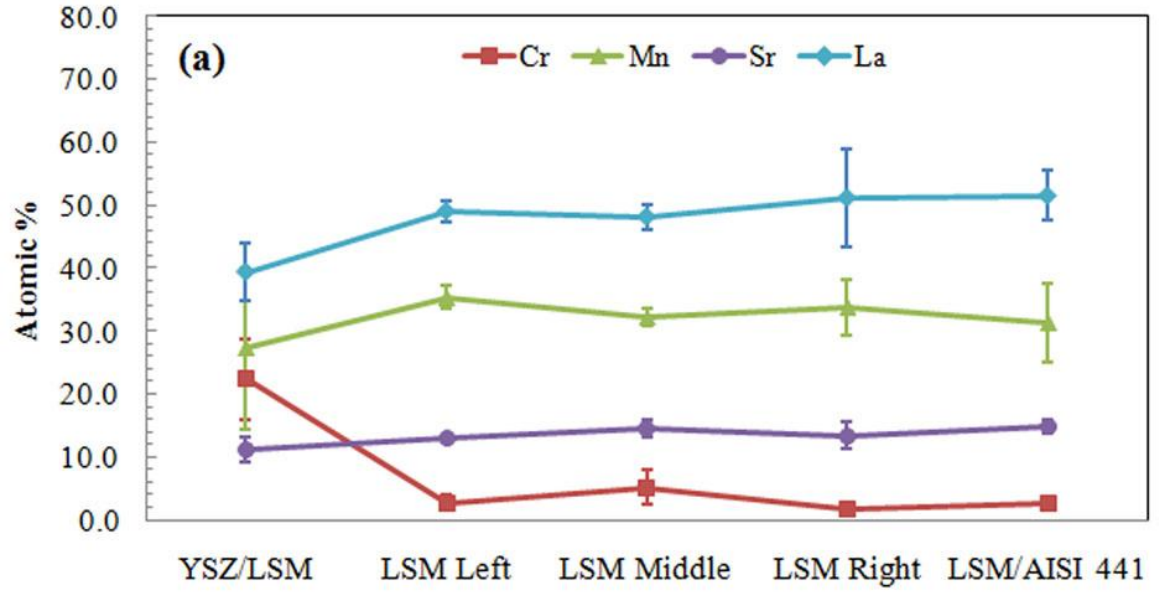
(a)
Cr
Mn
Sr
La
Atomic %
80.0
70.0
60.0
50.0
40.0
30.0
20.0
10.0
0.0
YSZ/LSM
LSM Left
LSM Middle
LSM Right
LSM/AISI 441

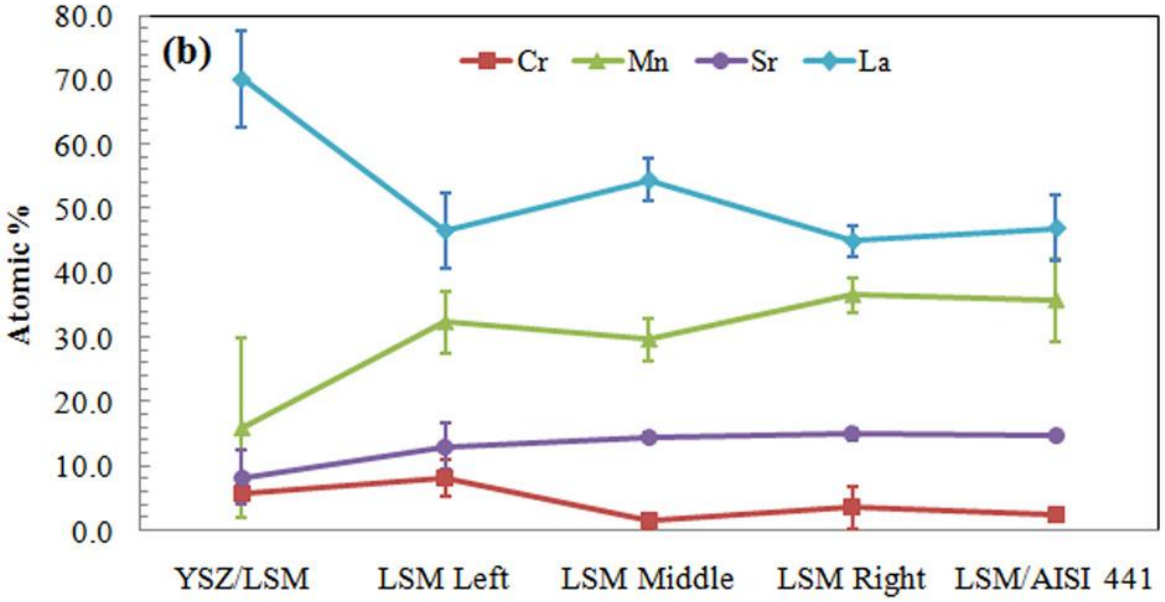
(b)
Cr
Mn
Sr
La
Atomic %
80.0
70.0
60.0
50.0
40.0
30.0
20.0
10.0
0.0
YSZ/LSM
LSM Left
LSM Middle
LSM Right
LSM/AISI 441

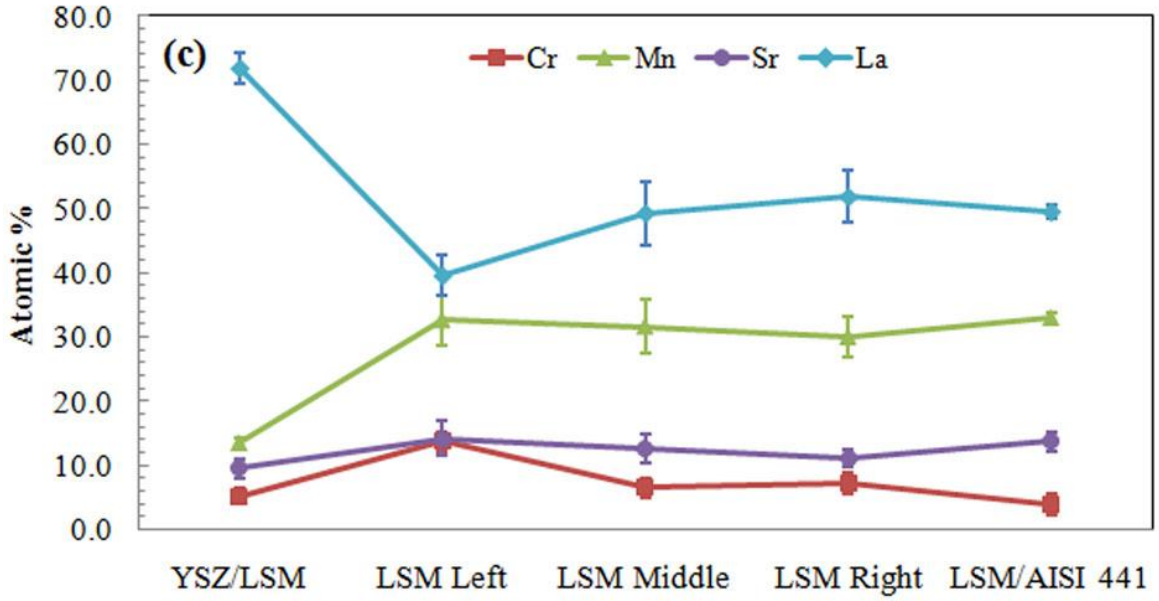

Fig. 5-4. Compositions of the LSM layer after the thermal treatment with a 200 $mA \cdot cm^{-2}$ current density: (a) LSM95, (b) LSM100, and (c) LSM105.

In Fig. 5-4, across the LSM layer, the compositions of the LSM samples (the major elements La, Sr, and Mn) are mostly stable without significant changes except for the locations close to the YSZ/LSM interface. The original compositions of the LSM samples with different stoichiometry are 39.0% La, 9.7% Sr, and 51.3% Mn for LSM95; 40.0% La, 10.0% Sr, and 50.0% Mn for LSM100; and 41.0% La, 10.2% Sr, and 50.8% Mn for LSM105. After the thermal treatment with the current, at the right side of the LSM porous layer (from LSM Middle to LSM/AISI 441 interface), the compositions are 48.1–51.4% La, 13.4–14.8% Sr, and 31.3–33.8% Mn for LSM95; 44.9–54.4% La, 14.5–14.9% Sr, and 29.7–36.6% Mn for LSM100; and 49.3–51.8% La, 11.1–13.6% Sr, and 30.0–32.9% Mn for LSM105. Higher La and Sr contents and lower Mn content are observed compared with the designed compositions. The La and Sr surface segregation of LSM is a well-known phenomenon for the as-sintered LSM and during the thermal treatment, which is caused by broken bonds and strain energy driven composition re-distribution [37,38]. Furthermore, after the thermal treatment with the current, the surface compositions of La, Sr, and Mn for all the three samples do not show significant differences (except for the locations close to the YSZ/LSM interface). The stoichiomerty influences are insignificant on the surface segregation of LSM.

Remarkable changes happen at the YSZ/LSM interface and the LSM Left location. At the the YSZ/LSM interface, Sr shows a slight drop for all the air electrode samples, which is likely because the Sr atomic percent is affected by the enrichment of other elements such as La and Cr. Sr itself does not react with other species for all the samples as to be discussed later. In addition, Mn shows a consistent depletion at the YSZ/LSM interface. From the LSM Left to the YSZ/LSM interface, Mn decreases to 27.2 ± 12.7%, 15.9 ± 14.0%, and 13.4 ± 0.9% respectively for LSM95, LSM100, and LSM105. La shows a surprisingly different trend for these three samples. For LSM95, La decreases to 39.3 ± 4.6%. For LSM100 and LSM105, instead, La increases rapidly; the contents are 70.1 ± 7.5% and 72.0 ± 2.4%, respectively. This means that for LSM95, La depletes slightly and Mn shows only a minor decrease. For LSM100 and LSM105, La enriches and Mn decreases significantly.

The concentration distribution of Cr indicates the gas diffusion and depostion process of the volatile Cr species, which are vaporized from the oxide scale of the AISI 441 surface [39,40]. For the LSM95 sample (Fig. 5-4(a)), the Cr deposition amounts are low across the LSM layer, 1.5–5.2%. At the YSZ/LSM interface, the Cr content suddenly increases to 22.3 ± 6.4%, which means Cr deposition is most significant at the YSZ/LSM interface. At the interface, Mn depletes but still shows a higher amount compared with those of LSM100 and LSM105. For the LSM100 sample, at the LSM Middle, LSM Right, and LSM/AISI 441 interface, the Cr contents are also low, from 1.4% to 3.6%. At LSM Left, the Cr content increases to 8.1 ± 2.9%. At the YSZ/LSM interface, the Cr content is 5.7 ± 1.3%. The Cr deposition mostly happens at the LSM location close to the YSZ/LSM interface. At the YSZ/LSM interface, the La content is as high as 70.1 ± 7.5% and seems to inhibit Cr deposition. For the LSM105 sample, the Cr contents from the LSM/AISI 441 interface to LSM Middle are 3.9–7.1%, higher than those of LSM95 and LSM100. Similar to the LSM100 sample, the Cr content increases to 13.6 ± 1.5% at LSM Left, and then decreases to 5.2 ± 1.2% at the YSZ/LSM interface. The La content, on the other hand, is 72.0 ± 2.4% at the YSZ/LSM interface. This result means that even though Cr has a tendency to accumulate at the YSZ/LSM interface, the La-containing phase at the interface lessens the Cr deposition. Overall, Mn depletion is beneficial for La enrichment, which in turns hinders Cr deposition at the YSZ/LSM interface.

5.3.3. Phase Analysis

XRD patterns at the YSZ/LSM interface show phase results (Fig. 5-5). For all the three samples thermally treated with the electric current, the YSZ phase is dominant after the LSM porous layers are peeled off. The new phases formed at the interface have very small amounts or even undetectable by XRD. For the LSM95 sample, the small cubic shape particles are likely Cr and Mn enriched phase based on the EDS and XPS results. However, the major peak of the possible phase $Mn_{1.5}Cr_{1.5}O_4$ is at $2\theta = 35.2°$, which overlaps with one of the YSZ peaks [41]. As a result, the Cr and Mn enriched phase cannot be unambiguously determined. Additional evidence is needed to confirm the phase of the small particles at the YSZ/LSM interface for LSM95. However, no techniques are available so far for phase analysis without disturbing the interface while detecting the low phase amount.

The XRD patterns show that La_2O_3 forms for all the samples at the YSZ/LSM interface. The low XRD peak means the La_2O_3 amount is low. For the LSM100 and LSM105 sample, the La-containing phases at the YSZ/LSM interface are consistent with the SEM and XPS results. This result means that the La enrichment at the YSZ surface does not lead to a large amount of La_2O_3 phase. The La_2O_3 peak is the highest for LSM105. On the other hand, it also shows that XRD is not a sensitive technique for low content phase analysis.

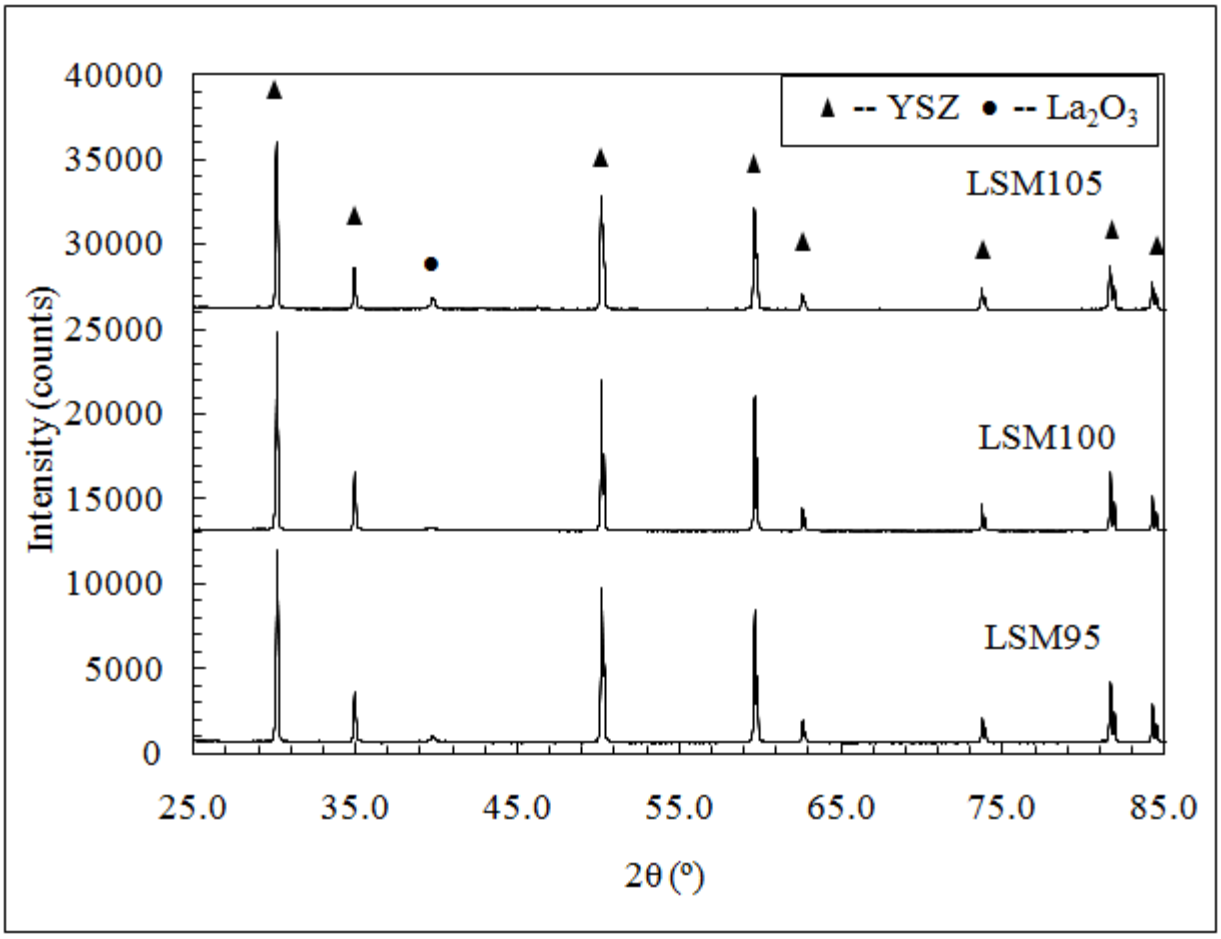

Fig. 5-5. XRD patterns of the YSZ/LSM interface after the thermal treatment at 800°C for 500 h under a 200 $mA \cdot cm^{-2}$ current density. The scan was on the YSZ surface after removing the LSM porous layer.

5.4. Discussion

Stoichiometry effects on the YSZ/LSM interfacial interaction have been studied before. Mitterdorfer et al. [29] believed that the formation of La_2O_3 is thermodynamically driven by the diffusion of La^{3+}. In this study, the excessive La in LSM105 leads to extensive La enrichment at the YSZ/LSM interface. The XPS surface analysis and the phase analysis also indicate that even for the LSM100 sample, La enriches at the interface and La_2O_3 forms, which means that in the case of x=1, this interaction is still substantial. When Mn is excessive, as in the case of LSM95, La_2O_3 formation can be suppressed. Based on the XRD result, the amount of La_2O_3 formation is qualitatively proportional to the La content in the LSM samples. The Cr deposition at the

YSZ/LSM interface is in inverse relationship to the La content. As La content increases, Cr deposition substantially decreases. Higher La content at the interface also leads to more significant Mn depletion at the YSZ/LSM interface.

Compared with the interfacial interaction between YSZ and LSM, which is mostly a thermodynamic process, Cr deposition at the interface is strongly accelerated by the electric current. The same tri-layer samples were investigated before with the same thermal treatment without the current applied [33]. At the YSZ/LSM interface, the Cr amounts were 12.7 ± 2.3% for LSM95, 9.0 ± 2.5% for LSM100, and 2.4 ± 2.2% for LSM 105 respectively. Cr deposition decreases from LSM95 to LSM105. With the electric current, the Cr amounts at the YSZ/LSM interface are 22.3 ± 6.4%, 5.7 ± 1.3%, and 5.2 ± 1.2% for LSM95, LSM100, and LSM105, respectively. The enrichment of Cr is most significant while the Mn depletion is least significant for the LSM95 sample. The microstructure shows small particles on the YSZ surface (Fig. 5-3(c)). This means that the new phase is related to the high amount of Cr deposition and excessive Mn, likely $Mn_{1.5}Cr_{1.5}O_4$. On the other hand, for the LSM100 and LSM105 samples, the electric current does not lead to more Cr deposition at the interface while the La content is high. This means that the Cr deposition at the YSZ/LSM interface is determined by two factors: i) enough Mn from the LSM to provide the sites for the deposition; ii) cathodic polarization modifying the electrical state of the surface Mn cations and causing more oxygen vacancies to accelerate the interaction [42,43]. Combining with Fig. 5-2(c) and 5-2(i), this also mean LSM grain size break-down for the Mn excessive condition and inhibited grain growth for the La excessive condition.

Different stoichiometries lead to different interactions across the LSM layer as well as at the YSZ/LSM interface. In the previous work, without an electric current, Cr shows a decrease from the AISI 441 side to the YSZ side across the 25–30 μm thick LSM layer, a typical result of the diffusion process [33]. For the LSM95 sample under polarization, the Cr deposition amount on the AISI 441 side is lower, because the more rapid reaction at the YSZ/LSM interface absorbs more volatile Cr species and changes the concentration gradient across the porous LSM layer. For the LSM100 sample, the Cr distribution shows a lower Cr content on the right side (far away from the YSZ/LSM interface, from LSM Middle to LSM/AISI 441 interface); and an increase at LSM Left. The Cr deposition at the YSZ/LSM interface for LSM100 is 5.7 ± 1.3%, much less than that for LSM95 at 22.3 ± 6.4%. For the LSM105 sample, the Cr deposition amount on the right side (LSM Middle to LSM/AISI 441 interface) is higher than that for LSM95 and LSM100,

which is comparable with the thermally treated samples with no electric current [33]. The Cr deposition increases at LSM Left and drops to 5.2 ± 1.2% at the YSZ/LSM interface. The results show that under an electric current, excessive Mn is still the key factor to cause more Cr deposition, similar to the situation without an electric current; and the polarization increases the Cr deposition rate.

The significant dependence of the Cr deposition on the Mn content under the same polarization condition demonstrates that the electrochemical reduction reaction of Cr volatile species is not as simple as some researchers proposed [44,45]:

$$2CrO_3(g) + 6e^- \rightarrow Cr_2O_3(s) + 3O^{2-}\text{ (electrolyte)} \quad (5\text{-}1)$$

The Cr deposition is associated with Mn^{2+} at the YSZ surface [46]. Although the Mn depletion at the LSM surface happens in all the samples with different stoichiomteries, the excessive Mn composition (LSM95) can still lead to some Mn ions diffusing to the YSZ/LSM interface. Under the cathodic polarization, the Mn ions are considered as partially reduced to Mn^{2+} [43]. In this process, the Mn^{2+} content at the YSZ surface causes the observed Cr-containing crystals at the YSZ surface (Fig. 5-3(c)). The reaction is believed to be:

$$3CrO_3(g) + 3Mn^{2+}\text{ (YSZ surface)} + 8e^- \rightarrow 2Cr_{1.5}Mn_{1.5}O_4(s) + O^{2-}\text{ (electrolyte)} \quad (5\text{-}2)$$

5.5. Conclusions

YSZ/LSM/AISI 441 tri-layers are thermally treated at 800°C in dry air for 500 h, and a 200 $mA \cdot cm^{-2}$ current density is applied to simulate SOFC working conditions. The electric current hinders LSM grain growth and bonding across the porous LSM layer. The formation of La_2O_3 at the YSZ/LSM interface is promoted by the electric current for the LSM100 and LSM105 samples. A very low amount of Cr deposits in the porous LSM layer far away from the YSZ/LSM interface. At the YSZ/LSM interface, for LSM100 and LSM105, a small amount of Cr deposits; LSM95 with excessive Mn results in a large amount of Cr deposition and the formation of small cubic shaped Cr/Mn-containing crystals.

References

1. Badwal, S.P.S. and Foger, K., Solid oxide electrolyte fuel cell review. Ceramics International, 1996. 22(3): p. 257-265.

2. Brandon, N.P., Skinner, S., and Steele, B.C.H., Recent advances in materials for fuel cells. Annual Review of Materials Research, 2003. 33: p. 183-213.
3. Minh, N.Q., Solid oxide fuel cell technology-features and applications. Solid State Ionics, 2004. 174(1-4): p. 271-277.
4. Minh, N.Q., Ceramic fuel cells. Journal of the American Ceramic Society, 1993. 76(3): p. 563-588.
5. Gorte, R.J., Kim, H., and Vohs, J.M., Novel SOFC anodes for the direct electrochemical oxidation of hydrocarbon. Journal of Power Sources, 2002. 106(1-2): p. 10-15.
6. McIntosh, S. and Gorte, R.J., Direct hydrocarbon solid oxide fuel cells. Chemical Reviews, 2004. 104(10): p. 4845-4865.
7. Mogensen, M. and Kammer, K., Conversion of hydrocarbons in solid oxide fuel cells. Annual Review of Materials Research, 2003. 33: p. 321-331.
8. Mahapatra, M.K. and Lu, K., Seal glass for solid oxide fuel cells. Journal of Power Sources, 2010. 195(21): p. 7129-7139.
9. Menzler, N.H., Tietz, F., Uhlenbruck, S., Buchkremer, H.P., and Stover, D., Materials and manufacturing technologies for solid oxide fuel cells. Journal of Materials Science, 2010. 45(12): p. 3109-3135.
10. Yamamoto, O., Solid oxide fuel cells: fundamental aspects and prospects. Electrochimica Acta, 2000. 45(15-16): p. 2423-2435.
11. Brett, D.J.L., Atkinson, A., Brandon, N.P., and Skinner, S.J., Intermediate temperature solid oxide fuel cells. Chemical Society Reviews, 2008. 37(8): p. 1568-1578.
12. Weber, A. and Ivers-Tiffee, E., Materials and concepts for solid oxide fuel cells (SOFCs) in stationary and mobile applications. Journal of Power Sources, 2004. 127(1-2): p. 273-283.
13. Wu, J.W. and Liu, X.B., Recent development of SOFC metallic interconnect. Journal of Materials Science & Technology, 2010. 26(4): p. 293-305.
14. Yang, Z.G., Recent advances in metallic interconnects for solid oxide fuel cells. International Materials Reviews, 2008. 53(1): p. 39-54.
15. Zhu, W.Z. and Deevi, S.C., Development of interconnect materials for solid oxide fuel cells. Materials Science and Engineering A, 2003. 348(1-2): p. 227-243.

16. Steele, B.C.H., Materials for IT-SOFC stacks 35 years R&D: the inevitability of gradualness? Solid State Ionics, 2000. 134(1-2): p. 3-20.
17. Fergus, J.W., Effect of cathode and electrolyte transport properties on chromium poisoning in solid oxide fuel cells. International Journal of Hydrogen Energy, 2007. 32(16): p. 3664-3671.
18. Hilpert, K., Das, D., Miller, M., Peck, D.H., and Weiss, R., Chromium vapor species over solid oxide fuel cell interconnect materials and their potential for degradation processes. Journal of the Electrochemical Society, 1996. 143(11): p. 3642-3647.
19. Jiang, S.P., Zhang, J.P., Apateanu, L., and Foger, K., Deposition of chromium species on Sr-doped $LaMnO_3$ cathodes in solid oxide fuel cells. Electrochemistry Communications, 1999. 1(9): p. 394-397.
20. Opila, E.J., Myers, D.L., Jacobson, N.S., Nielsen, I.M.B., Johnson, D.F., Olminsky, J.K., and Allendorf, M.D., Theoretical and experimental investigation of the thermochemistry of $CrO_2(OH)_2(g)$. Journal of Physical Chemistry A, 2007. 111(10): p. 1971-1980.
21. Paulson, S.C. and Birss, V.I., Chromium poisoning of LSM-YSZ SOFC cathodes - I. Detailed study of the distribution of chromium species at a porous, single-phase cathode. Journal of the Electrochemical Society, 2004. 151(11): p. A1961-A1968.
22. Taniguchi, S., Kadowaki, M., Kawamura, H., Yasuo, T., Akiyama, Y., Miyake, Y., and Saitoh, T., Degradation phenomena in the cathode of a solid oxide fuel cell with an alloy separator. Journal of Power Sources, 1995. 55(1): p. 73-79.
23. Matsuzaki, Y. and Yasuda, I., Dependence of SOFC cathode degradation by chromium-containing alloy on compositions of electrodes and electrolytes. Journal of the Electrochemical Society, 2001. 148(2): p. A126-A131.
24. Fujita, K., Ogasawara, K., Matsuzaki, Y., and Sakurai, T., Prevention of SOFC cathode degradation in contact with Cr-containing alloy. Journal of Power Sources, 2004. 131(1-2): p. 261-269.
25. Horita, T., Xiong, Y.P., Yoshinaga, M., Kishimoto, H., Yamaji, K., Brito, M.E., and Yokokawa, H., Determination of dhromium doncentration in solid oxide fuel cell cathodes: $(La,Sr)MnO_3$ and $(La,Sr)FeO_3$. Electrochemical and Solid State Letters, 2009. 12(10): p. B146-B149.

26. Konysheva, E., Mertens, J., Penkalla, H., Singheiser, L., and Hilpert, K., Chromium poisoning of the porous composite cathode effect of cathode thickness and current density. Journal of the Electrochemical Society, 2007. 154(12): p. B1252-B1264.
27. Jiang, S.P., Zhang, S., and Zhen, Y.D., Early interaction between Fe-Cr alloy metallic interconnect and Sr-doped $LaMnO_3$ cathodes of solid oxide fuel cells. Journal of Materials Research, 2005. 20(3): p. 747-758.
28. Jiang, S.P., Development of lanthanum strontium manganite perovskite cathode materials of solid oxide fuel cells: a review. Journal of Materials Science, 2008. 43(21): p. 6799-6833.
29. Mitterdorfer, A. and Gauckler, L.J., La_2Zr_2O7 formation and oxygen reduction kinetics of the $La_{0.85}Sr_{0.1}5Mn_yO_3$, O_2(g)/YSZ system. Solid State Ionics, 1998. 111(3-4): p. 185-218.
30. Liu, D.J., Almer, J., and Cruse, T., Characterization of Cr poisoning in a solid oxide fuel cell cathode using a high energy X-ray microbeam. Journal of the Electrochemical Society, 2010. 157(5): p. B744-B750.
31. Caillol, N., Pijolat, M., and Siebert, E., Investigation of chemisorbed oxygen, surface segregation and effect of post-treatments on $La_{0.8}Sr_{0.2}MnO_3$ powder and screen-printed layers for solid oxide fuel cell cathodes. Applied Surface Science, 2007. 253(10): p. 4641-4648.
32. la O, G.J., Savinell, R.F., and Shao-Horn, Y., Activity enhancement of dense strontium-doped lanthanum manganite thin films under cathodic polarization: A combined AES and XPS study. Journal of the Electrochemical Society, 2009. 156(6): p. B771-B781.
33. Jin, T. and Lu, K., Surface and interface behaviors of $(La_{0.8}Sr_{0.2})_xMnO_3$ air electrode for solid oxide cells. Journal of Power Sources. In Press, Corrected Proof.
34. Jin, T. and Lu, K., Chemical compatibility between Sr-doped lanthanum manganite air electrode and AISI 441 interconnect. International Journal of Hydrogen Energy, 2011. 36(7): p. 4440-4448.
35. Wang, W. and Jiang, S.P., Effect of polarization on the electrode behavior and microstructure of $(La,Sr)MnO_3$ electrodes of solid oxide fuel cells. Journal of Solid State Electrochemistry, 2004. 8(11): p. 914-922.
36. Jiang, S.P. and Wang, W., Sintering and grain growth of $(La,Sr)MnO_3$ electrodes of solid oxide fuel cells under polarization. Solid State Ionics, 2005. 176(13-14): p. 1185-1191.

37. Dulli, H., Dowben, P.A., Liou, S.H., and Plummer, E.W., Surface segregation and restructuring of colossal-magnetoresistant manganese perovskites $La_{0.65}Sr_{0.35}MnO_3$. Physical Review B, 2000. 62(22): p. 14629-14632.

38. Mannella, N., Rosenhahn, A., Nambu, A., Sell, B.C., Mun, B.S., Yang, S.H., Marchesini, S., Watanabe, M., Ibrahim, K., Ritchey, S.B., Tomioka, Y., and Fadley, C.S., Surface characterization of colossal magnetoresistive manganites $La_{1-x}Sr_xMnO_3$ using photoelectron spectroscopy. Journal of Electron Spectroscopy and Related Phenomena, 2006. 153(1-2): p. 37-57.

39. Jin, T. and Lu, K., Compatibility between AISI441 alloy interconnect and representative seal glasses in solid oxide fuel/electrolyzer cells. Journal of Power Sources, 2010. 195(15): p. 4853-4864.

40. Mahapatra, M.K. and Lu, K., Effect of atmosphere on interconnect-seal glass interaction for solid oxide fuel/electrolyzer cells. Journal of the American Ceramic Society, 2011. 94(3): p. 875-885.

41. Tietz, F. and Sebold, D., Interface reactions between electrically conductive ceramics and ferritic steel-I. The system Cr-22Fe-0.5Mn/Mn_2O_3/(La,Ca)(Cr,Co,Cu)O_3. Materials Science and Engineering B-Advanced Functional Solid-State Materials, 2008. 150(2): p. 135-140.

42. Lee, H.Y., Cho, W.S., Oh, S.M., Wiemhofer, H.-D., and Gopel, W., Active reaction sites for oxygen reduction in $La_{0.9}Sr_{0.1}MnO_3$/YSZ electrodes. Journal of the Electrochemical Society, 1995. 142(8): p. 2659-2664.

43. Backhaus-Ricoult, M., Adib, K., Clair, T.S., Luerssen, B., Gregoratti, L., and Barinov, A., In-situ study of operating SOFC LSM/YSZ cathodes under polarization by photoelectron microscopy. Solid State Ionics, 2008. 179(21-26): p. 891-895.

44. Badwal, S.P.S., Deller, R., Foger, K., Ramprakash, Y., and Zhang, J.P., Interaction between chromia forming alloy interconnects and air electrode of solid oxide fuel cells. Solid State Ionics, 1997. 99(3-4): p. 297-310.

45. Horita, T., Xiong, Y.P., Kishimoto, H., Yamaji, K., Brito, M.E., and Yokokawa, H., Chromium poisoning and degradation at (La,Sr)MnO_3 and (La,Sr)FeO_3 cathodes for solid oxide fuel cells. Journal of the Electrochemical Society, 2010. 157(5): p. B614-B620.

46. Jiang, S.P. and Zhen, Y.D., Mechanism of Cr deposition and its application in the development of Cr-tolerant cathodes of solid oxide fuel cells. Solid State Ionics, 2008. 179(27-32): p. 1459-1464.

Chapter 6

Conclusions and future directions

6.1. Conclusions

After the thermal treatment at 800°C for 500 h, the microstructure of the LSM porous layer changes. For different stoichiometries after sintering, the LSM95 sample shows the most compact network. For the other two samples, local porous regions are more prevalent and the grains in the LSM100 and LSM105 samples bond less. After thermal treatment in different moisture levels, the LSM100 grains show more grain growth and bonding in dry air than that in moisture atmospheres. A 200 $mA \cdot cm^{-2}$ current density significantly prohibits the grain growth and bonding during the thermal treatment for LSM95 and LSM105. The polarization effect of the microstructure is less extensive for the LSM100 sample.

The bonding between the YSZ and the LSM is affected by the atmosphere; it is more extensive as the moisture content increases. For the LSM100 sample, at the YSZ/LSM interface, moisture leads to La-containing particle formation on the YSZ surface. Higher moisture leads to more extensive particle formation and Mn depletion at the YSZ surface. For the different stoichiometries, LSM95 shows the strongest bonding between the YSZ substrate and the LSM porous layer while LSM105 shows the poorest bonding of this interface.

Surface segregation of Sr and La is detected for all the LSM samples. Small amounts of Cr deposition are also observed at the LSM surface in all cases. The Cr deposition amount is slightly higher for the samples thermally treated in the moisture atmosphere. A small amount of $Cr_{1.5}Mn_{1.5}O_4$ is detected on the LSM surface for all the samples, and $SrMn_3O_{6-x}$ is identified for the samples thermally treated in the moisture atmospheres. For different stoichiometries, Cr surface deposition inhibits the surface segregation of La and Sr for the LSM100 and LSM105 samples. For the LSM95 sample, the Sr surface segregation is accelerated by the Cr deposition. $SrMn_3O_{6-x}$ is identified in LSM95 and $Cr_{1.5}Mn_{1.5}O_4$ is identified in both LSM95 and LSM100. The cathodic polarization changes the Cr deposition across the LSM porous layer, but did not lead to formation of more other phases at the LSM surface.

Cr deposition is detected across the porous LSM layer and shows various deposition amounts at the YSZ/LSM interface. For the conditions without an electric current applied, Cr deposition decreases with increasing distance from the AISI 441 interconnect but increases again and enriches at the YSZ/LSM interface for LSM95 and LSM100. The YSZ/LSM surface for LSM105 shows higher La concentration and less Cr deposition.

With the 200 $mA \cdot cm^{-2}$ current density during the thermal treatment, the Cr deposition increases at the locations close to the YSZ/LSM interface and decreases at the locations close to the LSM/AISI 441 interface compared to the condition without an electric current. For the LSM95 sample the current causes the highest Cr deposition at the TPB area, which is the result of the excessive Mn. The LSM100 and LSM105 samples show much less Cr deposition because the YSZ/LSM interaction forms $La_2Zr_2O_7$ phase and inhibits the Cr deposition. The most significant Cr deposition takes place at the YSZ/LSM interface when both excessive Mn in the LSM and the cathodic polarization are present.

6.2. Future Work Suggestions

For the interactions discussed above especially at the YSZ/LSM interface, with polarization and Cr deposition, the process is very complex. In the future, more study can be carried on to improve the understanding of the process.

1. The microstructure of the porous electrode affects the Cr vapor phase diffusion as well as the TPB length. Better control and quantitative characterization of the 3-D porous structure can help to improve the material's development. The advanced manufacturing technique helps to finely control the porous structure, and the new characterization techniques such as FIB 3-D tomography provide the quantitative results for optimization.
2. For the interaction research, improving the characterization is critical. If the resolution and detection limit of EDS, XRD, and XPS can be improved, more detailed composition and phase information of the materials can be achieved. On the other hand, developing new methods for the sample preparation can work as well, such as simplifying the YSZ/LSM interface as thin film deposition and using high Cr containing materials to increas Cr deposition in a shorter amount of time. The simplified samples can bring more significant results for analyzing the interactions.

Furthermore, rather than carrying out experiments, the data from the simplified samples can be used for computer simulation.

3. The interfacial interactions and the vapor phase deposition research could include more possible impurities such as Si, K (from glass sealing materials), S, and P (from contaminations of the fuel gas or air). In practice, other potential contaminations can also lead to degradation of the system too.